

# DESIGN, FABRICATION, AND CHARACTERISATION OF THREE-DIMENSIONAL PHOTONIC QUASICRYSTALS

Zur Erlangung des akademischen Grades eines  
DOKTORS DER NATURWISSENSCHAFTEN  
von der Fakultät für Physik des  
Karlsruher Instituts für Technologie (KIT)

genehmigte

DISSERTATION

von

Diplom-Physikerin Alexandra Ledermann  
aus Heidelberg

Tag der mündlichen Prüfung:	22.01.2010
Referent:	Prof. Dr. Martin Wegener
Korreferent:	Prof. Dr. Kurt Busch







# Publications

## Parts of this thesis have already been published:

In scientific journals and books:

- A. Ledermann, M. Wegener, and G. von Freymann, *Rhombicuboctahedral three-dimensional photonic quasicrystals*, Adv. Mater., accepted (2009).  
[DOI: 10.1002/adma.200903885]
- A. Ledermann, D. S. Wiersma, M. Wegener, and G. von Freymann, *Multiple scattering of light in three-dimensional photonic quasicrystals*, Opt. Express **17**, 1844 (2009).
- A. Ledermann, G. von Freymann, and M. Wegener, *Laue-Beugung auf dem Schreibtisch. Photonische Quasikristalle*, Physik in unserer Zeit **38**, 300 (2007).
- A. Ledermann, L. Cademartiri, M. Hermatschweiler, C. Toninelli, G. A. Ozin, D. S. Wiersma, M. Wegener, and G. von Freymann, *Three-dimensional photonic quasicrystals: Fabrication and characterization*, in Advances in Nanophotonics II: AIP Conference Proceedings **959**, 97 (American Institute of Physics, Melville, NY, 2007).
- A. Ledermann, L. Cademartiri, M. Hermatschweiler, C. Toninelli, G. A. Ozin, D. S. Wiersma, M. Wegener, and G. von Freymann, *Three-dimensional silicon inverse photonic quasicrystals for infrared wavelengths*, Nature Mater. **5**, 942 (2006).

At international conferences and colloquia (only own presentations):

- A. Ledermann, M. Kallenberg, D. S. Wiersma, M. Wegener, and G. von Freymann, *Multiple Scattering of Light in Three-Dimensional Photonic Quasicrystals*, contributed talk, Conference on Lasers and Electro-Optics and the International Quantum Electronics Conference (CLEO/IQEC), Baltimore, MD, U.S.A., June 2009.
- A. Ledermann, D. S. Wiersma, M. Wegener, and G. von Freymann, *Three-dimensional photonic quasicrystals*, invited talk, Colloquium at the University of Arizona, Tucson, AZ, U.S.A., January 2009.
- A. Ledermann, D. S. Wiersma, M. Wegener, and G. von Freymann, *Optical properties of three-dimensional photonic quasicrystals and their periodic approximants*, invited talk, The 39th Winter Colloquium on the Physics of Quantum Electronics (PQE), Snowbird, UT, U.S.A., January 2009.

- A. Ledermann, C. Toninelli, L. Cademartiri, G. A. Ozin, D. S. Wiersma, M. Wegener, and G. von Freymann, *Optical transport properties of three-dimensional photonic quasicrystals*, contributed talk, Conference on Lasers and Electro-Optics and the Quantum Electronics and Laser Science Conference (CLEO/QELS), San Jose, CA, U.S.A., May 2008.
- A. Ledermann, C. Toninelli, D. S. Wiersma, M. Wegener, and G. von Freymann, *Optical properties of three-dimensional photonic quasicrystals and their periodic approximants*, contributed talk, DPG Frühjahrstagung: Quantenoptik und Photonik, Darmstadt, Germany, March 2008.
- A. Ledermann, C. Toninelli, D. S. Wiersma, M. Wegener, and G. von Freymann, *Optical properties of three-dimensional photonic quasicrystals and their periodic approximants*, poster, 403. WE-Heraeus-Seminar: Periodic Nanostructures for Photonics, Bad Honnef, Germany, February 2008.
- A. Ledermann, L. Cademartiri, M. Hermatschweiler, C. Toninelli, G. A. Ozin, D. S. Wiersma, M. Wegener, and G. von Freymann, *Three-dimensional polymer and silicon inverse photonic quasicrystals for infrared frequencies*, poster, Photonic and Electromagnetic Crystal Structures Conference (PECS VII), Monterey, CA, U.S.A., April 2007.
- A. Ledermann, L. Cademartiri, M. Hermatschweiler, C. Toninelli, G. A. Ozin, D. S. Wiersma, M. Wegener, and G. von Freymann, *Three-dimensional polymer and silicon inverse photonic quasicrystals for infrared frequencies*, contributed talk, DPG Frühjahrstagung: Halbleiterphysik, Regensburg, Germany, March 2007.
- A. Ledermann, M. Wegener, L. Cademartiri, G. A. Ozin, D. S. Wiersma, and G. von Freymann, *Fabrication of three-dimensional photonic quasicrystals for the near-infrared spectral region*, contributed talk, Conference on Lasers and Electro-Optics and the Quantum Electronics and Laser Science Conference (CLEO/QELS), Long Beach, CA, U.S.A., May 2006.
- A. Ledermann, M. Wegener, L. Cademartiri, G. A. Ozin, D. S. Wiersma, and G. von Freymann, *3D photonic quasicrystals for near-infrared frequencies*, contributed talk, DPG Frühjahrstagung: Quantenoptik und Photonik, Frankfurt, Germany, March 2006.

# Contents

<b>Zusammenfassung</b>	<b>vii</b>
<b>1 Introduction</b>	<b>1</b>
<b>2 Fundamentals of Photonic Quasicrystals</b>	<b>5</b>
2.1 Introduction to Photonic Systems . . . . .	5
2.1.1 Photonic Crystals . . . . .	8
2.1.2 Disordered Photonic Systems . . . . .	11
2.2 Photonic Quasicrystals . . . . .	13
2.2.1 Theoretical Description . . . . .	14
2.2.2 Realisation of Photonic Quasicrystals . . . . .	19
2.2.3 Optical Properties of Photonic Quasicrystals . . . . .	20
<b>3 The Cut-and-Project Method</b>	<b>25</b>
3.1 Fundamentals of the Cut-and-Project Method . . . . .	25
3.1.1 Projection Matrix $\mathcal{M}$ . . . . .	28
3.1.2 Internal Space and Rational Approximants . . . . .	30
3.2 Three-Dimensional Icosahedral Quasicrystal and its Rational Approximants . . . . .	33
3.3 Three-Dimensional Rhombicuboctahedral Quasicrystal . . . . .	37
<b>4 Fabrication, Characterisation and Calculation Techniques</b>	<b>43</b>
4.1 Fabrication via Direct Laser Writing . . . . .	43
4.2 Optical Characterisation . . . . .	46
4.2.1 Laue Diffraction Measurements . . . . .	46
4.2.2 Time-Resolved Transmittance Spectroscopy . . . . .	46
4.2.3 Transmittance and Reflectance Measurements . . . . .	48
4.2.4 Normal Incidence and Angle-Resolved Transmittance Spectroscopy . . . . .	49
4.3 Scattering Matrix Calculations . . . . .	50
4.3.1 Transmittance and Reflectance . . . . .	50
4.3.2 Polarisation-Resolved Transmittance . . . . .	56
4.3.3 Time-Resolved Transmittance . . . . .	60
<b>5 Three-Dimensional Icosahedral Photonic Quasicrystals</b>	<b>63</b>
5.1 Fabrication of High-Quality SU-8 Samples . . . . .	63
5.2 Experimental Studies of Optical Properties and Initial Interpretation . . . . .	70
5.2.1 Transmittance and Reflectance Spectra . . . . .	70

---

5.2.2	Time-Resolved Transmittance Spectra . . . . .	77
5.3	Calculations and Re-Interpretation of Experimental Results . . . . .	81
5.3.1	Test of Rational Approximant Approach . . . . .	81
5.3.2	Time-Resolved Transmittance Calculations . . . . .	84
5.3.3	Normal Incidence Transmittance and Reflectance Spectra . . . . .	89
5.3.4	Laue Diffraction Patterns . . . . .	93
5.4	Silicon Inverse Icosahedral Photonic Quasicrystals . . . . .	95
<b>6</b>	<b>Three-Dimensional Rhombicuboctahedral Photonic Quasicrystals</b>	<b>97</b>
6.1	Blueprint of Three-Dimensional Rhombicuboctahedral Quasicrystals . . . . .	97
6.2	Fabrication of High-Quality SU-8 Samples . . . . .	100
6.3	Laue Diffraction Patterns . . . . .	102
6.4	Experimental Studies of Optical Properties . . . . .	105
<b>7</b>	<b>Conclusions and Outlook</b>	<b>111</b>
<b>A</b>	<b>Shaded-Ring Filter and Voxel-Shape</b>	<b>117</b>
	<b>Bibliography</b>	<b>119</b>
	<b>Acknowledgements</b>	<b>127</b>

# Zusammenfassung

Das Forschungsgebiet der Photonik hat trotz seiner relativ jungen Geschichte bereits enormen Einfluss auf unser tägliches Leben genommen. Laser werden in der industriellen Produktion und chirurgischen Medizin eingesetzt, Leuchtdioden ersetzen nach und nach unsere ineffizienten konventionellen Glühbirnen, und Glasfasern ermöglichen die optische Datenübertragung mit sehr hohen Datenraten. Die Erfindung der optischen Glasfaser und die des CCD-Sensorchips wurden mit dem Physik-Nobelpreis 2009 ausgezeichnet. Diese und viele weitere Anwendungen der Photonik entwickelten sich aus der Grundlagenforschung und werden stets weiter verbessert oder durch Neuentdeckungen ergänzt. Hierfür suchen Wissenschaftler ständig nach neuen innovativen Designs, um das Licht und sein Ausbreitungsverhalten gemäß bestimmter Anforderungen zu beeinflussen und zu lenken. Für diesen Zweck ist der Einsatz von künstlich hergestellten photonischen Systemen – Systeme, die aus mindestens zwei verschiedenen Materialien unterschiedlicher Brechungsindizes aufgebaut und auf einer optischen Längenskala strukturiert sind – sehr aussichtsreich. Der Zusammenhang zwischen dem speziellen Design eines photonischen Systems und dessen Einfluss auf die Lichtausbreitung ist eine fundamentale Fragestellung aktueller Forschung. Denn dieses Wissen bildet die Grundlage dafür, photonische Systeme für spezielle optische Anwendungen zu entwickeln und zu konzipieren. Ein vielversprechendes Forschungsfeld innerhalb der photonischen Systeme beschäftigt sich mit photonischen Quasikristallen. Diese zeigen eine einzigartige, komplexe Struktur, die eine langreichweitige Ordnung und eine hochgradige Rotationssymmetrie aufweist, jedoch keine Translationssymmetrie besitzt. Das Licht wird vielfach gestreut und bewegt sich deshalb auf komplizierten Wegen durch die Struktur. Dadurch ergibt sich ein erstaunliches und vielfältiges Ausbreitungsverhalten des Lichts bzw. der Photonen.

Die systematische Erforschung von (dreidimensionalen) photonischen Systemen begann, als im Jahre 1987 das Konzept der photonischen Kristalle – auch bekannt unter dem Namen „photonische Bandlückenmaterialien“ – eingeführt wurde. Photonische Kristalle sind periodisch strukturierte dielektrische Materialien und werden als optisches Analogon der elektronischen Halbleiter betrachtet. Bei geeignetem Design weisen sie eine vollständige photonische Bandlücke auf, d.h. Licht gewisser Wellenlängen kann nicht durch die Struktur propagieren, sondern wird vollständig reflektiert.

Neben der Untersuchung perfekter photonischer Kristalle rückte der Einfluss von Defekten und Unordnung zunehmend in den Blickpunkt der Forschung. Ein sogenannter Punktdefekt kann die Lokalisierung von Licht innerhalb des photonischen Kristalls ermöglichen, wenn der Defekt gerade für Wellenlängen innerhalb der photonischen Bandlücke erlaubte Moden bereitstellt. Mit zunehmender Anzahl an Defekten bzw. zunehmender Unordnung verlieren photonische Kristalle ihre Bandstruktur, und diffuse Streuung an Defekten gewinnt an Bedeutung. Die

hierbei rückwärts gestreuten Lichtwellen können sich mit den vorwärts laufenden Lichtwellen konstruktiv überlagern, wodurch die Ausbreitung des Lichtes stark verlangsamt wird. Ab einem gewissen Grad an Unordnung kann diffuse Streuung sogar zur sogenannten Anderson-Lokalisierung der Photonen führen.

Erst vor wenigen Jahren fand die Strukturart der Quasikristalle, die in der Festkörperphysik seit 1984 bekannt ist, ihren Einzug in den Bereich der photonischen Systeme als sogenannte photonische Quasikristalle. Die Besonderheit der Quasikristallstruktur zeigt sich darin, dass sie eine langreichweitige Ordnung besitzt, die sich nicht auf Translationsinvarianz stützt. Vielmehr weisen Quasikristalle (hochgradige) Rotationssymmetrien auf, die mit Periodizität nicht kompatibel sind. Die fehlende Periodizität in Quasikristallstrukturen unterbindet die Möglichkeit, die zu erwartenden Eigenschaften mit den bisher bekannten theoretischen Konzepten, die sich auf Translationsinvarianz stützen, zu beschreiben. Bis jetzt konnte auch noch keine äquivalente Theorie für (zwei- und dreidimensionale) Quasikristalle entwickelt werden. Aufgrund der Tatsache, dass Quasikristalle einerseits deterministisch geordnete Strukturen sind und andererseits eine Vielzahl an nicht-äquivalenten quasiperiodischen Gitterpunkten besitzen, die sich in der Anordnung der benachbarten Gitterpunkte unterscheiden, werden Quasikristalle oft als Strukturart zwischen periodisch geordneten und amorphen (ungeordneten) Strukturen angesehen. Von photonischen Quasikristallen erwartet man daher die Existenz einer Bandstruktur ähnlich den photonischen Kristallen mit vielen sogenannten „Pseudo-Bandlücken“, die sich auf Minima in der Zustandsdichte zurückführen lassen. Allerdings wird die Bandstruktur der photonischen Quasikristalle wegen deren hochgradigen Rotationssymmetrien, die für periodische Strukturen nicht möglich sind, isotroper sein als die photonischer Kristalle, d.h. für verschiedene Raumrichtungen variiert die spektrale Lage der Pseudo-Bandlücken in photonischen Quasikristallen weniger als in photonischen Kristallen. Dies könnte den spektralen Überlapp der Pseudo-Bandlücken in allen Raumrichtungen und damit das Erzeugen einer sogenannten kompletten Bandlücke erleichtern. Aufgrund der vielen nicht-äquivalenten Gitterpunkte verspricht man sich außerdem verschiedenartige Ausprägungen von Lichtmoden und vielfältige optische Charakteristika. Das Verständnis dieser Phänomene eröffnet neue Möglichkeiten, photonische Systeme für spezifische optische Anwendungen zu konzipieren.

Die Struktur eines Quasikristalls ist sehr komplex und kann nicht so intuitiv wie die eines periodischen Kristalls durch Aneinanderreihen identischer Einheitszellen veranschaulicht werden. Seit ihrer Entdeckung wurden daher einige Methoden entwickelt, um Quasikristallstrukturen in ein, zwei und drei Dimensionen zu erzeugen. Im Rahmen dieser Arbeit wird die sogenannte „cut-and-project“-Methode zur Berechnung von dreidimensionalen Quasikristallen mit ikosaedrischer und rhombenkuboktaedrischer Symmetrie angewandt. Das ihr zugrunde liegende Konzept ist, eine quasiperiodische Struktur einer bestimmten Dimension mithilfe einer periodischen Struktur einer höheren Dimension zu konstruieren. Für den Fall eines dreidimensionalen ikosaedrischen Quasikristalls wird hierbei eine Sektion eines fiktiven sechsdimensionalen einfach-kubischen Gitters in den dreidimensionalen physikalischen Raum projiziert. Die Größe der Sektion wird hierbei durch die Projektion der Wigner-Seitz-Zelle des sechsdimensionalen Gitters in den verbleibenden dreidimensionalen sogenannten internen Raum, der senkrecht auf dem physikalischen Raum steht, bestimmt. Auf ähnliche Weise wird der dreidimensionale rhombenkuboktaedrische Quasikristall erzeugt: Eine Sektion eines fiktiven zwölfdimensionalen

einfach-kubischen Gitters wird in den dreidimensionalen physikalischen Raum projiziert. Die Größe der Sektion wird durch die Projektion der Wigner-Seitz-Zelle des zwölfdimensionalen Gitters in den verbleibenden neundimensionalen internen Raum, der senkrecht auf dem physikalischen Raum steht, bestimmt. Während die Projektionsvorschrift für den ikosaedrischen Fall bereits aus der Literatur bekannt ist, wird diese für den Fall des rhombenkuboktaedrischen Quasikristalls im Rahmen dieser Arbeit selbst erstellt. Mit der erfolgreichen Konstruktion dieser Projektionsvorschrift wird die Klasse der rhombenkuboktaedrischen Quasikristalle erstmals eingeführt. In den generierten Quasikristallstrukturen werden die einzelnen quasiperiodischen Gitterpunkte auf wohldefinierte Weise verbunden, um durch die so entstandenen Netzwerke die Stabilität der Strukturen zu gewährleisten. Die eingeführten Verbindungen stören die quasiperiodische Symmetrie der Strukturen nicht, wie sich experimentell anhand der erzeugten Laue-Beugungsbilder belegen lässt. Als Verbindungslänge werden wenige Mikrometer gewählt, so dass die photonischen Quasikristalle interessante optische Charakteristika und ihre erwarteten fundamentalen photonischen Pseudo-Bandlücken im infraroten Spektralbereich aufweisen.

Die berechneten Netzwerke an Quasikristallstrukturen werden mit der Technik des Direkten Laserschreibens mittels Multi-Photon-Polymerisation im Photolack SU-8 realisiert. Diese Technik ermöglicht im Prinzip die Herstellung beliebiger dreidimensionaler Strukturen mit sub-beugungsbegrenzten Strukturgrößen. Ein gepulster Laser mit einer Photonenenergie unterhalb der Ein-Photon-Absorptionskante wird durch ein Mikroskopobjektiv sehr stark in ein photoempfindliches Material, in diesem Fall in den Photolack SU-8, fokussiert. Im Bereich des Fokus ist die Intensität ausreichend hoch, um den Photolack durch Multiphoton-Prozesse zu belichten. Das belichtete Volumen, das als „Voxel“ bezeichnet wird, ist elliptisch geformt, wobei die lange Achse entlang der optischen Achse des Objektivs liegt. Durch Verschieben des Photolacks relativ zur Fokusposition lässt sich eine beliebige dreidimensionale Struktur in den Photolack schreiben.

Der Hauptteil dieser Arbeit widmet sich der Herstellung und der Charakterisierung von dreidimensionalen photonischen Quasikristallen mit ikosaedrischer und rhombenkuboktaedrischer Symmetrie. Zur Charakterisierung der strukturellen Qualität werden Elektronenmikroskop-Aufnahmen sowie die vom photonischen Quasikristall erzeugten Laue-Beugungsbilder herangezogen. Die erwarteten Beugungsbilder lassen sich über eine modifizierte Form der „cut-and-project“-Methode berechnen, die die eingeführten Verbindungslinien jedoch nicht berücksichtigt. Die optischen Eigenschaften werden anhand von Transmissions- und Reflexionsexperimenten sowie mittels zeitaufgelöster Transmissionsspektroskopie untersucht. Zur Bewertung der experimentellen Spektren werden geeignete Streumatrix-Rechnungen herangezogen.

Kapitel 5 dieser Arbeit befasst sich mit der Klasse der dreidimensionalen photonischen Quasikristalle mit ikosaedrischer Symmetrie. Diese Klasse ist bereits seit 1984 aus elektronischen Systemen bekannt, hält jedoch immer noch einige Überraschungen bezüglich ihrer besonderen Eigenschaften bereit. Die für den infraroten Spektralbereich hergestellten photonischen Quasikristallstrukturen zeigen eine hohe strukturelle Qualität. Die Laue-Beugungsbilder zeigen die erwartete ikosaedrische Symmetrie. Die beobachtete gute Übereinstimmung der gemessenen und berechneten Laue-Beugungsbilder lässt erschließen, dass die eingeführten Verbindungen die quasiperiodische Symmetrie der Strukturen nicht stören. Wird die Dicke der Strukturen erhöht, so ist jedoch zu beobachten, dass die Laue-Beugungsbilder unerwarteterweise einen

körnigen Untergrund (Specklemuster) entwickeln, der an von Unordnung ausgelöste diffuse Streuung erinnert. Da zudem die einzelnen Beugungspunkte immer schärfer werden, wird es insgesamt mit zunehmender Dicke schwieriger, die Symmetrie der Laue-Beugungsbilder zu erkennen. In Transmissions- und Reflexionsexperimenten werden Hinweise auf die Existenz einer fundamentalen Pseudo-Bandlücke gefunden, die für eine ikosaedrische Quasikristallstruktur mit einer Verbindungslänge von  $2\ \mu\text{m}$  an der spektralen Position von etwa  $4\ \mu\text{m}$  liegt. Ihre spektrale Position verschiebt sich wie erwartet mit Veränderung der Verbindungslänge oder des effektiven Brechungsindex.

Die experimentellen Untersuchungen an den ikosaedrischen Quasikristallstrukturen offenbaren weitere unerwartete optische Eigenheiten, die üblicherweise mit ungeordneten photonischen Systemen assoziiert werden. Die Summe der gemessenen Transmissions- und Reflexionsspektren, die in dem verwendeten experimentellen Aufbau nur innerhalb eines begrenzten Öffnungswinkels aufgenommen werden, ist deutlich unter 1, d.h. ein bedeutender Anteil des einfallenden Lichts wird in einen Raumwinkel gestreut, der nicht detektiert wird. Außerdem zeigen zeitaufgelöste Transmissionsmessungen, dass zeitlich kurze gaußförmige Lichtimpulse (etwa 150 Femtosekunden) bei der Propagation durch die Struktur stark verzögert werden und sich verformen, d.h. insbesondere einen exponentiellen zeitlichen Abfall ausbilden. Die Werte der Verzögerung sowie der Zeitkonstanten des exponentiellen Abfalls hängen von der zentralen Wellenlänge des einfallenden gaußförmigen Lichtimpulses (d.h. von den Eigenschaften der gerade untersuchten Bänder der photonischen Bandstruktur) und der Dicke der Struktur ab. Nach der Transmission durch die Struktur sind die zunächst linear polarisierten Lichtimpulse stark depolarisiert, d.h. ein wesentlicher Anteil des Lichts hat den Polarisationsstatus beim Durchgang verändert. Das Pendant zu den beobachteten langen Abfällen in der Zeitdomäne sind spektral schmale Strukturen in der Frequenzdomäne. Diese werden auch experimentell mittels eines speziellen Transmissionsaufbaus, bei dem das Ideal einer senkrecht einfallenden ebenen Welle fast erreicht wird, nachgewiesen.

Mithilfe eines neu entwickelten theoretischen Modells können diese experimentellen Ergebnisse, die üblicherweise mit Unordnung in photonischen Systemen assoziiert werden, intrinsischen optischen Eigenschaften der (idealen) ikosaedrischen photonischen Quasikristalle zugeschrieben werden. Das theoretische Modell basiert auf einer Kombination der Rationale-Approximanten-Methode mit Streumatrix-Rechnungen. Rationale Approximanten sind periodische Strukturen, die innerhalb ihrer Einheitszelle mit dem ursprünglichen Quasikristall identisch sind. Hierbei unterscheidet man verschiedene Ordnungen der rationalen Approximanten, die sich auf die Größe der Einheitszelle beziehen. Zunächst wird die Anwendbarkeit des theoretischen Modells überprüft. Dazu werden verschiedene Ordnungen von rationalen Approximanten und die zugehörige Quasikristallstruktur mittels Direkten Laserschreibens hergestellt und im Anschluss deren winkelaufgelöste Transmissionsspektren experimentell und theoretisch ausgewertet. Es zeigt sich, dass die experimentell aufgenommenen Spektren der rationalen Approximanten mit zunehmender Größe der Einheitszelle gegen das Spektrum des Quasikristalls konvergieren. Zudem ist eine sehr gute Übereinstimmung zwischen Experiment und Theorie zu finden. In weiteren geeigneten Streumatrix-Rechnungen können die bereits erwähnten experimentellen Ergebnisse der Transmissions- und Reflexionsmessungen sowie der zeitaufgelösten Transmissionsspektroskopie reproduziert und auf Vielfachstreuung innerhalb der komplexen, langreichweitig geordneten Quasikristallstruktur zurückgeführt werden. Durch Vielfachstreuung ergeben sich für die Photonen komplizierte räumliche Wege durch den photonischen Qua-

sikristall, die sich abhängig von der gewählten Wellenlänge entweder größtenteils konstruktiv oder destruktiv überlagern, was zu spektral schmalen Strukturen bzw. langen zeitlichen Abfällen führt. Vielfachstreuung erklärt auch die beobachtete Dickenabhängigkeit der Effekte, da mit zunehmender Dicke die Zahl der Streuzentren erhöht wird. Außerdem wird das vielfach gestreute Licht in zahlreiche Beugungsordnungen gebeugt, weshalb bei Transmissions- und Reflexionsexperimenten, die nicht den gesamten (jeweiligen) Halbraum detektieren, in der Summe Werte kleiner als 1 gemessen werden. Je dicker die Quasikristallstruktur ist, desto mehr Intensität gelangt durch Vielfachstreuung in die vielen verschiedenen Beugungsordnungen des mit Beugungspunkten unendlich dicht besetzten Laue-Beugungsbildes. Dies erklärt das experimentell beobachtete Auftreten des körnigen Untergrunds (Specklemuster) in den Laue-Beugungsbildern von dickeren Strukturen.

Auch in ungeordneten photonischen Systemen spielt Vielfachstreuung des Lichts eine wesentliche Rolle. Daher liegt die Vermutung nahe, dass der Transportmechanismus des Lichts in ikosaedrischen photonischen Quasikristallen dem in ungeordneten photonischen Systemen ähnlich ist. Die theoretische Studie darüber, wie sich das gesamte transmittierte Licht (d.h. alle vorwärts gestreuten Beugungsordnungen sind berücksichtigt) mit der Dicke der Struktur verhält, zeigt jedoch, dass der Transportmechanismus in den Quasikristallstrukturen weder dem Ohmschen Gesetz folgt, wie es für ungeordnete photonische Systeme erwartet wird, noch dem Beerschen Gesetz, das für periodische (langreichweitig geordnete) photonische Kristalle gilt. Für viele Wellenlängen sinkt die Transmission innerhalb eines bestimmten Dickenbereichs auf einen konstanten Wert ungleich 0, was vermutlich gerade dem Lichtanteil entspricht, der das Laue-Beugungsbild ausbildet.

Insgesamt machen die Experimente und die theoretischen Berechnungen deutlich, dass die Vielfachstreuung von Licht innerhalb der auf langreichweitiger Ordnung basierenden, komplexen Quasikristallstruktur von großer Bedeutung ist, um die optischen Eigenschaften ikosaedrischer photonischer Quasikristalle zu verstehen, selbst für die im Rahmen dieser Arbeit untersuchten Polymerstrukturen, die einen recht geringen Brechungsindexkontrast aufweisen. Die optischen Eigenschaften zeigen Merkmale, die üblicherweise ungeordneten Systemen zugeschrieben werden. Sie weisen aber auch Besonderheiten auf, die sich von ungeordneten Systemen unterscheiden, wie sich beispielsweise im Transportverhalten und in den schönen, klar definierten Laue-Beugungsbildern zeigt.

Im Kapitel 6 dieser Arbeit wird die neue Klasse der dreidimensionalen rhombenkuboktaedrischen Quasikristalle vorgestellt. Die Polymerstrukturen bekunden im Laue-Beugungsbild die erwartete rhombenkuboktaedrische Symmetrie. Die experimentellen Untersuchungen an diesen Quasikristallstrukturen ergeben Resultate, die qualitativ mit denen an den ikosaedrischen vergleichbar sind: Die Laue-Beugungsbilder lassen eine klare Dickenabhängigkeit erkennen. Transmissions- und Reflexionsmessungen, bei denen das Licht nur innerhalb eines eingeschränkten Öffnungswinkels detektiert wird, zeigen in der Summe Werte deutlich kleiner als 1. Zeitlich kurze, linear polarisierte, gaußförmige Lichtimpulse werden bei der Propagation stark verlangsamt, entwickeln einen exponentiellen Abfall und sind depolarisiert. Die Verzögerung des transmittierten Lichtimpulses, die Zeitkonstanten des exponentiellen Abfalls sowie der Anteil an depolarisiertem Licht sind abhängig von der Dicke der Quasikristallstruktur und der zentralen Wellenlänge des einfallenden Lichtimpulses (d.h. von den Eigenschaften der gerade untersuchten Bänder der photonischen Bandstruktur).

Auf den ersten Blick scheinen die optischen Eigenschaften von ikosaedrischen und rhombenkuboktaedrischen Quasikristallen recht ähnlich. Quasiperiodizität bietet einen dichten Satz an reziproken Gittervektoren für Beugung, weshalb komplizierte Vielfachstreuung die Propagation der Photonen bestimmt. Dennoch werden auch merkbare Unterschiede zwischen diesen beiden Klassen erwartet, da sie sich in ihrer Quasikristallstruktur und damit in der Materialverteilung unterscheiden. Dies wird schon durch ihre verschiedenartige Symmetrie im Laue-Beugungsbild deutlich. Untersuchungen an zweidimensionalen photonischen Quasikristallen mit unterschiedlichen Symmetrien und Materialverteilungen haben gezeigt, dass die Materialverteilung ausschlaggebend ist für den Mechanismus, der die Ausbildung der Bandstruktur dominiert, und dass sie somit die zugehörigen optischen Eigenschaften beeinflusst. Ähnliches ist auch für den dreidimensionalen Fall zu erwarten.

Dieser Aspekt könnte in weiterführenden Experimenten untersucht werden, bei denen die optischen Eigenschaften und die Transporteigenschaften von ikosaedrischen und rhombenkuboktaedrischen Quasikristallen genau verglichen werden. Ein theoretisches Modell für rhombenkuboktaedrische Quasikristalle, ähnlich dem in dieser Arbeit eingeführten Modell für ikosaedrische Quasikristalle, könnte diese Analyse unterstützen. Zudem könnte eine genaue Untersuchung der Modenprofile, insbesondere an welchen (nicht-äquivalenten) Gitterpunkten der Quasikristallstruktur lokalisierte Moden auftreten, Aufschluss über den Einfluss der (lokalen) Symmetrie geben. Für die experimentellen Untersuchungen wäre eine weitere Reduzierung der Verbindungsstäbe unter 1 Mikrometer vorteilhaft, um die erwarteten fundamentalen Pseudo-Bandlücken in einen spektralen Bereich zu verschieben, der von konventionellen Detektoren, zum Beispiel von Silizium-Photodioden, abgedeckt wird. Die Reduzierung der Verbindungslänge würde gleichzeitig die Herstellung von effektiv dickeren Strukturen – die effektive Dicke ist in Relation zu der Verbindungslänge zu sehen und bestimmt die Anzahl der Streuzentren in Propagationsrichtung der Photonen – erleichtern, in denen folglich die Vielfachstreuung stärker zum Tragen kommt. Eine Verstärkung der auf Vielfachstreuung basierenden Effekte kann auch durch Konversion oder Inversion der Quasikristallstrukturen in hochbrechende Materialien erreicht werden. Dies ist im Rahmen dieser Arbeit am Beispiel der ikosaedrischen Quasikristallstruktur, die erfolgreich in Silizium invertiert wird, gezeigt.

Dem Beispiel des rhombenkuboktaedrischen Quasikristalls folgend, könnten noch weitere Klassen an dreidimensionalen Quasikristallen mit neuen Symmetrien konstruiert werden. Diese neukonstruierten Klassen würden den Satz an dreidimensionalen Quasikristallen, der für zukünftige Untersuchungen ihrer einzigartigen optischen Eigenschaften, besonders hinsichtlich ihrer spezifischen Symmetrie, zur Verfügung steht, noch erweitern. Gleichzeitig eröffnen sich durch solche Neukonstruktionen Möglichkeiten für neue flexible Designs, um photonische Systeme mit besonderen Charakteristika der Lichtausbreitung für optische Anwendungen zu konzipieren. Vielleicht finden photonische Quasikristalle irgendwann ihren Weg in Anwendungen wie zum Beispiel neuartige Lasersysteme oder komplexe Lichtwellenleiter.

Dies sind nur einige wenige Vorschläge für künftige Arbeiten auf dem noch jungen Forschungsgebiet der photonischen Quasikristalle, die jedoch interessante und spannende Einblicke in die Eigenheiten von Quasiperiodizität und in die damit verknüpften optischen Charakteristika versprechen.

# Chapter 1

## Introduction

Photonics is a fairly novel field of research, yet its impact on our daily life is already obvious, e.g., lasers are applied in industrial production and for surgery, light-emitting diodes are replacing inefficient electric light bulbs, and optical fibres allow for high-speed optical data transmission. The inventions of optical fibres and of charge-coupled device sensor arrays have been honoured by the 2009 Nobel Prize in Physics. These and many other applications have evolved from basic research in the field of photonics, and are still improved and complemented by new inventions. Scientists are permanently seeking for novel designs to manipulate the propagation of light according to specific demands. For this purpose, the usage of artificially manufactured photonic systems – systems which are composed of at least two kinds of materials that differ in their respective refractive indices and which are artificially structured on an optical length scale – holds a lot of promise. The relation between the specific design of the photonic systems and its impact on light propagation is a fundamental issue of current research, as this knowledge forms the basis for engineering and tailoring photonic systems for specific optical applications. One exciting research field within photonic systems is dealing with photonic quasicrystals. Their unique complex structure with long-range order and high-degree rotational symmetry, yet without any translational symmetry, leads to complicated light scattering effects manifesting in astonishing and manifold photon propagation characteristics.

The systematic research on the field of (three-dimensional) photonic systems was initiated, as in 1987 the concept of photonic crystals – also known as photonic band gap materials – was introduced independently by E. Yablonovitch [1] and S. John [2]. Both proposed periodically structured dielectric materials to cause the photon dispersion relation to organise in bands, analogous to the electronic band structure in solid crystalline substances. The thereby occurring photonic stop bands are related to Bragg diffraction at the interfaces of the different dielectric materials. By carefully designing the photonic crystals, the band structure can be tailored according to specific requirements. In particular, photonic crystals can possess a complete photonic band gap: photons with frequencies within this gap cannot propagate through the structure, but are completely reflected.

Apart from investigating the properties of perfect photonic crystals, which are theoretically well understood, research activities have extended progressively towards investigating the effects of defects and disorder in such structures, as these promise new fascinating optical phenomena. A so-called point defect can provide the means of localising light within the

photonic crystal, if the defect offers allowed modes within the complete photonic band gap. By increasing the number of defects and thus the amount of disorder, Bragg diffraction dies out, i.e., disordered photonic crystals lose their well-defined band structure, and diffusive scattering at defects gains in importance. Backscattered waves can interfere constructively with waves propagating in forward direction, and thus reduce the transport of light. At a certain level of disorder diffuse scattering can even lead to so-called Anderson localisation [3] of the photons. Of particular interest is the study of the transition from ordered propagation via diffusion towards Anderson localisation of photons, which can be observed in increasingly disordered strongly scattering dielectric media (see, e.g., Ref. [4]). During the transition complex optical features and unique mode structures arise.

In recent years, the increasing flexibility in fabricating photonic systems of rather sophisticated deterministic designs has offered the means to push the research of photonic systems into a new promising direction dealing with quasiperiodic structures. Photonic quasicrystals have drawn interest as appealing design for light manipulation, as the electronic counterparts have revealed unusual and fascinating propagation properties for electrons. In 1984, Shechtman *et al.* [5] discovered electronic quasicrystals in metallic alloys as a new form of condensed matter, which differs from both, crystalline and disordered (amorphous) materials. Quasicrystals exhibit a noncrystallographic rotational order, which is incompatible with periodicity, combined with a long-range order, which was associated only with periodic structures until then. Researchers dealt with the obvious question whether quasiperiodicity generates physical properties which differ significantly from those of periodic crystals and of disordered systems. The electronic band structure of quasicrystals revealed a lot of “pseudo-gaps” related to minima in the density of states. In decagonal quasicrystalline alloys, which exhibit quasiperiodicity in a plane and periodicity in the direction perpendicular to this plane, the physical properties showed a corresponding anisotropy. In the quasiperiodic plane, the electric conductivity was very low, whereas it was high along the periodic direction. Introducing disorder reduced the conductivity in the periodic direction, but increased the low conductivity associated with quasiperiodicity. Similar findings were obtained from three-dimensional icosahedral electronic quasicrystals, the only class of real three-dimensional quasicrystals found in electronic systems to date. However, the observed unusual electronic properties are still not completely understood as electron-electron interaction and spin-orbit effects have to be considered and, moreover, quasiperiodicity precludes the application of the well-established concepts based on the translational invariance of solids. Since photons do not interact, photonic quasicrystals can assist the task of understanding and studying the impact of quasiperiodicity on the unique propagation properties.

Photonic quasicrystals, although disposing of periodicity, are deterministically ordered and exhibit a huge number of nonequivalent quasilattice sites, i.e., the configuration and the number of nearest neighbours varies for different sites. Thus, photonic quasicrystals are considered as an intermediate state between periodic and disordered systems. In periodic photonic crystals, the propagation characteristics of photons are determined by the photonic band structure, while in completely disordered photonic systems any band structure has vanished and diffusive scattering dominates the transport properties. Hence, the question arises, how photons will propagate in photonic quasicrystals. Based on the experimental results of electronic quasicrystals, one expects to obtain a kind of photonic band structure, similarly to

---

photonic crystals. Then again, the peculiarity of having many nonequivalent quasilattice sites promises to produce manifold features in the mode structure and diverse optical characteristics. Studying and understanding these phenomena will open new possibilities for tailoring photonic systems according to specific optical applications.

Most experiments dealing with photonic quasicrystals designed for the infrared regime, i.e., with features sizes in the  $\mu\text{m}$  range, are restricted to the one-dimensional and two-dimensional case. The complex structure of quasicrystals combined with the requirements of high structuring precision puts an enormous challenge on the fabrication process, especially if these photonic quasicrystals are to be structured in all three dimensions.

In this thesis, we will fabricate and optically characterise high-quality three-dimensional photonic quasicrystals operating at infrared frequencies. For the fabrication we will employ the technique of multi-photon direct laser writing, which provides the opportunity for arbitrarily structuring photosensitive materials in all three dimensions with sub-diffraction limited feature sizes. Following the model of electronic quasicrystals, we will study icosahedral three-dimensional photonic quasicrystals at first. By developing a suitable theoretical model for the first time we will be able to decently evaluate their optical properties.

Electronic systems are constrained to configurations that meet the condition of being thermodynamically stable or at least meta-stable. In photonics, no comparable limitations do exist. Accordingly, we will rationally construct and realise a novel class of three-dimensional photonic quasicrystals exhibiting rhombicuboctahedral symmetry rather than icosahedral symmetry. This rhombicuboctahedral class has not been observed in electronic systems yet.

## **Outline of this thesis**

In chapter 2, we will outline the characteristics of photonic quasicrystals. First, the basic concept of photonic systems and the underlying physics will be introduced. We will deal with periodic photonic crystals and disordered photonic systems, as photonic quasicrystals are commonly seen as an intermediate state in-between. Afterwards, we will focus on the peculiarities of quasiperiodic patterns. A brief overview of experimental realisations and previous studies on photonic quasicrystals will conclude this introduction.

The cut-and-project method will be described in chapter 3. This method provides the possibility to calculate quasiperiodic (and periodic) patterns, in particular these of three-dimensional quasicrystals of icosahedral and rhombicuboctahedral symmetry.

In chapter 4, the principle of direct laser writing and the corresponding experimental setup will be described, since we will use the technique of direct laser writing for fabricating high-quality three-dimensional nanostructures. The experimental setups for optically characterising the fabricated samples will be outlined in this chapter as well. The last section of this chapter will deal with the scattering matrix formalism, which will be applied to calculate the anticipated optical properties.

Chapter 5 will be dedicated to the experimental and theoretical work on three-dimensional icosahedral photonic quasicrystals. High-quality polymer (SU-8) icosahedral photonic qua-

quasicrystals will be used to investigate their optical properties. The existence of the anticipated pseudo-stop band in the photonic band structure will be revealed. Furthermore, photon propagation properties will be found which are usually associated with diffusion in disordered photonic systems. The development of a theoretical model based on scattering matrix calculations combined with appropriate periodic rational approximants will facilitate the interpretation of the experimental findings, namely as being intrinsic properties of (ideal) photonic quasicrystals caused by multiple scattering of light. Additionally, we will successfully demonstrate the ability to invert the structures into silicon to increase the refractive index contrast.

In chapter 6, we will introduce the novel class of three-dimensional rhombicuboctahedral photonic quasicrystals. Polymer (SU-8) nanostructures fabricated by direct laser writing will be characterised by electron microscopy and Laue diffraction. The optical properties will be studied by transmittance and reflectance spectroscopy as well as by time-resolved transmittance spectroscopy. The experimental findings will reveal similar features as for the icosahedral counterparts, demonstrating the impact of multiple scattering of light on the photon transport properties in these rhombicuboctahedral structures.

Finally, we will summarise our results obtained in the course of this thesis in chapter 7 and give an outlook on future experiments and research activities that will aim at gaining further insights into the specific properties of photonic quasicrystals.

# Chapter 2

## Fundamentals of Photonic Quasicrystals

The purpose of this chapter is to give a brief introduction to the materials called “photonic quasicrystals”. As the name implies, these structures belong to the superordinated class of photonic systems used to manipulate the propagation of light, and they exhibit quasiperiodic order. Although quasiperiodic order generates a perfect long-range ordered lattice – just as perfect periodic crystals –, it lacks translational symmetry, i.e., each quasiperiodic lattice site has a different local configuration of surrounding lattice sites, comparable to amorphous (disordered) systems. Thus, quasicrystals seem to combine features of both, periodic crystals and disordered (or glassy) systems.

To underline this, the chapter is structured as follows: First, the general concept of photonic systems and their impact on the photon propagation is introduced (section 2.1). Then, we get more specific by turning our focus on two important representatives of such photonic systems – periodic photonic crystals [1, 6, 7] (section 2.1.1) and disordered photonic systems [2, 8] (section 2.1.2) – and by briefly discussing their distinct optical properties. The purpose is to provide the basis for comparing and differentiating their respective properties and those of photonic quasicrystals. Finally, photonic quasicrystals are discussed (section 2.2), in particular their characteristic structural configuration. Several results of theoretical and experimental studies on dielectric<sup>1</sup> photonic quasicrystals are reviewed in section 2.2.3.

### 2.1 Introduction to Photonic Systems

The term “photonic systems” refers to compositions of at least two different kinds of (dielectric or metallic) materials<sup>2</sup>, which are deterministically or randomly distributed in space on an optical length scale. Depending on the number of spatial directions a photonic system is structured along, it is called a one-dimensional, two-dimensional or three-dimensional photonic system. A two-dimensional photonic system, for instance, could be designed as a perforated dielectric slab (with airholes). Photonic systems are meant for manipulating the propagation of light in a spectral region that is in the order of the characteristic length describing the material distribution. In particular, properly designed photonic systems can prohibit the propagation of

---

<sup>1</sup>Since the photonic quasicrystals fabricated in the course of this thesis are exclusively composed of dielectric materials, we will restrict ourselves to dielectric photonic quasicrystals in this overview.

<sup>2</sup>Typically, material A is embedded in a host material B with a different refractive index. Note that the term “dielectric material” includes vacuum.

photons for specific wavelengths and specific propagation directions, i.e., the corresponding density of states is zero. This implies that the corresponding dispersion relation  $\omega(\vec{k})$  is modified accordingly.

In principle, the effect of photonic systems on the photon propagation can be described in mathematical terms using Maxwell's equations, which characterise the interaction of electromagnetic waves and matter. In this thesis, we will only consider photonic systems consisting of non-magnetic materials, i.e., the permittivity  $\epsilon(\vec{r})$  is modulated, whereas the magnetic permeability<sup>3</sup>  $\mu(\vec{r})$  equals 1.

Maxwell's equations (in SI units) are given by

$$\nabla \cdot \vec{D} = \rho \quad (2.1)$$

$$\nabla \cdot \vec{B} = 0 \quad (2.2)$$

$$\nabla \times \vec{E} = -\frac{\partial \vec{B}}{\partial t} \quad (2.3)$$

$$\nabla \times \vec{H} = \frac{\partial \vec{D}}{\partial t} + \vec{j}. \quad (2.4)$$

In a medium the relation between the electric field  $\vec{E}$  and the electric displacement  $\vec{D}$  and the relation between the magnetic field  $\vec{B}$  and the magnetic induction  $\vec{H}$  are given by

$$\vec{D} = \epsilon_0 \vec{E} + \vec{P} \quad (2.5)$$

$$\vec{B} = \mu_0 (\vec{H} + \vec{M}), \quad (2.6)$$

with the macroscopic polarisation  $\vec{P}$  and the magnetisation  $\vec{M}$ .

In linear optics, equations (2.5) and (2.6) simplify to

$$\vec{D} = \epsilon_0 \hat{\epsilon} \vec{E} \quad (2.7)$$

$$\vec{B} = \mu_0 \hat{\mu} \vec{H}, \quad (2.8)$$

with the electric permittivity function  $\hat{\epsilon}$  and the magnetic permeability function  $\hat{\mu}$ , which in general are both tensors.

Considering non-magnetic ( $\hat{\mu} = 1$ ), isotropic and homogeneous materials ( $\hat{\epsilon} = \epsilon$ ) and furthermore, neglecting free charges and currents ( $\rho = 0$ ,  $\vec{j} = 0$ ), the wave equation for the electric field derived from Maxwell's equations has the well-known form

$$\Delta \vec{E} - \frac{1}{c^2} \frac{\partial^2 \vec{E}}{\partial t^2} = 0, \quad (2.9)$$

with the velocity of light in the medium  $c = c_0/n$ , given by the vacuum velocity  $c_0$  divided by the refractive index<sup>4</sup>  $n = \sqrt{\epsilon}$ .

---

<sup>3</sup>At optical frequencies, all natural substances have  $\mu(\vec{r}) = 1$ . In order to have the effective permeability  $\mu(\vec{r}) \neq 1$  at optical frequencies, so-called metamaterials are required – artificial systems composed of specific dielectric and metallic components which are structured on a length scale much smaller than the optical wavelengths.

<sup>4</sup>Actually, the real part of the generally complex refractive index is the relevant factor.

However, in the case of photonic systems, the spatial dependence of the permittivity  $\epsilon(\vec{r})$  is significant and has to be taken into account. Furthermore, we extract the time dependence of the fields by expanding the fields in time harmonic modes:

$$\vec{E}(\vec{r}, t) = \vec{E}_\omega(\vec{r})e^{-i\omega t} \quad (2.10)$$

$$\vec{H}(\vec{r}, t) = \vec{H}_\omega(\vec{r})e^{-i\omega t}. \quad (2.11)$$

Note that  $\vec{E}_\omega(\vec{r})$  and  $\vec{H}_\omega(\vec{r})$  are both complex fields. At the end of the calculations, the real parts have to be extracted to obtain the physical relevant electromagnetic fields.

With this ansatz one can derive from Maxwell's equations the following wave equations:

$$\hat{\Xi}\vec{E}_\omega(\vec{r}) = \frac{1}{\epsilon(\vec{r})}\nabla \times (\nabla \times \vec{E}_\omega(\vec{r})) = \left(\frac{\omega}{c_0}\right)^2 \vec{E}_\omega(\vec{r}) \quad (2.12)$$

$$\hat{\Theta}\vec{H}_\omega(\vec{r}) = \nabla \times \left(\frac{1}{\epsilon(\vec{r})}\nabla \times \vec{H}_\omega(\vec{r})\right) = \left(\frac{\omega}{c_0}\right)^2 \vec{H}_\omega(\vec{r}). \quad (2.13)$$

These equations define an eigenvalue problem for the fields  $\vec{E}_\omega(\vec{r})$  and  $\vec{H}_\omega(\vec{r})$  with the eigenvalue  $(\omega/c_0)^2$ . The solutions of these wave equations define the properties of any photonic system, i.e., they define its impact on the electric and magnetic field vectors of the photons and likewise its impact on the dispersion relation  $\omega(\vec{k})$ . The group velocity  $\vec{v}_g$ , defining the velocity at which light waves propagate in the photonic system, is given by:

$$\vec{v}_g = \nabla_{\vec{k}} \omega(\vec{k}). \quad (2.14)$$

Since the operator  $\hat{\Theta}$  is hermitian, while  $\hat{\Xi}$  is not [6], at first equation (2.13) is solved for  $\vec{H}_\omega(\vec{r})$ , obtaining orthogonal eigenstates immediately. Afterwards, – instead of solving equation (2.12) and orthogonalising the obtained eigenstates – the electric field can be derived using

$$\vec{E}_\omega(\vec{r}) = \frac{i}{\omega\epsilon_0} \frac{1}{\epsilon(\vec{r})} \nabla \times \vec{H}_\omega(\vec{r}). \quad (2.15)$$

From equations (2.12) and (2.13) two important scaling properties of a photonic system can be derived:

- Reducing the spatial scale  $\vec{r}$  by a factor  $s^{-1}$  increases the frequency  $\omega$  by the factor  $s$ , i.e.:

$$\vec{r} \rightarrow \vec{r}/s \Leftrightarrow \omega \rightarrow \omega \cdot s. \quad (2.16)$$

- Scaling the refractive index  $n(\vec{r}) = \sqrt{\epsilon(\vec{r})}$  by a factor  $s^{-1}$  increases the frequency  $\omega$  by the factor  $s$ , i.e.:

$$n(\vec{r}) \rightarrow n(\vec{r})/s \Leftrightarrow \omega \rightarrow \omega \cdot s. \quad (2.17)$$

Having once obtained the solutions of the wave equations for a specific photonic system, these scaling properties allow for simply scaling these solutions appropriately instead of solving the wave equations all over again.

In general, solving the wave equation (2.13) is a difficult task, especially, if the distribution of the dielectric or metallic materials forming the photonic system is very complex, i.e.,  $\epsilon(\vec{r})$

becomes a highly sophisticated function. Direct solutions via, e.g., finite difference time domain approaches [9, 10], demand very high (or even too excessive) computational efforts in terms of memory space and CPU times when dealing with large photonic systems. Yet, more efficient approaches exploit the Bloch-Floquet theorem [11] and thus require periodicity. In the next section, we discuss periodic photonic crystals and the solutions of the respective wave equations via mathematical tools taking advantage of the Bloch-Floquet theorem. Subsequently, in section 2.1.2, we focus on the peculiar optical properties of disordered photonic systems, for which the permittivity  $\epsilon(\vec{r})$  displays randomly distributed dielectric or metallic materials.

### 2.1.1 Photonic Crystals

Photonic crystals are particular photonic systems which are strictly periodic and exhibit translational symmetry, i.e., the permittivity  $\epsilon(\vec{r})$  is periodically modulated and  $\mu(\vec{r}) = 1$ . The structure of a photonic crystal can be described in terms of Bravais lattices with respect to the permittivity  $\epsilon(\vec{r})$  and is completely defined, if the distribution of the permittivity within a unit cell or the Wigner-Seitz cell, respectively, is known.

Due to its periodicity the electric permittivity fulfils the property

$$\epsilon(\vec{r}) = \epsilon(\vec{r} + \vec{R}), \quad (2.18)$$

where  $\vec{R}$  represents the lattice vector of the periodically modulated permittivity, containing both the characteristic length and the direction of periodicity.

Furthermore, the lattice vector  $\vec{R}$  can be expressed in terms of the primitive lattice vectors  $\vec{a}_i$ :

$$\vec{R} = m_1 \vec{a}_1 + m_2 \vec{a}_2 + m_3 \vec{a}_3, \quad m_i \in \mathbb{Z}. \quad (2.19)$$

It is also possible to calculate the primitive reciprocal lattice vectors  $\vec{b}_i$ , which span the reciprocal lattice in  $k$ -space:

$$\vec{b}_i = \frac{2\pi}{\vec{a}_1 \cdot (\vec{a}_2 \times \vec{a}_3)} \sum_{j,k=1}^3 \epsilon_{ijk} \vec{a}_j \times \vec{a}_k, \quad i = 1, 2, 3. \quad (2.20)$$

Now, for all reciprocal lattice vectors  $\vec{G}$  of the form

$$\vec{G} = l_1 \vec{b}_1 + l_2 \vec{b}_2 + l_3 \vec{b}_3, \quad l_i \in \mathbb{Z} \quad (2.21)$$

the relation

$$\vec{G} \cdot \vec{R} = m \cdot 2\pi, \quad m \in \mathbb{Z} \quad (2.22)$$

holds.

The periodicity of the permittivity in photonic crystals allows the use of the Bloch-Floquet theorem [11] for solving the wave equation (2.13) for the magnetic field. Shifting a mode by a lattice vector  $\vec{R}$  leads to a phase factor only:

$$\vec{H}_\omega(\vec{r}) = \vec{H}_\omega(\vec{r}, \vec{k}) = e^{i\vec{k}\vec{r}} \vec{H}_\omega^{\vec{k}}(\vec{r}), \quad (2.23)$$

where  $\vec{k}$  is the so-called Bloch vector and  $\vec{H}_\omega^{\vec{k}}(\vec{r})$  is the periodic part of the Bloch function, which defines the amplitude of the magnetic field  $\vec{H}_\omega(\vec{r})$  and shows the same symmetry as the Bravais lattice:

$$\vec{H}_\omega^{\vec{k}}(\vec{r}) = \vec{H}_\omega^{\vec{k}}(\vec{r} + \vec{R}). \quad (2.24)$$

Here,  $\vec{k}$  lies within the first Brillouin zone, the Wigner-Seitz cell of the reciprocal lattice. The  $\vec{k}$ -vectors lying at the boundaries of the Brillouin zone can be identified with the waves forming standing waves due to Bragg diffraction inside the periodic photonic crystal (briefly discussed later on in this section). Larger  $\vec{k}$ -vectors are folded back into the first Brillouin zone by adding an appropriate reciprocal lattice vector  $\vec{G}$ , as the transformation  $\vec{k} \rightarrow \vec{k} + \vec{G}$  in equation (2.23) leads only to an additional phase factor  $e^{i\vec{G}\vec{R}} = 1$ . This back-folding is the reason, why for a given vector  $\vec{k}$  several frequencies  $\omega_\nu(\vec{k})$  exist and a photonic band structure arises. The index  $\nu$  is interpreted as the corresponding band index.

To actually solve Maxwell's equations and to derive the photonic band structure of a photonic crystal, several numerical approaches are commonly used. They can be divided into time domain techniques and frequency domain techniques. Time domain techniques, such as finite difference time domain calculations [9, 10], are practical for dealing with general electromagnetic problems. In order to calculate the band structure or the transmittance and reflectance spectra of photonic crystals, however, frequency domain techniques are more efficient and thus preferable; the plane wave expansion method [12, 13], for instance, is suitable for band structure calculations and the scattering matrix formalism [14, 15] (see also section 4.3) for deriving the spectra.

In the following, the plane wave expansion method is applied to derive the band structure of a photonic crystal. The eigenvalue problem for  $\vec{H}_\omega(\vec{r})$  defined in equation (2.13) is solved by exploiting the periodicity of the permittivity  $\epsilon(\vec{r})$  and applying the Bloch-Floquet theorem. Therefore, the magnetic field is expanded in Bloch functions:

$$\vec{H}_\omega(\vec{r}) = \sum_{\vec{G}, \sigma} \vec{H}_\omega^\sigma(\vec{G}) e^{i(\vec{k} + \vec{G})\vec{r}} \hat{e}_{\vec{G}}^\sigma, \quad (2.25)$$

summing over the reciprocal lattice vectors  $\vec{G}$  and the polarisations  $\sigma$ .

Similarly, the inverse dielectric function  $1/\epsilon(\vec{r})$  is expanded:

$$\frac{1}{\epsilon(\vec{r})} = \sum_{\vec{G}} \eta_{\vec{G}} e^{i\vec{G}\vec{r}}, \quad (2.26)$$

with the Fourier-coefficients  $\eta_{\vec{G}}$

$$\eta_{\vec{G}} = \frac{1}{V_{\text{WSC}}} \int_{\text{WSC}} \frac{1}{\epsilon(\vec{r})} e^{-i\vec{G}\vec{r}} d^3\vec{r}. \quad (2.27)$$

Here,  $V_{\text{WSC}}$  refers to the volume of the Wigner-Seitz cell.

Inserting the plane wave expansion ansatz (2.25) and (2.26) into equation (2.13), a matrix eigenvalue problem is obtained:

$$\sum_{\vec{G}', \sigma'} \Theta_{\vec{G}, \vec{G}'}^{\sigma, \sigma'}(\vec{k}) \vec{H}_\omega^{\sigma'}(\vec{G}') = \left(\frac{\omega}{c_0}\right)^2 \vec{H}_\omega^\sigma(\vec{G}), \quad (2.28)$$

with

$$\Theta_{\vec{G}, \vec{G}'}^{\sigma, \sigma'}(\vec{k}) = |\vec{k} + \vec{G}| |\vec{k} + \vec{G}'| \eta_{\vec{G} - \vec{G}'} \begin{pmatrix} \hat{e}_{\vec{G}}^2 \cdot \hat{e}_{\vec{G}'}^2 & -\hat{e}_{\vec{G}}^2 \cdot \hat{e}_{\vec{G}'}^1 \\ -\hat{e}_{\vec{G}}^1 \cdot \hat{e}_{\vec{G}'}^2 & \hat{e}_{\vec{G}}^1 \cdot \hat{e}_{\vec{G}'}^1 \end{pmatrix}, \quad (2.29)$$

since the polarisation vector  $\hat{e}_{\vec{G}}^\sigma$  is chosen such that  $\{\hat{e}_{\vec{G}}^1, \hat{e}_{\vec{G}}^2, \vec{k} + \vec{G}\}$  form an orthogonal tripod with only two remaining polarisation vectors.

The solutions of the eigenvalue problem [equation (2.28)] are the eigenfrequencies  $\omega_\nu(\vec{k})$  ( $\nu$  is the band index) which form the band structure as a function of  $\vec{k}$  and simultaneously display the dispersion relation of the photons. For specific frequency regions and along certain directions, the propagation of the photons can be prohibited, forming the so-called photonic stop bands, while for other frequencies or directions the photons are allowed to propagate in the photonic system. If the occurring photonic stop bands overlap for all propagation directions (and polarisations), the common “forbidden” frequency range is called “complete photonic band gap”.

The occurrence of the stop bands can be illustratively explained by considering a one-dimensional photonic crystal (Bragg mirror) of periodicity  $d$ , consisting of two alternating dielectric material slabs with different refractive indices, and by applying the electromagnetic variational theorem [7]. Due to Bragg diffraction at the spectral positions  $k = 2\pi/\lambda = m \cdot \pi/d$ ,  $m \in \mathbb{Z}$ , where  $\lambda = \lambda_0/n$  denotes the wavelength in the photonic crystal with the effective refractive index  $n$ , the incident and reflected (back-scattered) waves interfere constructively and form a standing wave. The nodes of the resulting standing wave are located either in the high-index layers or the low-index layers, leading to a difference in the respective energies of the system ( $\omega_-$ ,  $\omega_+$ ). Due to this energy difference, a gap – the stop band – opens in the otherwise linear dispersion relation  $\omega = ck$ , as depicted in Fig. 2.1. Increasing the refractive index contrast (difference of the refractive indices of the low-index and the high-index material) increases the difference in the respective energies and thus the size of the stop band. In consequence, a high refractive index contrast facilitates the opening of a complete photonic band gap in the case of two- or three-dimensional photonic crystals, i.e., the overlapping of photonic stop bands for different spatial directions [16, 17, 18].

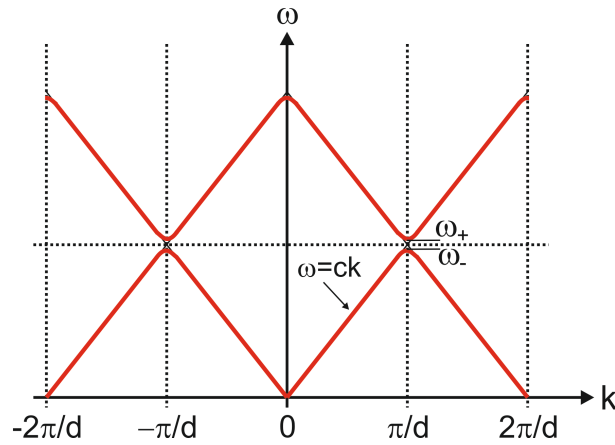


Figure 2.1: The dispersion  $\omega(k)$  of a photon in a one-dimensional photonic crystal is shown. Due to Bragg diffraction at  $k = m \cdot \pi/d$ ,  $m \in \mathbb{Z}$ , gaps open in the otherwise linear dispersion relation  $\omega = ck$ .

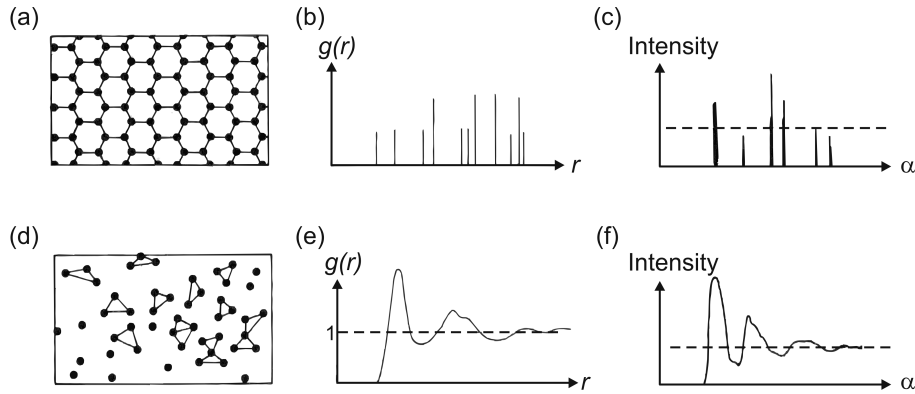


Figure 2.2: A periodic crystal (a) is described by a radial pair distribution function  $g(r)$  consisting of delta functions (b), and leads to sharp diffraction spots (c) at angles  $\alpha$  according to the condition  $|\Delta\vec{k}| = 2|\vec{k}|\sin\alpha = |\vec{G}|$ , see main text, section 2.1.1. The radial pair distribution function of an amorphous system with short-range order (d) is depicted in (e), the corresponding diffusive diffraction pattern in (f). After Ref. [22].

At frequencies within a photonic stop band, the light waves are evanescent and thus decay exponentially, while at frequencies within a photonic band the amplitude of the waves stay ideally constant during propagation as the waves are non-decaying propagating Bloch waves. Accordingly, the propagation of the light waves or photons is described by ballistic transport. In terms of the totally transmitted intensity  $T$ , i.e., integrated over all angles in forward direction, this translates into Beer's law, i.e.,  $T \propto \exp(-b \cdot L)$ , where  $b$  is a constant and  $L$  denotes the finite thickness of the photonic crystal. In the case of propagating Bloch waves the constant  $b$  is zero.

Studying the transmitted light, one observes Laue diffraction patterns displaying the reciprocal space or Fourier transform of the photonic crystal for a specific spatial direction. Since Bragg diffraction is the relevant mechanism for the formation of the band structure, the obtained diffraction pattern is related to the band structure as a cut at a specific frequency (and for a specific spatial direction) and thus is in principle depending on the wavelength of the light, the photonic crystal is probed with. In photonic crystals, light is diffracted strongly and leads to sharp Bragg diffraction peaks, if the difference of the wave vectors of the incident and diffracted light, respectively, corresponds to a reciprocal lattice vector, i.e.,  $|\Delta\vec{k}| = |\vec{k}_{\text{incident}} - \vec{k}_{\text{diffracted}}| = |\vec{G}|$  [cf. Fig. 2.2 (c)]. The sharpness of the diffraction spots indicates the long-range order inherent to periodic photonic crystals due to their translational symmetry.

At this point, we would like to leave our rather short introduction to the field of photonic crystals and refer the interested reader to some recommendable textbooks and recent reviews (e.g., Refs. [7, 6, 19, 20, 21]).

## 2.1.2 Disordered Photonic Systems

In this section, we like to focus on disordered photonic systems and point out some of their peculiar optical properties. Although in recent years increasing computational power has become available and thereby several quantitative approaches for directly solving Maxwell's equations for (rather small) disordered systems described by an adequate permittivity function  $\epsilon(\vec{r})$  have emerged [23, 24], we restrict ourselves to a more phenomenological description of the impact

of disorder on the photon propagation, as this section is meant to give a rather brief overview of the particular optical properties.

In contrast to photonic crystals, the distribution of the dielectric (or metallic<sup>5</sup>) materials forming a disordered photonic system cannot be described in terms of periodic lattices but rather in terms of statistics. The distribution of the dielectric material A embedded in the host material B can be described by the so-called pair distribution function, the probability density of finding two fundamental building blocks of material A separated by a vector  $\vec{r}$ , relative to all possible assemblies having the same average density of material A. Similarly, the radial pair distribution function  $g(r)$  is defined by averaging over all directions  $\vec{r}$ .

Maxima in the radial pair distribution function  $g(r)$  [cf. Fig. 2.2 (b), (e)] refer to the average pair distance of the first, second, ... neighbouring building blocks of material A. The width of such maxima measures the fluctuations in the distances, the area of the maxima refers to the number of building blocks found in the respective distance. The coherence length of the system can be defined as the distance at which maxima in the radial pair distribution function die out and form a uniform continuum. For a photonic crystal, the radial pair distribution function consists of delta functions referring to the periodic lattice sites, see Fig. 2.2 (b). In the case of an “amorphous” disordered system which is dominated by short-range order, the radial pair distribution function exhibits broadened short-distance peaks displaying the weak fluctuations in nearest neighbour distances, while for increasing distances the peaks smear out more and more until averaging finally into a uniform continuum, as depicted in Fig. 2.2 (e).

Due to having disordered, statistically distributed building blocks of dielectric material A embedded in material B, incident photons are scattered at these building blocks in a random fashion, and hence the photons propagate like in a “random walk”. Furthermore, the light rays impinging on and penetrating a disordered photonic system are scattered inside the system multiple times in a random fashion, yet coherently, i.e., the phase of each photon is well-defined and gives rise to interference effects. As a result of the interference of multiply scattered light, one can observe a granular distribution of the light intensity, the so-called speckle pattern [25], and coherent backscattering [26, 27], for instance.

In a simplified picture, neglecting any interference effects at first instance, the propagation of photons in a disordered system can be described as diffusive propagation with the scattering mean free path  $l$  (average step size in the random walk) and the diffusion constant  $D$ . Interference effects can now lead to a reduction of the mean free path  $l$  and a renormalisation of the diffusion constant  $D = D(L)$  such that it depends on the thickness  $L$  of the disordered photonic system and the degree of disorder. As a consequence, depending on the degree of disorder and the scattering strength of the disordered photonic system, one distinguishes in principle between three different regimes of photonic transport describing the photon propagation. The decisive parameter, the scattering strength, is characterised by the ratio of the wavelength  $\lambda$  of the considered light and the mean free path  $l$ , i.e., by  $\lambda/l$ .

In the diffusive regime or weak-scattering regime ( $\lambda/l \ll 1$ ) the photon propagation is described by the diffusion equation with the (constant) diffusion coefficient  $D = vl/3$ , where  $v$  is the (transport) velocity of the light wave propagating in the disordered system [28, 29].

---

<sup>5</sup>In the following, we will focus on dielectric disordered photonic systems to illustrate the specific optical properties, since metals induce additionally significant photon absorption at optical frequencies.

The phases of the scattered partial waves are (more or less) weakly uncorrelated and light is spread out diffusively. The intensity pattern of the transmitted light, the “diffraction pattern”, is dominated by “diffusive” scattering and the formation of speckle [25, 28, 30]. The actually obtained speckle pattern depends on the actual distribution of the materials forming the disordered photonic system rather than on the actual wavelength the disordered photonic system is probed with. For a sufficiently thick slab of the disordered photonic system, all photons are scattered many times in a random fashion such that the transmitted intensity becomes virtually independent of wavelengths. The totally transmitted intensity, integrated over all angles in forward direction, follows Ohm’s law, i.e.,  $T(L) \propto 1/L$ , and  $L$  is the thickness of the disordered photonic system slab [28, 31, 32]. Any partial or residual order, e.g., short-range order associated with amorphous systems, shows up as Bragg spots of fairly low intensity for only small values of  $\Delta\vec{k} = \vec{k}_{\text{incident}} - \vec{k}_{\text{diffracted}}$ , forming a kind of modulated diffusive scattering, see Fig. 2.2 (f).

If the scattering strength increases such that interference effects of multiple scattering reduce the photon propagation, the photon propagation is still characterised by the diffusion equation, but with the diffusion coefficient  $D(L)$  depending on the thickness  $L$  of the disordered photonic system. This is called the anomalous diffusive regime [28, 33].

If the scattering strength reaches a critical value,  $\lambda/l \geq 2\pi$ , known as Ioffe-Regel criterion [34], interference effects can produce Anderson localised states of the photons (cf. Anderson localisation [3]) and thus can trap light, i.e., the diffusion constant  $D \rightarrow 0$  [8]. In this regime, strong Mie resonances [35] are responsible for the formation of photonic band gaps. The transmitted intensity  $T(L)$  is exponentially small for light which is not resonant with a localised mode, and of the order of unity for resonant modes. This characterises the intensity pattern of the transmitted light [25, 30].

In general, in disordered photonic systems, the propagation of photons is very complex and one can find modes that are Anderson localised, extended or otherwise-confined in space. This is exploited, e.g., for random lasing [36, 37].

## 2.2 Photonic Quasicrystals

Photonic quasicrystals are perfectly ordered photonic systems, i.e., the dielectric (or metallic<sup>6</sup>) materials are arranged deterministically in a regular pattern. However, the pattern does not possess any translational symmetry or periodicity as in the case of photonic crystals, but so-called quasiperiodicity, and forms a so-called “quasilattice”. Due to the lack of periodicity, high-degree rotational symmetries can be found, which are not allowed for periodic crystals. Furthermore, the quasilattice shows self-similarity, yet exhibits a large number of non-equivalent quasilattice sites, since each quasilattice site has a distinct local environment, i.e., has a different dielectric configuration surrounding it. Accordingly, the structural configuration of a quasicrystal is quite complex and cannot be envisioned as intuitive as a periodic crystal. The latter can be composed by simply stacking unit cells side by side, which are all decorated with dielectric units in an identical manner. Then again, since quasicrystals exhibit long-range order, their structural composition also differs from random or amorphous systems, in which

---

<sup>6</sup>The photonic quasicrystals fabricated in the course of this thesis are exclusively composed of dielectric materials. Thus, we will restrict ourselves to dielectric materials in this section. When dealing with metallic materials, corresponding photon absorption has to be considered in addition.

short-range order dominates typically the formation of the structure. Accordingly, one expects interesting optical properties which deviate from those of photonic crystals and of disordered photonic systems.

Although the quasiperiodic pattern is perfectly ordered and deterministic, a complete theoretical description of photonic quasicrystals similar to that of photonic crystals (cf. section 2.1.1), especially regarding their optical properties, is fairly difficult due to the lack of periodicity. In the case of disordered photonic systems, a phenomenological approach could be developed to explain the experimentally observed optical properties. Similarly, one hopes to gain further insights into the interesting peculiarities of photonic quasicrystals starting from the experimental side, supported by suitable theoretical calculations. Thus investigated optical properties of photonic (non-metallic) quasicrystals are reviewed in section 2.2.3.

Still, the structural characteristics of photonic quasicrystals can be described by appropriate theoretical models and accordingly, some expected optical properties can be deduced from that, which is outlined in the following section 2.2.1.

### 2.2.1 Theoretical Description

The pattern of quasicrystals is perfectly deterministic and fulfils certain conditions: The “translational order” is quasiperiodic, i.e., the density function describing the distribution of the dielectric material can be expressed as a finite sum of periodic functions with incommensurate periods combined with the appropriate unit cell. But unlike just superimposing two periodic lattices with an irrational ratio of their periods, the quasilattice must obey the requirement of “minimal separation” between the quasilattice sites to prevent physically unrealistic short distances<sup>7</sup>. The connections or bond angles between neighbouring quasilattice sites must follow a defined orientational order and have long-range correlations.

Several theoretical models have been developed to generate an ideal quasicrystal pattern meeting the above mentioned conditions. In the following, we would like to introduce one of these models, the so-called “space tiling procedure”. This model is quite illustrative and thus gives a basic understanding of the composition and complexity of quasicrystals. In the next chapter, chapter 3, we will focus on another model, the cut-and-project method, as this particular method is applied to calculate the patterns of the photonic quasicrystals (and also of their so-called rational approximants, cf. section 3.1.2) which are studied in the course of this thesis. Further details concerning the various models, which are not all discussed in this thesis, can be found in Refs. [22, 38, 39, 40, 41, 42].

#### Space tiling procedure:

The well-known Fibonacci chain [43] is the most famous example of a quasicrystal in one dimension. Fibonacci has derived this sequence during his attempt to describe mathematically the population growth of rabbits. At the beginning there is a new-born couple of rabbits ( $S$ ). After growing up ( $L$ ), they give birth to a new couple of rabbits ( $S$ ) repeatedly after a certain period of time. With the assumption that rabbits do not die, the increase in population can be

<sup>7</sup>This can be understood from the fact that quasiperiodic patterns describe the arrangement of real atoms in electronic quasicrystals, see, e.g., Refs. [5, 22].

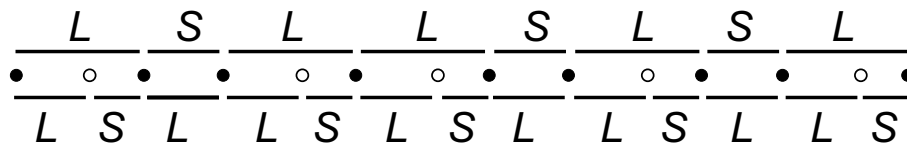


Figure 2.3: The original Fibonacci chain ( $L$ ,  $S$ ) is indicated by black solid dots. After one substitution step according to equations (2.30) and (2.31) (corresponding to one deflation operation), a new Fibonacci chain is generated, which is identical with the original one within rescaling. This reflects the self-similar character of the Fibonacci chain. After Ref. [22].

described with the following “substitution” rule:

$$S \longrightarrow L \quad (2.30)$$

$$L \longrightarrow LS. \quad (2.31)$$

If the ratio  $\tau = L/S$  is irrational, the generated sequence has no repetition distance, and thus is not periodic. The substitution operation (with  $\tau = (1 + \sqrt{5})/2$ , the so-called golden mean) is illustrated in Fig. 2.3.

As can be seen, by using this substitution procedure, a Fibonacci chain transforms into another Fibonacci chain within rescaling effects, which reflects the self-similarity implied in a quasiperiodic pattern. Thus, an alternative way to describe this generation rule is to start with a single line segment  $L$  and repeat deflation operations according to equation (2.30) and (2.31) (or inflation operations, respectively) iteratively, exploiting the self-similarity. This inflation/deflation also ensures the required long-range order.

It is also possible to build the Fibonacci chain by taking two segments with length  $L$  and  $S$ , respectively, and stack them side by side. However, to end up with a quasicrystal, the sequence of  $L$  and  $S$  cannot be chosen arbitrarily. Some so-called matching rules, which are more or less chosen to reproduce the results from the more general inflation/deflation method, have to be applied.

A two-dimensional quasicrystal can be generated similarly. The famous Penrose tiling, for instance, which shows ten-fold rotational symmetry, consists of two different types of rhombic tiles with equal edge lengths: a skinny tile with angles of  $36^\circ$  and  $144^\circ$  and a fat tile with angles of  $72^\circ$  and  $108^\circ$ . Applying matching rules, for example decorating the edges of the tiles with arrows and demanding that only edges arrowed in the same way are attached, gives a strict prescription of the space tiling [see Fig. 2.4 (a)]. Many different clusters can be generated without violating the matching rules. However, it is very difficult to ensure a perfect Penrose tiling, since many blind alleys can occur at each step of adding a new tile. The deflation/inflation method provides a more secure way to generate an ideal quasiperiodic pattern. Properly inflating/deflating the tiles iteratively forms a growing piece of the quasicrystal, as illustrated in Fig. 2.4 (b).

In principle, the tiling method can also be used for generating a three-dimensional quasicrystal. The basic tiles for a quasicrystal exhibiting icosahedral symmetry are a prolate and an oblate rhombohedron (see Fig. 2.5) with equal edge lengths.

However, although both, the matching rules and the inflation/deflation method, deterministi-

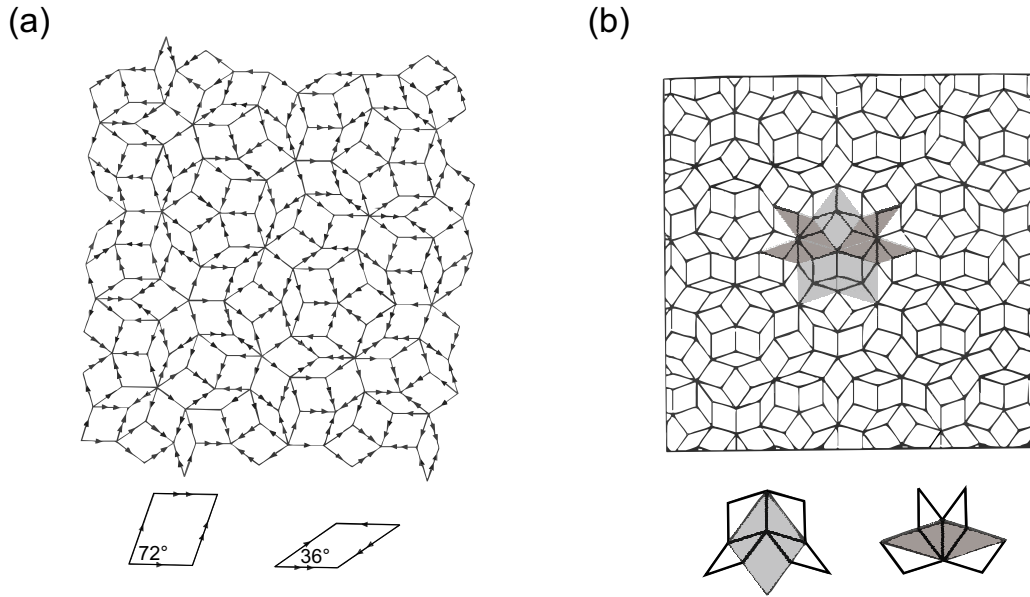


Figure 2.4: A two-dimensional Penrose tiling is generated (a) by attaching two rhombic tiles, where the decorations of the tile edges dictate the matching rules, and (b) by applying deflation operations. In the latter case, the original two types of rhombic tiles are subdivided into the same types within rescaling, depicted in the bottom part of (b). Iteratively deflating an initial tile generates, step by step, a growing piece of the Penrose tiling. After Ref. [22].

cally describe the successive composition of the quasiperiodic pattern, it is very complicated to automatise these procedures to generate a quasicrystal of reasonable size. That is why all patterns calculated and fabricated in the course of this thesis are generated by the cut-and-project method (cf. chapter 3).

Note that in electronic quasicrystals the real atoms are positioned at the vertices of the patterns obtained from the space tiling procedure.

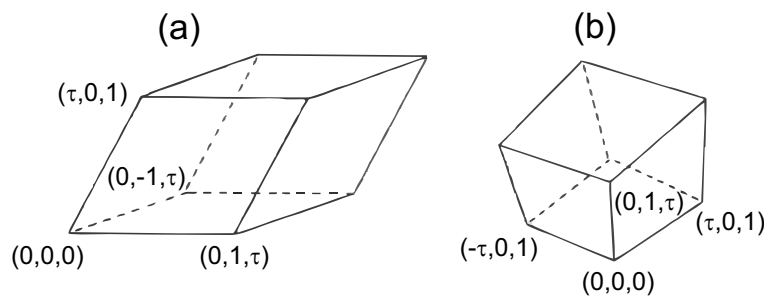


Figure 2.5: Two rhombohedra can be used to build up a three-dimensional icosahedral quasiperiodic pattern. The prolate rhombohedron is depicted in (a), the oblate rhombohedron in (b). After Ref. [22].

### Diffraction pattern:

The diffraction patterns of quasicrystals display their special structural properties, as these diffraction patterns actually consist of densely arranged sharp Bragg spots with a peculiar intensity distribution. The intensity distribution reflects the high-degree rotational symmetry of

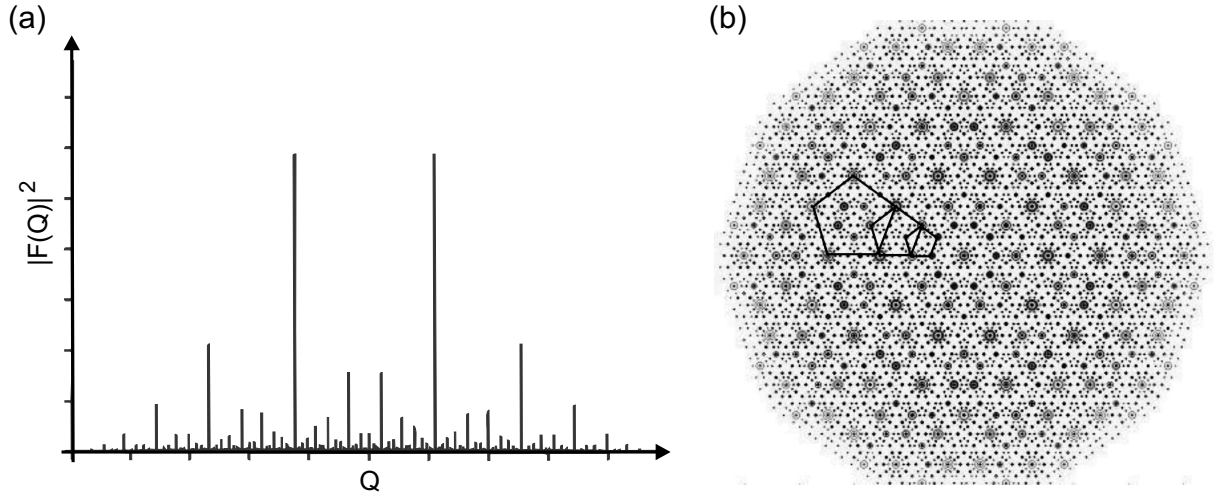


Figure 2.6: In (a), the Fourier spectrum of the one-dimensional Fibonacci chain (with 987 inflation steps) is depicted. After Ref. [22]. (b) shows the diffraction pattern (which is related to the Fourier spectrum) of a three-dimensional icosahedral quasicrystal oriented along a five-fold symmetry axis. The size of the circles is linearly related to the intensity of the Bragg spots. For reasons of clarity, only Bragg spots above a certain intensity are shown, since the diffraction pattern actually consists of a dense set of differently intense spots. The drawn pentagons connect Bragg spots of certain relative intensities. These self-similar pentagons, related by scaling with a specific factor  $\tau$ , illustrate the hierarchy of the diffraction pattern.

the respective quasicrystals [5, 22, 44, 45], but also shows a hierarchical character in terms of the relative strength of the sharp Bragg spots. The condition for sharp Bragg spots is that the difference of the wave vectors of the incident and diffracted light  $|\Delta\vec{k}| = |\vec{k}_{\text{incident}} - \vec{k}_{\text{diffracted}}|$  corresponds to a reciprocal lattice vector. This implies that a quasiperiodic pattern corresponds in principle to a dense set of delta-like Fourier components (and hence a countable dense set of points in reciprocal space) with an overall hierarchical amplitude distribution, while only few Fourier components show significant strength. This is illustrated in Fig. 2.6 (a) and (b).

The peculiar Fourier spectrum can be intuitively understood by turning back to the one-dimensional quasicrystal, the Fibonacci chain. The positions  $x_n$  of the  $n$  segments  $L$  and  $S$  (with  $L = S \cdot \tau$  and  $S = 1$ ), that form the one-dimensional (finite) Fibonacci chain, are given by

$$x_n = n + \frac{1}{\tau} \left\lfloor \frac{n+1}{\tau} \right\rfloor, \quad n \in \mathbb{N}_0. \quad (2.32)$$

Here,  $\left\lfloor \frac{n+1}{\tau} \right\rfloor$  presents the integer part or floor of  $\frac{n+1}{\tau}$ .

The function  $x_n$  can be divided into a sum of two functions, each of which describes a periodic spacing, yet with incommensurate periods. The first term defines a periodic spacing equal to one; the second term is also periodic (with  $\tau$ ), as it increases by  $\tau^{-1}$  each time  $n$  is increased by  $\tau$ . This translates into Bragg peaks spaced periodically with two incommensurate periods  $Q_1$  and  $Q_2$  in reciprocal space. Thus, the total diffraction pattern consists of the two sets of peaks from  $Q_1$  and  $Q_2$  plus additional peaks at linear combinations of  $Q_1$  and  $Q_2$ . As  $Q_1$  and  $Q_2$  are incommensurate, the result is a set of Bragg peaks that densely fill the reciprocal space.

Computing the Fourier components of the distribution of equation (2.32), which are non-zero

for

$$Q_{h,h'} = \frac{2\pi\tau^2}{\tau^2 + 1} \left( h + h' \frac{1}{\tau} \right), \quad h, h' \in \mathbb{Z}, \quad (2.33)$$

finally results in the following Fourier transform of the Fibonacci chain (for derivation see, e.g., Ref. [22]):

$$F(Q) = \sum_{h,h'} F_{h,h'} \delta(Q - Q_{h,h'}), \quad h, h' \in \mathbb{Z}, \quad (2.34)$$

where  $Q = \Delta \vec{k} = \vec{k}_{\text{incident}} - \vec{k}_{\text{diffracted}}$  and the amplitude factor  $F_{h,h'}$  is given by:

$$F_{h,h'} = \text{sinc} \left( \frac{\pi\tau}{\tau^2 + 1} (\tau h' - h) \right) \exp \left( i\pi \frac{\tau - 2}{\tau + 2} (\tau h' - h) \right), \quad h, h' \in \mathbb{Z}. \quad (2.35)$$

The diffraction peaks of the one-dimensional Fibonacci chain show an intensity distribution according to  $F_{h,h'}$  and are indexed by two integers  $h$  and  $h'$ . As any  $h'$  value can be associated with any  $h$ , the diffraction peaks form a very dense pattern. Yet, the individual diffraction peaks are still sharp peaks, just as the peaks obtained from periodic photonic crystals (see section 2.1.1), due to the inherent long-range order. Thus, the diffraction patterns of quasicrystals display a so-called singularly continuous Fourier spectrum. The brightest spots occur for  $Q_{h,h'}$  with  $\tau h' - h \cong 0$ , i.e., for  $h/h' \cong \tau$ , cf. equation (2.35), which defines the amplitude factor<sup>8</sup>  $F_{h,h'}$ . The corresponding Fourier spectrum is illustrated in Fig. 2.6 (a) and also in Ref. [46].

Analogously, the diffraction patterns of two- and three-dimensional quasicrystals represent a singularly continuous Fourier spectrum with an overall hierarchical amplitude distribution [39, 47], yet only few Fourier components show significant strength [cf. Fig. 2.6 (b)<sup>9</sup>].

The most intense diffraction spots are considered to represent the principal Bragg diffraction planes and thus can be used to generate a quasi-Brillouin zone in reciprocal space analogue to the Brillouin zone of periodic crystals. The constructed quasi-Brillouin zone is a highly circular polygon or a highly spherical polyhedron reflecting the high-degree symmetry of the respective two- or three-dimensional quasicrystals (cf. Fig. 3.7).

### Density of states, band structure and mode structure:

The peculiar diffraction patterns of quasicrystals give some indications for the expected density of states. The intense diffraction spots, which are associated with strong Bragg diffraction at the quasi-Brillouin zone boundaries, should be revealed as pseudo-stop bands or pseudo-gaps (distinct non-zero minima) in the transmittance spectra or density of states, see Refs. [46, 50]. Furthermore, as the diffraction pattern shows a hierarchical character, this should be reflected in the density of states as a dense set of sharp spikes of narrow width. Each spike will translate into a flat and narrow band of low group velocity, cf. equation (2.14). Bragg diffraction is one mechanism which can induce the formation of photonic stop bands in the band structure. In this case, a strong correlation of the transmittance and the Fourier spectrum will be obtained, as also found for photonic crystals. Yet, in quasiperiodic patterns another mechanism based on short-range order can also cause the appearance of stop bands due to Mie resonances of the individual scattering objects [46], cf. disordered photonic systems in section 2.1.2. However, a general

<sup>8</sup>The derivation of the amplitude factor implies single scattering.

<sup>9</sup>The computation of the depicted diffraction pattern will be explained in section 5.1 and follows the procedure of Refs. [22, 48, 49].

statement which mechanism dominates the opening of photonic stop bands in the photonic band structure of photonic quasicrystals is difficult to issue, since it will presumably depend on the scattering strength of the scattering objects and on the actual configuration (nearest neighbour-distance distribution) of the quasiperiodic pattern. The latter is directly related to its inherent rotational symmetry.

The unique structure of the quasiperiodic pattern itself is expected to give rise to so-called critically localised modes [46, 51, 52, 53], which do not decrease exponentially but with a power-law dependence with distance. The localisation occurs due to the broken translational symmetry (similar to disordered photonic systems), yet the self-similarity of the quasiperiodic pattern causes resonances between self-similar lattice configurations. As a consequence, the amplitude of a critical wave function has its maximum at a certain quasiperiodic lattice site, but has a series of subsidiary non-zero values at other lattice sites related by self-similarity due to “tunneling effects”. Simultaneously, also extended modes co-exist due to the present long-range order, similar to photonic crystals.

### 2.2.2 Realisation of Photonic Quasicrystals

In this section, we review some realisations of dielectric photonic quasicrystals which are mechanically stable and thus applicable for experimental studies of their optical properties.

Since the structural composition of photonic quasicrystals is generally very complex, most scientists have limited themselves to studying one- and two-dimensional photonic quasicrystals operating at infrared frequencies, i.e., with feature sizes in the  $\mu\text{m}$ -scale. For one-dimensional photonic quasicrystals, layers of two different dielectric materials are stacked in a quasiperiodic fashion, following the famous Fibonacci chain [46, 54, 55, 56] or the Thue-Morse sequence [46, 57], for instance. Such structures can be fabricated via, e.g., molecular beam epitaxy. A two-dimensional photonic quasicrystal can be realised either by arranging cylindrical shaped dielectric rods vertically on a substrate [58, 59] or by embedding small air rods in a dielectric environment [60]. The fabricated two-dimensional quasicrystals are stable, since the dielectric cylinders are connected firmly to the substrate and the air rods are fixed within the dielectric material, respectively. A novel flexible approach for the fabrication of two-dimensional quasicrystal patterns is based on single beam computer-generated holography exposing a polymeric liquid crystal film [61]. This technique offers the possibility of generating two-dimensional quasicrystals of any rotational symmetry, yet has the drawback of fairly low spatial resolution and low refractive index contrast ( $\Delta n \approx 0.2$ ).

For fabricating three-dimensional photonic quasicrystals, one requires a technique with the ability to distribute the dielectric materials arbitrarily in all three spatial directions and furthermore, to stabilise the generated pattern afterwards. To achieve this, one method is the use of optical tweezers, performed by Roichman *et al.* [62]. Colloidal silica microspheres are organised into the required quasiperiodic arrangement by using a holographic optical trapping technique. Computer-generated holograms are projected through a microscope objective of high numerical aperture to create three-dimensional arrays of optical traps. Applying this technique, the generated quasicrystal is quite similar to electronic quasicrystals where the real atoms ‘float’ in vacuum via their binding potential.

An alternative way to obtain a stable three-dimensional photonic quasicrystal was shown by W. Man *et al.* [63] in 2005, who fabricated an icosahedral photonic quasicrystal for the microwave regime by stereolithography. The authors generated a mechanically stable quasiperiodic network by connecting the “atoms” at the quasiperiodic lattice sites via plastic rods of 1 cm length in a well-defined manner. A similar method is used in this thesis to fabricate three-dimensional icosahedral photonic quasicrystals for infrared wavelengths [49] consisting of well-defined rods of few  $\mu\text{m}$  length which connect the “photonic atoms” mechanically. To achieve such a stable quasiperiodic pattern, we apply the cut-and-project method which will be described in more detail in chapter 3. For the fabrication we employ the technique of direct laser writing, cf. section 4.1.

More recent approaches deal with the fabrication of three-dimensional icosahedral photonic quasicrystals via laser interference holography [64] or of three-dimensional *axial* photonic quasicrystals by phase-mask lithography [65, 66]. These techniques also generate cross-linked mechanically stable quasiperiodic patterns, yet with connections that do not necessarily consist of rods of equal length and do not define a strict orientational order. Furthermore, the three-dimensional nanostructures generated via phase-mask lithography [65, 66] are in fact comprised of quasiperiodic planes, i.e., two-dimensional quasiperiodic patterns similar to the phase-mask, that are periodically stacked in axial direction. Thus, they are called three-dimensional *axial* photonic quasicrystals.

### 2.2.3 Optical Properties of Photonic Quasicrystals

As already indicated in section 2.2.1, some interesting and unique optical properties are expected for photonic quasicrystals due to their peculiar structural configurations. While measurements performed on one-dimensional photonic quasicrystals focus on the self-similarity and the absence of periodicity in these patterns, experiments on two-dimensional and three-dimensional photonic quasicrystals are even more interesting, since these patterns do not only lack the periodicity, but additionally possess high-degree rotational symmetry.

#### **Photonic band structure:**

The band structure of photonic quasicrystals is assumed to show self-similarity, since the quasiperiodic pattern itself is self-similar and the diffraction pattern reflects a hierarchical structure as well. Accordingly, the density of states reveals a fractal character with multiple sharp spikes and pseudo-gaps (cf. section 2.2.1). To the best of our knowledge, this fractal character has been confirmed only for the case of one-dimensional photonic quasicrystals yet [54, 55, 57].

Various studies on two-dimensional and three-dimensional quasicrystals deal with the issue of complete photonic band gaps. Since two-dimensional and three-dimensional quasicrystals can exhibit higher degree rotational symmetries than periodic crystals, the constructed quasi-Brillouin zone is consequently more circular or spherical, respectively. The boundaries of the quasi-Brillouin zone are associated with Bragg diffraction and thus with the opening of photonic stop bands in the band structure. In a more spherical Brillouin zone, the transmittance and reflectance spectra along different directions should be rather similar, i.e., more isotropic. Thus, one expects a larger spectral overlap of the stop bands in different spatial directions and it might be possible to open complete band gaps in photonic quasicrystals at lower

refractive index contrast than that required in photonic crystals [67]. The existence of a complete photonic band gap in a two-dimensional photonic quasicrystal with a rather low index contrast was shown experimentally by Zoorob *et al.* [60]. In this case, the photonic quasicrystal consisted of small air holes, which were quasiperiodically distributed in silicon nitride ( $n = 2.02$ ). Zhang *et al.* [68] calculated the existence of a complete band gap in a two-dimensional photonic quasicrystal approximated by “supercells” (forming the so-called rational approximants, cf. section 3.1.2) using a multiple-scattering method. The considered geometry, airholes in a dielectric host material, however, required a higher refractive index contrast ( $n_{\text{host}} > 2.64$ ) to open a complete photonic band gap than that Zoorob *et al.* had used in their experiment ( $n_{\text{host}} = 2.02$ ). The discrepancy between these published results has not been worked out yet, but generally one should be cautious about quantitative results obtained from calculations using periodic rational approximants<sup>10</sup>. Further studies on two-dimensional photonic quasicrystals consisting of dielectric rods in air were performed experimentally by Hase *et al.* [69] and theoretically by Yin *et al.* [70] who applied finite difference time domain calculations. Both have shown that such two-dimensional photonic quasicrystals can indeed open complete photonic bandgaps for fairly low refractive index contrasts ( $n_{\text{rods}} \approx 1.55$ ).

W. Man *et al.* [63] determined experimentally the transmittance spectra of a three-dimensional icosahedral photonic quasicrystal designed for the microwave regime. The measured spectra showed some sizeable stop bands and allowed to derive the quasi-Brillouin zone, which revealed indeed a quite spherical shape.

### Point and line defects:

After having found complete photonic band gaps in two-dimensional photonic quasicrystals, the next step was the introduction of defects into the structure. The peculiarity of photonic quasicrystals of having a large number of nonequivalent lattice sites leads to rich defect mode properties and interesting waveguiding effects. Cheng *et al.* [58] and Jin *et al.* [59] investigated the properties of microcavities (point defects) and waveguides (line defects) in a two-dimensional photonic quasicrystal consisting of dielectric cylinders in air. Depending on the local environment of the removed cylinder forming the microcavity, different properties of the defect states were observed. By simply choosing the position of the microcavity inside the quasicrystal, the number of defect modes, the defect mode frequencies and the mode field distributions could be easily varied and controlled. By introducing waveguides into the photonic quasicrystal, one could observe a highly structured transmittance spectrum and only few frequencies inside the original stop band showed high transmittance [58, 59]. Considering a bent waveguide, the position of the bend or rather the arrangement of the cylinders forming the bend influenced strongly the selected frequencies of high transmittance. As the channel width was increased, the waveguide lost its selectivity and finally approached the transmittance character of a waveguide in a photonic crystal. However, the intrinsic frequency selectivity of waveguides in photonic quasicrystals is very interesting and might be exploited for better tunability in certain optical applications.

---

<sup>10</sup>When working with periodic rational approximants, special care has to be taken to dispose of any features arising on account of the artificially introduced periodicity.

### Photonic mode structure, lasing and localisation of light:

The photonic wave functions are expected to be critically localised, which might lead to interesting properties of the photons inside quasiperiodic patterns (cf. section 2.2.1). But as long-range order is present in photonic quasicrystals as well, one might also find well-defined delocalised extended modes. Standing waves coherently spread throughout the whole quasicrystal could be used to fulfil lasing conditions. The ability of coherent lasing action was investigated in a two-dimensional decagonal photonic quasicrystal by Notomi *et al.* [71]. Several lasing modes could be found due to the wide variety of available reciprocal lattice vectors, which is in agreement with the dense set of Fourier components associated with a quasiperiodic pattern. The corresponding diffraction patterns, emitted in the out-of plane direction of the quasicrystal laser, revealed ten-fold symmetry. However, the actual appearance of the spot patterns, e.g., the relative intensities of observable diffraction orders, depended on the local configuration around the lasing mode. Similar experiments on one-dimensional [56] and three-dimensional [72] photonic quasicrystals followed, exploiting the existence of delocalised modes and the densely filled reciprocal space to satisfy the lasing condition. In the three-dimensional case, “multi-mode” lasing was observed as some of the lasing modes were spatially close together. However, the experimentally observed amplitudes of the excited lasing modes as well as their dependence on the actual polarisation of the exciting beam could not be explained yet, since theoretical calculations of three-dimensional quasicrystals and their optical properties are still very challenging. One step into this direction is taken in the course of this thesis by combining scattering matrix calculations with a rational approximant approach (cf. section 4.3 and section 5.3). Another theoretical approach was recently introduced by Rodriguez *et al.* [50] who proposed to calculate the optical properties of  $n$ -dimensional photonic quasicrystals by taking an  $N$ -dimensional version of Maxwell’s equations ( $N \geq 2n$ ) and projecting the solutions into  $n$  dimensions according to the cut-and-project method (cf. chapter 3). However, these authors have not delivered explicit findings for ( $n \geq 1$ )-dimensional quasicrystals.

In contrast to the observed delocalised extended modes responsible for lasing action, K. Wang [52] theoretically investigated localisation of light in an octagonal two-dimensional photonic quasicrystal consisting of infinite high dielectric cylinders ( $n \approx 3.6$ ) in air. The adequate Maxwell’s equations of rational approximants were solved for TM polarisation using a plane wave method. The calculations showed that the light wave modes at the photonic band gap edges were strongly localised on specific quasilattice sites, namely on those with highest local symmetry, i.e., they had eight nearest-neighbours. This indicates that the localisation effect is based on nearest-neighbour resonances. The corresponding bands just below the main photonic gaps were very flat. This flatness implies very low group velocity, which is consistent with the strong localisation of the wave functions. As disorder was introduced into the quasiperiodic lattice, the light waves got more extended and the group velocity increased due to less flat bands. This observation is completely contrary to the behaviour expected for periodic photonic crystals, where disorder usually disturbs the photon propagation by (partly) destroying their long-range phase coherence, and thus reduces the (former ballistic) transport velocity (cf. section 2.1.2). K. Wang’s prediction and explanation, that the localised modes occurring in two-dimensional photonic quasicrystals are predominantly caused by short-range effects, was recently confirmed by appropriate experimental analyses by K. Mnaymneh and R. C. Gauthier [53].

**Nonlinear effects and dense reciprocal space:**

Several experiments are dealing with nonlinearity in quasiperiodic nanostructures. B. Freedman *et al.* [73], for instance, studied two-dimensional photonic quasicrystals fabricated by the optical induction technique. Exploiting the nonlinearity of the used dielectric material SBN:75 ( $\text{Sr}_{0.75}\text{Ba}_{0.25}\text{Nb}_2\text{O}_6$ ), the formation and propagation of lattice solitons could be observed. Moreover, the dynamics of defects in quasiperiodic patterns could be investigated by observing the motion of dislocations. The photonic quasicrystal “healed” itself by a sequence of so-called “phason” flips. These phason flips were in principle rearrangements of the tiles forming the quasicrystal pattern (cf. the space tiling procedure in section 2.2.1) in order to dispose of any dislocations and to satisfy quasiperiodicity again. The “healing” of the quasicrystal was a long-range effect, which means, that the caused rearrangements in the quasiperiodic pattern still influenced the configuration quite distant from the initial defect.

Further experiments on nonlinear (one-dimensional and two-dimensional) photonic quasicrystals exploit the nature of a densely filled reciprocal space, which provides the possibility of broad-band efficient quasi-phase matching for nonlinear interactions, such as second-harmonics generation and third-harmonics generation [74, 75, 76, 77, 78].

Photonic quasicrystals have also found their way into the field of light-emitting diodes (LEDs) [79, 80], as the surface of LEDs has been patterned in a quasiperiodic way. Thereby, the light extraction could be enhanced due to efficient Bragg scattering into the various (high-degree) rotational symmetry directions of the quasicrystal, exploiting the peculiarity of its reciprocal space.

Up to now, most experiments in the near-infrared regime have dealt with one- or two-dimensional photonic quasicrystals only. However, the mentioned properties, such as the possibility of opening complete photonic band gaps for rather low refractive index contrast, the frequency selectivity in waveguiding as well as the great variety of reciprocal lattice vectors available for achieving lasing and quasi-phase matching, attract experimentalists to intensify the efforts of fabricating and studying high-quality *three*-dimensional photonic quasicrystals designed for near-infrared frequencies. The studies might not only reveal new surprising optical phenomena and features exploitable for future applications of photonic quasicrystals, but could also contribute to a more fundamental understanding of the properties of quasiperiodic patterns itself. The latter is desirable when aspiring to design and tailor photonic quasicrystals for specific optical applications.



# Chapter 3

## The Cut-and-Project Method

The cut-and-project method [22, 44, 49] is a very flexible tool commonly used for generating quasiperiodic patterns and is applied in the course of this thesis to calculate the patterns of three-dimensional photonic quasicrystals and of related rational approximants. The basic idea of this method is to project points of an  $N$ -dimensional periodic lattice into an  $n$ -dimensional subspace ( $n \leq N/2$ ), the so-called “physical space”. The requested  $n$ -dimensional quasiperiodic pattern is achieved by using appropriate “selection rules” to specify, if a periodic lattice point is actually projected into physical space or not. These selection rules are deduced from the remaining  $p$ -dimensional so-called “internal space” ( $p = N - n$ ,  $p \geq n$ ).

### 3.1 Fundamentals of the Cut-and-Project Method

In this section the principle of the cut-and-project method is explained in more detail (see also Ref. [22]). For illustration purposes, we pick generating a one-dimensional quasicrystal by cutting and projecting a two-dimensional periodic lattice into one-dimensional physical space, as depicted in Fig. 3.1. We assume a two-dimensional simple cubic lattice, i.e., a square lattice, and introduce a Cartesian coordinate system such that the slope  $\alpha$  of the axes with respect to the rows of the lattice is irrational, i.e., each axis passes only through one single lattice point, namely the origin<sup>1</sup>. One axis of the introduced coordinate system represents the one-dimensional physical space  $r^{\text{physical}}$ , onto which the two-dimensional periodic lattice points are projected to form a quasiperiodic pattern. The second axis, which is orthogonal to the first axis, represents the one-dimensional internal space  $r^{\text{internal}}$  and provides the selection rules for the projection into  $r^{\text{physical}}$ . Without such selection rules, all two-dimensional periodic lattice points would be projected into physical space and the resulting structure would consist of an infinite number of densely arranged points, which rather form a line than a quasicrystal. The selection rules work as follows: First, one determines the Wigner-Seitz cell of the two-dimensional periodic lattice and projects the edges into internal space  $r^{\text{internal}}$ . These projections mark the boundaries of the so-called “acceptance domain”, in this one-dimensional case represented by a line of length  $\Delta$ . Now, each two-dimensional periodic lattice point is projected into internal space first (cf. Fig. 3.1), and only if the projection lies within the acceptance domain, the lattice point is actually projected into physical space to form the quasiperiodic pattern.

---

<sup>1</sup>The projection of this origin is the single point of exact high-degree rotational symmetry which is inherent in the generated  $n$ -dimensional quasiperiodic pattern.

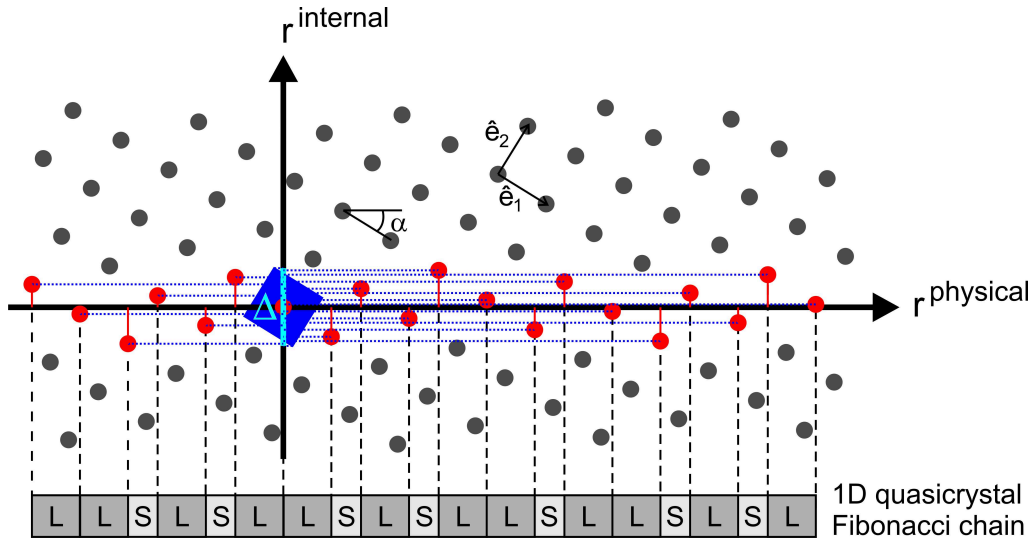


Figure 3.1: The cut-and-project method for generating a one-dimensional quasiperiodic pattern is illustrated. The Wigner-Seitz cell of the periodic two-dimensional lattice projected into internal space  $r^{\text{internal}}$  determines the size of the acceptance domain, a line of length  $\Delta$  (depicted in blue). Those two-dimensional periodic lattice points, whose coordinates projected into internal space are within  $\Delta$ , are highlighted in red and are projected into physical space  $r^{\text{physical}}$  to form a quasiperiodic pattern – if the slope  $\alpha$  is irrational<sup>2</sup>. In particular, we choose  $\alpha = 1/\tau = 2/(1 + \sqrt{5})$  and therefore the generated quasicrystal corresponds to the Fibonacci chain composed of two building blocks  $L$  and  $S$  with length  $\tau$  and 1, respectively.

The choice of the slope  $\alpha$  of the introduced coordinate axes with respect to the rows of the periodic lattice determines the properties of the generated pattern<sup>2</sup>. For instance, if  $\alpha$  is related to the golden mean  $\tau = (1 + \sqrt{5})/2$ , the generated one-dimensional quasiperiodic pattern is the famous Fibonacci chain, cf. Fig. 3.1 and section 2.2.1.

Up to this point, the description of the cut-and-project method has been quite illustrative. In the following, we would like to express the method more mathematically by an appropriate matrix notation.

As said, we start from a two-dimensional simple cubic lattice, which is defined by the two (canonic unit) lattice vectors

$$\hat{e}_1 = \begin{pmatrix} 1 \\ 0 \end{pmatrix}, \hat{e}_2 = \begin{pmatrix} 0 \\ 1 \end{pmatrix}, \quad (3.1)$$

and consequently, the two-dimensional simple cubic lattice points with coordinates  $(x_1, x_2)$  can be described by ordinary linear combinations of these two lattice vectors  $\hat{e}_1$  and  $\hat{e}_2$ :

$$\vec{x}_{2D} = \begin{pmatrix} x_1 \\ x_2 \end{pmatrix} = x_1 \cdot \hat{e}_1 + x_2 \cdot \hat{e}_2, \quad x_i \in \mathbb{Z}. \quad (3.2)$$

For each two-dimensional simple cubic lattice point the corresponding coordinates in physi-

<sup>2</sup>Depending on  $\alpha$ , the generated pattern is either periodic or quasiperiodic, cf. section 3.1.2.

cal space  $r^{\text{physical}}$  and internal space  $r^{\text{internal}}$ , respectively, are calculated via

$$\underbrace{\begin{pmatrix} \tau & 1 \\ 1 & -\tau \end{pmatrix}}_{\mathcal{M}_{2 \times 2}} \cdot \begin{pmatrix} x_1 \\ x_2 \end{pmatrix} = \begin{pmatrix} r^{\text{physical}} \\ r^{\text{internal}} \end{pmatrix}. \quad (3.3)$$

The first row of the matrix  $\mathcal{M}_{2 \times 2}$  implies that a connecting line between two adjacent periodic lattice points is projected to a line of either length 1 or  $\tau$ , which are the two building blocks ( $L$  and  $S$ , see Fig. 3.1) of the Fibonacci chain. The acceptance domain is determined by projecting the vertices of the Wigner-Seitz cell of the two-dimensional simple cubic lattice, a square with vertices at  $(\pm 0.5, \pm 0.5)$ , into internal space, which is a line of size  $\Delta = (\tau + 1)$ . The slope  $\alpha$  of the coordinate system with respect to the lattice points is  $1/\tau$ , which can be derived from the projected coordinates of two adjacent periodic lattice points.

This one-dimensional case can be easily transferred into higher dimensions to generate  $n$ -dimensional quasiperiodic patterns. In general, the cut-and-project method can be expressed by:

$$\mathcal{M}_{N \times N} \cdot \vec{x}_N = \begin{pmatrix} \vec{x}_n^{\text{physical}} \\ \vec{x}_p^{\text{internal}} \end{pmatrix}. \quad (3.4)$$

The  $N$ -dimensional periodic lattice points with coordinates  $\vec{x}_N$  are transformed by a  $N \times N$ -dimensional matrix  $\mathcal{M}$ , the so-called ‘‘projection matrix’’. After this transformation the coordinates of the points can be separated into two independent spaces, the physical space of dimension  $n$  and the internal space of dimension  $p = N - n$ . Equivalently, the  $N \times N$ -dimensional projection matrix  $\mathcal{M}$  can be divided into two parts, the  $n \times N$ -dimensional submatrix  $\mathcal{M}^{\text{physical}}$ , which determines the physical space, and the  $p \times N$ -dimensional submatrix  $\mathcal{M}^{\text{internal}}$ , which is related to the internal space and hence to the selection rules:

$$\mathcal{M}_{N \times N} = \begin{pmatrix} [\mathcal{M}_{n \times N}^{\text{physical}}] \\ [\mathcal{M}_{p \times N}^{\text{internal}}] \end{pmatrix}. \quad (3.5)$$

Accordingly, the individual matrix elements  $m_{ij}$  of the  $N \times N$ -dimensional projection matrix  $\mathcal{M}$  can be arranged as:

$$\begin{pmatrix} m_{11} & \cdots & m_{1N} \\ \vdots & & \vdots \\ m_{N1} & \cdots & m_{NN} \end{pmatrix} = \begin{pmatrix} \begin{bmatrix} m_{11}^{\text{physical}} & \cdots & m_{1N}^{\text{physical}} \\ \vdots & & \vdots \\ m_{n1}^{\text{physical}} & \cdots & m_{nN}^{\text{physical}} \end{bmatrix} \\ \begin{bmatrix} m_{11}^{\text{internal}} & \cdots & m_{1N}^{\text{internal}} \\ \vdots & & \vdots \\ m_{p1}^{\text{internal}} & \cdots & m_{pN}^{\text{internal}} \end{bmatrix} \end{pmatrix} = \begin{pmatrix} \vec{u}_1 \\ \vdots \\ \vec{u}_n \\ \vec{v}_1 \\ \vdots \\ \vec{v}_p \end{pmatrix}. \quad (3.6)$$

Here, the  $N$ -dimensional vectors  $\vec{u}_i$  and  $\vec{v}_i$  denote the row-vectors of the projection matrix  $\mathcal{M}$ , or to be precise of the individual submatrices  $\mathcal{M}^{\text{physical}}$  and  $\mathcal{M}^{\text{internal}}$ , respectively.

Obviously, the determination of the projection matrix  $\mathcal{M}$  is crucial for generating the  $n$ -dimensional structure on request, as it effects the projected coordinates in physical space as well as the projected coordinates in internal space and with that the selection rules for the projection.

In the following section, some important properties of the projection matrix  $\mathcal{M}$  are specified. A good understanding of this matrix gives us the possibility not only to generate already well-known one-, two- or three-dimensional quasicrystals, but also to create related structures, e.g., the so-called periodic rational approximants, by modifying existing projection matrices. Furthermore, it is even possible to generate new kinds of quasiperiodic patterns by creating appropriate new projection matrices.

### 3.1.1 Projection Matrix $\mathcal{M}$

As mentioned previously, the  $N \times N$ -dimensional projection matrix  $\mathcal{M}$  consists of two submatrices, submatrix  $\mathcal{M}^{\text{physical}}$  and submatrix  $\mathcal{M}^{\text{internal}}$ .

The  $n \times N$ -dimensional submatrix  $\mathcal{M}^{\text{physical}}$  consists of  $N$   $n$ -dimensional vectors, which represent the  $N$  different directions of connecting lines (or rods) forming the  $n$ -dimensional quasicrystal<sup>3</sup>. This means, that a connecting line (or rod) between two adjacent points of the  $N$ -dimensional periodic lattice, if they are both projected into the  $n$ -dimensional physical space in accordance to the selection rules, corresponds to one of the  $N$   $n$ -dimensional vectors of  $\mathcal{M}^{\text{physical}}$ . This automatically guarantees that the rods forming the quasiperiodic pattern have a defined orientational order (cf. section 2.2.1). The missing matrix elements of  $\mathcal{M}$ , i.e., the elements of submatrix  $\mathcal{M}^{\text{internal}}$ , can be completed, as the following properties must be fulfilled in order to obtain a quasiperiodic pattern:

- condition (1): All row-vectors  $\vec{u}_i$  and  $\vec{v}_j$  of the projection matrix  $\mathcal{M}$  must be orthogonal to all other row-vectors  $\vec{u}_{k \neq i}$  and  $\vec{v}_{l \neq j}$ :

$$\vec{u}_i \cdot \vec{u}_{k \neq i} = \vec{u}_i \cdot \vec{v}_j = \vec{v}_j \cdot \vec{v}_{l \neq j} = 0 \quad \forall i, j, k, l.$$

- condition (2): All row-vectors  $\vec{u}_i$  and  $\vec{v}_i$  have the same absolute value:

$$\|\vec{u}_i\| = \|\vec{v}_i\| = \text{const.} \quad \forall i.$$

- condition (3): The internal space should be equivalent to the physical space, i.e., physical space and (adequate parts of the) internal space are exchangeable, to account for the fact that the allocation of the physical space is arbitrary.

Following these rules, the submatrix  $\mathcal{M}^{\text{internal}}$  can be determined – often with several possible solutions. However, all solutions lead to the same quasicrystal, as the acceptance domains and hence the selection rules are simultaneously effected by the choice of  $\mathcal{M}^{\text{internal}}$ .

In the following, we would like to illustrate the creation of such a projection matrix  $\mathcal{M}$  by considering two examples of two-dimensional quasicrystals – the octagonal quasicrystal and

---

<sup>3</sup>The rods are required to obtain a mechanically stable three-dimensional photonic quasicrystal, see section 2.2.2.

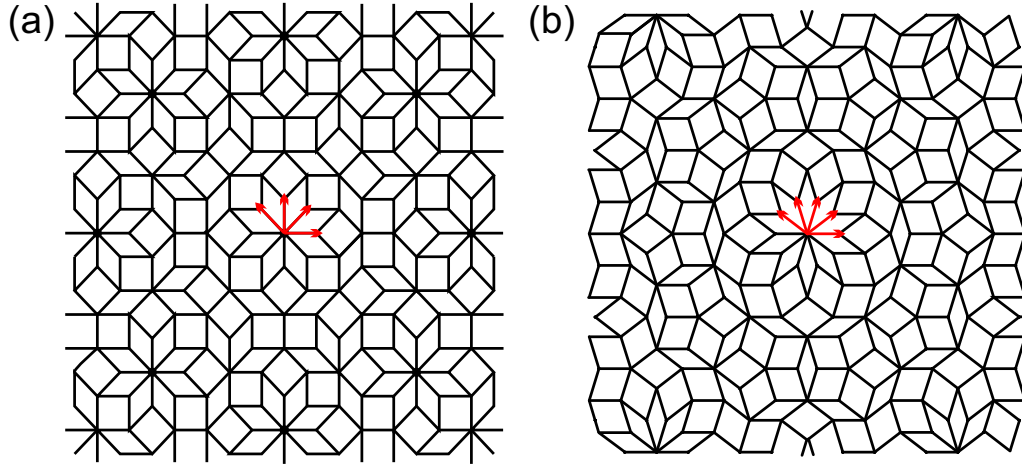


Figure 3.2: (a) The two-dimensional octagonal quasicrystal consists of two tilings, a rhombus and a square, that are quasiperiodically arranged. The edges of these tiles point along four different directions. These four vectors of unit length are rotated by the angle  $\phi = 2\pi/8$  with respect to each other, which reflects the eight-fold symmetry of the octagonal quasicrystal. (b) The Penrose tiling is formed by two rhombi. The edges of these rhombi are described by five vectors, rotated by  $\phi = 2\pi/10$  with respect to each other, which reflects the ten-fold symmetry of the Penrose tiling.

the Penrose tiling, both depicted in Fig. 3.2.

The two-dimensional octagonal quasicrystal with eight-fold rotational symmetry is formed by two different tiles, a square and a rhombus, of equal edge length, cf. Fig. 3.2 (a). The edges of these tiles, which represent the connecting lines forming the quasicrystal, point along the following directions:

$$\vec{x}_{m+1} = \begin{pmatrix} \cos(\frac{2\pi}{8} \cdot m) \\ \sin(\frac{2\pi}{8} \cdot m) \end{pmatrix}, m = 0..7$$

$$\text{with } \vec{x}_5 = -\vec{x}_1, \vec{x}_6 = -\vec{x}_2, \vec{x}_7 = -\vec{x}_3, \vec{x}_8 = -\vec{x}_4. \quad (3.7)$$

Four of these vectors,  $\vec{x}_1$  to  $\vec{x}_4$ , are sufficient to determine all directions of the connecting lines. Thus, these four two-dimensional vectors form the  $2 \times 4$ -dimensional submatrix  $\mathcal{M}^{\text{physical}}$ . Consequently, the remaining submatrix  $\mathcal{M}^{\text{internal}}$  is  $2 \times 4$ -dimensional as well. Following the conditions (1) to (3) for finding the missing matrix elements, as mentioned above, one possible solution of the total projection matrix is:

$$\mathcal{M}_{\text{Octagon}} = \begin{pmatrix} \cos(\frac{2\pi}{8} \cdot 0) & \cos(\frac{2\pi}{8} \cdot 1) & \cos(\frac{2\pi}{8} \cdot 2) & \cos(\frac{2\pi}{8} \cdot 3) \\ \sin(\frac{2\pi}{8} \cdot 0) & \sin(\frac{2\pi}{8} \cdot 1) & \sin(\frac{2\pi}{8} \cdot 2) & \sin(\frac{2\pi}{8} \cdot 3) \\ \cos(\frac{2\pi}{8} \cdot 0) & \cos(\frac{2\pi}{8} \cdot 5) & \cos(\frac{2\pi}{8} \cdot 2) & \cos(\frac{2\pi}{8} \cdot 7) \\ \sin(\frac{2\pi}{8} \cdot 0) & \sin(\frac{2\pi}{8} \cdot 5) & \sin(\frac{2\pi}{8} \cdot 2) & \sin(\frac{2\pi}{8} \cdot 7) \end{pmatrix}. \quad (3.8)$$

The projection matrix  $\mathcal{M}_{\text{Penrose}}$  of the famous Penrose tiling, which exhibits ten-fold symmetry, can be derived similarly. In this case, five two-dimensional vectors determine the directions

of the connecting lines, which mark the edges of the two different rhombic tiles of the Penrose tiling, as shown in Fig. 3.2 (b). These vectors are:

$$\vec{x}_{m+1} = \begin{pmatrix} \cos(\frac{2\pi}{10} \cdot m) \\ \sin(\frac{2\pi}{10} \cdot m) \end{pmatrix}, m = 0..9$$

$$\text{with } \vec{x}_6 = -\vec{x}_1, \vec{x}_7 = -\vec{x}_2, \vec{x}_8 = -\vec{x}_3, \vec{x}_9 = -\vec{x}_4, \vec{x}_{10} = -\vec{x}_5. \quad (3.9)$$

Consequently, the submatrix  $\mathcal{M}^{\text{internal}}$  is  $3 \times 5$ -dimensional, which can be divided into a two-dimensional space, consisting of five two-dimensional vectors, which represents the equivalent to the physical space [see condition (3)], and a one-dimensional row. This row, the row-vector  $\vec{v}_3$ , consists of five matrix elements and must be chosen such as to fulfil conditions (1) and (2) mentioned above. In total, the projection matrix we obtain is:

$$\mathcal{M}_{\text{Penrose}} = \begin{pmatrix} \cos(\frac{2\pi}{10} \cdot 0) & \cos(\frac{2\pi}{10} \cdot 1) & \cos(\frac{2\pi}{10} \cdot 2) & \cos(\frac{2\pi}{10} \cdot 3) & \cos(\frac{2\pi}{10} \cdot 4) \\ \sin(\frac{2\pi}{10} \cdot 0) & \sin(\frac{2\pi}{10} \cdot 1) & \sin(\frac{2\pi}{10} \cdot 2) & \sin(\frac{2\pi}{10} \cdot 3) & \sin(\frac{2\pi}{10} \cdot 4) \\ \cos(\frac{2\pi}{10} \cdot 0) & -\cos(\frac{2\pi}{10} \cdot 2) & \cos(\frac{2\pi}{10} \cdot 4) & \cos(\frac{2\pi}{10} \cdot 1) & -\cos(\frac{2\pi}{10} \cdot 3) \\ \sin(\frac{2\pi}{10} \cdot 0) & -\sin(\frac{2\pi}{10} \cdot 2) & \sin(\frac{2\pi}{10} \cdot 4) & \sin(\frac{2\pi}{10} \cdot 1) & -\sin(\frac{2\pi}{10} \cdot 3) \\ 1/\sqrt{2} & -1/\sqrt{2} & 1/\sqrt{2} & -1/\sqrt{2} & 1/\sqrt{2} \end{pmatrix}. \quad (3.10)$$

Please note that it is often useful to introduce a normalisation factor for each projection matrix such that the connecting lines or rods in the finally obtained quasicrystal have unit length.

### 3.1.2 Internal Space and Rational Approximants

This section is dedicated to the selection rules appearing in the cut-and-project method. As described previously, the selection rules are strongly related to the internal space defined by the projection matrix  $\mathcal{M}$ , or more precisely by the submatrix  $\mathcal{M}^{\text{internal}}$ . In general, the selection rules are derived by projecting the Wigner-Seitz cell of the  $N$ -dimensional periodic lattice into the  $p$ -dimensional internal space. Please note, if  $p > n$ , the internal space can be subdivided into  $x$   $n$ -dimensional subspaces, which are equivalent to the  $n$ -dimensional physical space and one  $t$ -dimensional subspace ( $t = p - x \cdot n$ ). Yet, the Wigner-Seitz cell is projected into the complete  $p$ -dimensional internal space to define the  $p$ -dimensional acceptance domain. In the case of the Penrose tiling, for instance, which was discussed in the previous section, one gets  $x=1$  two-dimensional subspaces and one ( $t = 1$ )-dimensional subspace. The ( $N = 5$ )-dimensional Wigner-Seitz cell is projected into the complete ( $p = 3$ )-dimensional internal space and one gets a ( $p = 3$ )-dimensional polyhedron as acceptance domain.

In the following, we would like to discuss the influence of the definition of the internal space on the generated structure in more detail. Therefore, we turn back to the illustrative example of the one-dimensional Fibonacci chain. In Fig. 3.1 the slope  $\alpha$  is chosen irrational, in particular  $\alpha = 1/\tau$ , to derive the Fibonacci chain. Yet, if the slope  $\alpha$  was chosen rational, the generated structure would not be quasiperiodic, but periodic, since the axes pass repeatedly through the two-dimensional periodic lattice points. The distance between such periodically passed lattice points determines the size of the unit cell of the periodic structure.

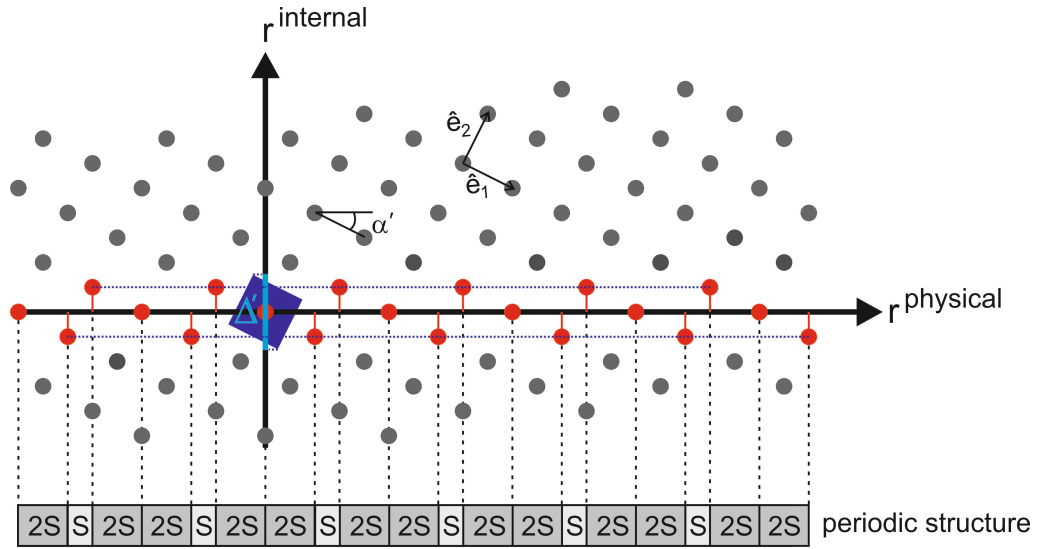


Figure 3.3: A one-dimensional periodic structure is generated via the cut-and-project method. The slope  $\alpha'$  is chosen rational, here  $\alpha' = 1/2$ . The Wigner-Seitz cell of the periodic two-dimensional lattice projected into internal space determines the size of the acceptance domain, a line of length  $\Delta'$  (depicted in blue). Those two-dimensional periodic lattice points, whose coordinates projected into internal space are within  $\Delta'$ , are highlighted in red and are projected into physical space to form the obviously periodic structure, composed of two building blocks of length  $S$  and  $2S$  ( $S = 1$ ), respectively.

In Fig. 3.3 the slope  $\alpha'$  is set to  $1/2$ . The generated structure is periodic, consisting of two different lines of length 1 and length 2, respectively. The corresponding matrix notation is:

$$\begin{pmatrix} 2 & 1 \\ 1 & -2 \end{pmatrix} \cdot \begin{pmatrix} x_1 \\ x_2 \end{pmatrix} = \begin{pmatrix} r^{\text{physical}} \\ r^{\text{internal}} \end{pmatrix}. \quad (3.11)$$

Compared to the Fibonacci chain, the lengths of the two lines and especially the ratio  $R$  of the respective lengths are changed, namely from  $R = 1/\tau$  to  $R = 1/2$ .

Yet, if we combine equation (3.3) and equation (3.11), in the following way

$$\begin{pmatrix} \tau & 1 \\ 1 & -2 \end{pmatrix} \cdot \begin{pmatrix} x_1 \\ x_2 \end{pmatrix} = \begin{pmatrix} r^{\text{physical}} \\ r^{\text{internal}} \end{pmatrix}, \quad (3.12)$$

we end up with a periodic structure which is similar to the Fibonacci chain, as it is also formed by the two lines of length 1 and  $\tau$ , see Fig. 3.4. Such a periodic structure is called “rational approximant”, since the irrational value of slope  $\alpha$  (*here*:  $1/\tau \approx 1/1.61803\dots$ ) is replaced by a rational value (*here*:  $1/2$ ) in the submatrix  $\mathcal{M}^{\text{internal}}$ . A good approximant structure will be achieved, if the rational value is close to the original irrational value. Depending on the actual chosen rational value the size of the unit cell of the rational approximant differs – the better the approximation of the irrational value, the larger is the size of the unit cell. The golden mean  $\tau$  is usually approximated stepwise by the rational Fibonacci numbers  $1/1=1$ ,  $2/1=2$ ,  $3/2=1.5$ ,  $5/3=1.\bar{6}$ , ... Accordingly, the rational approximants are named  $1/1$ ,  $2/1$ ,  $3/2$ , ... rational approximants and have successively increasing sizes of their specific unit cells. Illustratively, the naming of the various rational approximants is directly connected to the periodic lattice points that are hit by the coordinate axis  $r^{\text{internal}}$ . In the  $a/b$ -approximant with slope  $\alpha' = b/a$

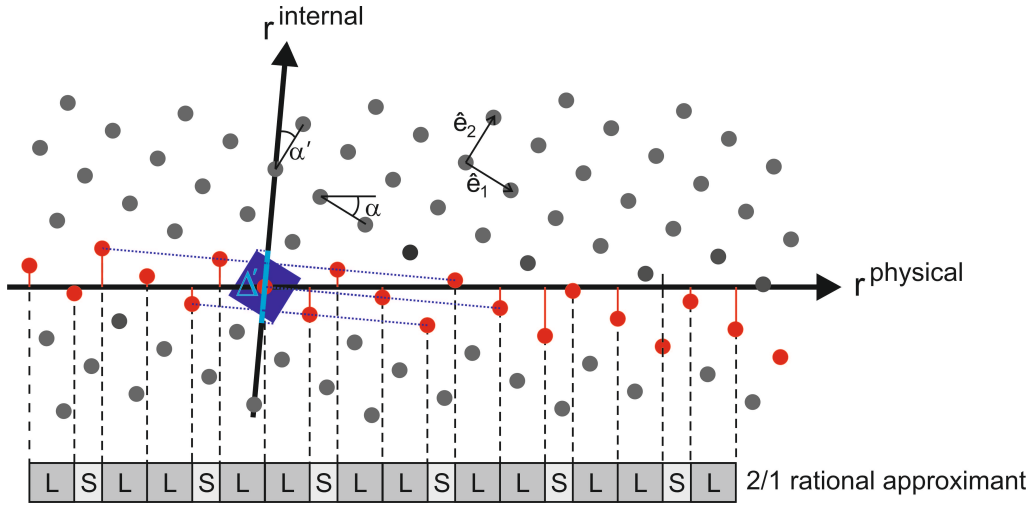


Figure 3.4: The cut-and-project method for generating a one-dimensional periodic rational approximant is depicted. The two coordinate axes which represent physical and internal space, respectively, are no longer orthogonal, as the slopes  $\alpha$  and  $\alpha'$  are chosen differently, in particular,  $\alpha = 1/\tau$  and  $\alpha' = 1/2$ . The Wigner-Seitz cell of the periodic two-dimensional lattice projected into internal space determines the size of the acceptance domain, a line of length  $\Delta'$  (depicted in blue). Those two-dimensional periodic lattice points, whose coordinates projected into internal space are within  $\Delta'$ , coloured in red, are projected into physical space to form the periodic rational approximant, which is composed of two building blocks  $L$  and  $S$  with length  $\tau$  and 1, just as the Fibonacci chain.

the periodic lattice points are repeatedly hit after  $a$  steps along  $\hat{e}_2$  and  $b$  steps along  $\hat{e}_1$ . Please note that changing the submatrix  $\mathcal{M}^{\text{internal}}$  effects in general also the size of the acceptance domain  $\Delta'$ .

This concept of periodic rational approximants can be transferred to the  $n$ -dimensional case: The  $p$ -dimensional submatrix  $\mathcal{M}^{\text{internal}}$ , which defines the selection rules, is modified, while the  $n$ -dimensional submatrix  $\mathcal{M}^{\text{physical}}$ , which determines the actual coordinates and rods of the requested  $n$ -dimensional pattern, is left unchanged. Obviously, as a consequence, the rows of the projection matrix  $\mathcal{M}$  are generally no longer orthogonal to each other. Yet, within the two submatrices  $\mathcal{M}^{\text{physical}}$  and  $\mathcal{M}^{\text{internal}}$  the row-vectors are still orthogonal to each other, i.e., each submatrix is still an orthogonal matrix, but  $\mathcal{M}^{\text{physical}}$  and  $\mathcal{M}^{\text{internal}}$  do not define independent and orthogonal subspaces any longer. This can be clearly seen in the case of the rational approximant of the Fibonacci chain: Firstly, in Fig. 3.4 the coordinate axes, representing physical space and internal space, respectively, are no longer orthogonal to each other, and secondly, in the corresponding  $2 \times 2$ -dimensional projection matrix, cf. equation (3.12), the first row-vector, which is associated with the coordinates in physical space, is no longer orthogonal to the second row-vector, that is associated with the coordinates in internal space.

In order to get a meaningful  $n$ -dimensional rational approximant, the modification of  $\mathcal{M}^{\text{internal}}$  is crucial. Yet, changing the “slope  $\alpha$ ” of the submatrix  $\mathcal{M}^{\text{internal}}$  to a rational value in the  $N$ -dimensional case is in general not very intuitive.

## 3.2 Three-Dimensional Icosahedral Quasicrystal and its Rational Approximants

The purpose of this section is to apply the cut-and-project method for generating three-dimensional icosahedral quasicrystals and related icosahedral rational approximants – patterns we study in the course of this thesis. At first, we focus on the icosahedral quasicrystal and its projection matrix, before we turn to the modifications of the projection matrix that are required to obtain the rational approximants. In order to compute the respective structures, we have implemented the cut-and-projected method in  $C^{++}$ , cf. Ref. [48].

The three-dimensional icosahedral quasicrystal exhibits icosahedral symmetry, which implies the existence of fifteen axes which show two-fold rotational symmetry, ten axes of three-fold rotational symmetry and six axes of five-fold rotational symmetry. The latter gives clear evidence to quasiperiodicity, as five-fold rotational symmetry is forbidden for periodic structures. Since the overall symmetry of the quasicrystal is icosahedral, it is suggesting to use the icosahedron as model to determine the vectors defining the submatrix  $\mathcal{M}^{\text{physical}}$ . The icosahedron consists of twenty equilateral triangular faces, five of which meet at every vertex. It has twelve vertices in total, which lie on a sphere around its central point. The icosahedron is characterised by the vectors pointing from the center to the twelve vertices. Depending on the actual orientation of the coordinate system the icosahedron is placed in, e.g., whether the  $z$ -axis points along one of its two-fold or five-fold rotational symmetry axes [see Fig. 3.5 (a) and (b)], these (unit) vectors are defined as

$$\vec{v}_{1..4}^{2\text{fold}} = \text{Norm} \cdot \begin{pmatrix} 0 \\ \pm 1 \\ \pm \tau \end{pmatrix}, \quad \vec{v}_{5..8}^{2\text{fold}} = \text{Norm} \cdot \begin{pmatrix} \pm 1 \\ \pm \tau \\ 0 \end{pmatrix}, \quad \vec{v}_{9..12}^{2\text{fold}} = \text{Norm} \cdot \begin{pmatrix} \pm \tau \\ 0 \\ \pm 1 \end{pmatrix}, \quad (3.13)$$

with  $\text{Norm} = 1/\sqrt{\tau^2 + 1}$  and the golden mean  $\tau = (1 + \sqrt{5})/2 \approx 1.61803$ ,

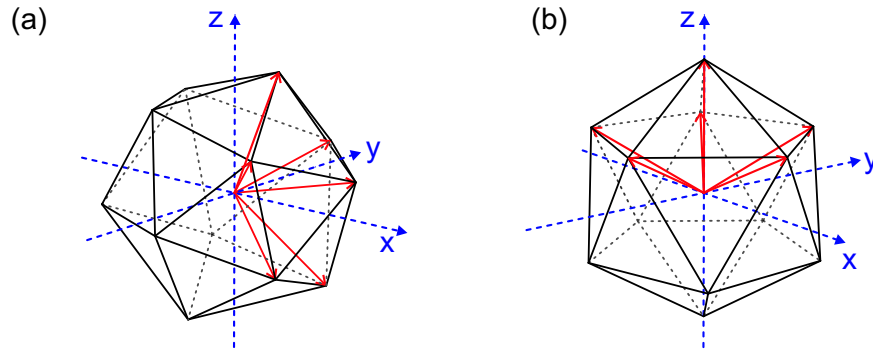


Figure 3.5: The icosahedron is illustrated. In (a) the icosahedron is oriented such that the  $z$ -axis of the Cartesian coordinate system points along a two-fold rotational symmetry axis, while in (b) the  $z$ -axis points along a five-fold rotational symmetry axis. The red coloured vectors mark the six vectors, pointing from the central point of the icosahedron to six vertices, which are used for defining the icosahedron [see equations (3.13) and (3.14)].

or as

$$\vec{v}_{1,2}^{5\text{fold}} = \begin{pmatrix} 0 \\ 0 \\ \pm 1 \end{pmatrix}, \quad \vec{v}_{i+3}^{5\text{fold}} = \begin{pmatrix} \sin(\phi) \cos(\frac{2\pi}{5} \cdot i) \\ \sin(\phi) \sin(\frac{2\pi}{5} \cdot i) \\ \cos(\phi) \end{pmatrix}, \quad i = 0..9. \quad (3.14)$$

The angle  $\phi = \arccos(\tau/(\tau + 2)) \approx 63.4349$  is irrational and defines the angle between the twelve vectors.

As the icosahedron is symmetric to its central point, six vectors pointing from the center to six of the vertices are sufficient to define the icosahedron [see Fig. 3.5 (a) and (b)], and thus to define the respective  $3 \times 6$ -dimensional submatrix  $\mathcal{M}^{\text{physical}}$ . These vectors define the directions of the rods in the finally obtained quasicrystal – the rods are the connecting lines between two adjacent six-dimensional periodic lattice points, if both are projected into physical space in accordance to the selection rules, cf. Refs. [44, 48, 49]. Hence, the rods follow a well-defined orientational order (cf. section 2.2.1) and ensure a mechanically stable quasiperiodic pattern. To complete the respective projection matrices,  $\mathcal{M}^{2f}$  or  $\mathcal{M}^{5f}$ , the likewise  $3 \times 6$ -dimensional respective submatrices  $\mathcal{M}^{\text{internal}, 2f}$  and  $\mathcal{M}^{\text{internal}, 5f}$  can be determined following conditions (1) to (3) described in section 3.1.1.

At the end, the projection matrix of the icosahedral quasicrystal with the  $z$ -axis oriented along a two-fold axis  $\mathcal{M}^{2f}$  is given by (cf. Ref. [81]):

$$\mathcal{M}^{2f} = \text{Norm} \cdot \begin{pmatrix} \tau & \tau & 0 & -1 & 0 & 1 \\ 0 & 0 & 1 & \tau & 1 & \tau \\ 1 & -1 & -\tau & 0 & \tau & 0 \\ \tau & -\tau & 1 & 0 & -1 & 0 \\ -1 & -1 & 0 & -\tau & 0 & \tau \\ 0 & 0 & \tau & -1 & \tau & -1 \end{pmatrix}, \quad (3.15)$$

with  $\text{Norm} = 1/\sqrt{\tau^2 + 1}$  and the golden mean  $\tau = (1 + \sqrt{5})/2 \approx 1.61803$ .

The projection matrix  $\mathcal{M}^{5f}$ , i.e., the  $z$ -axis points along a five-fold axis, is:

$$\mathcal{M}^{5f} = \begin{pmatrix} 0 & \cos(0) \sin \phi & \cos(\theta) \sin \phi & \cos(2\theta) \sin \phi & \cos(3\theta) \sin \phi & \cos(4\theta) \sin \phi \\ 0 & \sin(0) \sin \phi & \sin(\theta) \sin \phi & \sin(2\theta) \sin \phi & \sin(3\theta) \sin \phi & \sin(4\theta) \sin \phi \\ 1 & \cos \phi \\ 0 & \cos(0) \sin \phi & \cos(2\theta) \sin \phi & \cos(4\theta) \sin \phi & \cos(\theta) \sin \phi & \cos(3\theta) \sin \phi \\ 0 & \sin(0) \sin \phi & \sin(2\theta) \sin \phi & \sin(4\theta) \sin \phi & \sin(\theta) \sin \phi & \sin(3\theta) \sin \phi \\ -1 & \cos \phi \end{pmatrix} \quad (3.16)$$

with  $\phi = \arccos(\tau/(\tau + 2))$  and  $\theta = \frac{2\pi}{5}$ , which indicates the five-fold symmetry.

It is obvious that in both projection matrices,  $\mathcal{M}^{5f}$  and  $\mathcal{M}^{2f}$ , the two submatrices defining physical and internal space, respectively, are equivalent, as both submatrices are formed by six of the twelve vectors which define the icosahedron in the respective coordinate system [cf. equations (3.13) and (3.14)]. The acceptance domain, derived from projecting the six-dimensional Wigner-Seitz cell into internal space, is a three-dimensional polyhedron, the

triacontahedron [depicted in Fig. 3.7 (b)] which also exhibits icosahedral symmetry. The triacontahedron consists of 30 equilateral rhombi and 32 vertices. The vertices lie on two different spheres of slightly different radii  $r_1 = \tau = (1 + \sqrt{5})/2 \approx 1.618$  and  $r_2 \approx 1.473$ . Hence the acceptance domain can be approximated by a sphere of radius  $r_1$  [48]. Besides, this triacontahedron also represents the so-called quasi-Brillouin zone of the icosahedral quasicrystals, the result of projecting the Wigner-Seitz cell of the six-dimensional reciprocal lattice into physical space.

Please note that the normalisation of the respective projection matrices is chosen such that the rods of the finally obtained quasicrystals, the connecting lines of two adjacent six-dimensional periodic lattice points after projection, have a rod length of 1.

Applying one of the two matrices  $\mathcal{M}^{5f}$  and  $\mathcal{M}^{2f}$ , three-dimensional icosahedral quasicrystals can be generated with the surface normal ( $z$ -axis) pointing along a five-fold or a two-fold rotational symmetry axis, respectively. Additionally, the orientation of the generated three-dimensional quasicrystal, i.e., that the  $z$ -axis points along a two-fold, three-fold or five-fold rotational symmetry axis, can be changed by rotating the three-dimensional structure after the projection into physical space appropriately [5, 22].

At this point, we also would like to recall that the generated quasiperiodic patterns exhibit one single point of exact icosahedral symmetry which corresponds to the projection of the origin  $(0,0,0,0,0,0)$  into physical space.

In the course of this thesis, we are also interested in generating and studying periodic rational approximants of such three-dimensional icosahedral quasicrystals (cf. section 5.3) – structures which are identical to the quasicrystal within their specific unit cell and which do qualitatively resemble the quasicrystal appearance outside of their unit cell in a periodic manner. Depending on the actual rational approximant, the size of the unit cell differs and likewise the degree of representing the original quasicrystal. Such rational approximants are obtained by appropriately modifying the submatrix  $\mathcal{M}^{\text{internal}}$  of the original quasicrystal and hence by changing the selection rules, as described in section 3.1.2.

In analogy to the one-dimensional  $a/b$  rational approximant of the Fibonacci chain, for which the golden mean  $\tau$  is replaced by rational values  $a/b$  in the submatrix  $\mathcal{M}^{\text{internal}}$  [cf. equation (3.12)], we generate the rational approximant of the three-dimensional icosahedral quasicrystal by substituting the golden mean  $\tau$  accordingly in the projection matrix  $\mathcal{M}^{2f}$ . Consequently, the icosahedral  $a/b$  rational approximant is generated with the modified projection matrix  $\mathcal{M}_{\text{approx}}^{2f}$ :

$$\mathcal{M}_{\text{approx}}^{2f} = \text{Norm} \cdot \begin{pmatrix} \tau & \tau & 0 & -1 & 0 & 1 \\ 0 & 0 & 1 & \tau & 1 & \tau \\ 1 & -1 & -\tau & 0 & \tau & 0 \\ a/b & -a/b & 1 & 0 & -1 & 0 \\ -1 & -1 & 0 & -a/b & 0 & a/b \\ 0 & 0 & a/b & -1 & a/b & -1 \end{pmatrix}, \quad (3.17)$$

with  $\text{Norm} = 1/\sqrt{\tau^2 + 1}$  and the golden mean  $\tau = (1 + \sqrt{5})/2 \approx 1.61803$ .

The edge length  $l^{a/b}$  of the cubic unit cell of the icosahedral  $a/b$  rational approximant is

given by:

$$l^{a/b} = 2(a\tau + b) \cdot \text{Norm} \cdot \text{rod length} \quad (3.18)$$

with  $\text{Norm} = 1/\sqrt{\tau^2 + 1}$  and the golden mean  $\tau = (1 + \sqrt{5})/2 \approx 1.61803$ .

In the course of this thesis, we generate and study three different kinds of rational approximants of the icosahedral quasicrystal, the icosahedral 1/1 rational approximant, the icosahedral 2/1 rational approximant and the icosahedral 3/2 rational approximant, i.e., the golden mean  $\tau$  is substituted by the values 1.0, 2.0 and 1.5, respectively. The lengths  $l^{a/b}$  of the corresponding cubic unit cells of the respective icosahedral  $a/b$  rational approximants are therefore:

- $l^{1/1} = 2.75276 \cdot \text{rod length}$
- $l^{2/1} = 4.45402 \cdot \text{rod length}$
- $l^{3/2} = 7.20683 \cdot \text{rod length}$ .

We restrict ourselves to these three choices of rational approximants of the icosahedral quasicrystal for two reasons: First, the surface normals of these icosahedral rational approximants point along a two-fold rotational symmetry axis. Since we obtain a cubic unit cell we do not break the symmetry in this two-fold symmetric case, as we would do in a five-fold symmetric case, for instance. Second, the size of the unit cell of the icosahedral 3/2 rational approximant is already fairly large and demands already excessive computational power when calculating the transmittance and reflectance properties via the scattering matrix approach (see section 4.3). Moreover, for our purpose, the icosahedral 2/1 rational approximant is already sufficient to approximate the icosahedral quasicrystal (cf. section 5.3.1).

We have implemented the cut-and-project method in  $C^{++}$  to compute the patterns of three-dimensional icosahedral quasicrystals and of corresponding rational approximants alike. Therefore, we describe the six-dimensional simple cubic lattice points of coordinates  $\vec{x}_{6D}$  by linear combinations of the six canonic unit vectors  $\hat{e}_i$ . The coordinates  $\vec{x}_{6D}$  are transformed by the respective matrices  $\mathcal{M}^{2f}$ ,  $\mathcal{M}^{5f}$  and  $\mathcal{M}_{\text{approx}}^{2f}$ . The respective three-dimensional acceptance domains, which define the specific selection rules for the projection into the respective physical spaces, are determined by projecting the Wigner-Seitz cell into the respective internal spaces. The obtained acceptance domains are approximated by spheres of appropriate radii. Additional selection rules are introduced for the physical space to specify the shape of the obtained structure, cf. Ref. [48].

### 3.3 Three-Dimensional Rhombicuboctahedral Quasicrystal

In the previous section, we have successfully applied the cut-and-project method to generate a three-dimensional quasicrystal of icosahedral symmetry – to the best of our knowledge, the only class of three-dimensional quasicrystals that was discovered in electronic systems, i.e., in metallic alloys [5, 45], to date. As a result, all studies of three-dimensional electronic as well as of artificially fabricated three-dimensional photonic and phononic quasicrystals that are known to us dealt with icosahedral ones so far. However, given the high flexibility of the cut-and-project method, that only requires an “irrational slope” of the introduced coordinate system with respect to the  $N$ -dimensional periodic lattice, and taking into account that in two dimensions several kinds of quasicrystals with different rotational symmetries are known, e.g., the octagonal quasicrystal and the Penrose tiling (both discussed in section 3.1.1), the obvious question arises, if the icosahedral quasicrystal is really the sole three-dimensional quasicrystal that is achievable. The purpose of this section is to answer this question and to discuss in more detail the requirements for creating quasicrystals of specific symmetries via the cut-and-project method.

In section 3.1.1 and section 3.2, we have already derived the projection matrices of the two-dimensional octagonal quasicrystal, the two-dimensional Penrose tiling and of the three-dimensional icosahedral quasicrystal to be used in the cut-and-project method. First of all, one will notice that all these projection matrices  $\mathcal{M}$  are quadratic ( $N \times N$ ), yet they differ in their respective dimension  $N$ . The dimension is related to the symmetry the created quasicrystal should obtain – or more precisely to the number  $N$  of the vectors which describe the quasiperiodic pattern and its symmetry. The octagonal quasicrystal needs four vectors, while the Penrose tiling requires five vectors and the icosahedral quasicrystal even six vectors to completely define its pattern, as depicted in Fig. 3.2 (a), (b) and Fig. 3.5. Obviously, some knowledge about the pattern of the quasicrystal is essential right from the beginning to derive its appropriate projection matrix.

In two-dimensions, any quasicrystal of arbitrary  $2k$ -rotational symmetry can be described by the vectors  $\vec{v}_{i+1}^{2k\text{-fold}}$ :

$$\vec{v}_{i+1}^{2k\text{-fold}} = \begin{pmatrix} \cos\left(\frac{2\pi}{2k} \cdot i\right) \\ \sin\left(\frac{2\pi}{2k} \cdot i\right) \end{pmatrix}, \quad i = 0..(k-1). \quad (3.19)$$

However, in the case of the three-dimensional icosahedral quasicrystal it is not that intuitive any more to find the vectors that define the quasicrystal and one has to use the model of the icosahedron (see section 3.2).

To proceed now with our attempt of finding a “new” three-dimensional quasicrystal with a “new” high-degree rotational symmetry, we have to find an appropriate model that exhibits this new symmetry. One property of the two- and three-dimensional quasicrystals is that all connecting lines (or rods) forming the respective patterns are of equal length. Therefore, the tiles forming the two-dimensional quasicrystals are of equal edge lengths, and also the icosahedron serving as model for the icosahedral quasicrystal consists of equilateral triangles. Moreover, the vertices of the icosahedron lie on a sphere. Unfortunately, the icosahedron is already the highest-symmetric “platonic solid” – solids composed of congruent regular

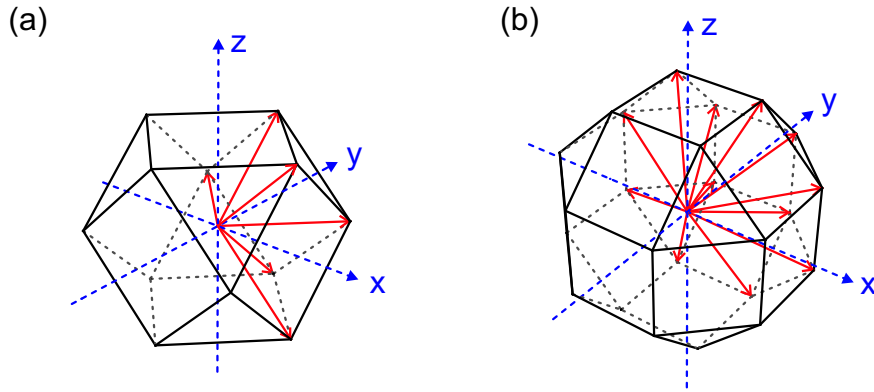


Figure 3.6: (a) The cuboctahedron is illustrated. The red coloured vectors mark the six vectors, pointing from the central point of this polyhedron to six vertices, which are sufficient for defining the cuboctahedron. (b) The rhombicuboctahedron is displayed. The red coloured vectors mark the twelve vectors, pointing from its central point to twelve vertices, which define the rhombicuboctahedron.

polygons, with the same number of faces meeting at each vertex. The platonic solids have the unique property that the faces, edges and angles of each solid are all congruent. Yet, as the two-dimensional quasicrystals are composed of (at least) two different kind of tiles, we expect that polyhedra which are composed of two different kinds of polygons with equal edge lengths, are still suitable as model for the “new” three-dimensional quasicrystal. Such highly symmetric polyhedra are called “archimedean solids”. They are composed of two or more types of regular polygons meeting in identical vertices.

In order to obtain a three-dimensional quasicrystal with axes showing eight-fold rotational symmetry, we consider the cuboctahedron and the (small) rhombicuboctahedron, depicted in Fig. 3.6 (a) and (b), respectively, as possible models.

The cuboctahedron composed of eight equilateral triangles and six squares has twelve vertices in total, which lie on a sphere around its central point – just as the icosahedron. The vectors  $\vec{v}_i$  pointing from the central point to the vertices [cf. Fig. 3.6 (a)] are given by

$$\vec{v}_{1..4} = \begin{pmatrix} 0 \\ \pm 1 \\ \pm 1 \end{pmatrix}, \quad \vec{v}_{5..8} = \begin{pmatrix} \pm 1 \\ \pm 1 \\ 0 \end{pmatrix}, \quad \vec{v}_{9..12} = \begin{pmatrix} \pm 1 \\ 0 \\ \pm 1 \end{pmatrix}. \quad (3.20)$$

These vectors are very similar to the vectors  $\vec{v}_i^{2\text{fold}}$  as defined in equation (3.13), yet  $\tau$  is substituted by 1. Accordingly, the corresponding cuboctahedral projection matrix will be similar to  $\mathcal{M}^{2f}$  with  $\tau$  substituted by 1:

$$\mathcal{M}_{\text{Cuboctahedral}} = \frac{1}{\sqrt{2}} \begin{pmatrix} 1 & 1 & 0 & -1 & 0 & 1 \\ 0 & 0 & 1 & 1 & 1 & 1 \\ 1 & -1 & -1 & 0 & 1 & 0 \\ 1 & -1 & 1 & 0 & -1 & 0 \\ -1 & -1 & 0 & -1 & 0 & 1 \\ 0 & 0 & 1 & -1 & 1 & -1 \end{pmatrix} \quad (3.21)$$

Obviously, the submatrix  $\mathcal{M}^{\text{internal}}$  of this cuboctahedral projection matrix is identical to the internal space of the 1/1 rational approximant of the icosahedral quasicrystal, see equation (3.17) with  $a/b$  set to 1/1. Therefore, we expect and actually get a periodic pattern, when applying the cuboctahedral projection matrix [equation (3.21)] to the cut-and-project method. After all, this is not that surprising, as the angles between the cuboctahedral vectors  $\vec{v}_i$ , defined in equation (3.20), are rational, namely  $45^\circ$  and  $90^\circ$ .

Since the cuboctahedron did not lead to success to create a “new” three-dimensional quasicrystal, we turn our focus on the rhombicuboctahedron, depicted in Fig. 3.6 (b), a more complex archimedean solid composed of eight equilateral triangles and eighteen squares. It has 24 vertices in total, which lie on a sphere around its central point. The vectors  $\vec{v}_i$  pointing from the central point to the vertices [cf. Fig. 3.6 (b)] are given by

$$\vec{v}_{1..8} = \begin{pmatrix} \pm\sigma \\ \pm 1 \\ \pm 1 \end{pmatrix}, \quad \vec{v}_{9..16} = \begin{pmatrix} \pm 1 \\ \pm\sigma \\ \pm 1 \end{pmatrix}, \quad \vec{v}_{17..24} = \begin{pmatrix} \pm 1 \\ \pm 1 \\ \pm\sigma \end{pmatrix}, \quad (3.22)$$

with the silver ratio  $\sigma = 1 + \sqrt{2}$ .

As the rhombicuboctahedron is symmetric to its central point, twelve of these vectors are sufficient to define this polyhedron. Starting from those twelve vectors and following the conditions (1) to (3) defined in section 3.1.1, the following  $12 \times 12$ -dimensional projection matrix  $\mathcal{M}_{\text{Rhombicuboctahedral}}$  was finally obtained [82] – after having spent considerable CPU time in our search for possible solutions employing a dedicated home-built  $C^{++}$ -programme:

$$\mathcal{M}_{\text{Rhombicuboctahedral}} = \frac{1}{\sqrt{2 + \sigma^2}} \begin{pmatrix} 1 & 1 & \sigma & \sigma & -\sigma & -\sigma & 1 & 1 & -1 & -1 & -1 & -1 \\ 1 & 1 & 1 & 1 & 1 & 1 & \sigma & \sigma & \sigma & \sigma & 1 & 1 \\ \sigma & -\sigma & 1 & -1 & 1 & -1 & 1 & -1 & 1 & -1 & \sigma & -\sigma \\ 1 & 1 & -1 & -1 & -1 & -1 & -1 & -1 & \sigma & \sigma & -\sigma & -\sigma \\ 1 & -1 & -\sigma & \sigma & 1 & -1 & -\sigma & \sigma & -1 & 1 & 1 & -1 \\ -\sigma & \sigma & 1 & -1 & \sigma & -\sigma & -1 & 1 & 1 & -1 & 1 & -1 \\ \sigma & \sigma & -\sigma & -\sigma & -1 & -1 & 1 & 1 & -1 & -1 & 1 & 1 \\ 1 & -1 & -1 & 1 & \sigma & -\sigma & 1 & -1 & 1 & -1 & -\sigma & \sigma \\ -1 & 1 & -1 & 1 & 1 & -1 & \sigma & -\sigma & -\sigma & \sigma & 1 & -1 \\ -1 & 1 & -\sigma & \sigma & -1 & 1 & 1 & -1 & \sigma & -\sigma & 1 & -1 \\ -1 & -1 & -1 & -1 & 1 & 1 & \sigma & \sigma & -1 & -1 & -\sigma & -\sigma \\ \sigma & \sigma & 1 & 1 & \sigma & \sigma & -1 & -1 & -1 & -1 & -1 & -1 \end{pmatrix} \quad (3.23)$$

where  $\sigma = 1 + \sqrt{2}$  is the silver ratio.

It is obvious that the total projection matrix can be separated into four different but equivalent three-dimensional subspaces, as each subspace contains twelve vectors that define the rhombicuboctahedron. One subspace is chosen as physical space, the remaining three subspaces form the internal space.

In order to derive the selection rules for the rhombicuboctahedral quasicrystal, the Wigner-Seitz cell of the twelve-dimensional simple cubic lattice is projected into the nine-dimensional internal space. As result, one gets a complex nine-dimensional polyhedron, which is approximated by a nine-dimensional sphere of radius  $r = (2 + 2\sigma)/\sqrt{2 + \sigma^2} \approx 2.4405$  (similar to the approach for the icosahedral quasicrystal, described in section 3.2). If the coordinates of a twelve-dimensional simple cubic lattice point projected into internal space lie within the nine-dimensional acceptance domain, or rather the sphere of radius  $r$ , the lattice point is actually projected into the three-dimensional physical space to form the rhombicuboctahedral quasicrystal<sup>4</sup>. The rods of the final quasicrystal are obtained by keeping the connecting lines between two adjacent twelve-dimensional periodic lattice points, if both lattice points are projected. Hence, the rods point along twelve different directions, namely along the rhombicuboctahedral vectors (cf. Fig. 3.6 (b) and equation (3.22)], and thus, create the well-defined rotational and orientational order of the generated pattern. Furthermore, in this way a mechanically connected and stable quasiperiodic network is generated.

The angles  $\phi_1$ ,  $\phi_2$ ,  $\phi_3$  between the respective rods are irrational, namely:

$$\begin{aligned}\phi_1 &= \arccos\left(\frac{2\sigma + 1}{2\sigma + 3}\right) \approx 41.882\dots, \\ \phi_2 &= \arccos\left(\frac{2\sigma - 1}{2\sigma + 3}\right) \approx 60.722\dots, \\ \phi_3 &= \arccos\left(\frac{1}{2\sigma + 3}\right) \approx 82.661\dots,\end{aligned}\tag{3.24}$$

where  $\sigma = 1 + \sqrt{2}$  is the silver ratio.

Therefore, we expect to obtain a quasiperiodic pattern rather than a periodic structure (see chapter 6 and Ref. [82]).

The thus created quasicrystal is expected to show rhombicuboctahedral symmetry, also known as the achiral octahedral symmetry  $O_h$ . Therefore, one expects to find principal symmetry axes showing eight-fold, three-fold, and two-fold symmetry. The corresponding quasi-Brillouin zone, depicted in Fig. 3.7 (a), is a complex three-dimensional polyhedron obtained by projecting the Wigner-Seitz cell of the twelve-dimensional reciprocal lattice into physical space (or into one of the three three-dimensional subspaces forming the internal space). This polyhedron consists of a truncated cube (or truncated hexahedron) and six octagonal pyramids attached to the six octagonal faces and reflects the rhombicuboctahedral symmetry. Its 30 vertices lie on two different spheres of radii  $r_1 = (2\sigma + 4)/\sqrt{2 + \sigma^2} \approx 3.1553$  and  $r_2 = \sqrt{26\sigma + 11}/\sqrt{2 + \sigma^2} \approx 3.0697$ , due to the vertices of the truncated cube (or truncated hexahedron) and of the pyramid peaks, respectively.

To study all principal symmetry axes the three-dimensional rhombicuboctahedral quasicrys-

---

<sup>4</sup>The radius  $r \approx 2.4405$  of the spherical acceptance domain is chosen such that a reasonable density of projected points is obtained. The actual choice of the radius does not effect the overall symmetry of the final rhombicuboctahedral quasicrystal.

tal is rotated in physical space appropriately. The required rotation matrices are:

$$\begin{aligned}\mathcal{R}_{8\text{fold}} &= \begin{pmatrix} 1 & 0 & 0 \\ 0 & 1 & 0 \\ 0 & 0 & 1 \end{pmatrix}, \\ \mathcal{R}_{3\text{fold}} &= \begin{pmatrix} \cos(\alpha) & \sin(\beta) \sin(\alpha) & \cos(\beta) \sin(\alpha) \\ 0 & \cos(\beta) & -\sin(\beta) \\ -\sin(\alpha) & \sin(\beta) \cos(\alpha) & \cos(\beta) \cos(\alpha) \end{pmatrix}, \quad \alpha \approx 34.238\dots, \quad \beta = 45, \quad (3.25) \\ \mathcal{R}_{2\text{fold}} &= \begin{pmatrix} 1 & 0 & 0 \\ 0 & \cos(\beta) & -\sin(\beta) \\ 0 & \sin(\beta) & \cos(\beta) \end{pmatrix}, \quad \beta = 45.\end{aligned}$$

In order to compute the rhombicuboctahedral quasicrystal, we use a  $C^{++}$ -programme similar to that used for the icosahedral quasicrystal (cf. Ref. [48]). The points of the twelve-dimensional simple cubic lattice  $\vec{x}_{12D}$  are defined by linear combinations of the twelve canonic unit vectors and are transformed by the matrix  $\mathcal{M}_{\text{Rhombicuboctahedral}}$ . The acceptance domain specifying the selection rules for the projection into physical space is approximated by a nine-dimensional sphere. Additional selection rules are introduced for the physical space to define the shape of the final quasicrystal.

At this point we would like to recall that the generated quasiperiodic pattern exhibits one single point of exact rhombicuboctahedral symmetry. This singularity is obtained from the projection of the origin  $(0,0,0,0,0,0,0,0,0,0,0,0)$  of the twelve-dimensional periodic lattice into physical space.

From the respective quasi-Brillouin zones of the rhombicuboctahedral and the icosahedral quasicrystal shown in Fig. 3.7 (a) and (b), one clearly observes the high-degree rotational symmetry of these three-dimensional quasicrystals, as these quasi-Brillouin zones are more spherical than that of the “best” three-dimensional periodic crystal – the diamond lattice [16, 17, 18, 63, 83].

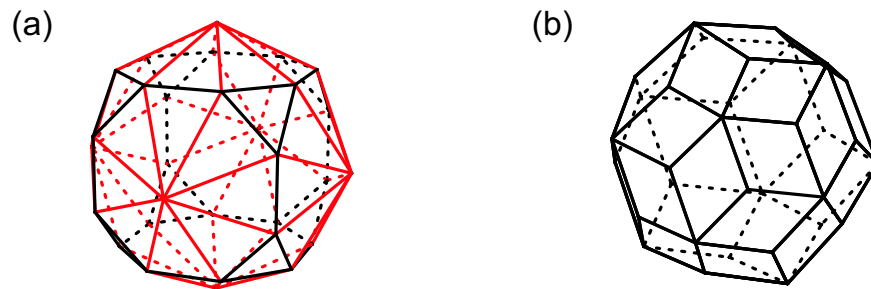


Figure 3.7: (a) The quasi-Brillouin zone of the rhombicuboctahedral quasicrystal is depicted. This complex polyhedron is formed by a truncated cube (black lines) with six octagonal pyramids on top of its six octagonal faces (red lines). (b) shows the quasi-Brillouin zone of the icosahedral quasicrystal, the triacontahedron, composed of 30 rhombi meeting at 32 vertices.



# Chapter 4

## Fabrication, Characterisation and Calculation Techniques

The previous chapter dealt with the cut-and-project method, which is used to calculate the patterns of quasicrystals and of related rational approximants. In this chapter, we describe the techniques we use to experimentally realise such patterns as photonic nanostructures and to characterise their optical properties. The first section (section 4.1) is dedicated to the fabrication technique, the so-called direct laser writing, a method which is already well-established in our group [84]. Subsequently, we give a brief overview of several experimental setups which are used to optically characterise the quality and properties of the fabricated photonic nanostructures (section 4.3). Finally, the scattering matrix formalism is described (section 4.3), a method to calculate the expected optical transmittance and reflectance properties of (periodic) photonic nanostructures (cf. section 2.1.1). This theoretical tool<sup>1</sup> offers the opportunity to analyse and interpret the experimentally obtained data (see section 5.3).

### 4.1 Fabrication via Direct Laser Writing

The fabrication of (complex) three-dimensional photonic nanostructures requires a flexible laser lithography system to expose a photosensitive material appropriately in all three dimensions. Direct laser writing comprises such a system. It exploits multi-photon polymerisation and is meanwhile a well-established method to fabricate three-dimensional photonic nanostructures [85]. In the following, we will restrict ourselves to a short discussion of this fabrication method, since the basic principle of direct laser writing and its experimental implementation are already explained in detail in Refs. [48, 84, 86]. In the course of this thesis, the setup has been modified to allow for an (even) more computer-controlled and automated way of fabrication. We will comment on these modifications in this section where appropriate.

The basic concept of direct laser writing is to expose a photosensitive material, in our

---

<sup>1</sup>Rodriguez *et al.* [50] have recently introduced another approach for calculating the optical properties of  $n$ -dimensional photonic quasicrystals. The authors suggested to take an  $N$ -dimensional version of Maxwell's equations ( $N \geq 2n$ ) and to project the solutions into  $n$  dimensions according to the cut-and-project method (cf. chapter 3). However, the authors have primarily used this method to study the properties of the ( $n = 1$ )-dimensional Fibonacci chain and have not delivered explicit findings adaptable to our ( $n = 3$ )-dimensional case.

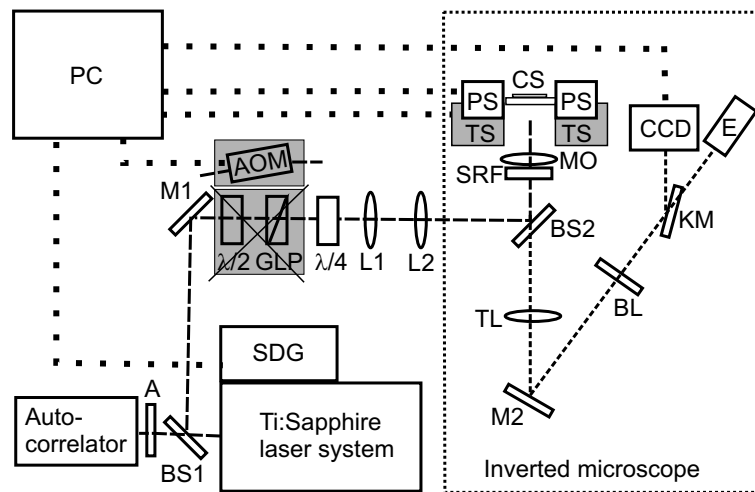


Figure 4.1: The direct laser writing setup is schematically illustrated. The grey-shaded components indicate the modifications of the setup, implemented in the course of this thesis. SDG: computer-controllable electronic interface; BS1, BS2: beam splitters (BK7 glass wedge and glass plate, respectively); A: attenuator; M1, M2: silver mirrors;  $\lambda/2$ ,  $\lambda/4$ : half-wave plate and quarter-wave plate, respectively; GLP: Glan-Laser polariser; AOM: acousto-optical modulator; L1, L2: lenses with  $f=50.2$  mm and  $f=100$  mm, respectively; SRF: shaded-ring filter; MO: microscope objective; CS: glass substrate covered with SU-8; TS: two-axes translational stage; PS: three-axes piezo scanning stage; TL: tube lens; BL: blocker; KM: kinematic mirror; CCD: CCD camera; E: eyepiece, PC: personal computer.

case the commercially available negative-tone photoresist SU-8 (MicroChem Corp.), not by single-photon absorption, but two- or multi-photon absorption. Therefore, a laser system is required that provides short pulses with a photon energy well below the one-photon absorption edge of the photoresist. Yet, by tightly focusing the laser light into the photoresist, the intensity in the focus can get sufficiently high to expose the photoresist eventually by a two- or multi-photon process. The volume of the photoresist that is exposed by one laser pulse in this manner, is called “voxel” (shortened from volume pixel). The experimental setup, originally established by M. Deubel [84] and further improved in the past years, is schematically depicted in Fig. 4.1; the grey-shaded components indicate the modifications performed in the course of this thesis.

The regeneratively amplified Ti:Sapphire laser system (Spectra Physics Hurricane) provides short pulses (around 120 fs) at a central wavelength of 800 nm, at which the single-photon absorption in SU-8 is negligible. At beam splitter BS1 only a small amount ( $\approx 1\%$ ) of the laser intensity is reflected into the direct laser writing setup, while the larger part ( $\approx 99\%$ ) is transmitted and after attenuation (A) coupled into the autocorrelator to determine the temporal pulse width, which can be adjusted by the external pulse compressor in the laser system. The laser beam reflected at BS1 passes a combination of a half-wave plate ( $\lambda/2$ ) and a Glan-Laser polariser (GLP), which allows to adjust the intensity of the laser beam for the exposure of the photoresist and thus to control the actually obtained voxel size<sup>2</sup>, cf. Refs.

<sup>2</sup>Shape and size of the voxels are related to the curves of constant time-averaged electric energy density in the focal plane of the microscope objective. These curves can be calculated by adopting the vectorial electromagnetic diffraction theory by Török *et al.* [87, 88]. The applied laser intensity determines the exposing threshold value within these curves and thus the actual voxel size. See also chapter A of the appendix.

[84, 86]. In the course of this thesis, this combination of half-wave plate and Glan-Laser polariser is replaced by an acousto-optical modulator (AOM), which provides the possibility of a computer-controlled manipulation of the laser intensity via a personal computer (PC). The subsequent quarter-wave plate ( $\lambda/4$ ) has the purpose to avoid any polarisation effects in exposing and polymerising the photoresist SU-8, since the output beam of the Hurricane laser is initially linearly polarised<sup>3</sup>. The lenses L1 and L2 serve as a telescope to expand the beam from 6 mm to 12 mm diameter before entering the custom-built inverted microscope (Leica DR-IRM). At the beam splitter BS2, the laser beam is reflected, passes through the shaded-ring filter (SRF) and is finally focused into the sample (CS) by an oil-immersion microscope objective (MO) with a numerical aperture NA of 1.4 and an input pupil of 5.6 mm in diameter. The obtained voxel is of ellipsoidal shape with the long axis pointing along the optical axis of the focusing microscope objective, cf. Refs. [84, 86]. The aspect ratio  $\chi$  of the axial and lateral extension of the voxel is effected, in particular reduced, by the shaded-ring filter<sup>4</sup>, cf. Refs. [18, 48, 89]. The samples, 170  $\mu\text{m}$  thick glass substrates covered with 20  $\mu\text{m}$  thick SU-8 films, are mounted on a three-axes piezo scanning stage (PS, Physik Instrumente P-527.3CL). The piezo-stage is controlled by the personal computer (PC). In the course of this thesis, the piezo scanning stage is mounted onto a two-axes computer-controlled (PC) translational stage (TS, Märzhäuser C9712-9012K, Vexta Stepping Motor, Wetzlar), in order to shift the lateral position of the sample, i.e., the position in the plane perpendicular to the optical axis of the microscope objective, in relatively large steps (several hundreds of  $\mu\text{m}$ ). The PC also drives the electronic interface (SDG), which is responsible for switching the laser output on and off by controlling the respective pockels cells<sup>5</sup> and which sets the repetition rate of the laser pulses. Thus, the piezo scanning operation and the laser output can be synchronised via computer control for the fabrication process of photonic nanostructures. An alternative light path, depicted in short dashed lines, uses the imaging function of the inverted microscope to pre-position the sample with respect to the focus of the microscope objective. The image formed by the tube lens TL can be observed through the eyepiece (E) or by a charge-coupled-device (CCD) camera, depending on the position of the kinematic mirror (KM). This light path can be blocked by the blocker BL, when the laser is active to write the photonic nanostructures into the photoresist.

The direct laser writing setup is operated in the so-called “Fast Writing Mode”. In this mode, the laser output is switched on and provides short pulses with a repetition rate of 1 kHz for exposing the photoresist, while the piezo-stage is scanning interconnected parts of the photonic nanostructure. These interconnected parts are programmed as sequences of points forming trajectories (imported as ASCII-files). As the trajectories are generally positioned obliquely in space, one requires controlling all three spatial directions equally fast and synchronised. For this purpose, an output board (National Instruments PCI-6731) with four synchronised and hardware triggered output channels is implemented. A second card (PCI-MIO-16XE10) is used to check the target position of the piezo-stage each time before the

---

<sup>3</sup>Without the quarter-wave plate, the curves of constant time-averaged electric energy density, cf. Ref. [84], are not rotationally symmetric, but slightly elliptical with the long axis pointing along the direction of the incident linear polarisation. This was also experimentally observed as a clear dependence of the thickness and the stability of the written lines on their orientation with respect to the linear polarisation of the exposing laser beam.

<sup>4</sup>The effect of the shaded-ring filter is described in more detail in chapter A of the appendix.

<sup>5</sup>The control of the laser status via the pockels cell gets expendable as soon as the laser intensity coupled into the microscope objective is controlled by the acousto-optical modulator (AOM).

laser output is switched on (or the laser intensity is modified accordingly via the acousto-optical modulator) for writing one of the trajectories. A dedicated LabVIEW software (running on the PC) synchronises the piezo scanning stage operation and the switching of the laser status (or laser intensity) appropriately to write all the required trajectories of the photonic nanostructures.

After the exposure with the Hurricane laser, the SU-8 film is post-baked and developed for several minutes in the commercially available SU-8 developer mr-600 (MicroChem Corp.), which dissolves the non-exposed parts in the sample. Thus, the finally obtained photonic nanostructure consists of air and deterministically distributed exposed SU-8. Further details on the polymerisation mechanism and the processing steps of SU-8 can be found in Refs. [84, 90].

## 4.2 Optical Characterisation

### 4.2.1 Laue Diffraction Measurements

The quality and rotational symmetry properties of the fabricated photonic quasicrystals can be characterised by measuring the Laue diffraction patterns, following the experiments on quasiperiodic metallic alloys which led to the discovery of quasicrystals in 1984 [5]. For this purpose, monochromatic visible light, from a solid-state laser emitting at 532 nm wavelength or a Helium-Neon laser emitting at 633 nm wavelength, is focused onto the photonic quasicrystals by a lens (L) with focal length  $f=50.2$  mm. The overall setup is schematically depicted in Fig. 4.2. The arising Laue pattern is scattered off a white sheet of paper serving as screen (S). Since the zeroth-order diffracted spot is overly intense, it is blocked appropriately by a blocker (B) to allow for photographing the Laue diagram without overloading the camera. Neutral density filters (NDF) can be inserted into the setup to adjust the intensity of the laser beam.

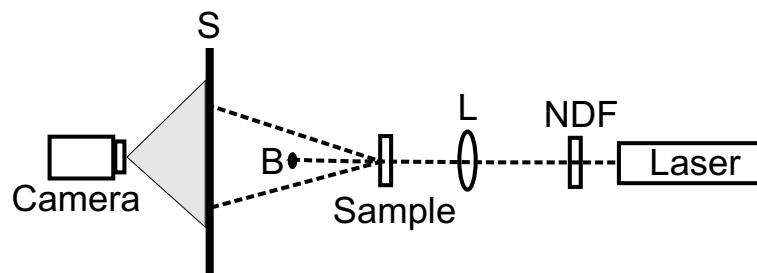


Figure 4.2: The setup of the Laue diffraction experiment is schematically sketched. A monochromatic laser beam is focused onto the sample, the occurring Laue diffraction pattern is photographed. NDF: neutral density filter; L: lens with  $f=50.2$  mm; B: blocker for non-diffracted light; S: screen.

### 4.2.2 Time-Resolved Transmittance Spectroscopy

In cooperation with the European Laboratory for Nonlinear Spectroscopy (LENS) in Florence, where the time-resolved transmittance spectroscopy setup depicted in Fig. 4.3 is operated, the transport properties of photonic systems, and in particular of our photonic quasicrystals, can be investigated [49, 85]. The Ti:Sapphire oscillator system (Spectra Physics Tsunami) delivers short pulses ( $\leq 100$  fs) at a central wavelength of 800 nm. These pulses are converted into

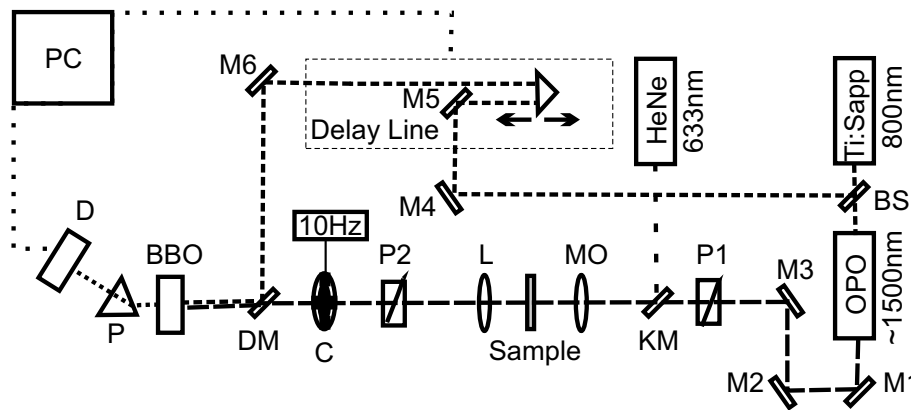


Figure 4.3: The setup for time-resolved transmittance measurements is schematically illustrated. In the nonlinear BBO crystal the reference Ti:Sapphire beam is mixed with the infrared beam, transmitted through the sample. The upconverted signal is detected by a combination of a photomultiplier and a dual channel gated photon counter (D). The Helium-Neon laser is coupled in by the kinematic mirror (KM) to position the sample correctly in the focus of the microscope objective (MO). The pair of polarisers P1 and P2 permits polarisation-resolved measurements. BS: beam splitter, M1-M6: silver mirrors; P1, P2: pair of polarisers; KM: kinematic mirror; MO: microscope objective; L: lens with  $f=25$  mm; C: chopper; DM: dichroic mirror; BBO: nonlinear BBO crystal; P: prism, D: detector (photomultiplier and a dual channel gated photon counter), PC: personal computer.

tunable infrared pulses from 1400 nm to 1570 nm wavelengths with 150 fs pulse duration by an optical parametric oscillator (OPO) system (Spectra Physics OPAL). The infrared pulses are focused onto the sample via a microscope objective (MO, numerical aperture  $NA=0.42$ ). Such tight focusing is essential to guarantee that the laser light probes solely the rather small (typically 100  $\mu\text{m}$  in diameter) photonic nanostructures under study, i.e., that the light has no possibility to pass unintendedly through the bare substrate surrounding the sample. The light transmitted through the sample is collected and collimated by the lens (L) of half opening angle  $\theta=27^\circ$  before it impinges on the 1 mm thick nonlinear beta-barium-borate (BBO) crystal. In there, it is mixed with the reference Ti:sapphire beam (800 nm central wavelength) which is reflected onto the BBO crystal by the dichroic mirror (DM). The upconverted signal, appropriately selected by the prism P, is detected by a combination of a photomultiplier and a dual channel gated photon counter (D). The reference Ti:sapphire beam is delayed variably in the delay line to allow for time-resolved transmittance measurements. The chopper, driven at 10 Hz, serves as a trigger for the photon counter to identify the background noise in the detected signal. The chopper fixes definite time slices, at which the infrared beam transmitted through the sample can pass to mix with the reference Ti:sapphire beam or at which the infrared beam is blocked and, consequently, the detected signal should be zero. The respective time slices are synchronised with the photon counter to distinguish the background noise during the blocked periods and the true upconverted signal (after subtracting the background noise) during the unblocked periods. The pair of polarisers P1 and P2 provides the possibility of polarisation-resolved measurements by analysing the light, which is transmitted through the sample, more diligently, i.e., if the polarisation state of the transmitted light has changed or not. Especially, studying the case when the polarisers have orientations orthogonal to each other (referred to as cross polarisation configuration) is advantageous as the directly transmitted beam is blocked and only the light, which has changed its polarisation state is detected. Thus, one can observe

predominantly the light which has actually interacted with the sample<sup>6</sup>.

In order to align the sample correctly within the setup, i.e., with respect to the foci of the microscope objective MO and of the lens L, the Helium-Neon laser is coupled into the light path by a kinematic mirror (KM) and focused onto the sample. Observing the arising Laue diffraction pattern, one can easily adjust the position of the sample in all three directions.

Performing time-resolved measurements, the tunable wavelength of the infrared beam, obtained from the OPO system, is set to a specific value. The total length of the delay line is chosen to be varied in 4  $\mu\text{m}$  steps, which sets the temporal resolution to 14 fs in this case. In order to protect the photomultiplier from overloading, appropriate filters are inserted into the setup right after the prism P.

### 4.2.3 Transmittance and Reflectance Measurements

In the course of this thesis, we fabricate photonic nanostructures with rod lengths in the  $\mu\text{m}$  range. Thus, any interesting features in the photonic band structures are expected in the infrared (cf. chapter 5). For a fast optical characterisation of the rather small photonic nanostructures (around 100  $\mu\text{m}$  in diameter), the commercially available Bruker Optics system, a combination of a Fourier transform infrared (FTIR) spectrometer (EQUINOX 55) and an infrared microscope (HYPERION 2000), is used to obtain reflectance and transmittance spectra. The system exhibits two measurement ranges to cover the overall spectral range from 500 nm to 5000 nm at a resolution of  $\Delta\lambda=0.5$  nm at  $\lambda=1.0$   $\mu\text{m}$ . A NIR/VIS tungsten halogen lamp serves as the light source. For the near-infrared regime (1000 nm to 5000 nm), a  $\text{CaF}_2$  beam splitter is installed in the interferometer and a liquid-nitrogen cooled InSb detector in the microscope, while for the visible spectral range a quartz beam splitter and a silicon photodiode detector are used. In the case of measuring reflectance, a 36x cassegrain reflective microscope objective with a numerical aperture of  $\text{NA}=0.5$  focuses light on the sample and collects the reflected light simultaneously. For transmittance measurements, the transmitted light is collected by the same microscope objective, while a second identical microscope objective focuses light on the sample from the opposite side. This system provides the possibility to investigate small samples in the order of several  $\mu\text{m}$  or specific areas of larger samples, respectively, by introducing apertures in the intermediate image plane to spatially filter the transmittance or reflectance. For polarisation-resolved measurements, polarisers and analysers can be put into the light path.

However, a major drawback of this setup results from the design of the cassegrain microscope objectives, which on the other hand just provide the big advantage of measuring over a large spectral range (500 nm to 5000 nm). The numerical aperture  $\text{NA}=0.5$  corresponds to an opening angle of  $30^\circ$ , while the cassegrain design blocks the angles from  $0^\circ$  to  $15^\circ$ . Hence, normal incidence cannot be measured and the transmittance and reflectance spectra are averaged over the cone from  $15^\circ$  to  $30^\circ$ . This has to be kept in mind, when measuring non-homogeneous samples with strongly angle-dependent reflectance and transmittance properties.

---

<sup>6</sup>The cross polarisation configuration is particularly sensitive to diffusively scattered components, e.g., in disordered photonic systems (cf. section 2.1.2), and is commonly applied to measure diffusive light propagation in such photonic systems.

#### 4.2.4 Normal Incidence and Angle-Resolved Transmittance Spectroscopy

For normal incidence transmittance measurements, a dedicated setup in which the half-opening angle of the incident light is reduced down to  $5^\circ$  (or even smaller) by using conventional optics has been built in our group [84]. This home-built setup also offers the opportunity for angle-resolved and polarisation-resolved transmittance measurements.

In Fig. 4.4, the setup is schematically sketched. A 100 W power tungsten halogen lamp, yielding black-body emission with a surface temperature of around 3000 K, serves as light source. The light is coupled into an IR/VIS optical fibre with a 200  $\mu\text{m}$  core by the lens L1 to be transmitted to the actual transmittance setup. Lens L2 collimates the light emerging from the fibre. Using polariser P1, the linear polarisation of the light is controlled which is finally focused onto the sample by the microscope objective MO1 (Zeiss Achroplan LD 20x KO, NA=0.4). The sample itself is mounted onto a goniometer placed on a rotation stage such that the sample can be aligned strictly perpendicular to the optical axis. Furthermore, it is possible to rotate the sample by defined angles with respect to the normal incidence case to allow for angle-resolved transmittance measurements. By closing the circular aperture CA1 placed directly in front of the microscope objective MO1, the half-opening angle of the light focused onto the sample can be reduced to  $5^\circ$ . By inserting a 200  $\mu\text{m}$  pinhole<sup>7</sup> right in front of the microscope objective MO1, it is even possible to actually nearly accomplish the ideal of an incident plane wave, reducing the full-opening angle down to even  $1.5^\circ$ . The combination of the microscope objective MO2 and the circular aperture CA2 behind the sample allows for collecting the transmitted light within a specific half-opening angle reaching from  $24^\circ$  (open circular aperture) down to  $5^\circ$  (closed circular aperture). A second polariser (P2) can be inserted into the setup to analyse the polarisation state of the transmitted light. Lens L3 in combination with the objective MO2 is used to image the sample to an intermediate image plane in which knife-edges (KE) are placed to spatially select the sample area which is to be studied. This selected area is finally imaged onto an IR/VIS optical fibre with a 200  $\mu\text{m}$  core using lens L4 and microscope objective MO3 (Newport M-10x, NA=0.25). The fibre is then connected to the detecting system, which is typically an optical spectrum analyser (OSA, Ando AQ 6315 B) with a fairly large spectral range from 500 nm to 1750 nm. For some delicate measurements required in the course of this thesis (see section 5.3.3), however, the output of the optical fibre is coupled via lenses L6 and L7 to a grating spectrometer (SPM, Acton SP 2150i, focal length  $f=150$  mm, entrance slit set to 30  $\mu\text{m}$ ) connected to a sensitive liquid-nitrogen cooled back-illuminated silicon CCD camera (CCD (Si), Roper Scientific, LN/CCD-1340/100-EB), which gives the opportunity to detect transmitted light of even quite low light levels with high resolution (of  $\approx 1$  nm) [91]. Yet, this detecting system has the drawback of a limited spectral range – from 700 nm to 840 nm wavelength for the applied grating (300 per cm, blazed at 1.0  $\mu\text{m}$ , central wavelength set to 800 nm).

In order to align the sample with respect to the foci of the microscope objectives MO1 and MO2 and to adjust the knife-edge aperture in the intermediate image plane, the kinematic mirror KM can be introduced into the setup to image the intermediate image plane via lens L5 onto an infrared CCD camera (CCD, Panasonic) with a magnification of  $\approx 62.5\times$ .

---

<sup>7</sup>Introducing the pinhole has the drawback of relatively low light levels impinging on the sample, and moreover, being transmitted through the sample.

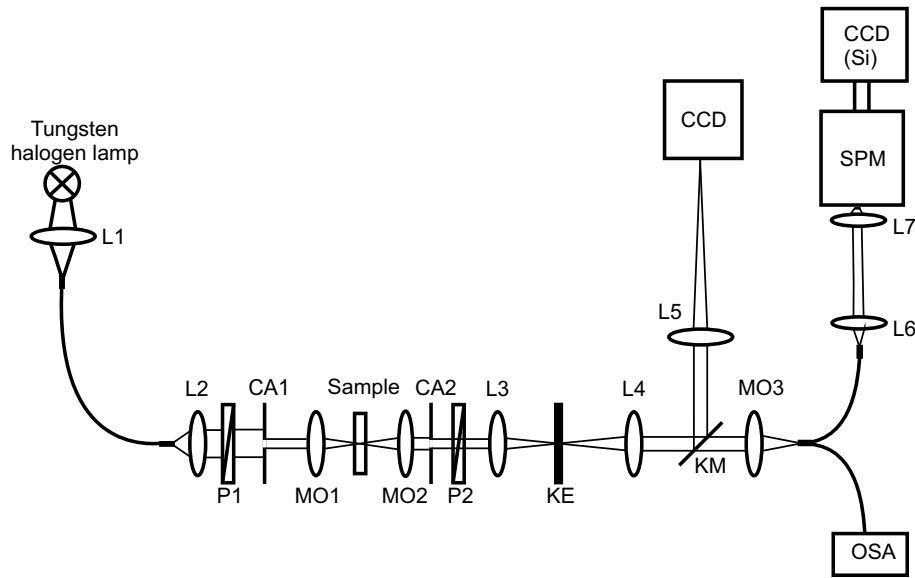


Figure 4.4: The setup for normal incidence, angle-resolved and polarisation-resolved transmittance measurements is illustrated. Light is focused onto a small sample with a fairly small opening angle. The transmitted light is re-imaged onto an intermediate image plane where knife-edges can be adjusted to select the sample area. This can be monitored by a CCD camera. For spectrally resolved detection, either an optical spectrum analyser or a grating spectrometer connected to a CCD camera is used. L1: lens with  $f=50.2$  mm; L2: lens with  $f=25.4$  mm; P1, P2: pair of Glan-Thompson polarisers; CA1, CA2: circular apertures; MO1, MO2: microscope objectives (NA=0.4); L3, L4: lenses with  $f=150$  mm; KE: knife-edge aperture; KM: kinematic mirror; MO3: microscope objective (NA=0.25); OSA: optical spectrum analyser; L5: lens with  $f=500$  mm; CCD: CCD camera; L6: lens with  $f=25.0$  mm; L7: lens with  $f=50.2$  mm; SPM: spectrometer; CCD (Si): silicon CCD camera.

## 4.3 Scattering Matrix Calculations

In the previous section, several optical setups have been described which are used to experimentally characterise the optical properties of the photonic nanostructures fabricated by direct laser writing. Yet, in order to interpret the experimental results, it is necessary to have a theoretical tool at hand to calculate the expected optical properties and characteristics. In the course of this thesis, we use the scattering matrix formalism for computing the optical transmittance and reflectance properties of (periodic) photonic nanostructures and to compare the experimentally obtained data with. Thus, information about the optical quality of the fabricated photonic nanostructures and of their intrinsic properties can be deduced. In the following sections, we would like to briefly introduce the scattering matrix formalism and additionally, we like to outline the modifications we made to the home-built scattering matrix programme code of S. Linden in order to take account of the distinct experimental conditions of our setups.

### 4.3.1 Transmittance and Reflectance

A commonly used method to characterise photonic nanostructures is to determine their transmittance and reflectance properties. This is schematically depicted in Fig. 4.5. Coming from half space  $V$  with refractive index  $n_V$ , a plane wave of frequency  $\omega$  and amplitude  $A_V^+$  impinges on the photonic nanostructure and is partially transmitted into half space  $S$  with refractive index  $n_S$  and partially reflected back into half space  $V$ . The amplitudes of the transmitted and

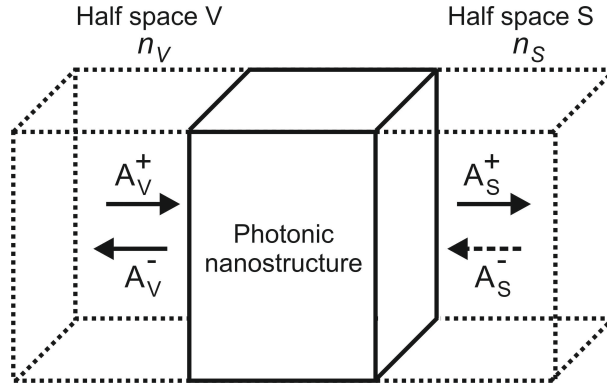


Figure 4.5: Schematic sketch of a typical transmittance/reflectance experiment.  $A_{S/V}^{+/-}$  denote the respective amplitudes of the plane waves propagating in half space  $V$  or  $S$  in different directions.

reflected parts are  $A_S^+$  and  $A_V^-$ , respectively. In principle, one can have a wave impinging on the sample from half space  $S$  with amplitude  $A_S^-$  as well, yet in most experiments this wave is absent and thus its amplitude is usually set to zero.

In this thesis, the transmittance and reflectance spectra of photonic nanostructures are calculated by applying the scattering matrix formalism, which was implemented in our group by S. Linden and follows the approach described in the publications of Whittaker and Culshaw [14] and Thikhodeev *et al.* [15]. In this formalism the incoming amplitudes  $A_V^+$  and  $A_S^-$  are connected with the outgoing amplitudes  $A_S^+$  and  $A_V^-$  via the so-called scattering matrix  $\mathcal{S}$ :

$$\begin{pmatrix} A_S^+ \\ A_V^- \end{pmatrix} = \mathcal{S} \begin{pmatrix} A_V^+ \\ A_S^- \end{pmatrix} = \begin{pmatrix} S_{11} & S_{12} \\ S_{21} & S_{22} \end{pmatrix} \begin{pmatrix} A_V^+ \\ A_S^- \end{pmatrix}. \quad (4.1)$$

Obviously, the scattering matrix  $\mathcal{S}$  is essential to calculate the outgoing amplitudes  $A_S^+$  and  $A_V^-$  which finally define the transmittance and reflectance properties of the structure under study.

In our case, we probe the photonic nanostructures with electromagnetic waves and thus the scattering matrix can be derived by solving Maxwell's equations [equations (2.1) to (2.4)] using a plane wave expansion method (cf. section 2.1.1). As this approach is described in detail in Refs. [14, 15, 92], we will just point out some important facts.

In our calculations, we consider linearly polarised electromagnetic waves of frequency  $\omega$  and wave vector  $\vec{k}_{\text{in}}$ , with a non-zero component  $k_z$  along the propagation direction  $z$ , impinging on the photonic nanostructures (cf. Fig. 4.6). Thus, the amplitudes  $A_{S/V}^{+/-}$  refer to the amplitudes of the electric and magnetic fields. In the following description, we will omit the frequency  $\omega$  as variable for reasons of readability.

Generally, the three-dimensional photonic nanostructures under study are quite complex. Yet, in order to apply the scattering matrix formalism based on the plane-wave expansion method (see section 2.1.1), we have to split the photonic nanostructure, which has a finite thickness in the propagation direction  $z$ , into a finite number of slabs which are homogeneous in the propagation direction  $z$  and periodic in the  $xy$ -plane. This is illustrated in Fig. 4.6 (a). The thickness of each slab is  $L$ , the periodicity in the  $xy$ -plane is defined by the lattice constants  $a_x$  and  $a_y$ , respectively. In each slab, Maxwell's equations are solved by a plane-wave ansatz for

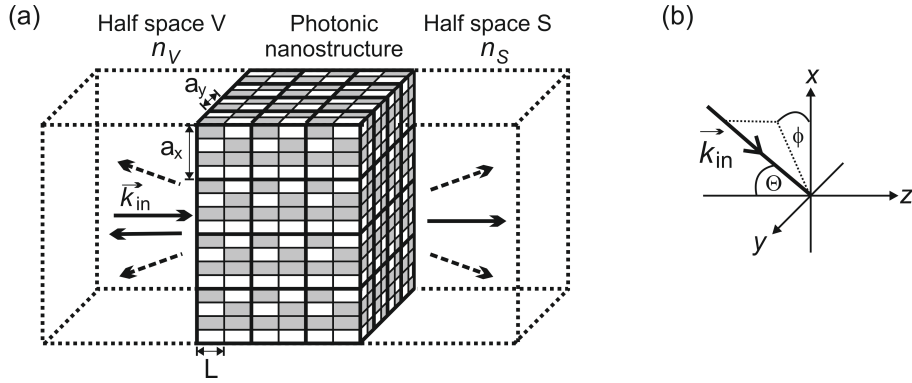


Figure 4.6: (a) The electromagnetic wave of wave vector  $\vec{k}_{\text{in}}$  impinges on a complex photonic nanostructure and is partly reflected and partly transmitted – diffraction in forward and backward direction (dashed arrows) is included. The complex photonic nanostructure, in this case a composite of two different dielectric materials of refractive indices  $n_1$  and  $n_2 \neq n_1$  (white- and grey-coloured cuboids), is segmented into homogeneous slabs of thickness  $L$ . Each slab is periodic in  $x$ - and  $y$ -direction with lattice constants  $a_x$  and  $a_y$ , respectively. (b) The wave vector  $\vec{k}_{\text{in}}$  is depicted for oblique incidence.

the eigenmodes of the magnetic field<sup>8</sup>  $\vec{H}_n$ , which are Bloch modes in the  $xy$ -plane and exhibit an exponential dependence along  $z$ . Afterwards, the in-plane (i.e.,  $x$ - and  $y$ -) components of the local electromagnetic fields are derived. Finally, the eigenmodes of the individual slabs are connected in order to construct the (total) scattering matrix  $\mathcal{S}$  of the complete photonic nanostructure.

As we do separate the problem into slabs which are homogeneous in  $z$ , yet periodic in the  $xy$ -plane, we similarly decompose the vectors  $\vec{r}$  and  $\vec{k}$  into their components parallel and perpendicular to the  $xy$ -plane. Hence, the plane-wave expansion of  $\vec{H}_n$  gives:

$$\begin{aligned} \vec{H}_n(\vec{r}_{\parallel}, z, t) &= \\ &= \sum_{\vec{G}} \left[ H_{x,n}(\vec{G}) \cdot \left( \hat{e}_x - \frac{1}{q_n} (k_x + G_x) \hat{e}_z \right) + H_{y,n}(\vec{G}) \cdot \left( \hat{e}_y - \frac{1}{q_n} (k_y + G_y) \hat{e}_z \right) \right] \quad (4.2) \\ &\times e^{i(\vec{k}_{\parallel} + \vec{G})\vec{r}_{\parallel}} e^{iq_n z} e^{-i\omega t}, \end{aligned}$$

where  $H_{x,n}(\vec{G})$  and  $H_{y,n}(\vec{G})$  are expansion coefficients, and  $\vec{G}$  are the two-dimensional reciprocal lattice vectors:

$$\vec{G} = \vec{G}_i = 2\pi \left( \frac{m_x}{a_x}, \frac{m_y}{a_y} \right) = \vec{G}_{(m_x, m_y)}, \quad i \in \mathbb{N}, \quad m_x, m_y \in \mathbb{Z}. \quad (4.3)$$

This ansatz automatically results in  $\nabla \cdot \vec{H} = 0$ .

In equation (4.2), the  $x$ - and  $y$ -components  $k_x$  and  $k_y$  of the wave vector  $\vec{k}$  with  $|\vec{k}| = 2\pi/\lambda$  are complemented by the component  $q_n$ , which refers to the propagation constant in  $z$ -direction.

<sup>8</sup>The eigenmodes are solved for the magnetic field as its operator of the wave equation [equation (2.13)] is hermitian (cf. section 2.1).

For homogeneous media, i.e.,  $\epsilon(\vec{r}) = \epsilon_m = \text{const.}$ ,  $q_n$  is given by:

$$q_n = \sqrt{\frac{\omega^2 \epsilon_m}{c_0^2} - (k_x + G_x)^2 - (k_y + G_y)^2}, \quad (4.4)$$

while for a truly spatially dependent permittivity  $\epsilon(\vec{r})$ , the value of  $q_n$  is derived from the eigenvalue problem, defined below in equation (4.6). Depending on the actual result of  $q_n$ , being real or imaginary, the corresponding eigenmode is a propagating mode or an exponentially decaying evanescent mode along  $z$ .

In numerical calculations, the number of reciprocal lattice vectors is restricted by a cutoff  $\vec{G}_{max}$ . In the case of two-dimensional square lattices with  $a_x = a_y$ , which we consider in the course of this thesis, this cutoff translates into the usage of  $N_g = (2g + 1)(2g + 1)$  reciprocal lattice vectors with  $|m_x| \leq g$ ,  $|m_y| \leq g$ , and  $g$  determines the number of orders which are accounted for.

The matrix  $\hat{\eta}$  of the inverse permittivity  $\epsilon^{-1}$  is defined by:

$$\hat{\eta} = \eta_{\vec{G}, \vec{G}'} = \eta_{\vec{G}-\vec{G}'} = \frac{1}{A_{\text{WSC}}} \int_{\text{WSC}} \epsilon^{-1}(\vec{r}_{\parallel}) e^{i(\vec{G}' - \vec{G})\vec{r}_{\parallel}} d^2 \vec{r}_{\parallel}, \quad (4.5)$$

where  $A_{\text{WSC}}$  is the area of the two-dimensional Wigner-Seitz cell.

Inserting equations (4.2) and (4.5) into Maxwell's equations results in an eigenvalue problem, which is to be solved to get the eigenmodes of the individual slabs:

$$\left[ \begin{pmatrix} \hat{\eta} & 0 \\ 0 & \hat{\eta} \end{pmatrix}^{-1} \left( \left( \frac{\omega}{c_0} \right)^2 \hat{I} - \hat{Z} \right) - \hat{K} \right] \begin{pmatrix} H_{x,n} \\ H_{y,n} \end{pmatrix} = \mathcal{Q}^2 \begin{pmatrix} H_{x,n} \\ H_{y,n} \end{pmatrix}. \quad (4.6)$$

Here,  $\hat{I}$  is the  $2N_g \times 2N_g$  unit matrix, and the vectors  $H_{x,n}$  and  $H_{y,n}$  indicate the expansion coefficients for each eigenmode for the finite number of reciprocal lattice vectors, i.e.,  $H_{i,n} = H_{i,n}(\vec{G}_1), \dots, H_{i,n}(\vec{G}_{N_g})$ ,  $i = x, y$ . Furthermore,  $\hat{Z}$ ,  $\hat{K}$  and  $\mathcal{Q}$  are defined as:

$$\hat{Z} = \begin{pmatrix} \hat{K}_y \hat{\eta} \hat{K}_y & -\hat{K}_y \hat{\eta} \hat{K}_x \\ -\hat{K}_x \hat{\eta} \hat{K}_y & \hat{K}_x \hat{\eta} \hat{K}_x \end{pmatrix}, \quad (4.7)$$

$$\hat{K} = \begin{pmatrix} \hat{K}_x \hat{K}_x & \hat{K}_x \hat{K}_y \\ \hat{K}_y \hat{K}_x & \hat{K}_y \hat{K}_y \end{pmatrix}, \quad (4.8)$$

with

$$\left( \hat{K}_i \right)_{\vec{G}, \vec{G}'} = (k_i + G_i) \delta_{\vec{G}, \vec{G}'}, \quad i = x, y, \quad (4.9)$$

and

$$\mathcal{Q} = \begin{pmatrix} q_1 & & & 0 \\ & q_2 & & \\ & & \ddots & \\ 0 & & & q_{2N_g} \end{pmatrix}, \quad (4.10)$$

while  $q_n^2$  are the eigenvalues of the eigenvalue problem [equation (4.6)].

Having obtained the eigenmodes  $H_{x,n}$  and  $H_{y,n}$  of the individual slabs, we can calculate the corresponding electric field components via:

$$\begin{pmatrix} -E_{y,n} \\ E_{x,n} \end{pmatrix} = \frac{1}{\omega\epsilon_0} \left( \frac{\omega^2}{c_0^2} \hat{I} - \hat{Z} \right) \begin{pmatrix} H_{x,n} \\ H_{y,n} \end{pmatrix} \mathcal{Q}^{-1}, \quad (4.11)$$

with  $E_{i,n} = E_{i,n}(\vec{G}_1), \dots, E_{i,n}(\vec{G}_{N_g}), i = x, y$ .

The weighting or amplitudes of the thus calculated eigenmodes, propagating along  $z$  (+) or opposite to  $z$  (-), i.e.,  $\propto e^{iq_n z - i\omega t}$  and  $\propto e^{-iq_n z - i\omega t}$ , are combined in the  $4N_g$ -dimensional amplitude vector  $\vec{A}(z)$  with

$$\vec{A}(z) = \begin{pmatrix} A^+(z) \\ A^-(z) \end{pmatrix}, \quad (4.12)$$

and

$$\vec{H}_{\parallel}(z) = \begin{pmatrix} H_x(z) \\ H_y(z) \end{pmatrix} = (\mathcal{H}, \mathcal{H}) \vec{A}(z). \quad (4.13)$$

The  $N_g$ -dimensional vectors  $H_i(z) = (H_i(\vec{G}_1, z), \dots, H_i(\vec{G}_{N_g}, z))^T, i = x, y$  state the amplitudes of the partial waves in the Fourier-decomposition of the in-plane ( $x$ - and  $y$ -) components of the magnetic fields. The  $2N_g \times 2N_g$ -dimensional matrix  $\mathcal{H}$  contains the eigenvectors  $(H_{x,n}, H_{y,n})^T$  of equation (4.6) as columns. Similarly, the representation of the electric field in terms of partial waves coefficients is derived by:

$$\vec{E}_{\parallel}(z) = \begin{pmatrix} -E_y(z) \\ E_x(z) \end{pmatrix} = (\mathcal{E}, -\mathcal{E}) \vec{A}(z), \quad (4.14)$$

where  $\mathcal{E}$  contains the eigenvectors  $(-E_{y,n}, E_{x,n})^T$  of equation (4.11) as columns.

In the next step, the fields between the individual slabs are connected by basically accounting for the propagation ( $+z$  and  $-z$ ) within the individual homogeneous slabs of thickness  $L$  and by applying the continuity conditions for the tangential components of the electric and magnetic fields at the respective interfaces between adjoining slabs.

In this manner, the (total) scattering matrix  $\mathcal{S} = \mathcal{S}_{V,S}$  of the complete (periodic) photonic nanostructure, connecting the input amplitudes  $A_V^+, A_S^-$  and output amplitudes  $A_S^+, A_V^-$  as defined in equation (4.1), can be calculated iteratively (adding slab by slab), using the condition  $\mathcal{S}_{V,V} = 1$  as starting point.

Subsequently, the complex electric and magnetic field amplitudes transmitted through and reflected from the photonic nanostructure can be derived for the respective reciprocal lattice vectors  $\vec{G}_{(m_x, m_y)}$ .

The corresponding transmittance  $T$  and reflectance  $R$  are calculated from the  $z$ -components of the Poynting vectors for incoming, transmitted and reflected waves:

$$T(\vec{G}_{(m_x, m_y)}) = \frac{\Re \left\{ \left( E_{x, \vec{G}_{(m_x, m_y), S}}^{\text{transm}} \right)^* \cdot \left( H_{y, \vec{G}_{(m_x, m_y), S}}^{\text{transm}} \right) - \left( E_{y, \vec{G}_{(m_x, m_y), S}}^{\text{transm}} \right)^* \cdot \left( H_{x, \vec{G}_{(m_x, m_y), S}}^{\text{transm}} \right) \right\}}{\Re \left\{ \left( E_{x, \vec{G}_{(0,0), V}}^{\text{incoming}} \right)^* \cdot \left( H_{y, \vec{G}_{(0,0), V}}^{\text{incoming}} \right) - \left( E_{y, \vec{G}_{(0,0), V}}^{\text{incoming}} \right)^* \cdot \left( H_{x, \vec{G}_{(0,0), V}}^{\text{incoming}} \right) \right\}} \quad (4.15)$$

and

$$R(\vec{G}_{(m_x, m_y)}) = \frac{\Re \left\{ \left( E_{x, \vec{G}_{(m_x, m_y), V}}^{\text{refl}} \right)^* \cdot \left( H_{y, \vec{G}_{(m_x, m_y), V}}^{\text{refl}} \right) - \left( E_{y, \vec{G}_{(m_x, m_y), V}}^{\text{refl}} \right)^* \cdot \left( H_{x, \vec{G}_{(m_x, m_y), V}}^{\text{refl}} \right) \right\}}{\Re \left\{ \left( E_{x, \vec{G}_{(0,0), V}}^{\text{incoming}} \right)^* \cdot \left( H_{y, \vec{G}_{(0,0), V}}^{\text{incoming}} \right) - \left( E_{y, \vec{G}_{(0,0), V}}^{\text{incoming}} \right)^* \cdot \left( H_{x, \vec{G}_{(0,0), V}}^{\text{incoming}} \right) \right\}}. \quad (4.16)$$

Please note that only propagating modes, i.e., with real  $q_n$ , must be considered for the determination of  $T$  and  $R$  (in the far-field).

Finally, we have to define the input amplitude  $A_V^+$ ; in typical experimental conditions  $A_S^-$  is just the zero-vector.

In general, the incoming linearly polarised electromagnetic field impinges on the photonic nanostructure with a certain azimuth angle  $\Theta$  and polar angle  $\phi$ , see Fig. 4.6 (b). The wave vector  $\vec{k}_{\text{in}}$  of the impinging electromagnetic wave is defined as:

$$\vec{k}_{\text{in}} = \begin{pmatrix} k_x \\ k_y \\ k_z \end{pmatrix} = |\vec{k}_{\text{in}}| \begin{pmatrix} \sin \theta \cos \phi \\ \sin \theta \sin \phi \\ \cos \theta \end{pmatrix}, \quad (4.17)$$

and accordingly the electric and magnetic field components are:

$$\vec{H}_s^{\text{incoming}} = (\cos \Theta \cos \phi, \cos \Theta \sin \phi, \sin \Theta)^T, \quad (4.18)$$

$$\vec{E}_s^{\text{incoming}} = (\cos \Theta \sin \phi, -\cos \Theta \cos \phi, \sin \Theta)^T, \quad (4.19)$$

$$\vec{H}_p^{\text{incoming}} = (-\sin \phi, \cos \phi, 0), \quad (4.20)$$

$$\vec{E}_p^{\text{incoming}} = (\cos \phi, \sin \phi, 0), \quad (4.21)$$

where  $s$  and  $p$  refer to linearly  $s$ - or  $p$ -polarised light.

Correspondingly, the incoming amplitudes  $A_{V,s/p}^+$  have only non-zero components for  $\vec{G}_1 = \vec{G}_{(0,0)} = (0, 0)$  and are defined as:

$$\begin{aligned} A_{V,s}^+ &= (A_{x, \vec{G}_1, V, s}^+, A_{x, \vec{G}_2, V, s}^+, \dots, A_{x, \vec{G}_{N_g}, V, s}^+, A_{y, \vec{G}_1, V, s}^+, A_{y, \vec{G}_2, V, s}^+, \dots, A_{y, \vec{G}_{N_g}, V, s}^+)^T \\ &= (\cos \Theta \cos \phi, 0, \dots, 0, \cos \Theta \sin \phi, 0, \dots, 0)^T, \end{aligned} \quad (4.22)$$

$$\begin{aligned} A_{V,p}^+ &= (A_{x, \vec{G}_1, V, p}^+, A_{x, \vec{G}_2, V, p}^+, \dots, A_{x, \vec{G}_{N_g}, V, p}^+, A_{y, \vec{G}_1, V, p}^+, A_{y, \vec{G}_2, V, p}^+, \dots, A_{y, \vec{G}_{N_g}, V, p}^+)^T \\ &= (-\sin \phi, 0, \dots, 0, \cos \phi, 0, \dots, 0)^T. \end{aligned} \quad (4.23)$$

The transmittance and reflectance spectra of a photonic nanostructure are finally obtained by performing the scattering matrix calculations for several frequencies  $\omega$  within the spectral range of interest.

As transmittance  $T$  and reflectance  $R$  are calculated for the individual reciprocal lattice vectors  $\vec{G}_{(m_x, m_y)}$ , cf. equation (4.15) and (4.16), it is possible to account for specific experimental conditions in which the transmittance and reflectance is measured within a specific opening angle  $\beta$  by adding up the values of  $T(\vec{G}_{(m_x, m_y)})$  and  $R(\vec{G}_{(m_x, m_y)})$  of the appropriate  $\vec{G}_{(m_x, m_y)}$  (cf. Ref. [15]).

### 4.3.2 Polarisation-Resolved Transmittance

In the previous section, we have dealt with the scattering matrix formalism to calculate the transmittance and reflectance properties of a photonic nanostructure probed by linearly polarised light. Yet, in some transmittance experiments it is useful not only to define a specific polarised light impinging on the sample, but also to locate polarisers behind the sample to analyse the transmitted light more diligently.

Generally, a complex photonic nanostructure diffracts light into several diffraction orders  $(m_x, m_y)$ , related to the reciprocal lattice vectors  $\vec{G}_{(m_x, m_y)}$ . In typical experiments, a lens is used to pick up and collimate the diffraction orders emerging from the sample within a specific opening angle before analysing the light using the polariser, i.e., the polariser is aligned perpendicular to the propagation direction  $\vec{k}^{(m_x, m_y)}$  of each diffraction order, cf. Fig. 4.7 (a). In the course of this thesis, we have implemented such analysing polarisers in the scattering matrix programme code, assuming normal incidence of the light impinging on the photonic nanostructure, i.e.,  $\vec{k}_{\text{in}} = (0, 0, |\vec{k}_{\text{in}}|)^T$ .

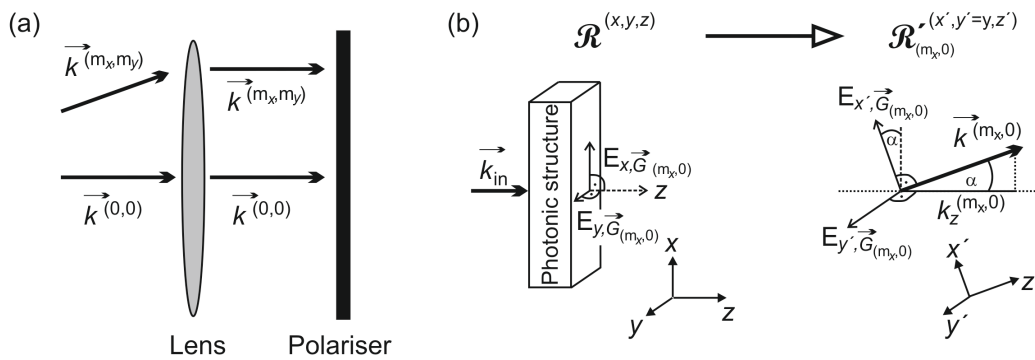


Figure 4.7: (a) The system of collimating lens and analysing polariser is depicted. The lens collimates the light such that all diffraction orders impinge on the polariser at normal incidence. (b) On the left, the electric field components  $E_{x, \vec{G}_{(m_x, m_y)}}$  and  $E_{y, \vec{G}_{(m_x, m_y)}}$  calculated by the scattering matrix formalism (see section 4.3.1) are defined in terms of the coordinate system  $\mathcal{R}$  of the photonic nanostructure, whereas on the right, the electric field components  $E_{x', \vec{G}_{(m_x, m_y)}}$  and  $E_{y', \vec{G}_{(m_x, m_y)}}$  are perpendicular to the propagation direction  $\vec{k}^{(m_x, m_y)} \parallel z'$  of the respective diffraction order  $(m_x, m_y)$ , which corresponds to the coordinate system  $\mathcal{R}'_{(m_x, m_y)}$ . This is illustrated for the diffraction order  $(m_x, m_y) = (m_x, 0)$ , which is diffracted in  $x$ -direction only. In this case, the new  $x'$ - and  $z'$ -axis are rotated with respect to the  $x$ - and  $z$ -axis of  $\mathcal{R}$ , while the  $y'$ -axis stays parallel to the  $y$ -axis.

The complex amplitudes of the transmitted magnetic and electric fields are calculated for the considered reciprocal lattice vectors  $\vec{G}_i$ ,  $i = 1 \dots N_g$  as described in the previous section. However, the calculated in-plane ( $x$ - and  $y$ -) components of the electric and magnetic fields are defined in the coordinate system  $\mathcal{R}$  based on the photonic nanostructure. This is depicted in Fig. 4.7 (b) on the left, showing the electric field components. The  $z$ -components of the electric and magnetic fields are zero.

Yet, in order to implement the system consisting of collimating lens and analysing polariser, we have to take care that the field components are defined in an orthogonal coordinate system  $\mathcal{R}'_{(m_x, m_y)}$  related to the propagation direction of the respective diffraction orders  $(m_x, m_y)$ , i.e., the  $x'$ -components and  $y'$ -components of the electric and magnetic fields define a plane perpendicular to the propagating direction  $\vec{k}^{(m_x, m_y)}$  of the respective diffraction orders  $(m_x, m_y)$  and  $\vec{k}^{(m_x, m_y)} \parallel z'$  - axis. This is illustrated in Fig. 4.7 (b) on the right, for the electric field components only, as the magnetic field can be treated likewise.

For switching each diffraction order to its new coordinate system  $\mathcal{R}'_{(m_x, m_y)}$  the following procedure is used:

The absolute value of the Poynting vector, which is used to calculate the transmitted intensity (cf. section 4.3.1 and Ref. [15]), must be conserved during the whole process of converting the field components from the coordinate system  $\mathcal{R}$  to the new one  $\mathcal{R}'_{(m_x, m_y)}$ .

The diffraction orders  $(m_x, m_y)$  propagate in (the homogeneous) half space  $S$  of refractive index  $n_S$  with the respective wave vectors  $\vec{k}^{(m_x, m_y)}$ :

$$\vec{k}^{(m_x, m_y)} = \begin{pmatrix} k_x^{(m_x, m_y)} \\ k_y^{(m_x, m_y)} \\ k_z^{(m_x, m_y)} \end{pmatrix} = \begin{pmatrix} 2\pi m_x / a_x \\ 2\pi m_y / a_y \\ \sqrt{(\omega n_S / c_0)^2 - (k_x^{(m_x, m_y)})^2 - (k_y^{(m_x, m_y)})^2} \end{pmatrix} \quad (4.24)$$

Note that we restrict ourselves here to the case of normal incident electromagnetic waves. To include oblique incidence, one has to add the non-zero  $x$ - and  $y$ - components of the incoming wave vector  $\vec{k}_{\text{in}}$  defined in equation (4.17) to the respective components of  $\vec{k}^{(m_x, m_y)}$  of equation (4.24).

As we consider electromagnetic plane waves propagating in a homogeneous medium, i.e., half space  $S$ , the following conditions must be satisfied:

$$\vec{k}^{(m_x, m_y)} \cdot \vec{E}_{\vec{G}_{(m_x, m_y)}, S}^{\text{transm}} = 0 \quad (4.25)$$

$$\vec{k}^{(m_x, m_y)} \cdot \vec{H}_{\vec{G}_{(m_x, m_y)}, S}^{\text{transm}} = 0. \quad (4.26)$$

Applying these conditions, the in-plane ( $x$ - and  $y$ -) components of the electric and magnetic field (defined in the coordinate system  $\mathcal{R}$ ) obtained from the scattering matrix formalism are

converted into new field components of  $\vec{E}$  and  $\vec{H}$  with the following  $z$ -components:

$$\tilde{E}_{z, \vec{G}(m_x, m_y), S}^{\text{transm}} = \frac{- \left( k_x^{(m_x, m_y)} \cdot \tilde{E}_{x, \vec{G}(m_x, m_y), S}^{\text{transm}} + k_y^{(m_x, m_y)} \cdot \tilde{E}_{y, \vec{G}(m_x, m_y), S}^{\text{transm}} \right)}{k_z^{(m_x, m_y)}} \quad (4.27)$$

$$\tilde{H}_{z, \vec{G}(m_x, m_y), S}^{\text{transm}} = \frac{- \left( k_x^{(m_x, m_y)} \cdot \tilde{H}_{x, \vec{G}(m_x, m_y), S}^{\text{transm}} + k_y^{(m_x, m_y)} \cdot \tilde{H}_{y, \vec{G}(m_x, m_y), S}^{\text{transm}} \right)}{k_z^{(m_x, m_y)}} \quad (4.28)$$

Subsequently, the coordinate system  $\mathcal{R}$  and likewise the components of the electric and magnetic field are transferred into the new respective coordinate systems  $\mathcal{R}'_{(m_x, m_y)}$  of each diffraction order by an appropriate rotation. The (normalised) rotation axis  $\vec{v}^{(m_x, m_y)}$  is given by

$$\vec{v}^{(m_x, m_y)} = \begin{pmatrix} v_1^{(m_x, m_y)} \\ v_2^{(m_x, m_y)} \\ v_3^{(m_x, m_y)} \end{pmatrix} = \frac{1}{m_x^2 + m_y^2} \begin{pmatrix} -m_y \\ m_x \\ 0 \end{pmatrix}, \quad (4.29)$$

and thus satisfies the conditions

$$\begin{aligned} \vec{v}^{(m_x, m_y)} \perp z\text{-axis} &\Leftrightarrow \vec{v}^{(m_x, m_y)} \in xy\text{-plane}, \\ \vec{v}^{(m_x, m_y)} \perp z'\text{-axis} &\Leftrightarrow \vec{v}^{(m_x, m_y)} \cdot \vec{k}^{(m_x, m_y)} = 0. \end{aligned} \quad (4.30)$$

The required rotation matrix  $\mathcal{D}^{(m_x, m_y)}$  is defined as:

$$\begin{aligned} \mathcal{D}^{(m_x, m_y)} &= \\ &= \begin{pmatrix} \cos \alpha + v_1^2(1 - \cos \alpha) & v_1 v_2(1 - \cos \alpha) - v_3 \sin \alpha & v_1 v_3(1 - \cos \alpha) + v_2 \sin \alpha \\ v_2 v_1(1 - \cos \alpha) + v_3 \sin \alpha & \cos \alpha + v_2^2(1 - \cos \alpha) & v_2 v_3(1 - \cos \alpha) - v_1 \sin \alpha \\ v_3 v_1(1 - \cos \alpha) - v_2 \sin \alpha & v_3 v_2(1 - \cos \alpha) + v_1 \sin \alpha & \cos \alpha + v_3^2(1 - \cos \alpha) \end{pmatrix}, \end{aligned} \quad (4.31)$$

with  $v_i = v_i^{(m_x, m_y)}$ ,  $i = 1, 2, 3$  defined in equation (4.29) and the rotation angle  $\alpha = \alpha(m_x, m_y)$  determined by:

$$\sin \alpha = - \frac{\sqrt{\left( k_x^{(m_x, m_y)} \right)^2 + \left( k_y^{(m_x, m_y)} \right)^2}}{|\vec{k}^{(m_x, m_y)}|}, \quad \cos \alpha = \frac{k_z^{(m_x, m_y)}}{|\vec{k}^{(m_x, m_y)}|}. \quad (4.32)$$

Performing the rotation of the electric and magnetic field components according to

$$\begin{pmatrix} E_{x', \vec{G}(m_x, m_y), S} \\ E_{y', \vec{G}(m_x, m_y), S} \\ E_{z', \vec{G}(m_x, m_y), S} \end{pmatrix} = \mathcal{D}^{(m_x, m_y)} \cdot \begin{pmatrix} \tilde{E}_{x, \vec{G}(m_x, m_y), S} \\ \tilde{E}_{y, \vec{G}(m_x, m_y), S} \\ \tilde{E}_{z, \vec{G}(m_x, m_y), S} \end{pmatrix} \quad (4.33)$$

and

$$\begin{pmatrix} H_{x', \vec{G}(m_x, m_y), S} \\ H_{y', \vec{G}(m_x, m_y), S} \\ H_{z', \vec{G}(m_x, m_y), S} \end{pmatrix} = \mathcal{D}^{(m_x, m_y)} \cdot \begin{pmatrix} \tilde{H}_{x, \vec{G}(m_x, m_y), S} \\ \tilde{H}_{y, \vec{G}(m_x, m_y), S} \\ \tilde{H}_{z, \vec{G}(m_x, m_y), S} \end{pmatrix}, \quad (4.34)$$

we end up with the field components  $E_{x',\vec{G}(m_x,m_y),S}$ ,  $E_{y',\vec{G}(m_x,m_y),S}$ ,  $E_{z',\vec{G}(m_x,m_y),S}$  and  $H_{x',\vec{G}(m_x,m_y),S}$ ,  $H_{y',\vec{G}(m_x,m_y),S}$ ,  $H_{z',\vec{G}(m_x,m_y),S}$  in the respective coordinate systems  $\mathcal{R}'_{(m_x,m_y)}$  of the various diffraction orders. Please note that in  $\mathcal{R}'_{(m_x,m_y)}$  the  $z'$ -components of electric and magnetic fields are identical to zero, as the propagation direction  $\vec{k}^{(m_x,m_y)}$  is parallel to the  $z'$ -axis.

The collimating effect of the lens rotates the propagation direction  $\vec{k}^{(m_x,m_y)} = (k_x^{(m_x,m_y)}, k_y^{(m_x,m_y)}, k_z^{(m_x,m_y)})^T$  of the diffraction orders to  $\vec{k}^{(m_x,m_y)} = (0, 0, |\vec{k}^{(m_x,m_y)}|)^T$ . This basically translates  $\mathcal{R}'_{(m_x,m_y)}$  back to  $\mathcal{R}$  and likewise the respective field components according to:

$$E_{x,\vec{G}(m_x,m_y),S}^{\text{transm}} = E_{x',\vec{G}(m_x,m_y),S} \quad , \quad (4.35)$$

$$E_{y,\vec{G}(m_x,m_y),S}^{\text{transm}} = E_{y',\vec{G}(m_x,m_y),S} \quad , \quad (4.36)$$

$$E_{z,\vec{G}(m_x,m_y),S}^{\text{transm}} = E_{z',\vec{G}(m_x,m_y),S} = 0 \quad , \quad (4.37)$$

$$H_{x,\vec{G}(m_x,m_y),S}^{\text{transm}} = H_{x',\vec{G}(m_x,m_y),S} \quad , \quad (4.38)$$

$$H_{y,\vec{G}(m_x,m_y),S}^{\text{transm}} = H_{y',\vec{G}(m_x,m_y),S} \quad , \quad (4.39)$$

$$H_{z,\vec{G}(m_x,m_y),S}^{\text{transm}} = H_{z',\vec{G}(m_x,m_y),S} = 0 \quad . \quad (4.40)$$

Now, the effect of the analysing polariser is taken into account when calculating the transmitted intensities for each diffraction order according to the orientation of the polariser with respect to the incident linearly polarised light:

$$I_p^{\text{same}}(\vec{G}(m_x,m_y)) = \frac{\Re \left\{ \left( E_{x,\vec{G}(m_x,m_y),S}^{\text{transm}} \right)^* \cdot \left( H_{y,\vec{G}(m_x,m_y),S}^{\text{transm}} \right) \right\}}{\Re \left\{ \left( E_{x,\vec{G}(0,0),V}^{\text{incoming}} \right)^* \cdot \left( H_{y,\vec{G}(0,0),V}^{\text{incoming}} \right) - \left( E_{y,\vec{G}(0,0),V}^{\text{incoming}} \right)^* \cdot \left( H_{x,\vec{G}(0,0),V}^{\text{incoming}} \right) \right\}} \quad , \quad (4.41)$$

$$I_p^{\text{cross}}(\vec{G}(m_x,m_y)) = \frac{\Re \left\{ - \left( E_{y,\vec{G}(m_x,m_y),S}^{\text{transm}} \right)^* \cdot \left( H_{x,\vec{G}(m_x,m_y),S}^{\text{transm}} \right) \right\}}{\Re \left\{ \left( E_{x,\vec{G}(0,0),V}^{\text{incoming}} \right)^* \cdot \left( H_{y,\vec{G}(0,0),V}^{\text{incoming}} \right) - \left( E_{y,\vec{G}(0,0),V}^{\text{incoming}} \right)^* \cdot \left( H_{x,\vec{G}(0,0),V}^{\text{incoming}} \right) \right\}} \quad , \quad (4.42)$$

$$I_s^{\text{same}}(\vec{G}(m_x,m_y)) = \frac{\Re \left\{ - \left( E_{y,\vec{G}(m_x,m_y),S}^{\text{transm}} \right)^* \cdot \left( H_{x,\vec{G}(m_x,m_y),S}^{\text{transm}} \right) \right\}}{\Re \left\{ \left( E_{x,\vec{G}(0,0),V}^{\text{incoming}} \right)^* \cdot \left( H_{y,\vec{G}(0,0),V}^{\text{incoming}} \right) - \left( E_{y,\vec{G}(0,0),V}^{\text{incoming}} \right)^* \cdot \left( H_{x,\vec{G}(0,0),V}^{\text{incoming}} \right) \right\}} \quad , \quad (4.43)$$

$$I_s^{\text{cross}}(\vec{G}(m_x,m_y)) = \frac{\Re \left\{ \left( E_{x,\vec{G}(m_x,m_y),S}^{\text{transm}} \right)^* \cdot \left( H_{y,\vec{G}(m_x,m_y),S}^{\text{transm}} \right) \right\}}{\Re \left\{ \left( E_{x,\vec{G}(0,0),V}^{\text{incoming}} \right)^* \cdot \left( H_{y,\vec{G}(0,0),V}^{\text{incoming}} \right) - \left( E_{y,\vec{G}(0,0),V}^{\text{incoming}} \right)^* \cdot \left( H_{x,\vec{G}(0,0),V}^{\text{incoming}} \right) \right\}} \quad . \quad (4.44)$$

The indices  $s$  and  $p$  refer to incident linearly  $s$ - or  $p$ -polarised light with  $\vec{H}_s^{\text{incoming}} = (1, 0, 0)^T$ ,  $\vec{E}_s^{\text{incoming}} = (0, -1, 0)^T$  and  $\vec{H}_p^{\text{incoming}} = (0, 1, 0)^T$ ,  $\vec{E}_p^{\text{incoming}} = (1, 0, 0)^T$  (cf. equations (4.18) to (4.21) for normal incidence) which is typically controlled by a polariser of adequate orientation in front of the sample. The indices “same” and “cross” refer to the orientation of the analysing polariser, which either is oriented parallel (same) or perpendicular

(cross) to the first polariser and thus blocks out the respective electric and magnetic field components.

The finite half opening angle  $\beta$  of the collecting lens is considered by a subsequent summation over the respective transmitted intensities of the appropriate  $\vec{G}_{(m_x, m_y)}$ , which satisfy the condition<sup>9</sup>:

$$|\vec{G}_{(m_x, m_y)}| \leq \sin \beta \cdot \frac{\omega n}{c_0}. \quad (4.45)$$

Typically, the refractive index  $n$  is here  $n = n_{\text{air}} = 1$ , since the lens is usually used to collect light propagating in air.

### 4.3.3 Time-Resolved Transmittance

As described in section 4.2.2, time-resolved transmittance measurements are used to study the transport properties of photonic systems. According theoretical calculations are performed using the scattering matrix formalism. In this section, the modifications are described which are required to compute the propagation of a linearly polarised Gaussian pulse  $\mathcal{G}_{\omega_0}(t)$  of central frequency  $\omega_0$  and time constant  $\tau$  through a photonic nanostructure as a function of time  $t$ .

The scattering matrix formalism described in the previous sections deals with plane waves of frequency  $\omega$  and processes each frequency of a whole spectral range independently. In particular, the input amplitudes  $A_{V,s}^+(\omega) = A_{V,s}^+$ ,  $A_{V,p}^+(\omega) = A_{V,p}^+$  for  $s$ - and  $p$ -polarised light are defined identically for all frequencies, cf. equations (4.22) and (4.23). In the following, we will modify the input amplitudes  $A_{V,s}^+(\omega)$  and  $A_{V,p}^+(\omega)$  to be truly dependent on frequency  $\omega$ , according to the Gaussian pulse  $\mathcal{G}_{\omega_0}(t)$ .

In the time-resolved transmittance studies, a linearly polarised Gaussian pulse  $\mathcal{G}_{\omega_0}(t)$  with

$$\mathcal{G}_{\omega_0}(t) \propto e^{-\frac{t^2}{\tau^2}}, \quad (4.46)$$

where  $\tau$  is the time constant and  $\omega_0$  its central frequency, is transmitted through the photonic nanostructure.

In the frequency domain this translates to:

$$\mathcal{G}_{\omega_0}(\omega) \propto e^{-\frac{(\omega - \omega_0)^2 \cdot \tau^2}{2}}, \quad (4.47)$$

For our numerical calculations, the Gaussian pulse  $\mathcal{G}_{\omega_0}(\omega)$  is discretised appropriately by considering a finite frequency interval  $\omega_a \leq \omega_k \leq \omega_b$  centered around  $\omega_0$  and thereby using a finite number of frequency-steps  $\Delta\omega$ :

$$\mathcal{G}_{\omega_0}(\omega_k) \propto e^{-\frac{(\omega_k - \omega_0)^2 \cdot \tau^2}{2}}, \quad \omega_a \leq \omega_k \leq \omega_b. \quad (4.48)$$

This discrete Fourier transformation  $\mathcal{G}_{\omega_0}(\omega_k)$  of the Gaussian pulse  $\mathcal{G}_{\omega_0}(t)$  determines the weighting of the input amplitudes  $A_{V,s}^+(\omega_k)$  and  $A_{V,p}^+(\omega_k)$  according to:

$$A_{V,s}^+(\omega_k) = \mathcal{G}_{\omega_0}(\omega_k) \cdot A_{V,s}^+, \quad (4.49)$$

$$A_{V,p}^+(\omega_k) = \mathcal{G}_{\omega_0}(\omega_k) \cdot A_{V,p}^+. \quad (4.50)$$

<sup>9</sup>In the currently discussed case of normal incident light, the  $x$ - and  $y$ -components of the incoming wave vector  $\vec{k}_{\text{in}}$  are zero.

Here,  $A_{V,s}^+$  and  $A_{V,p}^+$  are the input amplitudes defined in equations (4.22) and (4.23).

Applying the newly defined input amplitudes  $A_{V,s}^+(\omega_k)$  and  $A_{V,p}^+(\omega_k)$ , the (complex) transmitted electric and magnetic field components  $E_{x,\vec{G}(m_x,m_y)}^{\text{transm}}(\omega_k)$ ,  $E_{y,\vec{G}(m_x,m_y)}^{\text{transm}}(\omega_k)$  and  $H_{x,\vec{G}(m_x,m_y)}^{\text{transm}}(\omega_k)$ ,  $H_{y,\vec{G}(m_x,m_y)}^{\text{transm}}(\omega_k)$  are calculated via the scattering matrix formalism for the respective reciprocal lattice vectors  $\vec{G}_i$ ,  $i = 1 \dots N_g$ , see section 4.3.1. A system of collimating lens and analysing polariser in front of the detector can be included by converting the field components into the coordinate system  $\mathcal{R}'_{(m_x,m_y)}$  related to the propagation direction of the respective diffraction orders, as described in the previous section 4.3.2.

Subsequently, the inverse discrete Fourier transformation is performed to derive the time-resolved response of the electric and magnetic field components:

$$E_{x,\vec{G}(m_x,m_y)}^{\text{transm}}(t_j) \propto \sum_{\omega_k=\omega_a}^{\omega_b} E_{x,\vec{G}(m_x,m_y)}^{\text{transm}}(\omega_k) \cdot e^{i(\omega_k-\omega_0)t_j}, \quad (4.51)$$

$$E_{y,\vec{G}(m_x,m_y)}^{\text{transm}}(t_j) \propto \sum_{\omega_k=\omega_a}^{\omega_b} E_{y,\vec{G}(m_x,m_y)}^{\text{transm}}(\omega_k) \cdot e^{i(\omega_k-\omega_0)t_j}, \quad (4.52)$$

$$H_{x,\vec{G}(m_x,m_y)}^{\text{transm}}(t_j) \propto \sum_{\omega_k=\omega_a}^{\omega_b} H_{x,\vec{G}(m_x,m_y)}^{\text{transm}}(\omega_k) \cdot e^{i(\omega_k-\omega_0)t_j}, \quad (4.53)$$

$$H_{y,\vec{G}(m_x,m_y)}^{\text{transm}}(t_j) \propto \sum_{\omega_k=\omega_a}^{\omega_b} H_{y,\vec{G}(m_x,m_y)}^{\text{transm}}(\omega_k) \cdot e^{i(\omega_k-\omega_0)t_j}. \quad (4.54)$$

In our calculations, the time-response of the field components is discretised for the finite interval  $t_a \leq t_j \leq t_b$  using time-steps of  $\Delta t$ , taking account of the Nyquist–Shannon sampling theorem:

$$\Delta t \leq \left( 2 \left[ \frac{\omega_b}{2\pi} - \frac{\omega_a}{2\pi} \right] \right)^{-1}. \quad (4.55)$$

Typically, we use  $\Delta t=0.8$  fs,  $t_a=0$  fs and  $t_b=800$  fs.

Finally, the transmitted intensity for each diffraction order  $(m_x, m_y)$  is calculated either by equations (4.41) to (4.44), if a system of lens and analysing polariser is applied, or else by equation (4.15). Afterwards, the (finite) opening angle of the lens or detecting system is accounted for by adding up the corresponding intensities of the respective diffraction orders.



# Chapter 5

## Three-Dimensional Icosahedral Photonic Quasicrystals

This chapter is dedicated to our experimental and theoretical work on three-dimensional icosahedral photonic quasicrystals. Our studies have been inspired by the three-dimensional quasiperiodic patterns found in metallic alloys [5, 45] due to their unusual physical properties which are still not completely understood as well as through their aesthetics.

The icosahedral quasiperiodic pattern obtained from the cut-and-project method (see section 3.2) is realised by direct laser writing in the negative-tone photoresist SU-8. First, we characterise the quality of the fabricated samples by scanning electron micrograph (SEM) images, focused ion beam (FIB) cuts and visible-light Laue diffraction experiments (section 5.1). Having apparently succeeded in fabricating high-quality three-dimensional icosahedral photonic quasicrystals, we investigate their optical properties experimentally using the optical setups described in section 4.2 [49]. The first interpretation of the obtained experimental data is rather challenging (section 5.2) as a theoretical model for calculating the anticipated optical properties has only been developed over the course of this thesis: We adopt a combination of the rational approximant approach and the scattering matrix formalism (section 5.3) in order to distinguish *intrinsic* from *extrinsic* properties (e.g., sample imperfections) [91] and thus to revise our initial interpretation.

### 5.1 Fabrication of High-Quality SU-8 Samples

Applying the cut-and-project method as described in section 3.2, the pattern of the three-dimensional photonic quasicrystal of icosahedral symmetry is calculated, which consists of rods of equal length  $l$ . The length  $l$  of the rods, which is related to the scaling of the six-dimensional periodic lattice vectors used in the cut-and-project method, determines the order of magnitude of the central wavelength of the anticipated photonic pseudo-stop band. For our choice of the rod length  $l=2\ \mu\text{m}$ , we expect the fundamental pseudo-stop band around  $\lambda \approx 2 \cdot l = 4\ \mu\text{m}$  wavelength, i.e., in the infrared – just in accordance to down-scaling the results of Ref. [63].

The properly scaled icosahedral quasiperiodic pattern is realised as polymeric (SU-8) photonic quasicrystal using direct laser writing, as explained in section 4.1. To optimise the time of fabrication, the individual rods forming the pattern are combined to long paths via a specially developed  $C^{++}$ -programme where the starting point of each path is nearby the endpoint of the

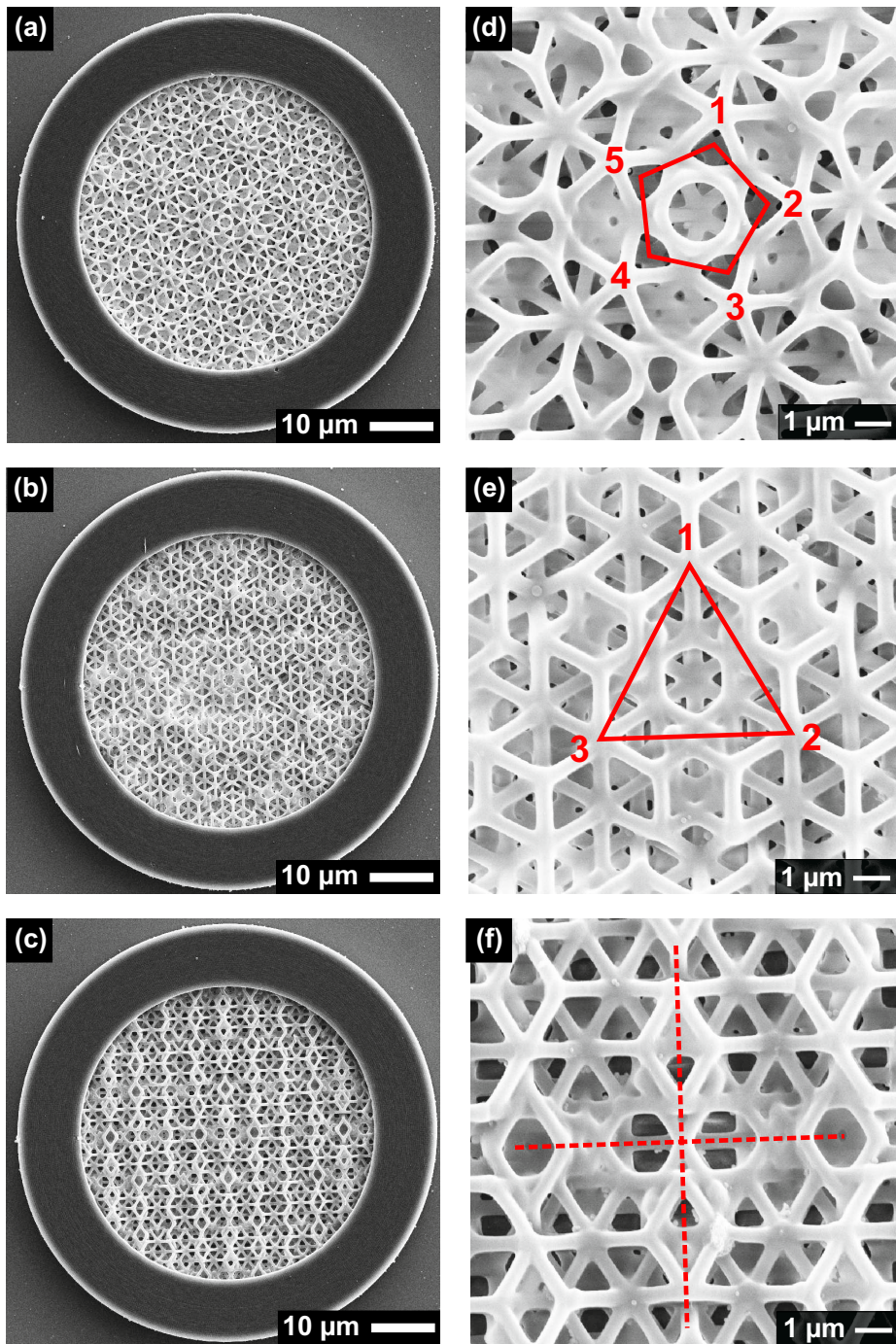


Figure 5.1: The SEM images give a normal view of three-dimensional icosahedral SU-8 photonic quasicrystals fabricated via direct laser writing. The samples have a diameter of  $48\ \mu\text{m}$ , a thickness of  $8\ \mu\text{m}$  and a rod length  $l$  of  $2\ \mu\text{m}$ . The depicted icosahedral photonic quasicrystals are oriented along a five-fold rotational symmetry axis (a), (d), along a three-fold axis (b), (e), and along a two-fold axis (c), (f). The left column (a) – (c) shows overviews of the respective icosahedral photonic quasicrystals, while the right column (d) – (f) displays the corresponding close-up views, which illustrate the respective rotational symmetries of the icosahedral quasicrystals (indicated by red coloured guides to the eyes). All graphs show the high quality of the fabricated nanostructures with nicely ordered, well-aligned and smooth rods.

previous path. These paths are scanned by the piezo scanning stage with a speed of 40  $\mu\text{m/s}$ . For cylindrically shaped photonic quasicrystals with rods of  $l=2\ \mu\text{m}$  and a diameter of up to 100  $\mu\text{m}$ , the fabrication takes 1 to 4 hours, depending on the actual thickness (4  $\mu\text{m}$  to 19  $\mu\text{m}$ ).

To reduce distortion of the fabricated photonic quasicrystals due to shrinkage of the SU-8 during development [93], we surround the photonic quasicrystals by a thick stabilising wall. The shape of the wall is chosen cylindrical for not breaking the symmetry of the icosahedral quasicrystals, especially when studying the Laue diffraction patterns where a rectangular wall would lead to a disturbing four-fold symmetric contribution.

However, due to the stabilising wall, we can access the photonic quasicrystals only from the top (perpendicular to the glass substrate) for optical measurements. Yet, to allow an overall optical characterisation of the three-dimensional icosahedral photonic quasicrystals, we fabricate the samples such that the surface normal points along one of the principal rotational (real-space) symmetry axes (cf. section 3.2), in particular along a five-fold symmetry axis, along a three-fold and along a two-fold symmetry axis.

A gallery of SEM images of icosahedral photonic quasicrystals fabricated by direct laser writing is illustrated in Fig. 5.1. The cylindrically shaped samples surrounded by the cylindrical stabilising wall have a diameter of 48  $\mu\text{m}$  and a thickness of 8  $\mu\text{m}$ . The rods of length  $l=2\ \mu\text{m}$  are very smooth and indicate the high quality of the fabricated nanostructures, which can be noticed for all three principal orientations, i.e., along a five-fold axis (a), (d), along a three-fold axis (b), (e) and along a two-fold axis (c), (f). In the corresponding close-up views (right column of Fig. 5.1), the respective rotational symmetries are highlighted in red [44]. The images of Fig. 5.1 and also the oblique-incidence overview in Fig. 5.2 (a), clearly reveal that the samples are of very high quality with well-aligned smooth rods and a well-defined surface. The FIB cut in Fig. 5.2 (b) through the icosahedral photonic quasicrystal oriented along a two-fold axis proves the highly ordered composition in the interior and the true three-dimensionality of the porous nanostructure. The advantage of cutting an icosahedral photonic quasicrystal oriented along a two-fold symmetry axis is the fact that three two-fold symmetry axes are perpendicular to each other. Thus, at the cutting plane one can obtain a definite symmetry, in particular a two-fold symmetry, which facilitates the analysis of the cut. The high three-dimensional quality of the icosahedral photonic quasicrystals is also illustrated in a non-destructive way using a Confocal microscope scanning through the sample, which was performed at the University of Toronto. In Fig. 5.2 (c), the central layer – containing the single point of exact icosahedral symmetry, i.e., the projected origin of the six-dimensional simple cubic periodic lattice – of the icosahedral photonic quasicrystal oriented along a three-fold rotational symmetry axis is depicted. The diameter of the structure is 100  $\mu\text{m}$ , the rod length  $l$  is 2  $\mu\text{m}$ .

The confirmation of well-aligned and ordered rods in the interior of the fabricated icosahedral photonic quasicrystals is important, as in the applied fabrication mode of direct laser writing the laser beam is focused through already exposed parts of the photoresist SU-8. In this mode, a sufficiently large change in the refractive index from unexposed to exposed parts can cause a noticeable shift of the focal position of the laser beam and thus can lead to misaligned rods, which is obviously not the case in our SU-8 samples.

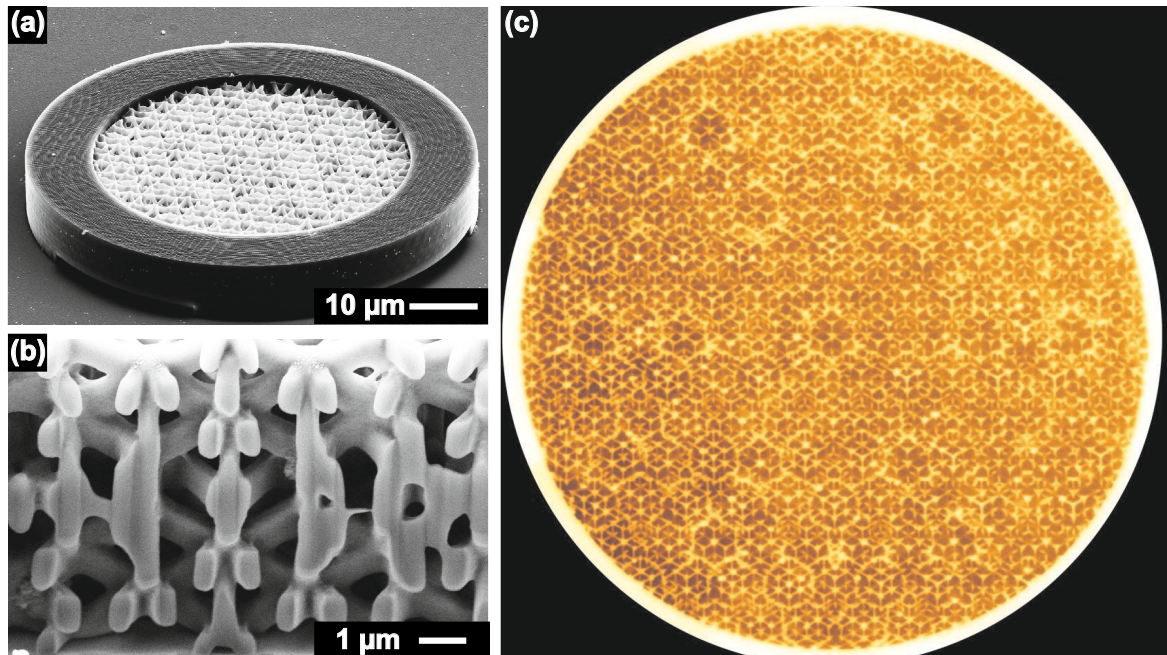


Figure 5.2: In (a), an oblique-incidence overview of the three-dimensional icosahedral photonic quasicrystal oriented along a five-fold axis [cf. Fig. 5.1 (a), (d)] is shown. A focused ion beam cut through an icosahedral photonic quasicrystal oriented along a two-fold axis [cf. Fig. 5.1 (c), (f)] is illustrated in (b) and reveals the three-dimensional character of the fabricated nanostructure with deterministically ordered rods in the interior. This is also confirmed by the confocal image in (c), which shows the central layer of an icosahedral photonic quasicrystal oriented along a three-fold rotational axis [cf. Fig. 5.1 (b), (e)].

Although the SEM and Confocal microscope images depicted in Fig. 5.1 and Fig. 5.2 give evidence of having succeeded in the fabrication of porous three-dimensional icosahedral photonic quasicrystals with well-aligned rods, another convincing proof of the high quality of our samples is certainly the performance in the Laue diffraction experiments (cf. section 4.2.1). The Laue diffraction patterns taken with visible light (532 nm wavelength emitted by a solid state laser) from the icosahedral photonic quasicrystals oriented along a five-fold, three-fold or two-fold symmetry axis (first column of Fig. 5.3) reveal sharp Laue diffraction spots with the expected rotational symmetries, i.e., the  $2 \times 5$ -fold, the  $2 \times 3$ -fold and the  $2 \times 2$ -fold symmetry, respectively [49]. This is depicted in Fig. 5.3 in the second and third column for 4  $\mu\text{m}$  and 8  $\mu\text{m}$  thick icosahedral photonic quasicrystals, respectively, which have a diameter of 100  $\mu\text{m}$  and a rod length  $l$  of 2  $\mu\text{m}$ . The overly intense non-diffracted zeroth-order spot is blocked for not overloading the camera, and the contrast of the images is enhanced via image processing. Since we can distinguish Laue diffraction spots even in high orders, the quality of the icosahedral photonic quasicrystals is obviously very good.

In the fourth (right) column of Fig. 5.3 the calculated Laue diffraction patterns are depicted, which are computed applying the cut-and-project method. Therefore, the reciprocal lattice of the six-dimensional simple cubic periodic lattice is projected into the three-dimensional physical reciprocal  $k$ -space resulting in a dense set of diffraction spots. The intensity of each spot is given by the square of the Fourier transform of the acceptance domain (projected Wigner-Seitz cell). In the case of a spherical acceptance domain of diameter  $\Delta$ , the intensity is proportional to

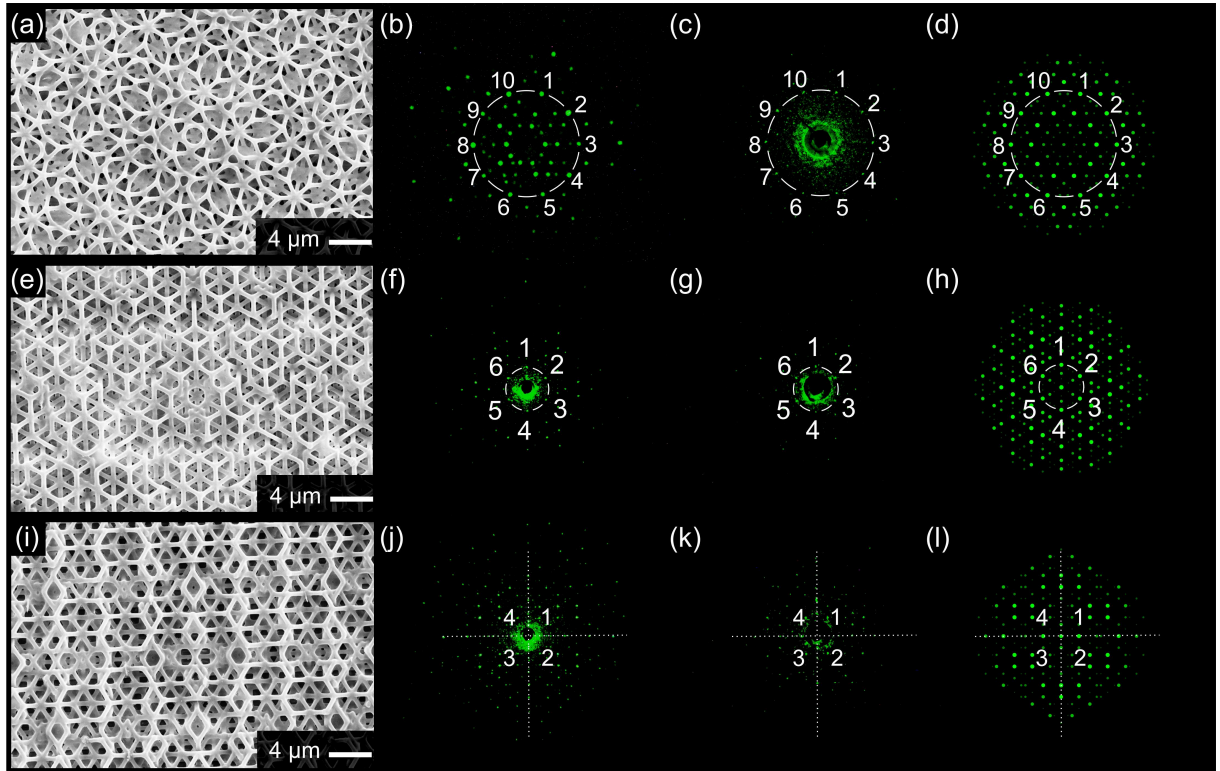


Figure 5.3: The first column (a), (e), (i) depicts SEM images of the icosahedral photonic quasicrystals with  $l=2$   $\mu\text{m}$  rods and of 8  $\mu\text{m}$  thickness oriented along a five-fold, three-fold and two-fold symmetry axis, respectively. Corresponding Laue diffraction patterns measured at 4  $\mu\text{m}$  thick icosahedral photonic quasicrystals are shown in the second column (b), (f), (j), while the third column (c), (g), (k) displays the Laue diffraction patterns obtained from 8  $\mu\text{m}$  thick samples. The measured Laue diffraction patterns agree very well with the calculated ones (d), (h), (l) in the fourth (right) column. After Ref. [49].

$\text{sinc}^2(\pi k \Delta)$ , where  $k$  is the modulus of the three-dimensional internal reciprocal  $k$ -space vector [22, 48, 49]. The intensity of each spot is visualised by the diameter and the brightness of the green spots. For reasons of clarity, spots below a certain intensity are not shown.

Comparing the measured Laue diffraction patterns (second and third column of Fig. 5.3) with theory (fourth column of Fig. 5.3) one clearly observes a very nice overall agreement [49]. This demonstrates again the high quality of the fabricated icosahedral photonic quasicrystals. Furthermore, as the Laue diffraction patterns are calculated without taking account of the rods, but only considering the vertices of the rods<sup>1</sup> as single scatterers, the good agreement indicates that the rods, which are required to obtain a stable mechanically connected pattern, do apparently not alter the overall rotational symmetry of the icosahedral photonic quasicrystals or cause any other disturbing effects in the quasiperiodic pattern.

Having a closer look at the Laue diffraction patterns of the icosahedral photonic quasicrystals, depicted in the second and third column of Fig. 5.3, one realises that it is much harder to discern the individual Laue diffraction spots when the sample thickness is increased (from second to third column). In thicker samples, the Laue diffraction spots get sharper,

<sup>1</sup>The vertices of the rods denote the positions of the projected six-dimensional periodic lattice sites in physical space and likewise the positions of the real atoms forming electronic quasicrystals [5, 22].

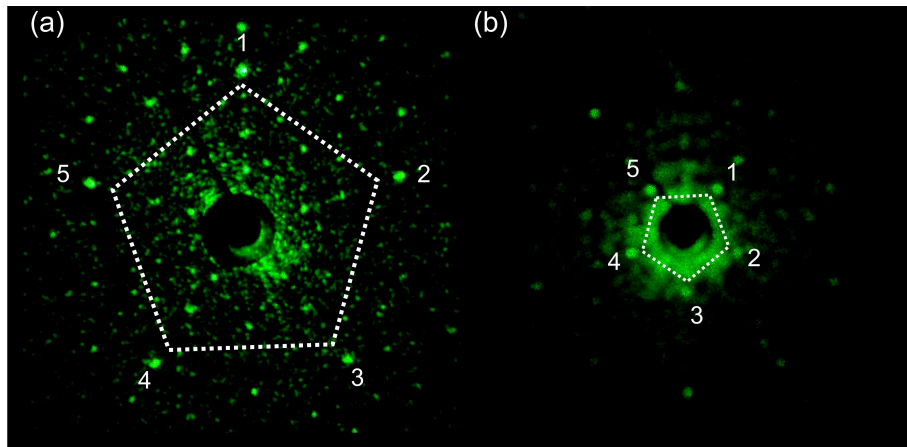


Figure 5.4: A very thin icosahedral photonic quasicrystal oriented along a five-fold rotational symmetry axis produces a  $1 \times 5$ -fold symmetric Laue diffraction pattern, see (a). The Laue diffraction pattern (b) of the highly filled icosahedral photonic quasicrystal oriented along a five-fold symmetry axis, which is a bulk block of SU-8 with a modulated surface only, shows also only a  $1 \times 5$ -fold rotational symmetry. This is in contrast to truly three-dimensional porous icosahedral photonic quasicrystals, which reveal  $2 \times 5$ -fold symmetry in the corresponding Laue diffraction patterns [cf. Fig. 5.3 (b), (c)].

probably because the impinging laser beam is scattered multiple times and does interact with an increased number of scattering centres. Additionally, the background intensity is enhanced in the Laue diagrams of thicker samples. This observation can be explained by two different effects. Firstly, due to an increased number of scattering events, laser light might also be diffracted into some of the many diffraction orders which are of only low intensity in the Laue diagrams of thinner samples and also in the calculated (hierarchical) ones (cf. fourth column of Fig. 5.3 and Fig. 2.6 (b) of section 2.2.1), as in the computations only single scattering is assumed. Having thus gained in intensity, the formerly low-intensity diffraction spots contribute to the background. Secondly, sample imperfections and distortions, e.g., caused by strain due to shrinkage of SU-8 during development [93] despite the stabilising wall, is presumably more pronounced for thicker samples and thus leads to an increase in the diffusive background (speckle).

Besides, the observed Laue diffraction patterns depicted in Fig. 5.3 give clear evidence of the porous three-dimensionality of the fabricated icosahedral photonic quasicrystals. In particular, icosahedral photonic quasicrystals oriented along a five-fold symmetry axis, which are very thin or which are basically bulk films with a modulated surface only, give rise to Laue diffraction patterns with only  $1 \times 5$ -fold rotational symmetry, as depicted in Fig. 5.4 (a) and (b), respectively, rather than  $2 \times 5$ -fold for a true three-dimensional icosahedral photonic quasicrystal of corresponding orientation.

Thus far, the studied icosahedral photonic quasicrystals contain the single point of exact icosahedral symmetry<sup>2</sup> in their respective centres. For testing that the observed Laue diffraction patterns are not just a result of this particular point, an icosahedral photonic quasicrystal oriented along a five-fold axis, which does not contain this single point of exact icosahedral

<sup>2</sup>This is the projection of the origin of the six-dimensional periodic lattice into physical space.

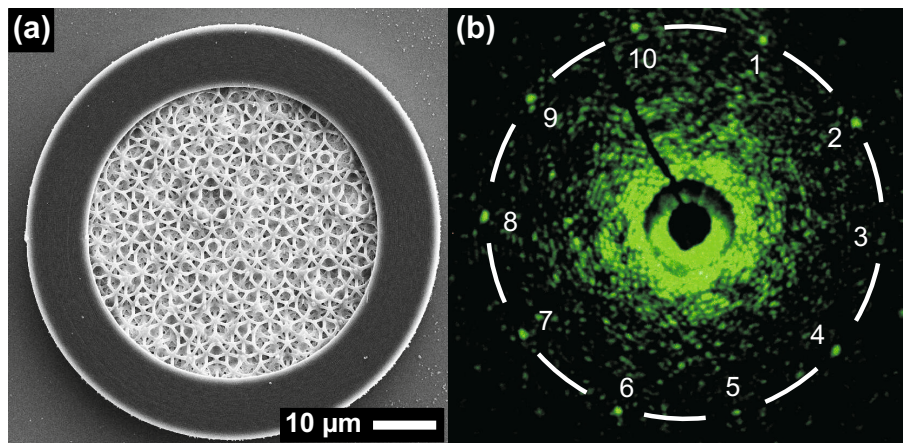


Figure 5.5: (a) shows the SEM image of an icosahedral photonic quasicrystal oriented along a five-fold rotational symmetry axis, cf. Fig. 5.1 (a), yet here the single point of exact icosahedral symmetry is shifted out of the fabricated nanostructure. In (b), the corresponding Laue diffraction pattern is depicted which shows the anticipated  $2 \times 5$ -fold rotational symmetry, which originates from the long-range quasiperiodic order of the icosahedral photonic quasicrystal.

symmetry is fabricated, see Fig. 5.5 (a). The corresponding measured Laue diffraction pattern is depicted in Fig. 5.5 (b) and reveals again the anticipated  $2 \times 5$ -fold rotational symmetry. This indicates that the icosahedral symmetry observed in the Laue diffraction patterns thus far is really a property of the long-range order present in the icosahedral photonic quasicrystals.

In conclusion, the SEM and Confocal microscope images as well as the obtained Laue diffraction patterns show that direct laser writing is a suitable method for fabricating complex three-dimensional nanostructures, in particular the icosahedral photonic quasicrystals, of high quality with well-aligned and nicely ordered rods [49]. Additionally, the performance in the Laue diffraction experiments indicates that the rods, which are necessary for the fabrication by direct laser writing to end up with a stable mechanically connected photonic nanostructure, do keep the overall rotational symmetry and quasiperiodic properties of the icosahedral photonic quasicrystals. This becomes apparent when, for instance, comparing the obtained results to Shechtman's findings [5] studied on electronic quasicrystals composed of real metal atoms that 'float' in vacuum due to their binding potential.

With the possibility to fabricate high quality porous three-dimensional icosahedral SU-8 photonic quasicrystals in reasonable time, we can start to further investigate the specific optical properties of these complex nanostructures.

## 5.2 Experimental Studies of Optical Properties and Initial Interpretation

While the previous section focused on analysing the quality of the icosahedral photonic quasicrystals fabricated by direct laser writing and the influence of the connecting rods on the icosahedral symmetry, this section deals with our experimental studies of their peculiar optical properties and our initial interpretation of the experimental results, i.e., ascribing the unusual findings to sample imperfections.

### 5.2.1 Transmittance and Reflectance Spectra

The transmittance and reflectance properties of the fabricated icosahedral photonic quasicrystals are studied using the experimental setup described in section 4.2.3, namely the combination of an FTIR-spectrometer and an infrared microscope. The samples are aligned with their surface perpendicular to the optical axis of the cassegrain microscope objectives in use. The obtained transmittance and reflectance spectra are normalised to the bare glass substrate and a silver mirror, respectively. For a complete characterisation, the orientations of the fabricated icosahedral photonic quasicrystals are chosen such that the surface normal points along the principal rotational symmetry axes, i.e., along a five-fold, three-fold and two-fold rotational symmetry axis.

In Fig. 5.6, the measured transmittance (left column) and reflectance (right column) spectra of icosahedral photonic quasicrystals are shown for the different principal orientations and for several thicknesses. The diameter of the cylindrically shaped samples is  $100\ \mu\text{m}$  and the rod length  $l=2\ \mu\text{m}$ . The particular thicknesses are depicted in the graphs. The filling fraction is ideally the same within each set of identically oriented samples, as the laser intensity is kept identically in their successive fabrication.

In the transmittance spectra, the first things to notice are the dips at wavelengths of  $2.9\ \mu\text{m}$  and  $3.4\ \mu\text{m}$ , which originate from intrinsic molecular absorptions of the photoresist SU-8, namely the excitation of O-H and C-H stretch vibrations (cf. Ref. [84]). These dips are labelled accordingly in the depicted spectra. The absolute values of these dips depend on the amount of SU-8 the actual photonic nanostructure is composed of, i.e., depend on its thickness and its filling fraction.

At the short wavelength side, the transmittance is quite low (below 15%) for all samples, decreasing even further with increasing thickness within each set of identically oriented quasicrystals. This is probably the result of strong (multiple) scattering into the residual solid angle, since the reflectance is very low as well (less than 5%, slightly decreasing with decreasing thickness); absorption plays no role at these frequencies. The scattering could either be caused by imperfections of the fabricated samples and surface roughness (cf. spectra of polymeric woodpiles in Ref. [84]) or might also be an intrinsic property of quasiperiodicity, since the reciprocal quasilattice consists of a dense set of reciprocal lattice vectors which in principle can all contribute to diffraction or scattering.

Moving to longer wavelengths, the transmittance increases at a wavelength of roughly  $1.7\ \mu\text{m}$ . The shape of the ascent (highlighted by a grey-shaded area) depends on the actual orientation of the icosahedral photonic quasicrystal, i.e., which rotational symmetry is present in the plane perpendicular to the optical axis of the cassegrain microscope objectives, cf.

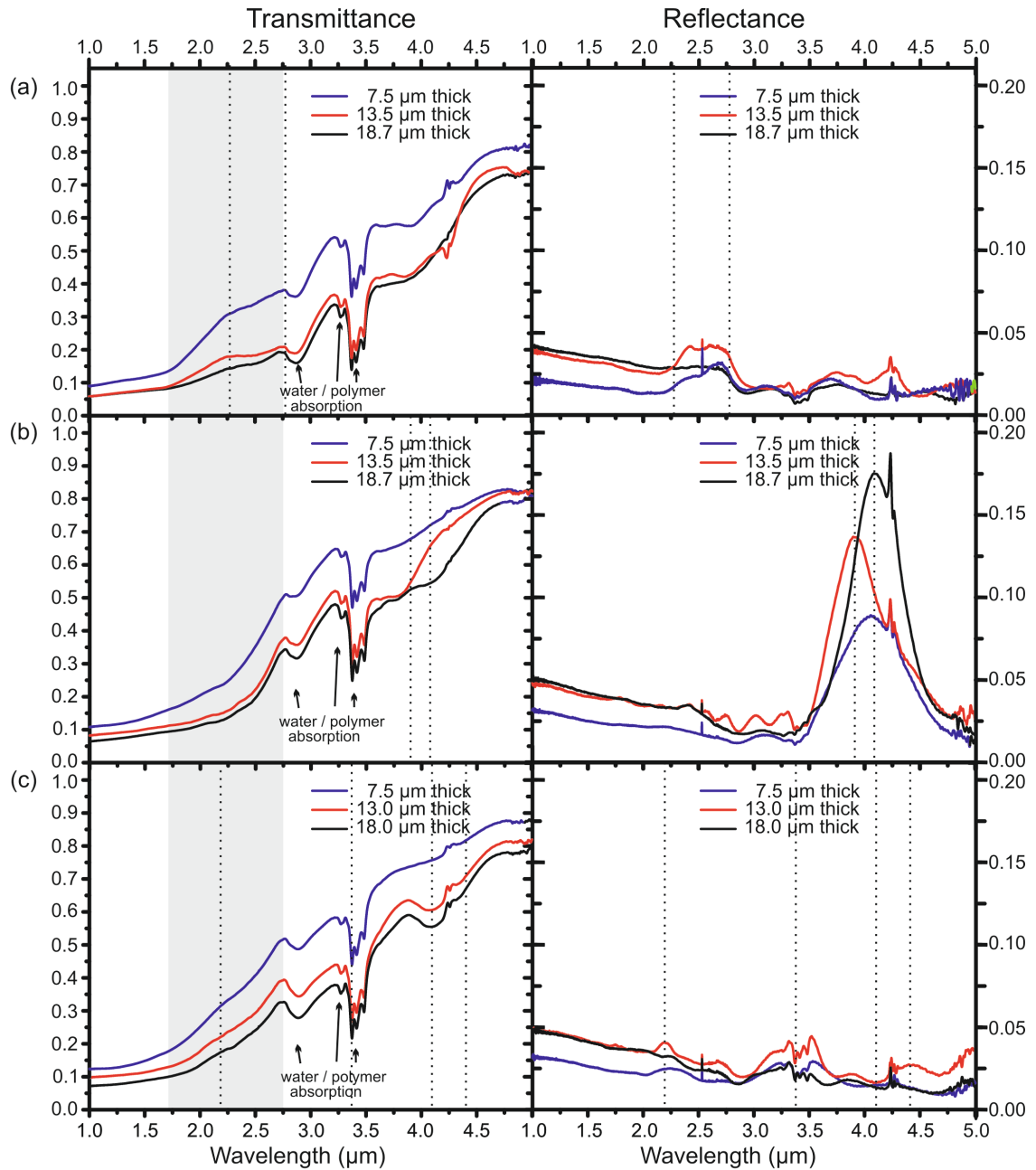


Figure 5.6: The influence of increasing the sample thickness on the transmittance (left column) and reflectance spectra (right column) is illustrated for icosahedral photonic quasicrystals oriented along a five-fold axis (a), along a three-fold axis (b) and along a two-fold axis (c). The photonic quasicrystals are cylindrically shaped with a diameter of  $100 \mu\text{m}$  and a rod length  $l$  of  $2 \mu\text{m}$ . Along the three-fold symmetry axis (b), the peak in reflectance at  $\lambda \approx 4.1 \mu\text{m}$  wavelength (marked by a dotted line) is very pronounced giving first evidence for a pseudo-stop band.

graphs (a) – (c). Even at the long wavelength side, the sum of transmittance and reflectance does not approach unity, as would be expected if the light could pass through the photonic quasicrystals without major scattering. Again, this could be either a property of quasiperiodicity diffracting light into the residual solid angle or caused by scattering losses due to the roughness of the rods and other imperfections.

Intuitively, one expects pronouncing any features in the spectra by increasing the thickness of the photonic nanostructures, since incident light is confronted with an increased number of scattering centres. Additionally, any transmittance dips and reflectance peaks caused by Fabry-Perot interference can be identified, since the spectral positions of these dips and peaks will shift accordingly with thickness and filling fraction of the samples. Thus, investigating the effects of increasing the thickness of the icosahedral photonic quasicrystals (cf. Fig. 5.6) can give further insights into the spectral features caused by quasiperiodicity.

Considering the spectra of the icosahedral photonic quasicrystals oriented along the five-fold axis in Fig. 5.6 (a), one can observe that with increasing thickness a valley develops in transmittance at the spectral region from 2.25  $\mu\text{m}$  to 2.75  $\mu\text{m}$  (indicated by dotted lines) and accordingly, a broad peak occurs in reflectance. This feature is obviously not due to Fabry-Perot fringes since the spectral positions of Fabry-Perot fringes should shift with increasing thickness of the sample.

In the set of samples oriented along a three-fold symmetry axis (b), of course the prominent peaks in reflectance around 4.1  $\mu\text{m}$  wavelength are eye-catching. Although the reflectance is generally very low (about 5%), one can clearly observe an appreciable increase up to 20% at this wavelength, which indicates the presence of a pseudo-stop band in the photonic band structure. An increase of the sample thickness enhances the peak in reflectance as expected. The observed shift of the spectral peak position for the 13.5  $\mu\text{m}$  thick photonic quasicrystal (depicted in red), however, is likely just an effect of a change in the filling fraction<sup>3</sup>. In transmittance, one can make out only some very small dips at the appropriate spectral positions. Nevertheless, the position of the distinct reflectance peak is consistent with the expected position of the pseudo-stop band due to the experiments of Ref. [63], if we scale down the rod length  $l$  to 2  $\mu\text{m}$  and take into account that the effective refractive index of our icosahedral photonic quasicrystals is larger because of a higher filling fraction (around 50%).

Graph (c) of Fig. 5.6 measured at the set of icosahedral photonic quasicrystals oriented along a two-fold symmetry axis shows the following noticeable features: In transmittance, a dip emerges at 4.1  $\mu\text{m}$  wavelength (marked by a dotted line), but no corresponding peak in reflectance can be obtained. Instead, there might be a slight increase of reflectance due to a pseudo-stop band at the spectral position around 3.4  $\mu\text{m}$ , indicated by a dotted line. Unfortunately, this coincides with absorption in SU-8, which covers any possible corresponding dip in transmittance. Other slight peaks in reflectance at 2.2  $\mu\text{m}$  and 4.4  $\mu\text{m}$ , both positions marked by dotted lines, have only a vague noticeable valley or dip in the transmittance as well.

In the following, we would like to confirm that the distinct peak in reflectance at around 4.1  $\mu\text{m}$  wavelength, observed for the icosahedral photonic quasicrystal oriented along the three-fold

---

<sup>3</sup>Although the intensity of the exposing laser beam is always set to the same value, one cannot exclude fluctuations in the laser intensity and thus fully ensure that the exposed volume and likewise the filling fraction is truly identical.

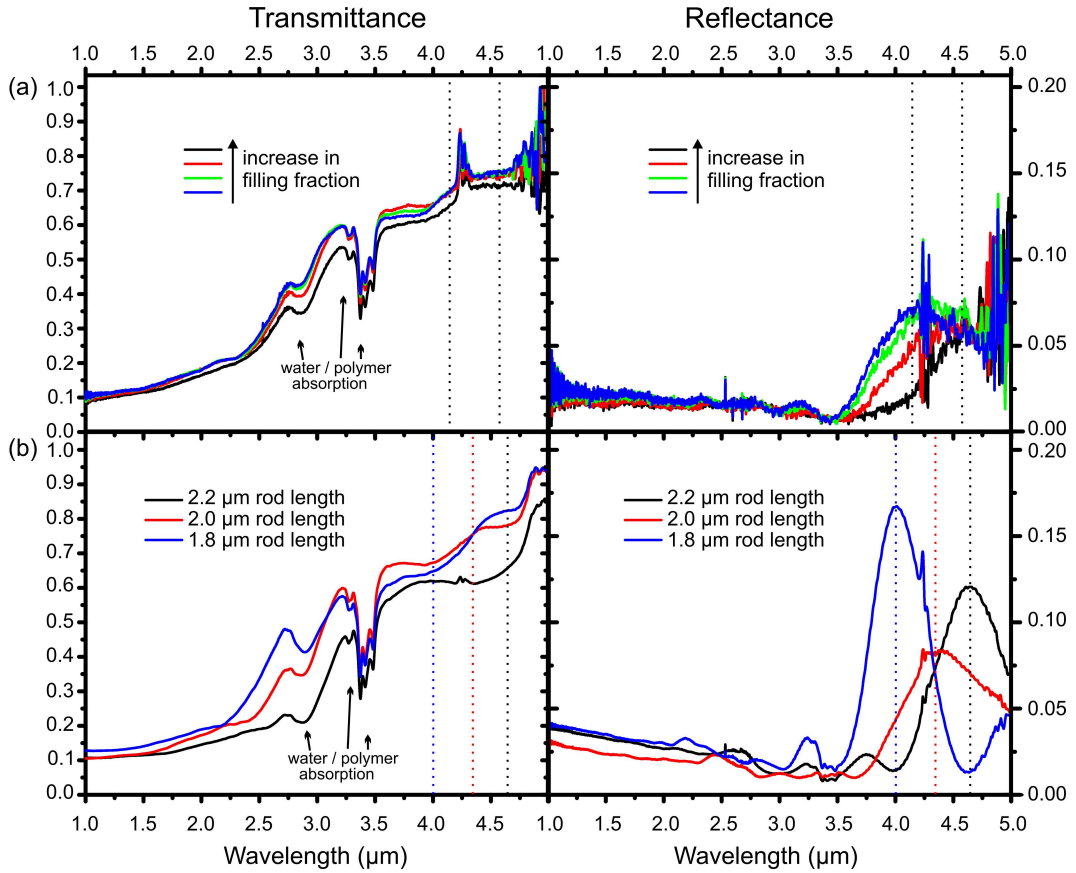


Figure 5.7: The influence of filling fraction and rod length  $l$  is depicted for a three-dimensional icosahedral photonic quasicrystal oriented along a three-fold axis. The peak in reflectance indicating the position of the pseudo-stop band in the photonic band structure shifts to longer wavelength with increasing filling fraction and increasing rod length, respectively (cf. Bragg's law).

axis in Fig. 5.6 (b), is actually related to the existence of a pseudo-stop band in the photonic band structure. Therefore, we investigate the influence of the filling fraction and the rod length  $l$  on its spectral position. Naively one expects a shift of its spectral position  $\lambda$  according to Bragg's law:  $2n_{\text{effective}} \cdot d = m \cdot \lambda$ ,  $m \in \mathbb{Z}$ ; the effective refractive index  $n_{\text{effective}}$  is related to the filling fraction and the distance  $d$  between two scattering centres to the rod length  $l$ . The according spectra are presented in Fig. 5.7 (a) and (b), the left column depicts transmittance, the right column reflectance.

In Fig. 5.7 (a), only the filling fraction of the cylindrical icosahedral photonic quasicrystals oriented along a three-fold symmetry axis (diameter of 48 μm, thickness of 8 μm and rod length  $l$  of 2 μm) is varied by choosing different intensities for exposing the photoresist. In the transmittance spectra, one can observe an overall slight increase in transmittance, while the filling fraction is decreased (colour-coding of the filling fraction is depicted in the graphs). Again, the transmittance is quite low (about 10%) at the short wavelength side for all samples, but starts to considerably increase with increasing wavelengths at about  $\lambda=2.5$  μm. The spectral position of this ascent in the transmittance spectra shifts slightly to the blue for samples with less filling fraction, i.e., with reduced effective refractive index. Furthermore, the peak in reflectance of roughly 8% comes up at shorter wavelength for reduced filling fractions, marked by dotted

lines at 4.1  $\mu\text{m}$  and 4.6  $\mu\text{m}$  wavelength for two different filling fractions. The spectral shift of the peak to the blue is perfectly consistent with the naive expectancy; the effective refractive index is reduced by reducing the filling fraction, while the distance between the scattering centres  $d$  remains the same. In transmittance, one can only vaguely detect any dips coinciding with the distinct peaks in reflectance (see dotted lines).

In Fig. 5.7 (b), the effect of changing the length  $l$  of the connecting rods of the icosahedral photonic quasicrystals is investigated. For this purpose, an appropriate set of cylindrically shaped photonic quasicrystals oriented along a three-fold symmetry axis with 100  $\mu\text{m}$  in diameter and about 8  $\mu\text{m}$  in thickness are fabricated. Three different values of the rod length  $l$  are chosen, in particular  $l=2.2$   $\mu\text{m}$ ,  $l=2.0$   $\mu\text{m}$  and  $l=1.8$   $\mu\text{m}$ , respectively. However, just decreasing the rod length  $l$ , while maintaining the exposing laser intensity at the same value, leads to an increase of the filling fraction, which shifts the spectral position to the red and, at the worst, might even cause an unwanted fusion of the rods in axial direction, i.e., perpendicular to the glass substrate, due to the elliptically shaped voxel (cf. section 4.1 and chapter A of the appendix). To compensate this, the intensity of the exposing laser was reduced accordingly for smaller rod lengths. Moreover, in the case of 2.2  $\mu\text{m}$  rod length, the thickness of the icosahedral photonic quasicrystal was increased to 8.6  $\mu\text{m}$  in order to account for the fact that an increase in rod length while keeping the sample thickness reduces effectively the number of quasiperiodic layers and thus scatterers in axial direction (along the three-fold axis). Yet, for 2.0  $\mu\text{m}$  and 1.8  $\mu\text{m}$  rod length, the thickness is for both 8  $\mu\text{m}$ . Thus, the respective numbers of quasiperiodic layers along the axial direction (perpendicular to the glass substrate) are 21 for the samples with rod lengths of 2.2  $\mu\text{m}$  and 2.0  $\mu\text{m}$ , and 23 layers with rod lengths of 1.8  $\mu\text{m}$ . With shorter rod length, the spectral position of the peak in reflectance (indicated by the dotted lines) obviously shifts to the blue, from 4.7  $\mu\text{m}$  to 4.0  $\mu\text{m}$  wavelength, which is consistent with Bragg's law. However, to what extent this shift is effected by the reduced rod length or by the change in the filling fraction cannot be decided completely. Most likely, the influence of the rod length dominates this shift, since the filling fraction is kept as constant as possible by changing the exposing laser intensity appropriately. Considering the shape and the height of the peak, one can say that the filling fraction of the sample with a rod length  $l=2.0$   $\mu\text{m}$  is obviously less ideal than for  $l=2.2$   $\mu\text{m}$  and  $l=1.8$   $\mu\text{m}$ . In the transmittance spectra, slight dips are visible at spectral positions coincident with the observed reflectance peaks, indicated by the dotted lines.

To summarise, the obtained spectra of the fabricated icosahedral photonic quasicrystals give some evidence for a pseudo-stop band. Especially, icosahedral photonic quasicrystals oriented along a three-fold axis show a distinct peak (up to 20%) in reflectance coinciding with a slight dip in transmittance at a spectral position of roughly 4  $\mu\text{m}$ . This feature shifts as expected to the blue (to smaller wavelengths) for less filling fraction and for smaller rod lengths.

At first, it is surprising that a prominent peak in reflectance is only observed for the icosahedral photonic quasicrystal oriented along a three-fold axis. However, a possible explanation for that might be the peculiar experimental condition caused by the usage of cassegrain microscope objectives. The cassegrain objectives probe the samples under a fairly large angle between  $15^\circ$  and  $30^\circ$  with respect to the surface normal. Thus, one does actually not measure along the symmetry axis the samples are oriented along. Considering the relative positions of the principal symmetry axes in the icosahedral symmetry group, one realises that for samples oriented along a three-fold axis a two-fold axis lies in this specific opening angle of  $15^\circ$  to  $30^\circ$ . Vice versa, for

samples oriented along a two-fold axis we actually measure along a three-fold axis, while for samples oriented along a five-fold axis, neither a two-fold nor a three-fold axis lies in this specific opening angle range. Additionally, the averaging over several angles in the measurements, namely from  $15^\circ$  to  $30^\circ$ , might conceal many anticipated features. In particular, as one has to keep in mind that in reciprocal space a quasiperiodic pattern in principle consists of a dense set of reciprocal lattice vectors, which can all contribute to diffraction. The low transmittance and reflectance at short wavelengths (shorter than  $2\ \mu\text{m}$ ) observed in all spectra indicate such light scattering caused by many different (more and less significant) reciprocal lattice vectors.

In conclusion, the interpretation of the obtained spectra is very challenging due to the averaging over angles between  $15^\circ$  and  $30^\circ$  with respect to the surface normal, for both probing the sample and detecting the transmitted or reflected light.

Certainly, a theoretical model is helpful and necessary to get further insights into the emerging features. A suitable theoretical model is developed by us over the course of this thesis and will be introduced in section 5.3.

Meanwhile, on the experimental side, we aim to shift the (expected) spectral features to shorter wavelengths by decreasing the rod length  $l$  and likewise the filling fraction further. Then, the dedicated home-built normal incidence transmittance setup (described in section 4.2.4), which covers a spectral range from 500 nm to 1750 nm, can be used to measure the transmittance spectra at normal incidence with a small opening angle ( $5^\circ$ ). The smallest rod length  $l$  that we have finally achieved, after having carefully adjusted the laser intensity and laser pulse duration for the exposure of SU-8 and having diligently customised the post-bake and development procedure, is  $l = 1\ \mu\text{m}$ , scaling down the spectral features of the samples studied thus far, by a factor of two.

The angle-resolved transmittance spectra of icosahedral photonic quasicrystals of rod length  $l = 1\ \mu\text{m}$ , with thicknesses of about  $4.5\ \mu\text{m}$ , and diameters of  $50\ \mu\text{m}$ , are depicted in Fig. 5.8 in false colour. Unfortunately, the expected fundamental pseudo-stop band around  $\lambda \approx 2 \cdot l = 2\ \mu\text{m}$  wavelength is just out of the spectral range of detection. Yet, another dip in transmittance is clearly visible in (a) and (b), i.e., for orientations along a two-fold and three-fold rotational symmetry axis, respectively, occurring around  $1.2\ \mu\text{m}$  and  $1.0\ \mu\text{m}$  wavelength at normal incidence (angle of  $0^\circ$ ). The respective dips split up into two branches with increasing angle of incidence. One branch shifts to longer wavelengths for increasing angle of incidence, the second branch forms the border or ascent between low transmittance (below 10%, depicted in blue colour) and higher transmittance (around 30%, depicted in green colour). In Fig. 5.8 (c), i.e., for the sample oriented along a five-fold rotational symmetry axis, the two branches at normal incidence (angle of  $0^\circ$ ), namely the dip at  $1.55\ \mu\text{m}$  wavelength and the ascent at around  $0.9\ \mu\text{m}$  wavelength, cf. graph (d), join up at an angle of around  $20^\circ$  for  $s$ -polarisation and of  $30^\circ$  for  $p$ -polarisation at the wavelength of  $1.25\ \mu\text{m}$ . These results are consistent with the experimental findings of W. Man *et al.* [63], demonstrating the good quality of the fabricated polymer (SU-8) icosahedral photonic quasicrystals with the reduced rod length  $l = 1\ \mu\text{m}$ .

Please note that the angle-resolved spectra are likewise consistent with the spectra of Fig. 5.6 and Fig. 5.7 measured with the combination of FTIR-spectrometer and infrared microscope averaging over a cone from  $15^\circ$  to  $30^\circ$ .

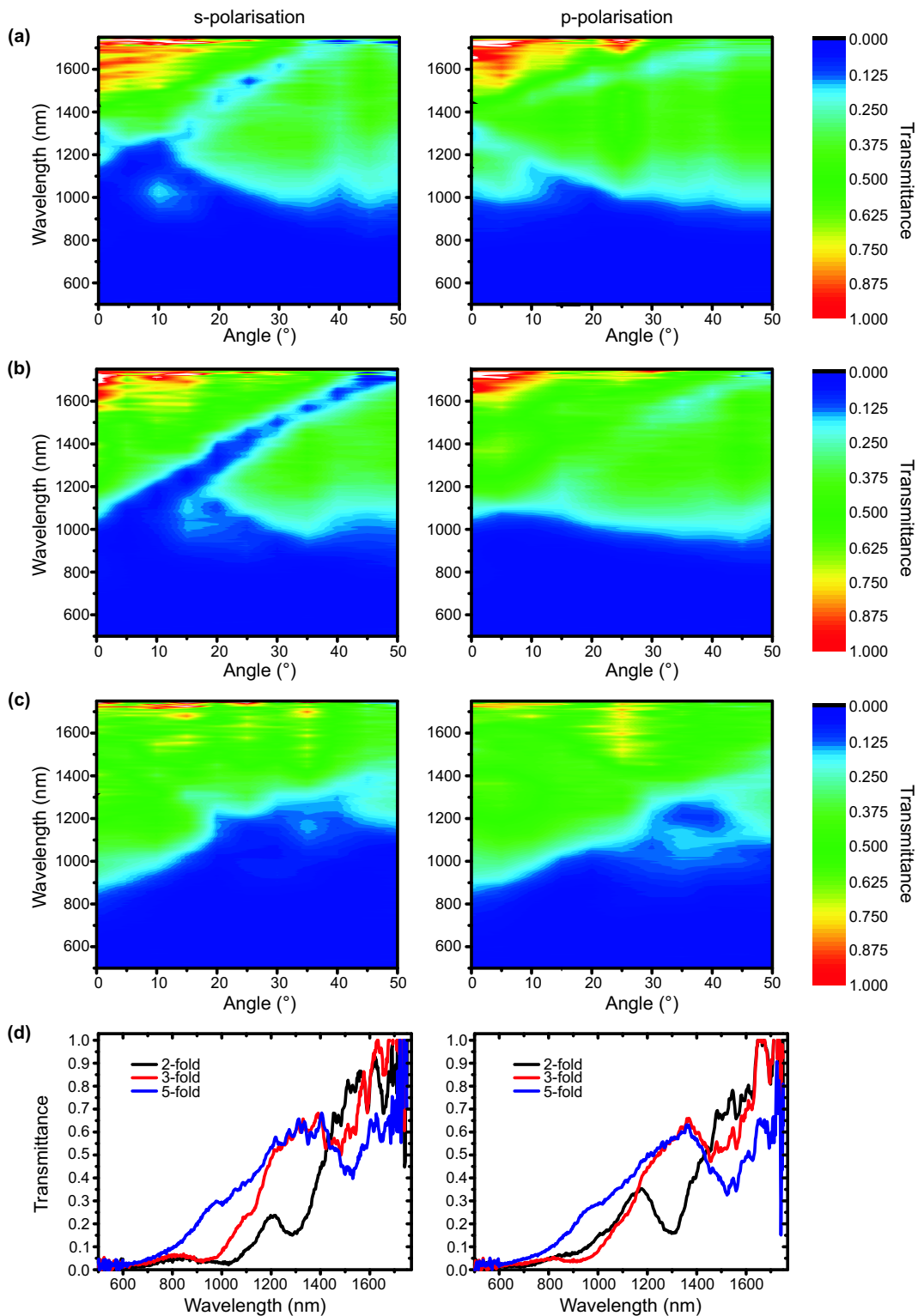


Figure 5.8: The measured angle-resolved transmittance spectra of three-dimensional icosahedral photonic quasicrystals with  $l=1\ \mu\text{m}$  rod length and  $4.5\ \mu\text{m}$  thickness oriented along a (a) two-fold, (b) three-fold and (c) five-fold rotational symmetry axis are illustrated as false colour plots. The incident light is either *s*-polarised (left column) or *p*-polarised (right column). Graph (d) shows cuts of (a) – (c) at  $0^\circ$  angle of incidence.

## 5.2.2 Time-Resolved Transmittance Spectra

Time-resolved transmittance spectroscopy is a useful method to investigate the optical transport properties of any photonic system. In cooperation with LENS in Florence, we characterise the time-resolved transmittance spectra and transport properties of the icosahedral photonic quasicrystals (cf. section 4.2.2). Lacking of any theoretical predictions of the expected results at this point, we mainly focus on studying icosahedral photonic quasicrystals oriented along a five-fold rotational symmetry axis, as this orientation covers the unusual symmetry distinctive for quasicrystals and forbidden for periodic crystals. The rod length  $l$  of the samples is  $2\ \mu\text{m}$ , the diameter  $100\ \mu\text{m}$ . The obtained time-resolved transmittance spectra are normalised to their individual pulse maxima – in the experiment, various filters have been used in order not to overload the photomultiplier, which prohibits the direct comparison of the absolute values of the respective pulse maxima.

As first aspect of the studies, the influence of the sample thickness on the experimentally obtained time-resolved transmittance spectra is investigated. The measured data are shown in Fig. 5.9. The two sets of samples differ in their respective filling fraction, yet within each set of samples, the filling fraction is kept constant. The samples are probed with a linearly polarised Gaussian pulse with a time duration of 150 fs, centered at 1500 nm wavelength, leading to the depicted autocorrelation (dotted line) measured without sample. The obtained autocorrelation defines the zero point of the time delay. The transmitted pulse is detected with the analysing polariser oriented parallel to the incident linearly polarised Gaussian pulse (referred to as same polarisation configuration), i.e., without sample, the pulse would be (ideally) completely transmitted. For both sets of samples (a) and (b), which differ in the actual filling fraction, the sample thickness has an obvious effect on the transmitted pulse on both its shape and the delay of its pulse maximum. The delay of the pulse maximum increases from 27 fs to 53 fs or 67 fs, respectively, (indicated in the graphs) with increasing thickness from  $7.5\ \mu\text{m}$  to  $18.7\ \mu\text{m}$ , and the transmitted pulse develops a (bumpy) exponentially decaying trailing tail. Exponential fits

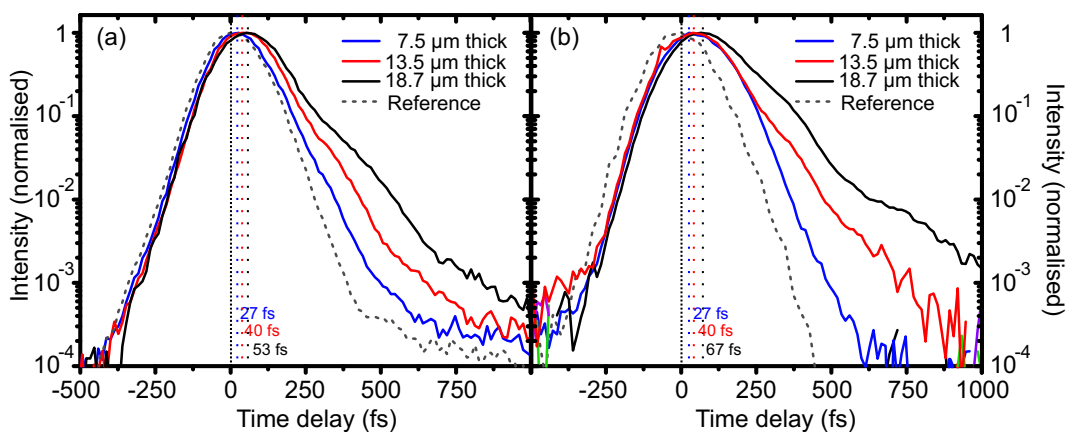


Figure 5.9: The depicted time-resolved transmittance data are obtained from linearly polarised Gaussian pulses of 1500 nm central wavelength which probe two different sets of three-dimensional icosahedral photonic quasicrystals oriented along a five-fold axis with  $l=2\ \mu\text{m}$  rod length and with different thicknesses. The set of samples in (a) differs from that in (b) in terms of the filling fraction. The analysing polariser is oriented parallel with respect to the incident linear polarisation (same polarisation configuration). The reference (dotted line) displays the autocorrelation of the setup with its pulse maximum at zero time delay.

to the exponential decays (similar to that illustrated in Fig. 5.11 in red) lead in (a) to decay time constants of about 64 fs, 84 fs and 107 fs with increasing thickness and in (b) of about 58 fs, 95 fs and 125 fs.

Our first interpretation of the exponential decay is related to diffusion due to sample imperfections, since the occurrence of diffusive exponential trailing tails is well-known from disordered photonic systems, see, e.g., Ref. [94], and has not been reported for ideal photonic crystals. To further investigate this assumption, we study the influence of the central wavelength of the incident Gaussian pulse, illustrated in Fig. 5.10 (a), in the same polarisation configuration. The respective autocorrelation of the different wavelengths is depicted in dotted and dashed lines in the appropriate colour. The characteristics of the transmitted pulse, namely its shape and the delay of its maximum, measured from a sample of  $18.7 \mu\text{m}$  thickness, are obviously strongly dependent on the central wavelength of the incident Gaussian pulse. For 1500 nm and 1530 nm central wavelength, the delay of the pulse maximum is about 40 fs, the fits to the exponentially decaying tails exhibit decay time constants of about 105 fs and 99 fs, respectively. However, for the latter case (1530 nm) the fit is quite tricky since the pulse is rather bumpy. For 1470 nm central wavelength, the pulse maximum is delayed by 80 fs, the exponential fit to the exponential tail results in a decay time constant of approximately 115 fs.

In Fig. 5.10 (b), the analysing polariser is additionally rotated by  $90^\circ$  such that the incident linearly polarised Gaussian pulse is ideally suppressed to zero (cross polarisation configuration). Thus, predominantly the transmitted light which has actually interacted with the sample and has accordingly changed its polarisation state is detected. The dramatic effect on the measured transmitted pulse is obvious, even for a fairly thin sample of only  $7.5 \mu\text{m}$  thickness. While in the same polarisation configuration the pulse maximum delay is negligible, i.e., below the finite time-resolution of the system of 14 fs (cf. section 4.2.2), the delay is about 147 fs in

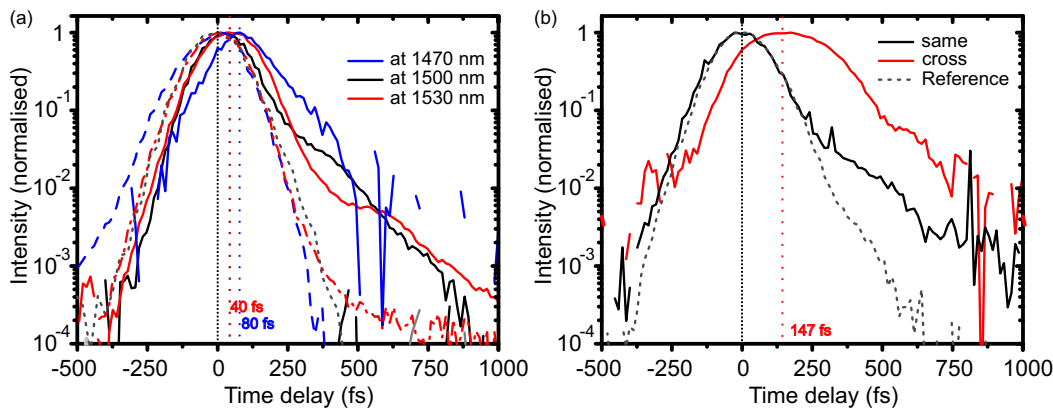


Figure 5.10: In (a), different central wavelengths of the incident linearly polarised Gaussian pulse probing the icosahedral photonic quasicrystal oriented along a five-fold axis ( $l=2 \mu\text{m}$  rod length,  $18.7 \mu\text{m}$  thickness) result in different outputs of the time-resolved transmitted pulse. The analysing polariser is set parallel to the incident linear polarisation. In (b), the transmitted pulse is depicted for the analysing polariser oriented parallel (same) and perpendicular (cross) to the incident linearly polarised Gaussian pulse (1500 nm central wavelength) probing the icosahedral photonic quasicrystal oriented along a five-fold axis ( $l=2 \mu\text{m}$  rod length,  $7.5 \mu\text{m}$  thickness). The references (dotted and dashed lines) in (a) and (b) display the autocorrelation of the setup for the respective central wavelengths of the probing Gaussian pulse.

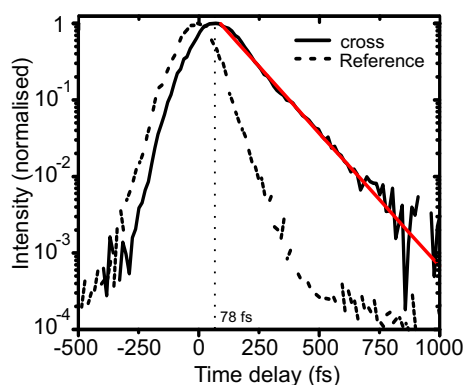


Figure 5.11: The time-resolved transmitted pulse is depicted for the analysing polariser oriented perpendicular to the incident linearly polarised Gaussian pulse of 1470 nm central wavelength that probes an icosahedral photonic quasicrystal oriented along a three-fold axis ( $l=2$   $\mu\text{m}$  rod length, 18.7  $\mu\text{m}$  thickness). The reference (dotted line) displays the autocorrelation of the setup. The red line shows the exponential fit to the exponentially decaying tail. After Ref. [49].

the cross polarisation configuration – much larger than the delay of 40 fs one would expect for an even bulk SU-8 film of same thickness. The decay time constant of the exponential decay increases from about 105 fs in the same polarisation configuration to approximately 136 fs in the cross polarisation configuration.

Exemplarily, time-resolved spectroscopy data obtained from an icosahedral photonic quasicrystal oriented along a *three-fold* rather than a five-fold symmetry axis, of 18.7  $\mu\text{m}$  thickness and 100  $\mu\text{m}$  diameter, composed of  $l=2$   $\mu\text{m}$  rods are shown in Fig. 5.11. The central wavelength of the incident linearly polarised Gaussian pulse is set to 1470 nm, the orientation of the analysing polariser is set according to the cross polarisation configuration. The autocorrelation of the setup is depicted in dotted lines. The red line displays the fit to the exponential decay, exhibiting a decay time constant of 126 fs. The pulse maximum is delayed by 78 fs with respect to the autocorrelation.

In conclusion, the time-resolved transmittance studies reveal the following findings: Linearly polarised Gaussian pulses change in shape and are significantly delayed considering the pulse maximum when transmitted through the icosahedral photonic quasicrystals. The reshaping of the pulse implies basically the development of a (bumpy) exponentially decaying trailing tail. The delay of the pulse maximum increases with increasing sample thickness, as naively expected for a bulk film of appropriate effective refractive index, yet the delay does depend on the central wavelength of the probing Gaussian pulse. Additionally, the decay time constant characterising the exponentially decaying trailing tail increases with increasing sample thickness and is also depending on the central wavelength of the probing pulse. Considering the cross polarisation configuration, in which the directly transmitted Gaussian pulse is blocked and primarily the light which has interacted with the sample is investigated, the pulse reshaping and the delay of the pulse maximum are even more pronounced.

The interpretation of these observations is rather challenging, yet the findings could be explained by disorder and imperfections occurring during the sample fabrication. Light scattered

few or many times within the samples due to disorder will result in a short or long temporal decay, which thus is a measure of the number of occurring scattering events. Thicker samples comprise a higher percentage of dislocated scatterers, enhancing the resulting diffusive exponential decay. Simultaneously, the maximum of the transmitted pulse is delayed due to randomly multiply scattered light. Furthermore, as the samples are not infinitely thick, the actual shape and delay of the transmitted pulse can be dependent on wavelength (cf. section 2.1.2.), and likewise be determined by the actual configuration of the disordered sample. In this interpretation, the cross polarisation configuration would basically detect the diffusively scattered light, scattered at sample imperfections.

Assuming that the observed exponential decay is exclusively caused by such diffusive scattering, the example depicted in Fig. 5.11 with a decay time constant of 126 fs leads to a diffusion coefficient<sup>4</sup> of  $2.6 \cdot 10^2 \text{ m}^2/\text{s}$  and accordingly to a mean free path of  $3.4 \text{ }\mu\text{m}$  [49]. This can be compared with state-of-the-art three-dimensional photonic crystals, which recently showed a mean free path of 5 to  $30 \text{ }\mu\text{m}$  [94].

Additionally, in this very wavelength range, the low transmittance and reflectance values of only few percent, which are measured within a rather small finite opening angle (cf. section 5.2.1) and which decrease further with increasing sample thickness, could likewise be ascribed to diffusive scattering and would lead to a comparable scattering mean free path assuming Beer's law [49]. Furthermore, regarding the measured Laue diagrams (see section 5.1), the development of the (diffusive) background for thicker samples would also be perfectly consistent with diffusive scattering due to disorder and sample imperfections.

Yet, in the following section, this initial interpretation, namely ascribing the experimentally obtained surprising effects to diffusive scattering caused by sample imperfections and disorder, is revised as a theoretical model for calculating the anticipated optical properties of *ideal* structures has been developed.

---

<sup>4</sup>From diffusion theory, the diffusion coefficient  $D$  is related to the decay time constant  $\tau$  by  $D \approx L^2/\pi^2/\tau$ , where  $L$  denotes the sample thickness, and is furthermore defined as  $D = (1/3)v_e l_s$ , with the mean free path  $l_s$  and the energy velocity  $v_e$  approximated by the phase velocity  $c_p = c_0/n_{\text{eff}} = c_0/1.3$ ,  $c_0$  being the vacuum speed of light and  $n_{\text{eff}} = 1.3$  the effective refractive index of the sample assuming a reasonable filling fraction of 50%.

## 5.3 Calculations and Re-Interpretation of Experimental Results

In the previous sections, several optical properties of icosahedral photonic quasicrystals have been studied by investigating Laue diffraction patterns, transmittance and reflectance spectra, and time-resolved transmittance properties. Our experimental findings, the development of a diffusive background in the Laue diagrams with increasing sample thickness, low transmittance and reflectance values measured within a rather small finite opening angle, and the occurrence of an exponential (diffusive) decay in the time-resolved measurements, are usually associated with diffusion in disordered photonic systems. However, the correct interpretation of the results is challenging, as the anticipated experimental results of an *ideal* icosahedral photonic quasicrystal, i.e., its intrinsic optical properties, are largely unknown due to the lack of adequate theoretical calculations.

For this reason, a systematic microscopic theory of the optical properties of ideal icosahedral photonic quasicrystals accounting for multiple photon-scattering effects [91] is developed on the basis of scattering matrix calculations (cf. section 4.3) combined with periodic rational approximants of the icosahedral quasicrystals (cf. section 3.2).<sup>5</sup>

### 5.3.1 Test of Rational Approximant Approach

In this section, we like to confirm the reliability of the rational approximant approach for representing the optical properties of icosahedral photonic quasicrystals. Therefore, icosahedral photonic quasicrystals oriented along a two-fold axis and corresponding rational approximants of different unit cell sizes (cf. section 3.2) are fabricated via direct laser writing. This is illustrated in Fig. 5.12. In the left column, the computer generated ray-tracing images of a (a) 1/1, (c) 2/1, (e) 3/2 rational approximant and (g) of the icosahedral quasicrystal are depicted from top to bottom. The respective unit cells of the rational approximants are highlighted in red and successively increase in size. On the right, i.e., (b), (d), (f), (h), the SEM images of correspondingly fabricated polymeric (SU-8) nanostructures with a rod length  $l$  of 2  $\mu\text{m}$  are shown, which agree very well with the blueprint (right column). This clearly demonstrates the high precision of the fabrication method as well as the high quality of the fabricated samples.

As a test for the applicability of the combination of scattering matrix calculations with the rational approximant approach, we compare calculated angle-resolved transmittance spectra for incident linearly polarised light and corresponding measured spectra, the latter experimentally obtained by using the home-built setup described in section 4.2.4. As the detecting system of this setup is limited to the spectral range from 500 nm to 1750 nm (cf. section 4.2.4), the rational approximants and the icosahedral quasicrystal are fabricated with a rod length  $l=1$   $\mu\text{m}$ , getting significant spectral features within the spectral range of detection, cf. Fig. 5.8. The thickness of the samples is around 4.5  $\mu\text{m}$ , the diameter about 50  $\mu\text{m}$ . The light impinges on the samples within the finite opening angle of about  $5^\circ$ . In the computations, we account for this by performing the scattering matrix calculations for ideal plane waves at different angles

---

<sup>5</sup>Note that the recently introduced alternative approach of Ref. [50] has not delivered explicit findings adaptable to our three-dimensional case.

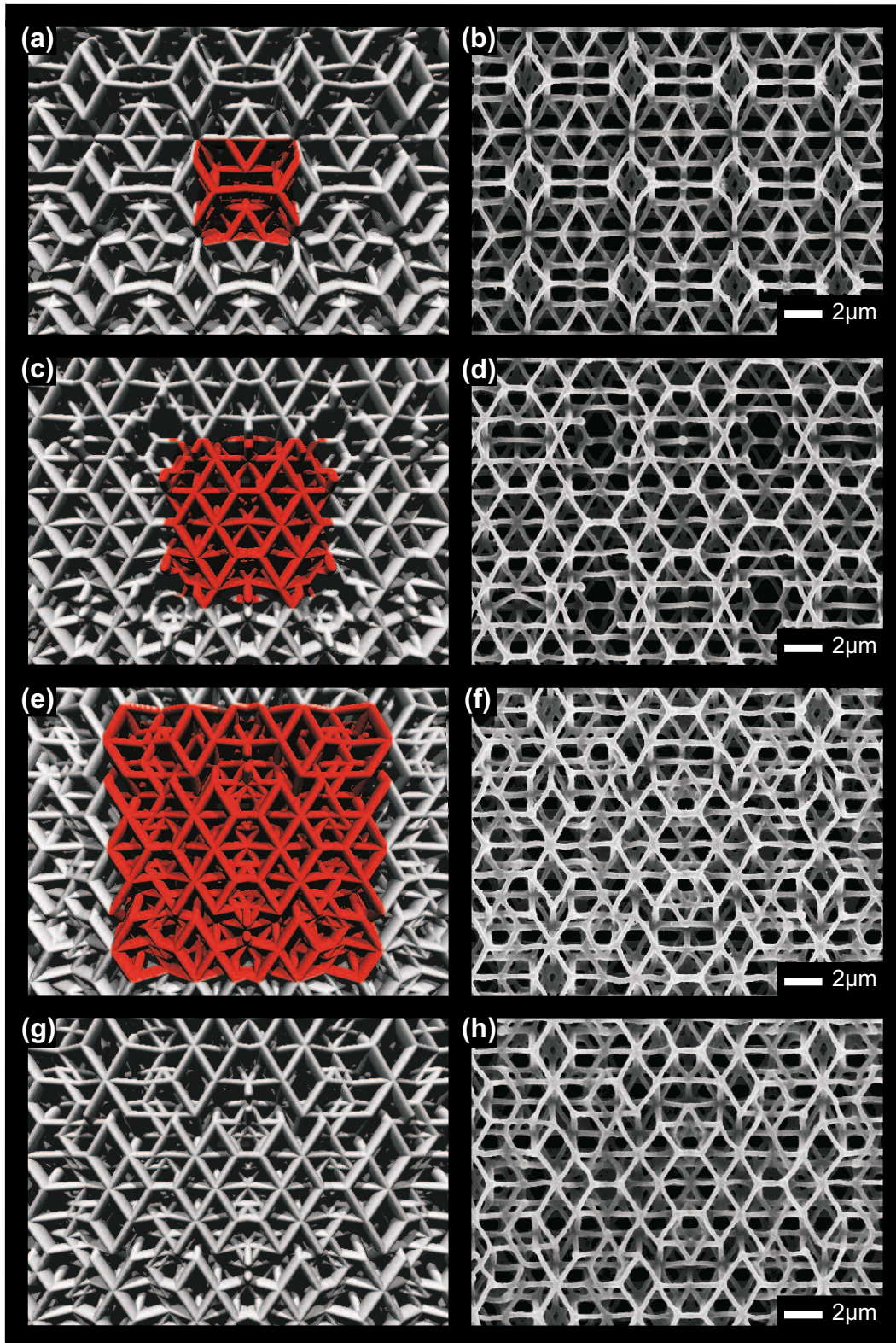


Figure 5.12: From top to bottom, rational approximants (a – f) with increasing size of the respective unit cells (highlighted in red in the left column) and the icosahedral photonic quasicrystal (g), (h) oriented along a two-fold rotational symmetry axis are shown. The left column shows computer generated images, the right column SEM images of corresponding SU-8 nanostructures fabricated via direct laser writing. After Ref. [91].

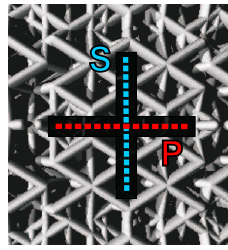


Figure 5.13: The orientation of the electric field vector with respect to the icosahedral photonic quasicrystal oriented along a two-fold axis is depicted for linearly  $s$ - (blue) and  $p$ -polarised (red) light.

of incidence (cf. section 4.3.1) and by averaging these spectra accordingly over an angle of  $5^\circ$ .

In the scattering matrix calculations, we account for as many as  $g=8$  orders of the reciprocal lattice vectors (cf. section 4.3) to ensure convergence for a given rational approximant. The real space discretisation is 20 nm, which has to be compared with the rod length  $l=1\ \mu\text{m}$  and with the extent of the three-dimensional cubic unit cells of the respective rational approximants, which has in the case of the 2/1 rational approximant [see Fig. 5.12 (c)] the edge length of about  $4.5\ \mu\text{m}$  (cf. section 3.2), for instance. The elliptical shape of the voxels with an aspect ratio between axial and lateral extension of about two, due to the fabrication via direct laser writing (cf. section 4.1 and chapter A of the appendix), is also accounted for. This allows reliable calculations for the 2/1 rational approximant, while memory space and CPU times are, however, already excessive for the 3/2 rational approximant. The refractive index of SU-8 is taken as 1.58 (and zero imaginary part) and that of the glass substrate, which is accounted for as half space (cf. section 4.3), as 1.52. The incident light is linearly  $s$ - or  $p$ -polarised, see Fig. 5.13.

The obtained results are summarised in Fig. 5.14 for incident linearly  $s$ -polarised light (see

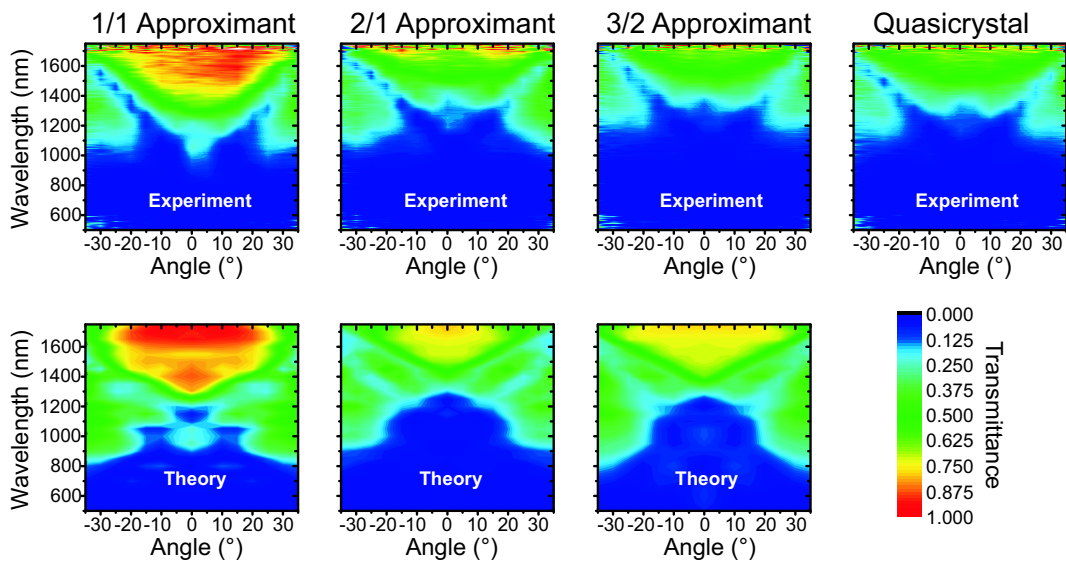


Figure 5.14: Measured (top) and calculated (bottom) angle-resolved transmittance spectra versus wavelength of light and versus angle of incidence with respect to the surface normal of the samples are depicted as false colour plots. The indicated rational approximants are illustrated in Fig. 5.12. After Ref. [91].

Fig. 5.13). The transmittance properties of the rational approximants rapidly converge to those of the icosahedral photonic quasicrystal with increasing size of the unit cell. Furthermore, the scattering matrix calculations agree well with our experimental data. We also find that the transmittance properties of the icosahedral photonic quasicrystal are already well reproduced by the 2/1 rational approximant, which is hence used in subsequent calculations [91]. The same observations and conclusions hold for incident  $p$ -polarised light, which is not shown here. The performed studies on rational approximants of different unit cell sizes give us confidence that the obtained optical properties are not due to the artificially introduced periodicity but caused by the complex arrangement of the dielectric material within the respective unit cells. Recall that within the respective unit cells the rational approximants are identical to the icosahedral quasicrystal (see section 3.2).

### 5.3.2 Time-Resolved Transmittance Calculations

In section 5.2.2, the experimentally obtained data of time-resolved transmittance spectroscopy on icosahedral photonic quasicrystals are discussed, yet the correct interpretation poses some difficulties in terms of distinguishing intrinsic from extrinsic properties (such as sample imperfections).

In the following, appropriate scattering matrix calculations, which are described in section 4.3.3, are performed for the 2/1 rational approximant to learn about the expected temporal response of ideal icosahedral photonic quasicrystals. In short, a linearly polarised incident Gaussian pulse with a time duration of 150 fs impinges on the sample. For each diffraction order, the time-resolved intensity (using finite time steps  $\Delta t=0.8$  fs) is obtained from the Fourier transform of the frequency-dependent transmitted electromagnetic field components (taking account of the actual orientation of the analysing polariser, cf. section 4.3.2). Additionally, the finite opening angle of  $27^\circ$  of the collecting lens is considered by summing over the respective diffraction orders. In the calculations, the scalability of Maxwell's equations (see also section 2.1) is exploited, i.e., the calculations are performed for 2/1 rational approximants with a rod length  $l$  of  $1 \mu\text{m}$  and of adequate thickness and the central wavelength of the impinging

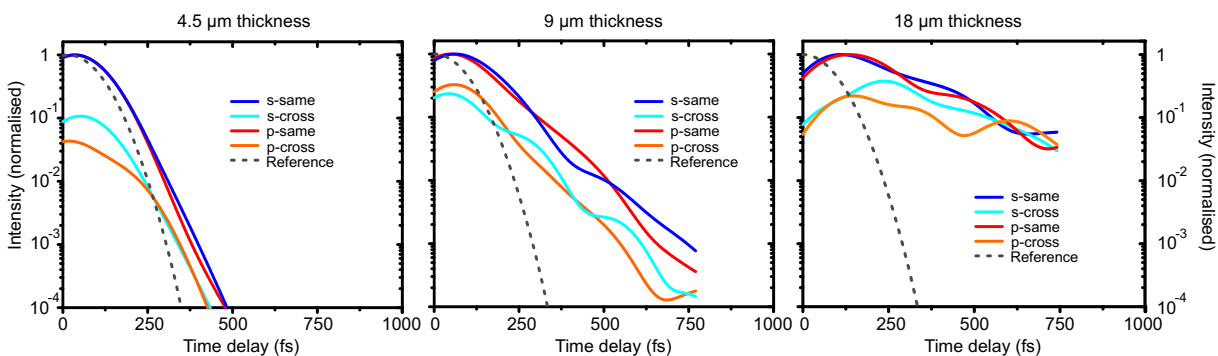


Figure 5.15: For a 2/1 rational approximant with  $l=1 \mu\text{m}$  rod length, the time-resolved transmittance of an incident linearly  $s$ - and  $p$ -polarised Gaussian pulse is calculated for three different thicknesses, increasing from left to right. The data are calculated for both detection channels, i.e., using the same and cross polarisation configuration. The graphs are normalised to the respective pulse maxima of the same polarisation configuration. The dashed line depicts the reference pulse propagating in vacuum with its maximum at zero time delay.

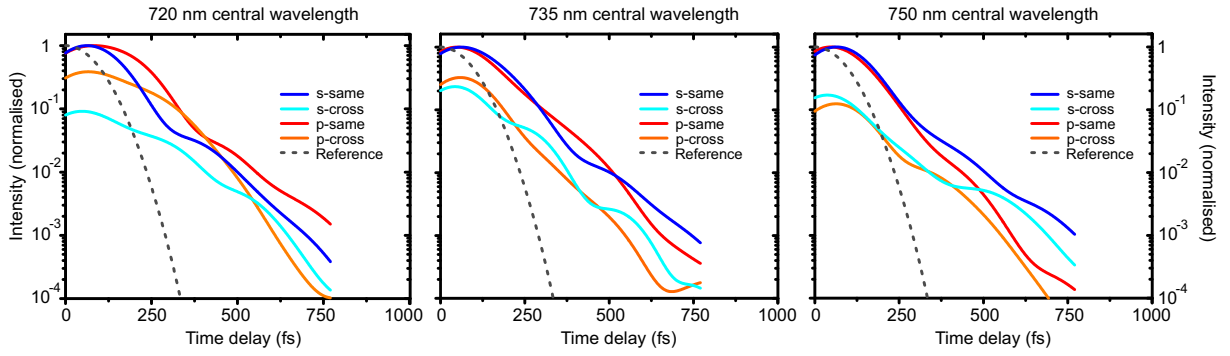


Figure 5.16: The calculated time-resolved transmittance of a 2/1 rational approximant with  $l=1 \mu\text{m}$  rod length and  $9 \mu\text{m}$  thickness is displayed for incident linearly  $s$ - and  $p$ -polarised Gaussian pulses of three different central wavelengths in the range of 720 nm to 750 nm (increasing from left to right). The data are calculated for both detection channels, i.e., using the same and cross polarisation configuration. The graphs are normalised to the respective pulse maxima of the same polarisation configuration. The dashed line depicts the reference pulse propagating in vacuum.

Gaussian pulse is likewise scaled down appropriately. In the obtained results, the qualitative behaviour of the experimental findings are reproduced (without attempting any fitting).

According to the experiments of Fig. 5.9, the influence of the sample thickness on the transmitted pulse is investigated. This is depicted in Fig. 5.15, where the incident linearly  $s$ - and  $p$ -polarised<sup>6</sup> Gaussian pulse (central wavelength of 735 nm) is detected in the same polarisation configuration and in the cross polarisation configuration. The calculated data are normalised to the maximum of the same polarisation configuration of the respective  $s$ - and  $p$ -polarised case. The transmitted intensity obtained in the cross polarisation configuration is only about one order of magnitude smaller than in the same polarisation configuration, indicating the strong depolarising character of the samples due to significant multiple scattering of the photons. The thickness of the sample increases from left to right, and likewise the respective delay of the pulse maxima increases and an exponential (bumpy) tail develops with an increasing decay time constant. This tendency is observed for both incident linear polarisations  $s$  and  $p$ , and for both detection channels, i.e., for the cross and same polarisation configuration. Furthermore, this tendency agrees very well with the experimental findings, cf. Fig. 5.9.

Changing the central wavelength of the incident Gaussian pulse, i.e., probing different photonic bands, effects the shape of the transmitted pulse and the delay of its maximum, as expected for light scattered multiple times within a long-range ordered structure. This aspect is illustrated in Fig. 5.16 considering fairly small shifts of the central wavelength of the Gaussian pulse impinging on a  $9 \mu\text{m}$  thick 2/1 rational approximant sample of  $l=1 \mu\text{m}$  rod length, which is comparable to the experiments depicted in Fig. 5.10 (a). The calculated data reproduce the experimentally obtained dependence of the delay of the pulse maximum and of its shape (i.e., forming a bumpy or exponentially decaying trailing tail of different time constants) on the

<sup>6</sup>Although normal incidence is considered, studying both,  $s$ - and  $p$ -polarisation, which differ in the orientation of the electric (and likewise of the magnetic) field vector, is useful, as the symmetry of the sample is two-fold, rather than four-fold (cf. Fig. 5.13).

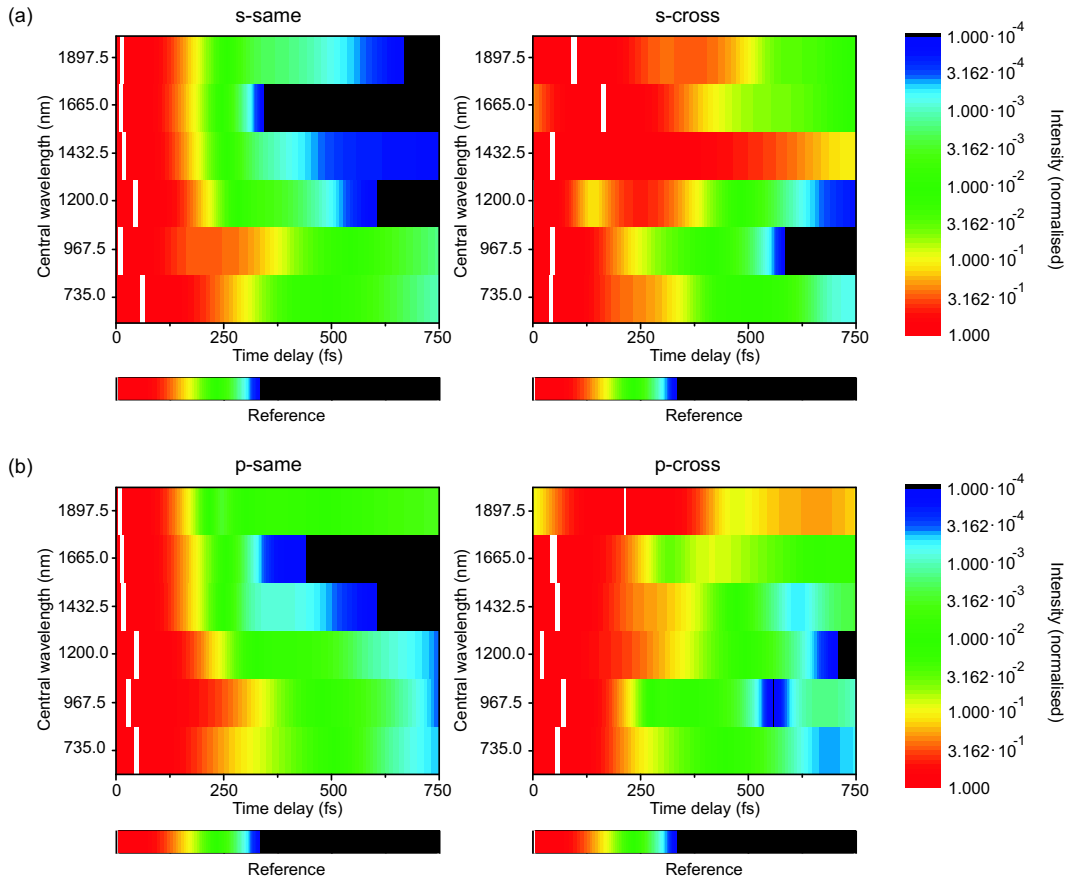


Figure 5.17: The calculated time-resolved transmittance of a  $2/1$  rational approximant with  $l=1 \mu\text{m}$  rod length and  $9 \mu\text{m}$  thickness is depicted as false colour graph for incident linearly  $s$ - (top) and  $p$ -polarised (bottom) Gaussian pulses of several different central wavelengths over a large range from  $735 \text{ nm}$  to  $1898 \text{ nm}$ . The data are calculated for both detection channels, i.e., using the same (left column) and cross (right column) polarisation configuration. The graphs are normalised to the respective pulse maxima (depicted in white) for each parameter set. The reference depicts a pulse propagating in vacuum with its maximum at zero time delay.

central wavelength. Furthermore, similar qualitative behaviour is found throughout a broad spectral range, i.e., for several different central wavelengths studied from  $735 \text{ nm}$  up to  $1.9 \mu\text{m}$  central wavelength, as shown in Fig. 5.17. The quantitative exponential decay time constants and temporal shifts of the pulse maxima clearly depend on the actual central wavelength of the incident Gaussian pulse, i.e., depend on the characteristics of the actually probed photonic bands, observed for both incident linear polarisations and both detection channels.

However, for studying the influence of quasiperiodicity in the experiment, it is favourable to concentrate on and to analyse the cross polarisation configuration, as the directly transmitted beam is blocked. In order to reproduce the experimental conditions of Fig. 5.11, calculations are performed for a  $9 \mu\text{m}$  thick  $2/1$  rational approximant with a rod length  $l$  of  $1 \mu\text{m}$  and for a linearly polarised Gaussian pulse of  $735 \text{ nm}$  central wavelength. The calculated data are depicted in Fig. 5.18 (a), which shows a very close qualitative behaviour to the experimental results of Fig. 5.11: The maximum of the transmitted pulse is similarly delayed (by  $99 \text{ fs}$ ) and an exponential tail develops with a comparable decay time constant of  $90 \text{ fs}$  [91]. In Fig. 5.18 (b), a reference calculation of a three-dimensional periodic photonic crystal

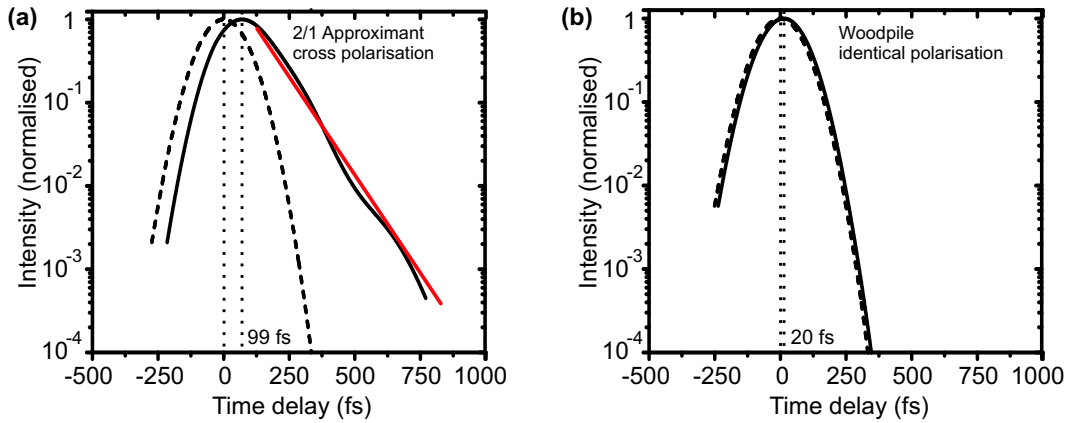


Figure 5.18: In (a), the time-resolved transmittance detected in the cross polarisation configuration is calculated for a 2/1 rational approximant of  $l=1 \mu\text{m}$  rod length and  $9 \mu\text{m}$  thickness with an incident linearly polarised Gaussian pulse centred at  $735 \text{ nm}$  wavelength. The red line displays the exponential fit with a decay time constant of  $90 \text{ fs}$ , the delay of the pulse maximum is about  $99 \text{ fs}$ . These parameters are comparable to the experimental results depicted in Fig. 5.11. After Ref. [91]. In (b), a reference calculation of a periodic photonic woodpile crystal of comparable parameters (see main text) is depicted. As the cross polarisation configuration results in negligibly small transmitted intensity, the same polarisation configuration is shown. The dashed lines display the respective reference pulses propagating in vacuum.

(a woodpile structure exhibiting four-fold rotational symmetry, see, e.g., Ref. [86]) with a rod spacing of  $1 \mu\text{m}$ , a lattice constant of  $1.414 \mu\text{m}$  and  $11.3 \mu\text{m}$  thickness, is shown. Since the transmitted intensity in the cross polarisation configuration is numerically zero, as expected from symmetry, the identical polarisation configuration is depicted instead, which reveals just a small shift of the incident Gaussian pulse, yet no exponentially decaying trailing tail.

Although in the time-resolved transmittance experiments, the half opening angle of the collecting lens is fixed to  $27^\circ$ , it can be changed in the theoretical calculations to study its influence on the obtained transmitted pulse. Increasing the half opening angle corresponds to collecting more (higher) orders of diffraction. The result is depicted in Fig. 5.19 considering few selected different half opening angles and probing a  $9 \mu\text{m}$  thick 2/1 rational approximant of rod length  $l=1 \mu\text{m}$  with a linearly  $s$ - and  $p$ -polarised Gaussian pulse of  $735 \text{ nm}$  central wavelength. The data are normalised to the maximum of the pulse which is obtained for collecting all transmitted diffraction orders (half opening angle of  $90^\circ$ ) for the respective detection channels, i.e., using the same and cross polarisation configuration. Obviously, light is scattered into higher-order diffraction spots as well, which in general exhibit different temporal behaviours. Depending on the actual opening angle, more or less diffraction orders add up to form the detected time-resolved transmitted pulse which consequently changes in shape and in shift of the pulse maximum. The different temporal behaviour of the individual Laue diffraction spots might be interesting for several optical applications and could be explored more diligently in future experimental studies, e.g., by selecting individual Laue diffraction spots via an appropriate aperture in the time-resolved transmittance spectroscopy setup.

The performed theoretical studies indicate that the temporal trailing tails observed in our experiments can arise due to intrinsic properties of ideal icosahedral photonic quasicrystals and are not exclusively caused by sample imperfections and disorder. The obtained temporal re-

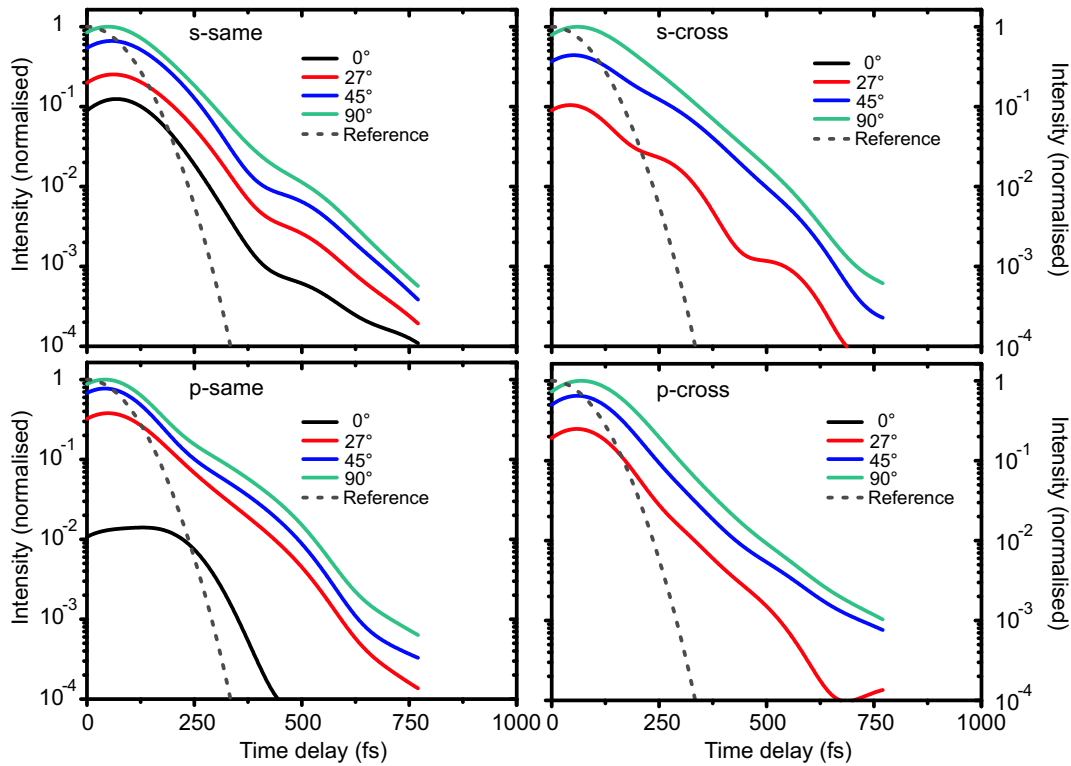


Figure 5.19: The dependence of the calculated time-resolved transmittance of a 2/1 rational approximant with  $l=1$   $\mu\text{m}$  rod length and 9  $\mu\text{m}$  thickness on the half opening angle for collecting the various diffraction orders is shown for incident linearly *s*- (top) and *p*-polarised (bottom) Gaussian pulses centered at 735 nm wavelength. The data are calculated for both detection channels, i.e., using the same (left column) and cross (right column) polarisation configuration. The graphs are normalised to the respective pulse maxima of the maximum half opening angle of  $90^\circ$ , which is why in the cross polarisation channel the data of  $0^\circ$  opening angle are not visible. The dashed line depicts the reference pulse propagating in vacuum.

sponse is caused by multiple scattering of light within the sample, which on one hand transfers intensity into many diffraction orders and on the other hand slows down multiply scattered components of the light. Moreover, the polarisation state of the light is modified such that a substantial amount of light is detected in the cross polarisation configuration. However, currently the relative contributions of intrinsic and extrinsic effects to the experimentally obtained exponentially decaying tail cannot be quantified.

### 5.3.3 Normal Incidence Transmittance and Reflectance Spectra

The long temporal response observed in our experiments and in the performed scattering matrix calculations consequently translates into fairly narrow spectral features in the frequency domain. These narrow spectral features are found in both, scattering matrix calculations and in the experiments [91]. As these expected spectral features can be easily obscured in the experiment when averaging over a finite opening angle of incidence, a dedicated setup with an almost ideal incident plane wave (see section 4.2.4) is required and has been accordingly constructed in the course of this thesis.

The measured data are shown in Fig. 5.20 (a) for icosahedral photonic quasicrystals of  $l=1 \mu\text{m}$  rod length and  $4.5 \mu\text{m}$  thickness. The transmitted light is detected within a finite half opening angle of  $24^\circ$  for both detection channels, i.e., the cross polarisation configuration and the same polarisation configuration<sup>7</sup>. The according scattering matrix calculations are shown in part (b) of Fig. 5.20. The overall qualitative agreement between experiment and theory is quite good and the characteristic scales of the obtained features do match. Obviously, a one-to-one correspondence of the highly structured spectra with the many maxima and minima cannot be expected at all, as these features do strongly depend on and shift with the actual parameters of the samples such as filling fraction. Very similar results are obtained for incident linearly  $p$ -polarised light, which are thus not depicted.

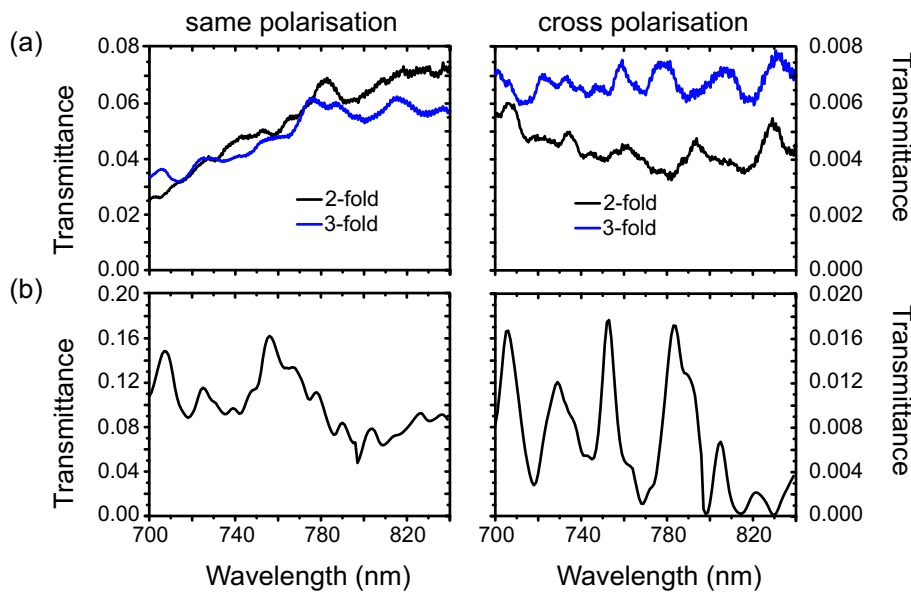


Figure 5.20: The normal incidence transmittance spectra measured at  $4.5 \mu\text{m}$  thick icosahedral photonic quasicrystals of  $l=1 \mu\text{m}$  rod length are displayed in (a), the corresponding scattering matrix calculations of the  $2/1$  rational approximant in (b). The left column depicts the results obtained for the same polarisation configuration, the right column for the cross polarisation configuration. The spectra are highly structured, the qualitative agreement between experiment and calculations is quite good. After Ref. [91].

<sup>7</sup>In the experiments, typical exposure times of the detecting system, i.e., the grating spectrometer connected to the liquid-nitrogen cooled CCD camera, are several seconds.

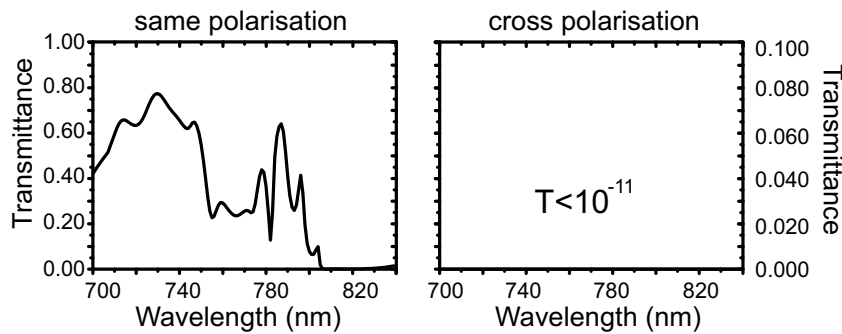


Figure 5.21: The normal incidence transmittance spectra calculated for a 5.7  $\mu\text{m}$  thick periodic photonic woodpile crystal of 1  $\mu\text{m}$  rod spacing are displayed. On the left, the graph obtained for the same polarisation configuration reveals a highly structured spectrum due to higher photonic bands, while the transmittance of the cross polarisation configuration (on the right) is close to zero. After Ref. [91].

As reference, the results of scattering matrix calculations of a three-dimensional periodic photonic crystal (woodpile structure) of comparable parameters (rod spacing of 1  $\mu\text{m}$ , thickness of 5.7  $\mu\text{m}$ ) are summarised in Fig. 5.21. In the cross polarisation configuration (right-hand side of Fig. 5.21), the transmittance is close to zero, as expected from symmetry, cf. Fig. 5.18 (b); for the same polarisation configuration, one finds a structured transmittance spectrum that is similar to that of icosahedral photonic quasicrystals, due to higher photonic bands.

The studies indicate that the observed results, i.e., the rather narrow spectral features with various minima and maxima, are an intrinsic property of the icosahedral photonic quasicrystals. Due to multiple scattering of light inside the (long-range ordered) icosahedral photonic quasicrystals, complicated spatial pathways of the photons interfere either mostly constructively or destructively, depending sensitively on the actual wavelength.

The calculated scattering matrix spectra shown in Fig. 5.22 support this intuitive explanation. Here, linearly *s*- and *p*-polarised light impinges on the samples with rod length  $l=1$   $\mu\text{m}$  and thicknesses of 4.5  $\mu\text{m}$  (a) or 9  $\mu\text{m}$  (b), and the transmitted and reflected light intensity is calculated without considering an analysing polariser. The following observations are valid for both polarisations of the probing beam. The transmittance (left column) and reflectance spectra (right column) are highly structured over a large spectral range. Furthermore, the directly (zeroth order) transmitted and reflected light intensity is rather low in the spectral region below 1.3  $\mu\text{m}$  wavelength, yet the total transmittance and total reflectance, i.e., the summation of all transmitted or reflected diffraction orders, respectively, is much higher, indicating that a lot of intensity is scattered into the various diffraction orders. This is presumably the reason for the low transmittance and low reflectance obtained in the experiments of section 5.2.1, as only a limited number of diffraction orders is detected by the cassegrain microscope objectives. In the calculated transmittance, the anticipated pseudo-stop band around 1.95  $\mu\text{m}$  wavelength is clearly visible. A closer look at the reflectance spectra, however, clearly reveals that the reflectance peak at this spectral position does not belong to the zeroth order reflected light, yet belongs to a higher diffraction order. This can explain the previous experimental findings that the prominent peak in reflectance measured with the FTIR-spectrometer (cf. section 5.2.1) was only observed for one specific orientation of the icosahedral photonic quasicrystal, as the

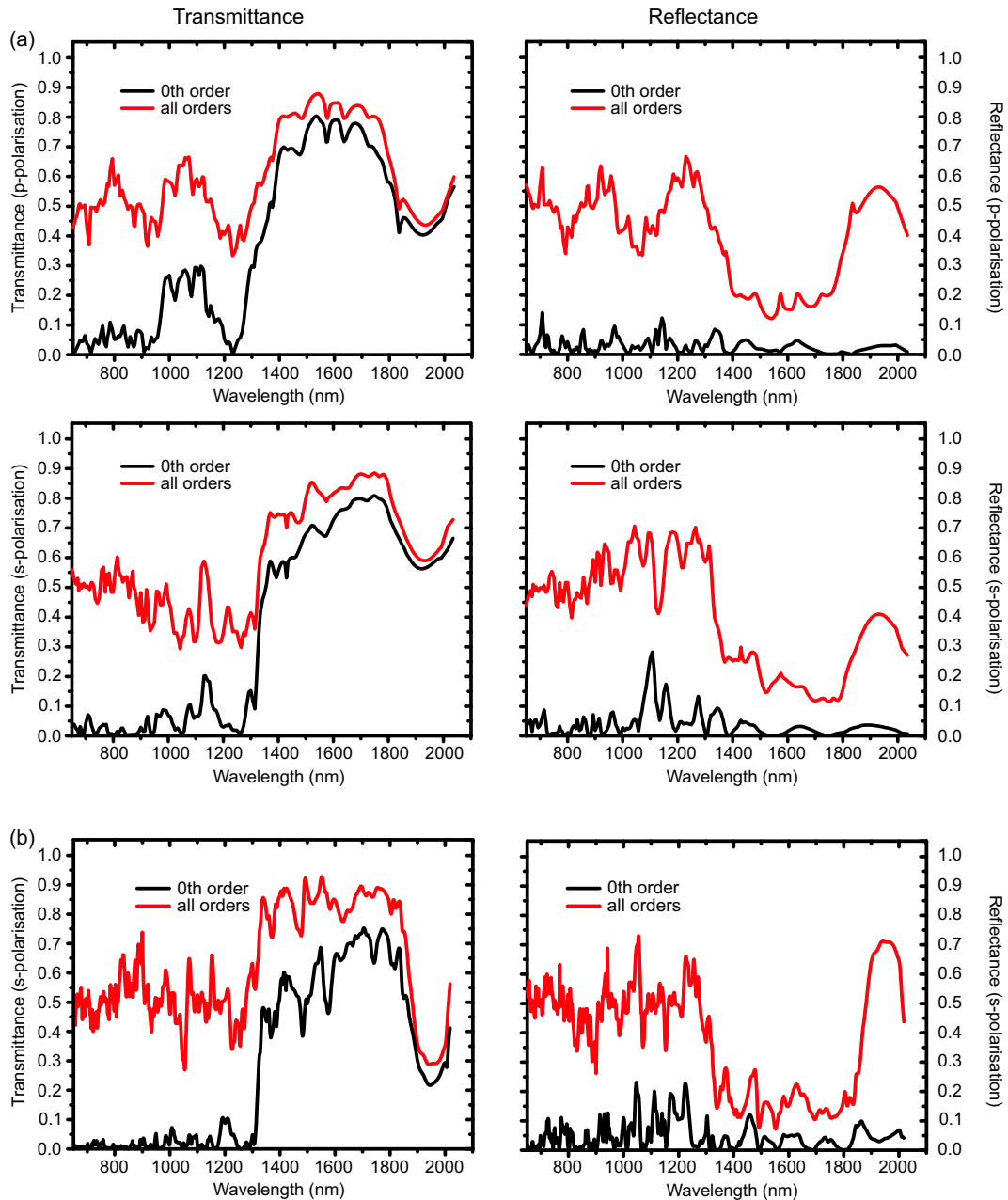


Figure 5.22: The transmittance (left column) and reflectance (right column) spectra calculated for a 2/1 rational approximant of  $l=1 \mu\text{m}$  rod length and thicknesses of  $4.5 \mu\text{m}$  (a) and  $9 \mu\text{m}$  (b) are shown. The undiffracted zeroth-order transmittance or reflectance is depicted in black, the total transmittance and total reflectance in red. The latter is obtained by integrating over all forward (total transmittance) or all backward (total reflectance) diffracted orders. The data reveal highly structured spectra over the depicted broad spectral range and indicates the significance of multiple light scattering into the various diffraction orders.

cassegrain microscope objectives probe the sample and detect the emerging light from the sample within the finite cone from  $15^\circ$  to  $30^\circ$ . Moreover, the dip in transmittance around  $1.25 \mu\text{m}$  wavelength and the sharp ascent to the longer wavelengths side can be found in the experimental spectra of section 5.2.1, yet still keeping in mind the specific experimental condition of averaging over angles from  $15^\circ$  to  $30^\circ$ . In the angle-resolved transmittance measurements of Fig. 5.8 and Fig. 5.14, this dip in transmittance is also obtained at the spectral position of around  $1.3 \mu\text{m}$  wavelength at normal incidence. Its spectral position shifts to longer wavelengths with increasing angle of incidence.

Increasing the sample thickness by a factor of two from Fig. 5.22 (a) to (b) enhances the peak in reflectance and the dip in transmittance around  $1.95 \mu\text{m}$  wavelength, as expected, since the light interacts with an increased number of scattering centres. Furthermore, the multiple scattering into the higher diffraction orders is intensified; the spectral features get even narrower and the difference between zeroth order transmittance (reflectance) and total transmittance (reflectance) increases. This is in total agreement with the observed results in the time-resolved experiments, as longer temporal trailing tails are found for thicker samples. Please note that in part (b) only *s*-polarisation is depicted, as for *p*-polarised incident light basically the same tendency is obtained.

In Fig. 5.23, the influence of the thickness is investigated in more detail by studying the total transmittance versus sample thickness. The aim is to compare the transport properties of the icosahedral photonic quasicrystals based on multiple light scattering to those of disordered photonic systems, which also reveal long temporal responses, and to those of periodic photonic crystals, which share the property of long-range order. As described in section 2.1.2, disordered photonic systems follow Ohm's law (transmittance inversely proportional to thickness) while periodic photonic crystals follow Beer's law (exponential correlation between transmittance and thickness), cf. section 2.1.1. In Fig. 5.23 (a), the total transmittance versus wavelength and versus sample thickness is displayed in false colour, while specific cuts are shown in (b). The overall behaviour is neither purely of Ohm's nor of Beer's type, yet for many wavelengths the transmittance drops within some thickness range to a finite constant value [91]. This aspect can be ascribed to the fact that forward scattering of light is responsible for the formation of the Laue diagram with its infinite number of diffraction spots in any finite solid angle.

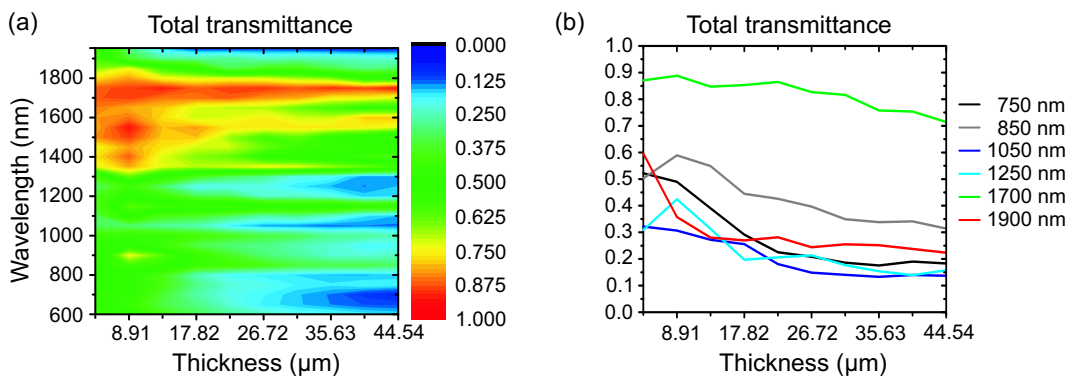


Figure 5.23: The total transmittance versus thickness versus wavelength is calculated for a  $2/1$  rational approximant of  $l=1 \mu\text{m}$  rod length and depicted as false colour plot in (a). Some cuts of (a) are shown in (b) for clarity. After Ref. [91].

Furthermore, the theoretical study indicates that the transport of light through the three-dimensional icosahedral photonic quasicrystals is generally different from both, transport in disordered photonic systems and in photonic crystals. The peculiar structure of quasicrystals, combining the presence of long-range order (just as periodic crystals) and of distinct nonequivalent local configurations (comparable to disordered systems), leads to unusual effects in the photon transport largely determined by multiple scattering of light. Unfortunately, the fabrication of icosahedral photonic quasicrystals with the large thicknesses shown in Fig. 5.23 is currently out of reach, preventing us from studying this aspect experimentally.

### 5.3.4 Laue Diffraction Patterns

In section 5.1, we have already pointed out that for increasing thicknesses of the icosahedral photonic quasicrystals, the observed Laue diffraction patterns change in terms of exhibiting sharper diffraction spots and developing a speckle-like background. This obvious dependence of the Laue diagrams on the sample thickness is not expected in the single-scattering limit, yet can be also explained by multiple scattering events. Recalling that the Laue diffraction patterns calculated via the cut-and-project method comprise single scattering only, the introduced scattering matrix approach combined with rational approximants can reveal the origin of the observed aspects, as multiple scattering events are intrinsically accounted for.

In Fig. 5.24, the Laue diffraction patterns of a  $2/1$  rational approximant of  $l=2\ \mu\text{m}$  rods obtained at 532 nm wavelength are depicted for increasing thicknesses from left to right. These calculations directly connect to the experimentally obtained Laue diagrams, shown in Fig. 5.3. The diameter and the brightness of the green spots are a measure of the intensity, which is normalised to that of the most intense diffraction orders. These calculations clearly reveal that the intensity of the various (but numerically limited)<sup>8</sup> diffraction orders of the Laue diagrams are indeed depending on the sample thickness. In particular, the thicker the sample, the more light is scattered into various (formerly low-intensity) diffraction orders which consequently gain in relative intensity and form a speckle-like background.

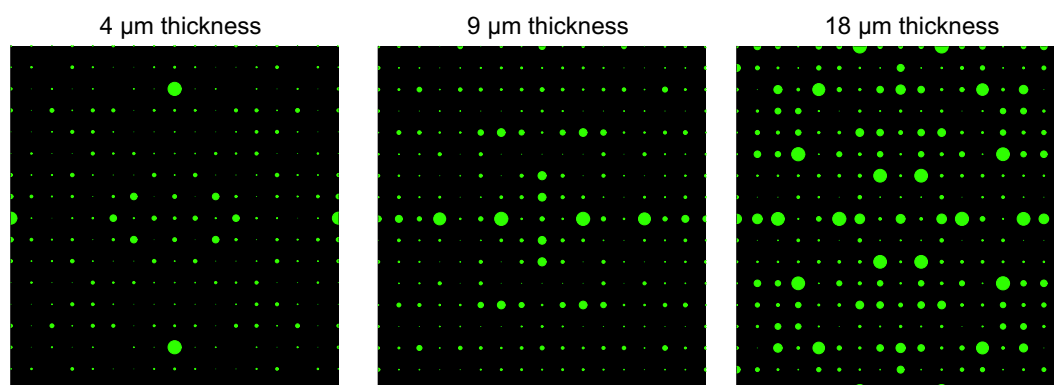


Figure 5.24: The calculated Laue diffraction patterns of a  $2/1$  rational approximant of  $l=2\ \mu\text{m}$  rod length are shown for increasing thicknesses from left to right, which reveal the development of a speckle-like background.

<sup>8</sup>Recall that the diffraction patterns of quasicrystals actually consist of densely arranged sharp Laue spots.

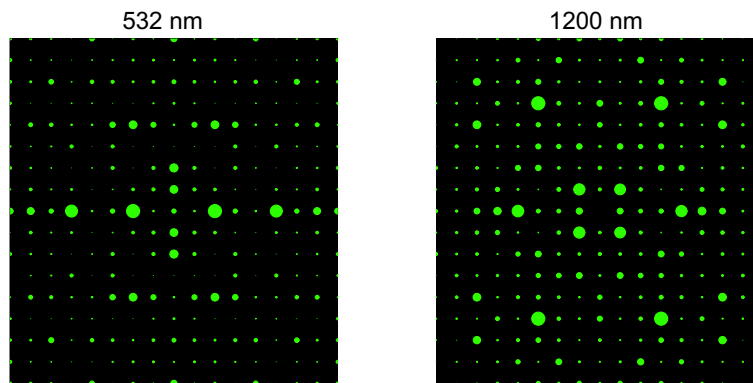


Figure 5.25: The calculated Laue diffraction patterns of a  $9\ \mu\text{m}$  thick  $2/1$  rational approximant of  $l=2\ \mu\text{m}$  rod length are shown for two selected wavelengths to illustrate the dependence of the Laue diagram on the actual wavelength.

Performing similar calculations of Laue diagrams at different wavelengths (see Fig. 5.25) clearly indicate that the Laue diagrams are also significantly depending on the photon wavelength, which is not expected in the single-scattering limit. In Fig. 5.25, two examples of Laue diagrams, namely taken at  $532\ \text{nm}$  wavelength (left) and at  $1200\ \text{nm}$  wavelength (right), are exemplarily depicted, calculated for a  $9\ \mu\text{m}$  thick sample with  $l=2\ \mu\text{m}$  rods. The obtained dependency on the photon wavelength is consistent with our previous experimental and theoretical findings as a frequency-independent behaviour of the Laue diagrams would correspond to an instantaneous response in the time domain.

This supports our interpretation that multiple photon scattering events are responsible for the unusual optical properties of icosahedral photonic quasicrystals, although the refractive index contrast of the studied polymeric (SU-8) photonic quasicrystals ( $n_{\text{SU-8}} \approx 1.58$ ) is fairly small for the standards of optics.

## 5.4 Silicon Inverse Icosahedral Photonic Quasicrystals

The observed unusual optical properties of (polymeric) icosahedral photonic quasicrystals based on multiple light scattering can be enhanced by increasing the refractive index contrast, e.g., by applying the silicon-inversion procedure [18]. This seems promising as we obviously have succeeded in fabricating high quality SU-8 icosahedral photonic quasicrystals [49], which can serve as templates. The polymer template with  $l=2\ \mu\text{m}$  rod length and the final silicon inverse icosahedral photonic quasicrystal oriented along a five-fold symmetry axis are depicted in Fig. 5.26 (a) and (b).

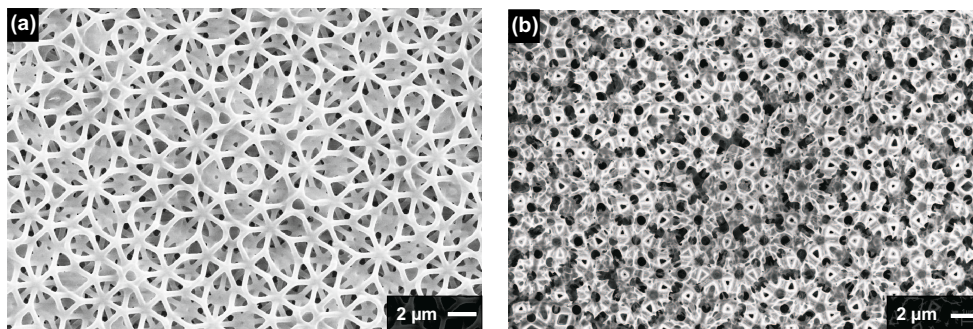


Figure 5.26: The polymer (SU-8) template (a) of the icosahedral photonic quasicrystal is successfully inverted into silicon (b). After Ref. [49].

The success of the silicon inversion is confirmed by the observed Laue diffraction pattern [49], which reveals the anticipated  $2\times 5$ -fold rotational symmetry, cf. Fig. 5.27 (a). Measurements of the time-resolved transmittance properties of only  $7\ \mu\text{m}$  thick silicon inverse samples, performed in cooperation with LENS in Florence, show a dramatic boost of multiple light scattering events within the sample as much longer temporal trailing tails are obtained than for equally thick SU-8 samples. Corresponding data are displayed in Fig. 5.27 (b) for both detection channels, namely using the same and the cross polarisation configuration.

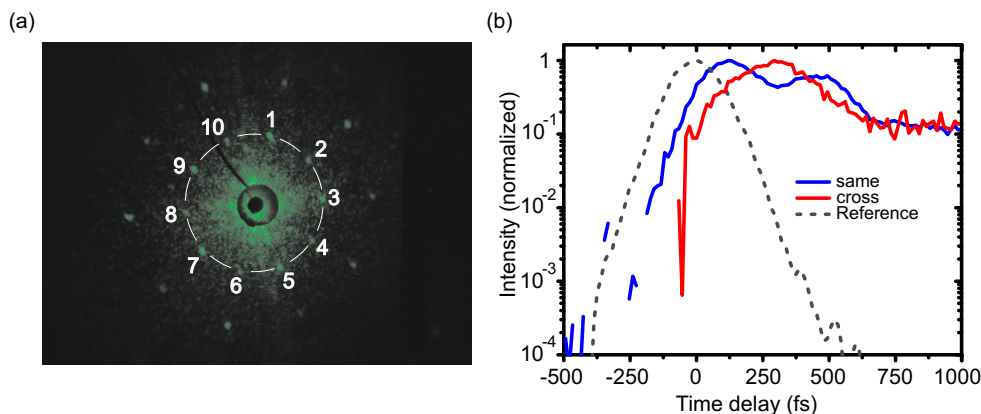


Figure 5.27: The  $2\times 5$ -fold rotationally symmetric Laue diffraction pattern of the silicon inverse icosahedral photonic quasicrystal oriented along a five-fold symmetry axis [cf. Fig. 5.26 (b)] is shown in (a). Corresponding time-resolved transmittance measurements are depicted in (b).



## Chapter 6

# Three-Dimensional Rhombicuboctahedral Photonic Quasicrystals

Electronic three-dimensional quasicrystals formed by real (metal) atoms have been found only in the icosahedral quasicrystal configuration so far [5, 45, 46]. Accordingly, all man-made, photonic and phononic three-dimensional quasicrystals following the model of electronic quasicrystals are icosahedral as well. However, the flexible fabrication method of direct laser writing allows for fabricating (almost) arbitrary three-dimensional nanostructures, as long as the final nanostructure is mechanically stable and provides appropriately connected air voids for the developer to wash out the unexposed parts of the photoresist (SU-8). Moreover, fabricating artificial photonic nanostructures by direct laser writing has the advantage over, e.g., electronic quasicrystals, of not being dependent on interparticle interactions forming merely thermodynamically stable (or meta-stable) atomic configurations and thus of not being restricted to any specific favourable quasiperiodic arrangements.

In this chapter, the blueprint of the novel class of three-dimensional *rhombicuboctahedral* quasicrystals [82], calculated via the cut-and-project method according to section 3.3, is presented (section 6.1) and realised as SU-8 photonic nanostructures (section 6.2). The anticipated rhombicuboctahedral symmetry, revealing eight-fold, three-fold and two-fold rotational symmetry axes, is demonstrated by Laue diffraction experiments (section 6.3). In the last section of this chapter, i.e., section 6.4, several experimental studies of the optical properties of three-dimensional rhombicuboctahedral photonic quasicrystals are discussed.

### 6.1 Blueprint of Three-Dimensional Rhombicuboctahedral Quasicrystals

In section 3.3, the procedure for constructing a three-dimensional quasicrystal of rhombicuboctahedral symmetry via the cut-and-project method is explained. The creation of the  $12 \times 12$ -dimensional projection matrix  $\mathcal{M}_{\text{Rhombicuboctahedral}}$  is described, which is applied to project a twelve-dimensional simple cubic periodic lattice into three-dimensional physical space.

Since rhombicuboctahedral quasicrystals represent a novel class of three-dimensional quasicrystals – in fact the second class after the icosahedral one – only recently introduced by us [82], this section is supposed to give an idea and basic understanding of the anticipated

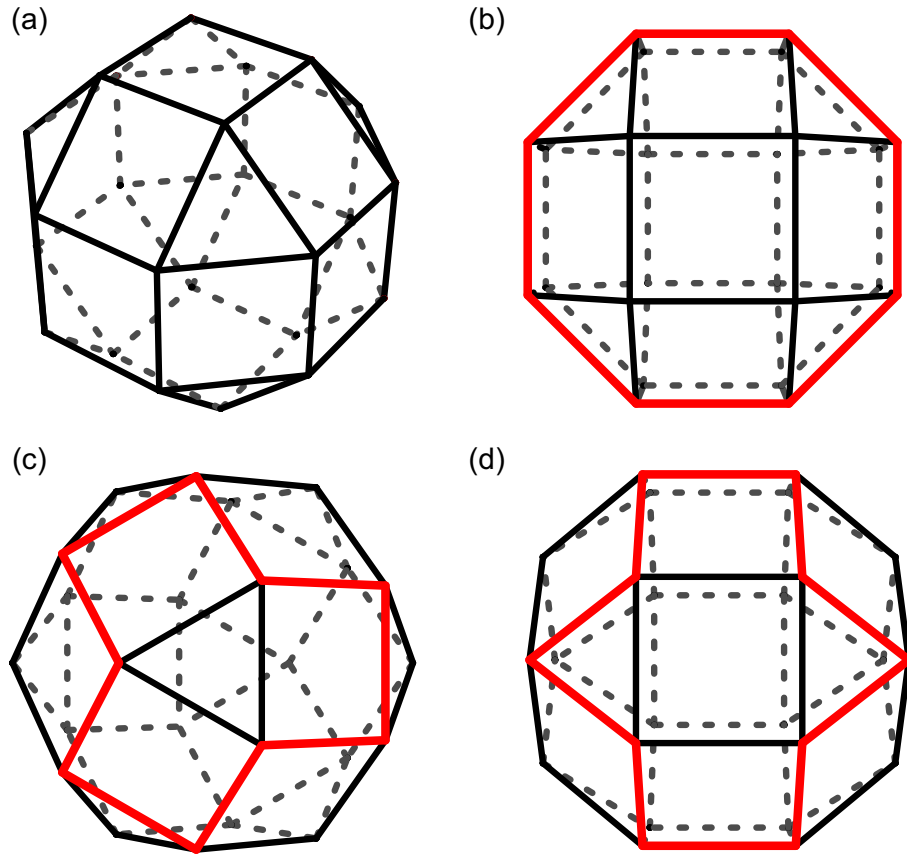


Figure 6.1: The (small) rhombicuboctahedron is depicted in four different views, in the oblique-incidence overview (a), and in three different topviews, namely along (b) an eight-fold rotational symmetry axis, (c) a three-fold rotational symmetry axis, and (d) a two-fold rotational symmetry axis. Red coloured guides to the eyes clarify the respective rotational symmetries. After Ref. [82].

complex structural configuration of such rhombicuboctahedral quasicrystals.

In Fig. 6.1, the rhombicuboctahedron, the model of the rhombicuboctahedral quasicrystal, is illustrated in oblique-incidence view (a), while graphs (b), (c) and (d) depict three specific orientations of the rhombicuboctahedron displaying its principal rotational symmetry axes, namely the eight-fold, three-fold and two-fold rotational symmetry axes.

By the use of the cut-and-project method and the appropriate projection matrix  $\mathcal{M}_{\text{Rhombicuboctahedral}}$  (cf. section 3.3), the rhombicuboctahedral symmetry is transferred to the generated (rhombicuboctahedral) quasicrystal. In particular, the anticipated unusual *eight-fold* rotational symmetry is distinctive for quasiperiodicity as this kind of symmetry is not compatible with periodic crystals. Analogue to the icosahedral photonic quasicrystals (cf. chapter 5), the constructed rhombicuboctahedral quasicrystals are composed of rods<sup>1</sup> of equal length  $l$  to guarantee a mechanically connected and stable structure which can be realised by direct laser writing. As the rhombicuboctahedral quasicrystal is generated by projecting a twelve-dimensional simple cubic periodic lattice into three-dimensional physical space via the

<sup>1</sup>The rods are the connecting lines between two projected adjacent twelve-dimensional periodic lattice points.

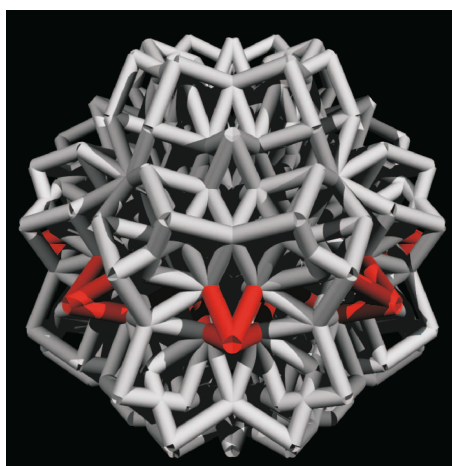


Figure 6.2: The outer boundaries of the blueprint of the three-dimensional rhombicuboctahedral quasicrystal are truncated according to the rhombicuboctahedron. The rods marked in red emphasise the unusual eight-fold rotational symmetry. After Ref. [82].

appropriate  $12 \times 12$ -dimensional projection matrix, the rods forming the rhombicuboctahedral quasicrystal point into twelve different directions, i.e., twelve rods meet at each vertex of the complex network. The corresponding blueprint is illustrated in Fig. 6.2 as computer generated ray-tracing image. The depicted piece of the rhombicuboctahedral quasicrystal contains the projected origin of the twelve-dimensional periodic lattice in its centre (cf. section 3.3), and its overall shape forms a rhombicuboctahedron (cf. Fig. 6.1). The red coloured rods highlight the eight-fold rotational symmetry.

However, to have eventually the chance of comparing the results obtained from rhombicuboctahedral quasicrystals with those of icosahedral ones (studied in chapter 5), we aim for fabricating rhombicuboctahedral quasicrystals of comparable feature sizes and of similar shape. Thus, appropriate cylindrically shaped rhombicuboctahedral quasicrystals are generated

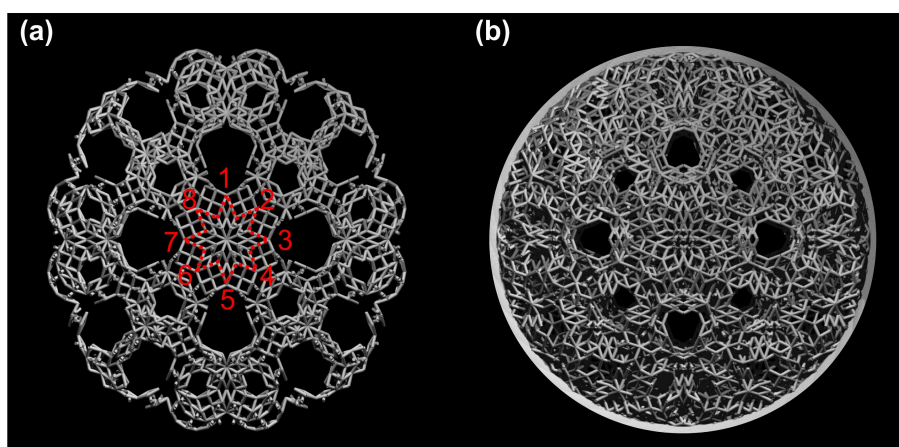


Figure 6.3: In (a), a very thin rhombicuboctahedral quasicrystal is shown as ray-tracing image. The blueprint depicted in (b) is thicker than (a) and contains (a) in its centre. In red, the eight-fold rotational symmetry is highlighted.

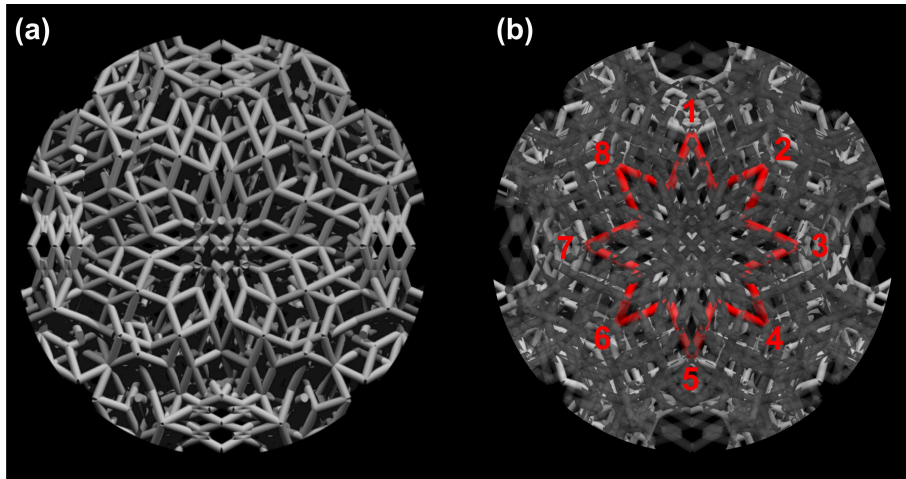


Figure 6.4: Ray-tracing images of the rhombicuboctahedral quasicrystal oriented along an eight-fold rotational symmetry axis are shown. The symmetry becomes apparent in (b) which differs from (a) as its upper layers are semi-transparent and thus, the red rods located in a lower layer are revealed. After Ref. [82].

via the cut-and-project method and corresponding ray-tracing images are shown in Fig. 6.3. The orientation is chosen along an eight-fold rotational symmetry axis, the centres of the depicted structures correspond to the projected origin  $(0,0,0,0,0,0,0,0,0,0,0,0)$  of the twelve-dimensional periodic lattice into physical space. The structure in part (a) of Fig. 6.3 is only three layers thick, revealing clearly the eight-fold rotational symmetry (highlighted in red). The structure depicted in Fig. 6.3 (b) consists of significantly more layers than (a), which makes it more difficult to observe the eight-fold rotational symmetry in this highly complex structure. Yet, as the layers of (a) form the central region of (b) the eight-fold rotational symmetry is obviously still present.

This is illustrated in Fig. 6.4, which shows the close-up view of Fig. 6.3 (b). While in Fig. 6.4 (a) the highly complex structure still seems to conceal the anticipated eight-fold rotational symmetry, in graph (b) the upper part of the structure is artificially made semi-transparent to reveal the red coloured rods which clearly demonstrate the eight-fold symmetry.

## 6.2 Fabrication of High-Quality SU-8 Samples

The purpose of the previous section was to illustrate the blueprint of the three-dimensional rhombicuboctahedral quasicrystals by generating several ray-tracing images following the cut-and-project method (cf. section 3.3). Having rationally constructed these blueprints, they can be realised as polymer (SU-8) nanostructures by means of direct laser writing. In chapter 5, dealing with three-dimensional icosahedral photonic quasicrystals, we have already shown that direct laser writing is a suitable technique to fabricate complex porous three-dimensional nanostructures.

In order to have feature sizes comparable to those of the studied icosahedral photonic quasicrystals, we chose the rod length  $l$  as  $l=3 \mu\text{m}$ . As twelve rods meet at each vertex of the rhombicuboctahedral quasicrystals rather than six rods as in the case of icosahedral quasicrystals, the rod length is slightly increased from  $l=2 \mu\text{m}$  to  $l=3 \mu\text{m}$  to reduce the risk of unwanted

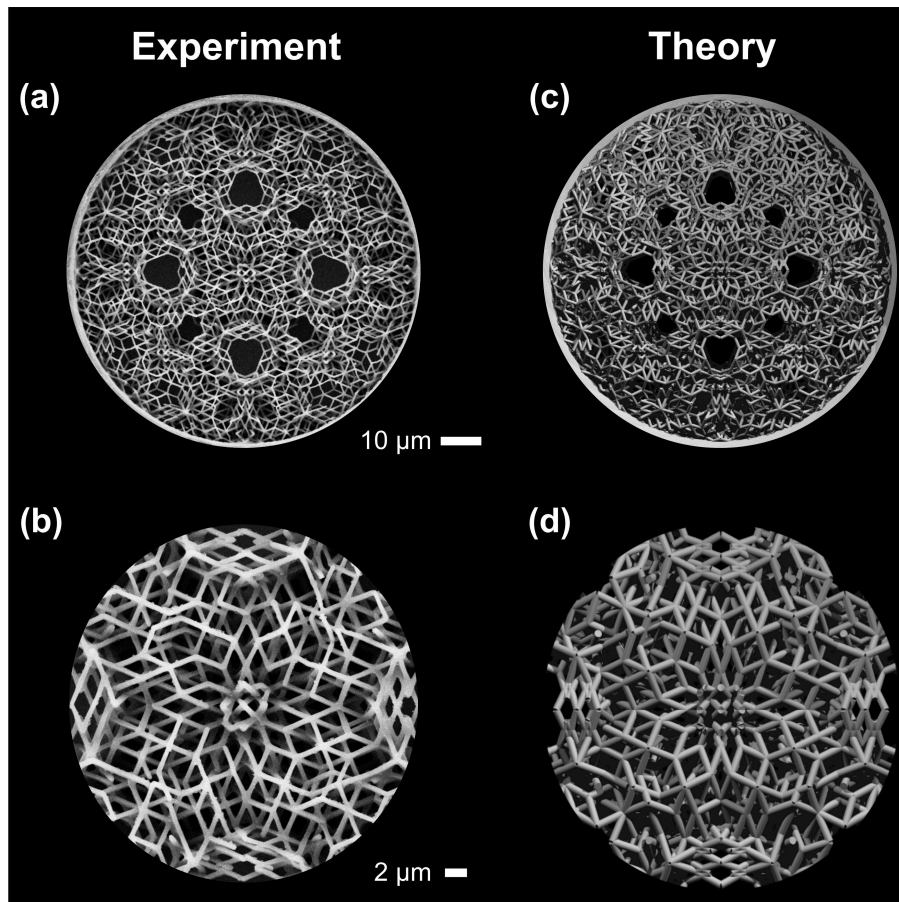


Figure 6.5: In the left column, i.e., (a), (b), SEM images of the fabricated rhombicuboctahedral photonic quasicrystals are depicted, which can be directly compared with the ray-tracing images (blueprints) in the right column, i.e., (c) and (d). (b) and (d) show close-up views of (a) and (c), magnifying the central part of the structure. After Ref. [82].

fusion of the elliptically shaped rods<sup>2</sup> in axial direction. Possible distortions of the fabricated nanostructures due to shrinkage of SU-8 during development are reduced by surrounding the nanostructures with a thick stabilising cylindrical wall.

In Fig. 6.5 (a) and (b), a correspondingly fabricated rhombicuboctahedral quasicrystal oriented along the eight-fold rotational symmetry axis with a diameter of 86  $\mu\text{m}$  and a thickness of about 11.5  $\mu\text{m}$  is illustrated by means of electron micrographs. Graph (b) gives a magnified view of the central part of (a). For comparison corresponding ray-tracing images following the blueprint of the structure are depicted in (c) and (d), which demonstrates the high precision of the fabrication method and the high quality of the fabricated samples.

To allow for a complete characterisation of the rhombicuboctahedral quasicrystals, similar samples are fabricated, yet with the surface normal pointing along a three-fold and along a two-fold rotational symmetry axis. Corresponding SEM graphs are depicted in Fig. 6.6. The rod length  $l$  is  $l=3 \mu\text{m}$ , the diameter about 86  $\mu\text{m}$  and the thickness is about 10  $\mu\text{m}$  for the three-fold axis sample and about 11  $\mu\text{m}$  for the two-fold axis sample.

<sup>2</sup>Due to direct laser writing, the voxels composing the rods are elongated in axial direction, cf. section 4.1 and chapter A of the appendix.

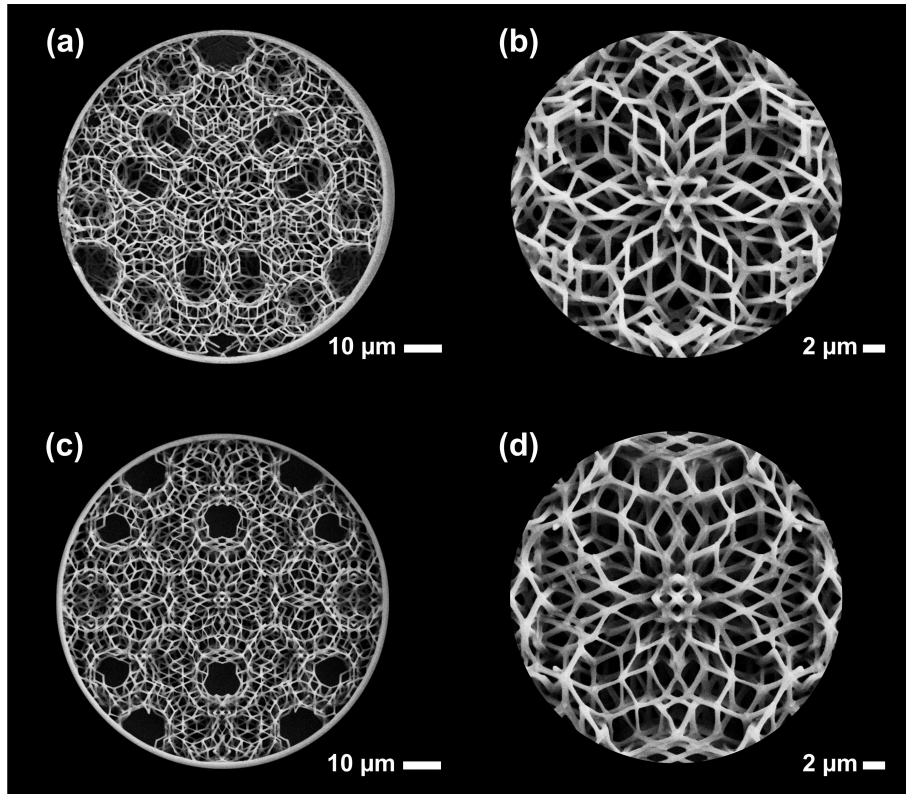


Figure 6.6: SEM images of rhombicuboctahedral photonic quasicrystals fabricated along a three-fold rotational symmetry axis (a), (b) and along a two-fold rotational symmetry axis (c), (d) are shown. (b) and (d) are close-up views of (a) and (c), magnifying the central part of the respective structures.

All SEM images shown in Fig. 6.5 and Fig. 6.6 demonstrate the high quality of the fabricated three-dimensional rhombicuboctahedral photonic quasicrystals with nicely ordered, well-aligned and smooth rods.

### 6.3 Laue Diffraction Patterns

As already known from icosahedral photonic quasicrystals, Laue diffraction experiments are very useful to investigate the overall rotational symmetry of the fabricated samples. Using the setup described in section 4.2.1, the Laue diagrams of several rhombicuboctahedral quasicrystals, oriented along an eight-fold, a three-fold or a two-fold rotational symmetry axis, of rod length  $l=3\ \mu\text{m}$ , with a diameter of  $86\ \mu\text{m}$  and with thicknesses between  $10\ \mu\text{m}$  and  $11.5\ \mu\text{m}$  (depending on the actual orientation) are taken with red light from a Helium-Neon laser. The SEM images of the respective rhombicuboctahedral quasicrystals are depicted in Fig. 6.5 and Fig. 6.6 of the previous section. The corresponding Laue diagrams are shown in Fig. 6.7 and reveal the anticipated symmetries consistent with rhombicuboctahedral symmetry [82]. To further investigate the rotational symmetry aspect, the measured Laue diagrams (left column of Fig. 6.7) are compared with corresponding calculations (right column) using the cut-and-project method<sup>3</sup>: To compute the Laue diagrams, the reciprocal lattice of the twelve-dimensional

<sup>3</sup>Note that the cut-and-project method assumes single scattering and neglects the connecting rods.

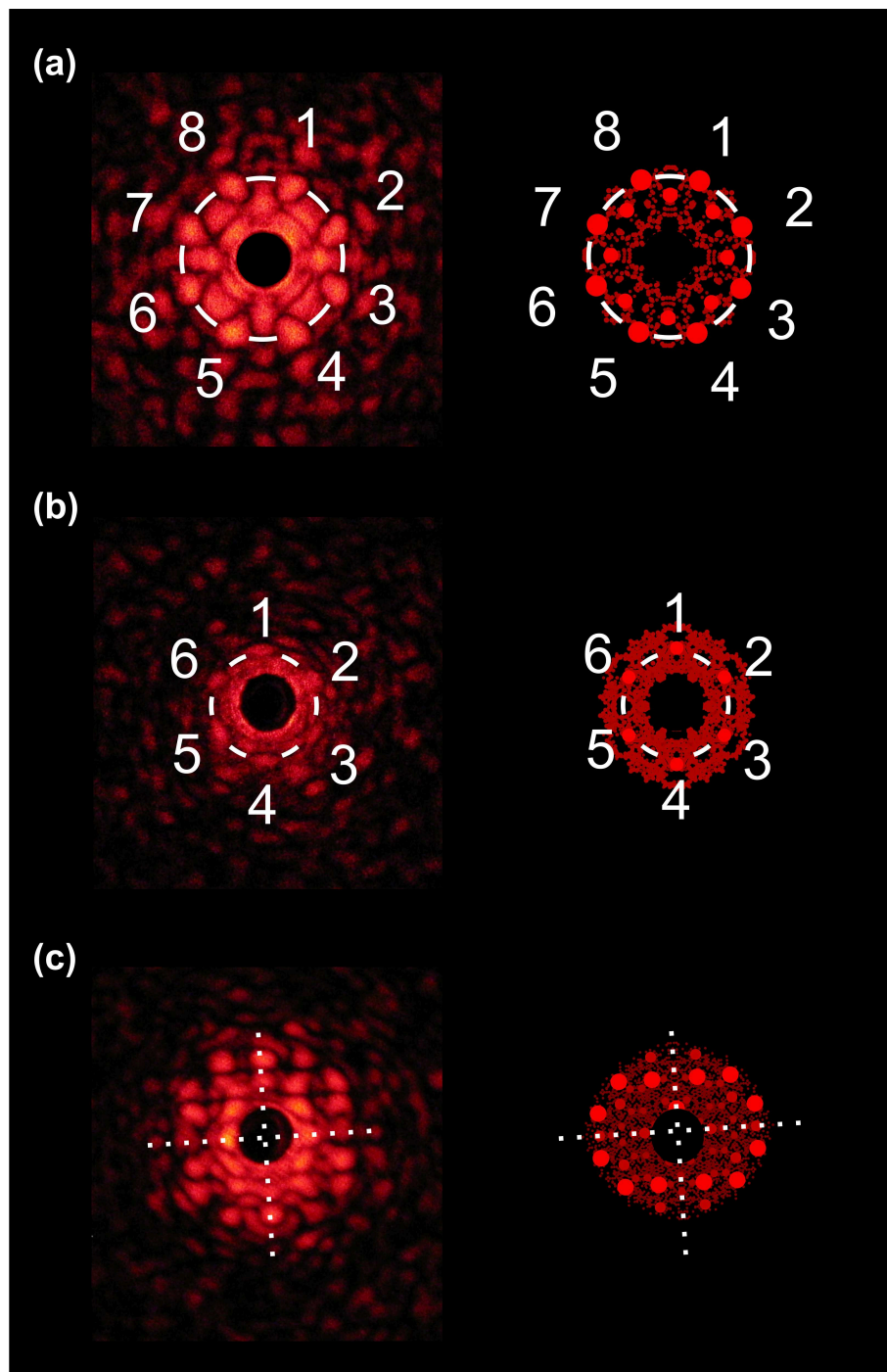


Figure 6.7: Laue diagrams of three-dimensional rhombicuboctahedral photonic quasicrystals are depicted which reveal the anticipated (a) eight-fold rotational symmetry, (b) six-fold rotational symmetry, and (c) two-fold rotational symmetry, for the samples oriented along the eight-fold [cf. Fig. 6.5 (a), (b)], three-fold [cf. Fig. 6.6 (a), (b)] and two-fold rotational symmetry axis [cf. Fig. 6.6 (c), (d)], respectively. In the left column, measured Laue diagrams taken with visible light are shown. Corresponding calculated Laue diagrams are depicted in the right column: the diameter and the brightness of the red spots are a measure of the intensity and, for reasons of clarity, spots below a certain intensity are not shown. As the undiffracted beam is blocked in the experiment, the corresponding area is blacked out in the calculations. After Ref. [82].

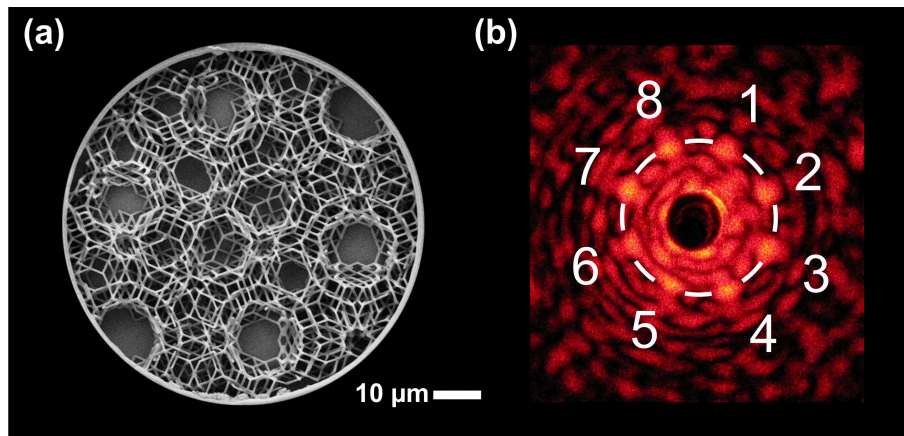


Figure 6.8: In (a), the SEM graph of a rhombicuboctahedral photonic quasicrystal oriented along the eight-fold rotational symmetry axis is depicted which does not contain the projected origin of the twelve-dimensional periodic lattice, i.e., the single point of exact rhombicuboctahedral symmetry. The measured Laue diagram (b) of this structure reveals the unusual eight-fold rotational symmetry. After Ref. [82].

simple cubic periodic lattice is projected into three-dimensional physical reciprocal  $k$ -space, yielding a pattern of densely arranged spots. The intensity  $I$  of each spot is related to the square of the Fourier transform of the nine-dimensional sphere of diameter  $\Delta$  which approximates the nine-dimensional acceptance domain, i.e.,  $I \propto \text{sinc}^2(\pi k \Delta)$ , where  $k$  is the modulus of the nine-dimensional internal reciprocal  $k$ -space vector of the spot (cf. section 5.1). The overall agreement between measured and calculated Laue diagrams is very nice, which demonstrates our success in fabricating high-quality quasicrystals of rhombicuboctahedral symmetry.

Yet, to rule out that the observed rotational symmetries, in particular the unusual eight-fold rotational symmetry which clearly indicates quasiperiodicity, are not caused by the single point of exact rhombicuboctahedral symmetry (i.e., the projection of the origin of the twelve-dimensional simple cubic periodic lattice) which lies in the centre of all the previously studied samples, a control sample is fabricated which does not contain this specific point. The corresponding rhombicuboctahedral quasicrystal oriented along an eight-fold rotational symmetry axis is depicted in Fig. 6.8 (a) and has a rod length  $l$  of  $l=3 \mu\text{m}$ , a thickness of  $6 \mu\text{m}$  and a diameter of  $76 \mu\text{m}$ . The measured Laue diagram in Fig. 6.8 (b) shows clearly the eight-fold rotational symmetry. Hence, we are confident that the rhombicuboctahedral symmetry is indeed caused by the long-range quasiperiodic order of the rhombicuboctahedral quasicrystals.

Additionally, we have examined the Laue diffraction patterns of thicker samples. Very similar to the experimental findings observed for icosahedral photonic quasicrystals (cf. section 5.1), an increase of the sample thickness makes it more difficult to discern the various diffraction spots. Presumably, this can be ascribed to multiple scattering effects, analogously to the icosahedral photonic quasicrystals. In thicker samples, the laser beam is scattered multiple times at an increased number of scattering centres, transferring intensity into many different diffraction orders, even into such which have quite low intensity in thinner samples. Additionally, sample imperfections and distortions might also become an issue in thicker samples and might lead to unwanted diffusive scattering.

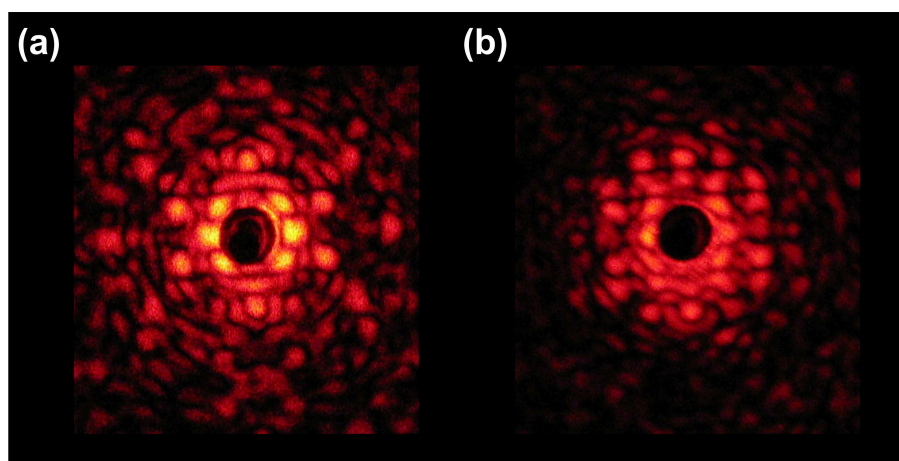


Figure 6.9: The measured Laue diagram of the rhombicuboctahedral quasicrystal oriented along a two-fold rotational symmetry axis of only 5  $\mu\text{m}$  thickness is depicted in (a), that of a 10  $\mu\text{m}$  thick sample in (b), taken with red laser light. The patterns are different in terms of the actual intensity of the individual Laue diffraction spots.

The influence of the sample thickness is exemplarily depicted in Fig. 6.9, for the case of a two-fold rotationally symmetric rhombicuboctahedral photonic quasicrystal. The rod length  $l$  is  $l=3 \mu\text{m}$ , the diameter  $86 \mu\text{m}$ , the thickness only 5  $\mu\text{m}$  in (a) and about 10  $\mu\text{m}$  in (b). Obviously, some of the Laue diffraction spots of (a) decrease in intensity, in particular the six yellowish appearing spots in the inner ring, and others gain in strength in thicker samples, cf. Fig. 6.9 (b). This demonstrates the transfer of intensity into higher diffraction orders due to multiple light scattering.

## 6.4 Experimental Studies of Optical Properties

The novel class of three-dimensional quasicrystals, namely the rhombicuboctahedral photonic quasicrystals, are expected to reveal optical properties quite similar to the icosahedral ones, concerning the impact of multiple light scattering. The Laue diffraction experiments have already indicated the importance of multiple scattering events, as the obtained Laue diagrams do depend on the thickness of the studied samples (cf. section 6.3).

The transmittance and reflectance spectra of three-dimensional rhombicuboctahedral photonic quasicrystals of rod length  $l=3 \mu\text{m}$  are measured in an optical setup similar to that described in section 4.2.3, i.e., the setup comprises a combination of an FTIR-spectrometer and an infrared microscope with cassegrain microscope objectives, yet it offers an increased spectral range of detection. The obtained transmittance and reflectance spectra are normalised to the bare glass substrate and a silver mirror, respectively. The respective orientations of the fabricated rhombicuboctahedral photonic quasicrystals are chosen such that the surface normal points along one of the principal rotational symmetry axes, i.e., along an eight-fold, a three-fold and a two-fold symmetry axes. Intrinsic molecular absorptions of the photoresist SU-8 are indicated in the spectra. A typical set of measured data obtained from samples of about 11  $\mu\text{m}$  thickness (cf. Fig. 6.5 and Fig. 6.6) is depicted in Fig. 6.10, which shows low reflectance (below 3 %) over a broad spectral range (1.5  $\mu\text{m}$  to 6  $\mu\text{m}$  wavelength) and low transmittance (about

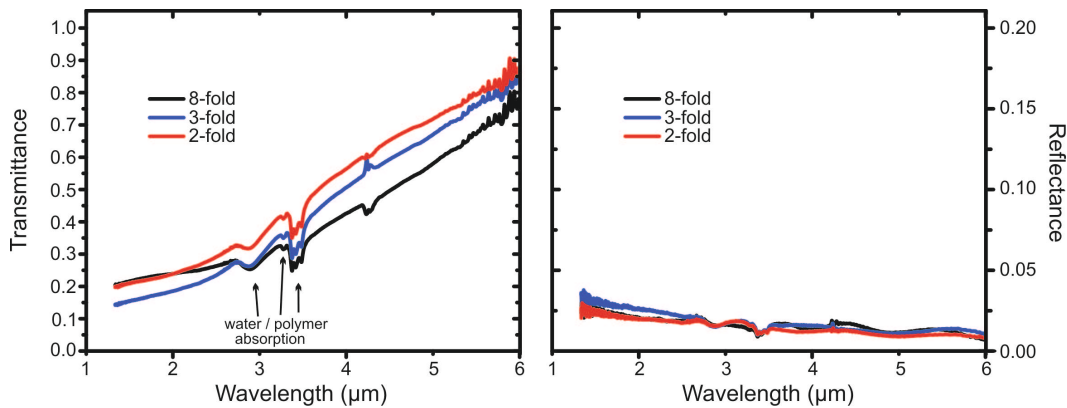


Figure 6.10: Measured transmittance (left) and reflectance (right) spectra of rhombicuboctahedral photonic quasicrystals with rod length  $l=3\ \mu\text{m}$  and thickness of about  $12\ \mu\text{m}$  are shown. The orientation of the samples, i.e., if the surface normal points along an eight-fold, a three-fold, and a two-fold rotational symmetry axis, is depicted in the graphs.

20%) from  $1.5\ \mu\text{m}$  to  $3\ \mu\text{m}$  wavelength, which increases up to 90% on the long wavelength side, very similar to the spectra obtained from icosahedral photonic quasicrystals. The rather low transmittance and reflectance is probably the result of strong (multiple) scattering into the residual solid angle, since the cassegrain microscope objectives probe the samples and detect the light emerging from the sample only within the cone from  $15^\circ$  to  $30^\circ$ . The orientation of the samples does apparently not influence the measured spectra very much. Yet, drawing any conclusions from that is very difficult, as one has to keep in mind that the orientation of the sample does not coincide with the direction of the measurement due to the design of the cassegrain microscope objectives. Furthermore, as already learned from icosahedral photonic quasicrystals, the interpretation of such transmittance and reflectance spectra is very challenging due to averaging over several angles in the measurements, namely from  $15^\circ$  to  $30^\circ$ . This averaging presumably conceals many anticipated features, particularly since the reciprocal space of quasicrystals consists in principle of a dense set of reciprocal lattice vectors, which can all contribute to diffraction. The low transmittance and reflectance for short wavelengths (shorter than  $3\ \mu\text{m}$ ) indicate such light scattering caused by many different (more and less significant) reciprocal lattice vectors.

The impact of multiple scattering of light is also revealed in time-resolved transmittance measurements. The experimental setup used for these measurements is similar to that described in section 4.2.2. It is based on upconverting the transmitted signal with the reference pulse using a nonlinear BBO crystal and recording the upconverted signal as a function of the time delay. Yet, in this particular setup, the central wavelength of the incident Gaussian pulse is at  $800\ \text{nm}$  (rather than  $1500\ \text{nm}$ ), the pulse duration is about  $120\ \text{fs}$ , and the signal is detected within the rather small finite half opening angle of only  $7^\circ$ . This setup has been built-up in our group by M. Kallenberg [95] and is currently operated by M. Renner, who performed the time-resolved transmittance experiments on the rhombicuboctahedral photonic quasicrystals.

For time-resolved transmittance spectroscopy, we rather use samples of  $l=2\ \mu\text{m}$  instead of  $l=3\ \mu\text{m}$  rod length, as the fundamental pseudo-stop band is naively expected at  $\lambda \approx 2 \cdot l$  wavelength and thus even for  $l=2\ \mu\text{m}$ , the Gaussian pulses of  $800\ \text{nm}$  central wavelength already probe high photonic bands. Using samples of  $l=2\ \mu\text{m}$ , the experimental results are supposedly better

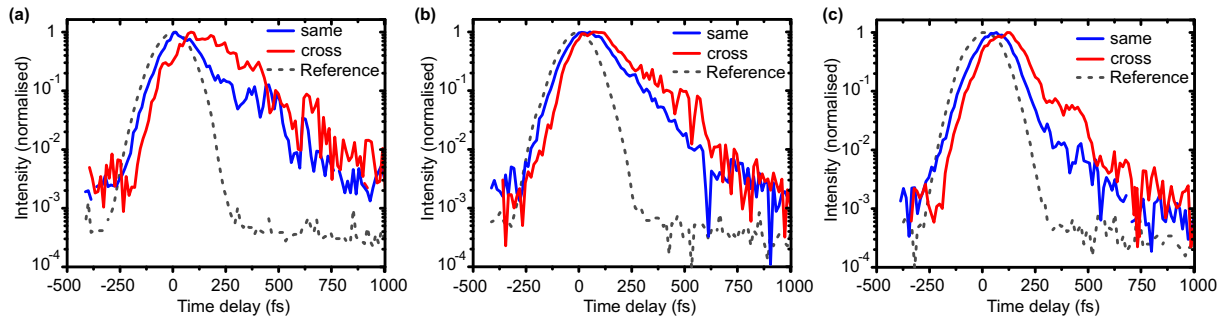


Figure 6.11: Measured time-resolved transmittance spectra of rhombicuboctahedral photonic quasicrystals with rod length  $l=2\ \mu\text{m}$  and thicknesses of  $18\ \mu\text{m}$  oriented along (a) an eight-fold, (b) a three-fold and (c) a two-fold rotational symmetry axis are shown, taken with a 120 fs Gaussian pulse at 800 nm central wavelength. The data are measured in the same (blue) and cross (red) polarisation configuration. The reference pulse (dashed line) displays the autocorrelation of the setup taken without sample, the pulse maximum is at zero time delay.

comparable to those of the icosahedral photonic quasicrystals of section 5.2.2. The measured transmittance and reflectance spectra of rhombicuboctahedral photonic quasicrystals of  $l=2\ \mu\text{m}$  rod length are similar to those depicted in Fig. 6.10, appropriately scaled.

A set of differently oriented rhombicuboctahedral photonic quasicrystals with rod length  $l=2\ \mu\text{m}$ , diameter of  $74\ \mu\text{m}$  and thickness of  $18\ \mu\text{m}$  is studied in Fig. 6.11. One clearly observes a shift of the pulse maximum and the occurrence of a trailing tail for both detection channels, i.e., using the same and the cross polarisation configuration, and for all three principal symmetry directions. For the eight-fold rotational symmetry (a), the decay time constant is about 140 fs for the same and the cross polarisation configuration, the delays of the pulse maxima are about 20 fs and 120 fs, respectively. For the three-fold rotational symmetry (b), the decay time constant is about 135 fs for the same and the cross polarisation configuration, the delays of the pulse maxima are about 20 fs and 100 fs, respectively. For the two-fold rotational symmetry (c), the decay time constant is about 90 fs for the same and the cross polarisation configuration, the delays of the pulse maxima are about 40 fs and 130 fs, respectively.

Although the data depicted in Fig. 6.11 are normalised to the respective pulse maxima, the measured raw data provide the possibility to compare the intensities obtained in the same and the cross polarisation configuration. In (a), the pulse maximum of the cross polarisation configuration is one order of magnitude less in intensity than that of the same polarisation configuration, in (b), both intensities are comparable and in (c), the cross polarisation configuration is again about one order of magnitude less in intensity. Yet, this clearly demonstrates the strong depolarising character of the samples due to significant multiple photon scattering, i.e., the polarisation state of the light is modified such that a substantial amount of light is detected in the cross polarisation configuration.

The delay of the pulse maxima and the occurrence of trailing tails are dependent on the sample thickness, as expected when multiple scattering is the origin of these phenomena. In particular, the observed effects are reduced when the sample thickness is reduced, as illustrated in Fig. 6.12 (a). In this graph, the time-resolved transmittance spectrum of the eight-fold rotationally symmetric rhombicuboctahedral photonic quasicrystal of  $l=2\ \mu\text{m}$ , diameter of  $74\ \mu\text{m}$  and thickness of only  $10\ \mu\text{m}$  is shown, which is to be compared to its thicker version in Fig. 6.11 (a). In the thin sample [Fig. 6.12 (a)], the decay time constant of the same polarisation configuration

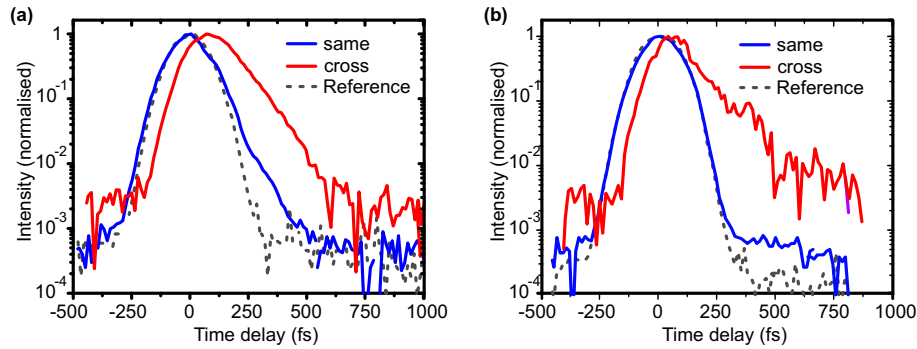


Figure 6.12: Measured time-resolved transmittance spectra of rhombicuboctahedral photonic quasicrystals oriented along an eight-fold rotational symmetry axis with (a) a rod length  $l=2\ \mu\text{m}$  and a thickness of  $10\ \mu\text{m}$ , and (b) a rod length  $l=3\ \mu\text{m}$  and a thickness of  $15\ \mu\text{m}$ , are depicted, taken with a 120 fs Gaussian pulse at 800 nm central wavelength. The data are measured in the same (blue) and cross (red) polarisation configuration. The reference pulse (dashed line) displays the autocorrelation of the setup taken without sample. The pulse maximum of the autocorrelation defines zero time delay.

is strongly reduced to only 75 fs (compared to 140 fs of the thicker version), yet only slightly reduced to 120 fs in the cross polarisation configuration. Furthermore, in Fig. 6.12 (a), the pulse maxima are less delayed compared to the thicker sample of Fig. 6.11 (a), namely only by 60 fs in the cross polarisation configuration and less than 14 fs (the resolution of the setup) in the same polarisation configuration. In Fig. 6.12 (a), the intensity of the pulse maximum in the same polarisation configuration is one order of magnitude higher than in the cross polarisation configuration, which is also the case in the thicker sample [Fig. 6.11 (a)].

In Fig. 6.12 (b), a rhombicuboctahedral photonic quasicrystal with (increased) rod length  $l=3\ \mu\text{m}$ , oriented along the eight-fold rotational symmetry axis is studied. The sample has a thickness of  $15\ \mu\text{m}$ , i.e., it is comparable to that of Fig. 6.12 (a) in terms of the number of scattering centres along the propagation direction of the probing Gaussian pulse. Yet, the effect on the transmitted pulse is different from that in (a): In the same polarisation configuration, the pulse does not develop a trailing tail at all, the maximum is delayed less than 14 fs (the resolution of the setup). In the cross polarisation configuration, the trailing tail exhibits a time constant of about 150 fs, which is slightly larger than in (a), the pulse maximum is delayed by 100 fs, slightly more than in (a). In Fig. 6.12 (b), the intensities of the pulse maxima in the cross polarisation and same polarisation configuration are comparable, i.e., they have the same order of magnitude, while in Fig. 6.12 (a) the difference in intensity is about one order of magnitude. The obvious difference in the temporal response between Fig. 6.12 (a) and (b) is not surprising, as by increasing the rod length  $l$  from  $l=2\ \mu\text{m}$  to  $l=3\ \mu\text{m}$ , the respective band structure is scaled accordingly by the factor of 1.5, yet the central wavelength of the Gaussian pulse is kept at 800 nm. Thus, the Gaussian pulse actually probes different high-order photonic bands in (a) and (b).

Due to multiple light scattering within the long-range ordered quasicrystal, the temporal behaviour of the transmitted pulse is expected and found to be dependent on the characteristics of the actually probed photonic bands. Rather than fabricating several samples of different rod lengths (cf. Fig. 6.12), it is more favourable to study one sample and to change the central wavelength of the incident linearly polarised Gaussian pulse. Corresponding measurements are illustrated in Fig. 6.13 for different central wavelengths (increasing from left to right),

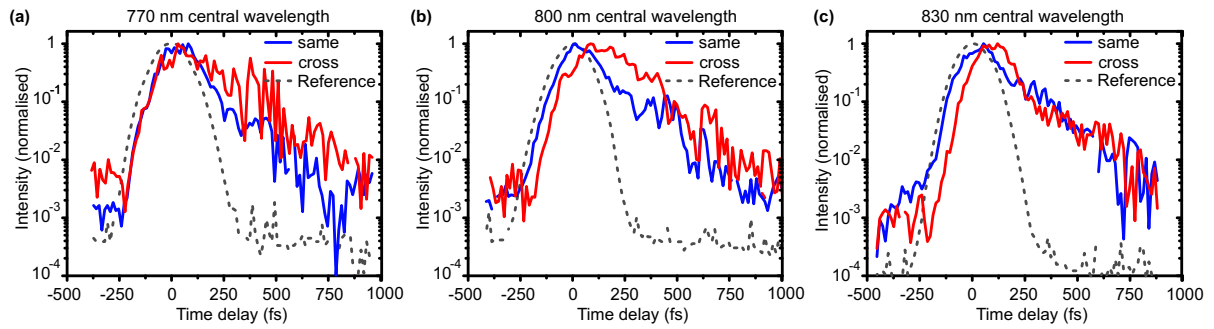


Figure 6.13: Measured time-resolved transmittance spectra of rhombicuboctahedral photonic quasicrystals of  $l=2$   $\mu\text{m}$  rod length and of  $18 \mu\text{m}$  thickness oriented along an eight-fold rotational symmetry axis are depicted, which are taken with a 120 fs Gaussian pulse at (a) 770 nm, (b) 800 nm and (c) 830 nm central wavelength. The data are measured in the same (blue) and cross (red) polarisation configuration. The reference pulse (dashed line) displays the autocorrelation of the setup measured without sample. The pulse maximum of the autocorrelation defines zero time delay.

namely for (a) 770 nm, (b) 800 nm and (c) 830 nm central wavelength. In the same polarisation configuration, the delay of the pulse maximum changes from about 30 fs (a) to 20 fs (b) to approximately 50 fs (c), the respective time constants are (a) 110 fs (b) 140 fs and (c) 135 fs. In the cross polarisation configuration, the delays are about 30 fs in (a), 120 fs in (b) and 110 fs in (c), the corresponding decay time constants are 160 fs, 140 fs and 130 fs, respectively. The intensity of the respective pulse maxima for same and cross polarisation configuration differs in (a) and (b) by one order of magnitude, while it is comparable in (c), emphasising the strong depolarisation of the transmitted pulse.

In conclusion, the experimental studies on rhombicuboctahedral photonic quasicrystals indicate that multiple scattering of light apparently plays a crucial role for their optical properties, very similar to icosahedral photonic quasicrystals. This is not surprising as in general quasiperiodicity is associated with a densely filled reciprocal space providing a great variety of reciprocal lattice vectors for multiple diffraction. However, as the structural configuration of the two classes of three-dimensional photonic quasicrystals, the icosahedral and the rhombicuboctahedral one, is obviously different – the Laue diagrams reveal different high-degree rotational symmetries – we simultaneously expect subtle differences in their respective peculiar optical properties.

Various studies on different classes of two-dimensional photonic quasicrystals composed of different kinds of tilings and thus exhibiting different kinds of rotational symmetries (e.g., eight-fold, ten-fold or twelve-fold rotational symmetries) support our expectation. It has been shown that the minimal distance between two vertices of the quasiperiodic pattern with respect to the tiling's edge length (the rod length) is decisive for the formation mechanism of the band structure, i.e., if the mechanism is dominated by Bragg scattering or by strong resonances of the individual scattering objects [46]. Accordingly, the obtained optical properties of the two-dimensional quasicrystals will be different, e.g., the mode profiles and the waveguiding properties.

However, to investigate this aspect for three-dimensional quasicrystals, more experimental

work is necessary to compare the peculiar behaviour of icosahedral and rhombicuboctahedral photonic quasicrystals in more detail. Furthermore, a theoretical model for calculating the anticipated optical properties of (ideal) rhombicuboctahedral quasicrystals is also clearly desirable in this context. Therefore, we propose a model similar to that introduced in section 5.3 for icosahedral photonic quasicrystals, based on a combination of the scattering matrix formalism and the rational approximant approach. Rational approximants of rhombicuboctahedral quasicrystals could be constructed using the so-called Pell numbers for successively approximating the silver ratio (cf. chapter 3).

# Chapter 7

## Conclusions and Outlook

Photonic quasicrystals have a peculiar and unique structure. They exhibit long-range order and well-defined high-degree rotational symmetries, yet are not periodic. In Fourier space this translates into a dense set of reciprocal lattice vectors. Thus, photonic quasicrystals promise interesting photonic band structure characteristics and fascinating optical phenomena.

In this thesis, we have fabricated two classes of three-dimensional photonic quasicrystals, icosahedral and rhombicuboctahedral ones, and have investigated their optical properties. The respective quasiperiodic networks were calculated via the cut-and-project method and were realised as polymeric (SU-8) samples by applying the technique of direct laser writing. The quasiperiodic networks are composed of rods to guarantee the mechanical stability of the fabricated photonic quasicrystals. The rods have equal length of few  $\mu\text{m}$ , so that the photonic quasicrystals exhibit interesting optical characteristics and the anticipated fundamental pseudo-stop bands at infrared wavelengths. Appropriate rotations of the quasiperiodic patterns during the calculations offer the possibility to study the accordingly fabricated photonic quasicrystals along all of their respective principal rotational symmetry axes.

For characterising the quality of the fabricated three-dimensional photonic quasicrystals, scanning electron microscopy and visible-light Laue diffraction experiments were applied. The anticipated Laue diagrams were calculated using the cut-and-project method and revealed good agreement with the measured ones. This demonstrated our success in fabricating high-quality three-dimensional photonic quasicrystals for infrared frequencies. Furthermore, we studied their optical properties in transmittance and reflectance experiments and via time-resolved transmittance spectroscopy. Appropriate scattering matrix calculations were applied to evaluate the experimental findings.

In the first part of this thesis, we focused on three-dimensional *icosahedral* photonic quasicrystals. This class is already known from electronic systems since 1984, yet several aspects of its peculiar properties are still not completely understood. The measured Laue diagrams of our photonic quasicrystals revealed the anticipated ten-fold, six-fold and two-fold rotational symmetries consistent with icosahedral symmetry. Yet unsuspectedly, with increasing thickness of the samples, the Laue diagrams developed a speckle-like background, reminiscent of disorder-induced diffusive scattering. Furthermore, the individual Laue diffraction spots became sharper. Thus, increasing the thickness made it more difficult to discern the overall symmetry of the patterns. Icosahedral photonic quasicrystals are expected to yield a photonic band

structure with a fundamental pseudo-stop band at a spectral position of about twice the rod length. The anticipated pseudo-stop band presented itself as a significant peak in the measured reflectance spectra at the adequate spectral position. The spectral position of the peak shifted accordingly when the effective refractive index or the rod length was changed.

However, the experimental studies of the optical properties revealed further unexpected features – usually attributed to disordered photonic systems. The sum of the transmittance and reflectance, measured within a rather small opening angle, was well below unity, i.e., a significant amount of light was scattered into the residual solid angle not detected in the experimental setup. In addition, time-resolved transmittance spectroscopy showed that transmitted femtosecond pulses were strongly delayed and developed a diffusive-like exponentially decaying trailing tail. The actual values of the exponential decay time constants and the temporal shifts were found to be dependent on the sample thickness and on the central wavelength of the probing pulse. The transmitted pulses were strongly depolarised, i.e., a substantial amount of the incident linearly polarised light had changed its polarisation state.

For a decent interpretation of the experimental results, we developed a theoretical model based on the rational approximant approach combined with scattering matrix calculations. Thereby, we were able to derive the anticipated optical properties of *ideal* three-dimensional icosahedral photonic quasicrystals.

The reliability of this approach was confirmed by fabricating icosahedral photonic quasicrystals and corresponding rational approximants of different unit cell sizes via direct laser writing and by comparing the measured and calculated angle-resolved transmittance spectra. With increasing unit cell size, the experimentally obtained spectra of the rational approximants converged rapidly to that of the quasicrystal. Furthermore, the experimental data agreed well with the corresponding scattering matrix calculations.

In subsequently performed adequate scattering matrix calculations, we could reproduce qualitatively all of the previously mentioned experimentally observed phenomena – without attempting any fitting. The peculiar temporal behaviour of the transmitted pulses, i.e., the strong delay of the pulse maximum, the development of the trailing tail and the depolarisation of the transmitted light, was confirmed. Additionally, we could demonstrate the dependency of pulse delay and trailing tail on both, on the sample thickness and on the central wavelength of the probing pulse (i.e., on the characteristics of the actually probed photonic bands) throughout a broad spectral range. Light that is scattered many times is delayed more strongly than light that is scattered only few times, which leads to the observed wavelength- and thickness-dependent temporal response. Calculated transmittance and reflectance spectra confirmed the existence of a photonic pseudo-stop band at the spectral position of twice the rod length. These spectra also indicated that multiple scattering of light is important to understand the unusual optical properties of icosahedral photonic quasicrystals: a substantial amount of light is diffracted into numerous (high-order) diffraction orders. Thus, only when collecting all of the various diffraction orders in forward and backward direction, the sum of transmittance and reflectance will be unity. The calculations also revealed rather narrow spectral features in a broad spectral range. Due to multiple photon scattering inside the icosahedral photonic quasicrystals, complicated spatial pathways of the photons interfere either mostly constructively or destructively, depending sensitively on the actual wavelength. We were able to experimentally demonstrate the occurrence of such narrow spectral features – the equivalent to the long response observed

in the time domain – after constructing a dedicated normal incidence setup with an almost ideal incident plane wave. The speckle-like background evolving in the Laue diagrams with increasing sample thickness was reproduced by scattering matrix calculations as well. With increasing thickness, more and more intensity is transferred into various (formerly low-intensity) high-order diffraction spots due to multiple scattering effects. Our theoretical studies also indicated that it might be promising to explore the distinct temporal behaviour of individual Laue diffraction spots in more detail via appropriate time-resolved transmittance spectroscopy experiments.

Theoretical studies of the total transmittance versus sample thickness revealed that the photon transport mechanism of icosahedral photonic quasicrystals differs from that of disordered photonic systems and of periodic photonic crystals. For many wavelengths, we found that the total transmittance dropped down within some thickness range to a finite constant value. This value presumably represents the fraction of light that is scattered in forward direction to form the Laue diagram, which in principle consists of a dense set of diffraction spots with an overall hierarchical intensity distribution.

To summarise this part of the thesis, the scattering matrix calculations showed that ideal three-dimensional icosahedral photonic quasicrystals mimic a diffusive behaviour which is usually known from disordered photonic systems, due to multiple scattering of light within these complex, yet long-range ordered structures. This was also observed in the performed experiments. Moreover, multiply scattered light is important to understand the peculiar optical properties of icosahedral quasicrystals even for polymeric ones with a fairly small refractive index contrast. Yet, the properties of photonic quasicrystals comprise also aspects that are significantly different from disordered systems due to their inherent long-range order. This is reflected in their distinct photon transport behaviour and in their beautiful well-defined diffraction patterns, for instance.

These experimental and theoretical studies on three-dimensional icosahedral photonic quasicrystals were inspired by the three-dimensional quasiperiodic patterns provided by nature, i.e., such quasicrystals have already been found in metallic alloys. However, our work on three-dimensional *rhombicuboctahedral* photonic quasicrystals went one step further: we introduced this novel class of three-dimensional photonic quasicrystals for the first time. After customising the cut-and-project method, we rationally constructed their blueprint and unique quasiperiodic configuration.

Correspondingly fabricated SU-8 samples revealed the anticipated eight-fold, six-fold and two-fold rotational symmetries in visible-light Laue diffraction experiments. This confirms the intrinsic rhombicuboctahedral symmetry of the samples. The Laue diffraction experiments as well as our experimental studies of transmittance and reflectance spectra and of time-resolved transmittance properties delivered results very similar to the icosahedral counterparts. The measured Laue diagrams showed clear dependence on the sample thickness. In transmittance and reflectance spectra, measured within a rather small finite opening angle, we obtained rather low values, as a significant amount of light is scattered into the residual solid angle. Finally, transmitted femtosecond pulses developed a long trailing tail, were strongly delayed and depolarised. The actual decay time constant, the delay and the amount of depolarised light were found to be dependent on the sample thickness and on the central wavelength of the probing pulse, i.e., on the characteristics of the actually probed photonic bands. These findings indicate the impact of multiply scattered light also for the optical properties of rhombicuboctahedral

photonic quasicrystals.

At first sight, the optical properties of these two classes of three-dimensional photonic quasicrystals, the icosahedral and the rhombicuboctahedral one, seem to be fairly similar. Quasiperiodicity provides a dense set of reciprocal lattice vectors for diffraction and multiple scattering of light dominates the photon propagation properties. Yet, we also expect subtle differences between the two classes due to their distinct quasiperiodic configurations and dielectric material distributions, manifesting in their different high-degree rotational symmetries. In analogy to the findings in two-dimensional photonic quasicrystals, the distribution of the dielectric material, in particular the minimal distance between the vertices of the quasiperiodic pattern with respect to the rod length, is supposed to strongly influence the formation mechanism of the photonic band structure and the related optical characteristics. This aspect could be investigated in future experimental studies by carefully comparing the peculiar optical properties and photonic transport characteristics of rhombicuboctahedral and icosahedral three-dimensional photonic quasicrystals. To support the analysis, we propose to construct adequate rational approximants of rhombicuboctahedral quasicrystals and to develop a theoretical model for their optical properties – equivalent to our model we have introduced for the icosahedral quasicrystals in the course of this thesis. Additionally, diligent examinations of the light wave mode profiles, e.g., at which of the (nonequivalent) quasilattice sites specific modes will be localised, might give further insights into the impact of the (local) symmetry aspect.

For these kinds of future studies, it will be advantageous to further decrease the rod length of rhombicuboctahedral and icosahedral photonic quasicrystals alike, down to approximately 750 nm. This will shift the anticipated fundamental pseudo-stop bands well inside the spectral range of conventionally available detectors for spectroscopy, such as silicon photodiode detectors or silicon charge-coupled-device cameras. Yet, the reduction to 1  $\mu\text{m}$  rod length that we have achieved in the course of this thesis, already posed a great challenge and required significant modifications of the conventional SU-8 post-exposure treatment. For further miniaturisation it is essential to prevent unwanted fusion of the elliptically shaped rods, especially in axial direction. One strategy might be the appropriate modification of the elliptical shape of the exposed volume via spatial manipulation of the electromagnetic field vectors of the exposing laser beam, similar to the principle exploited by the shaded-ring filter already in use. Additionally, each rod could be fabricated by exposing several slightly shifted lines with low intensity, which would add up to form the requested rod with a more circular cross-section. This procedure exploits the possibility of accumulating irradiation dose in the photoresist SU-8, when sequentially exposing it. Another strategy would be to replace the photoresist SU-8 by a photosensitive material with reduced shrinkage and without proximity effects, i.e., without unwanted accumulation of irradiation leading to unintended fusion of adjacent rods, especially in axial direction.

Presumably, decreasing the rod length will also facilitate the fabrication of three-dimensional icosahedral and rhombicuboctahedral photonic quasicrystals which are effectively thicker than those studied in this thesis – the effective thickness basically refers to the number of scattering centers along the light propagation direction and can be related to the rod length. Studying thicker samples is advantageous, as the unusual optical characteristics based on multiple scattering of light will be pronounced. Alternatively, multiple scattering effects could be enhanced by converting or inverting the polymeric photonic quasicrystals into high-refractive index materials. First steps along this road have already been shown in this work, as we have successfully

fabricated silicon inverse photonic quasicrystals.

Following our example of having created rhombicuboctahedral photonic quasicrystals for the first time, additional novel classes of three-dimensional quasicrystals exhibiting new kinds of (high-degree) symmetries could be rationally constructed. These newly constructed classes would expand the variety of three-dimensional photonic quasicrystals that are available for future studies on their unique optical properties, especially with regard to their specific high-degree rotational symmetries. Simultaneously, such a rational construction offers new flexible designs for tailoring photonic systems with distinct optical properties and photon propagation characteristics to meet the demands for certain optical applications. In future, three-dimensional photonic quasicrystals might provide the basis for novel lasing devices, complex waveguides or for sophisticated optical elements based on nonlinear interactions.

These suggestions for future work on the growing field of three-dimensional photonic quasicrystals show that it is an exciting and promising field of research, still in its early stages.



# Appendix A

## Shaded-Ring Filter and Voxel-Shape

The shaded-ring filter is basically a centred ring of reduced transmittance  $T$  with a certain inner and outer radius related to the angles  $\Theta_i$  and  $\Theta_a$ , schematically sketched in Fig. A.1. The shaded-ring filter is implemented into the optical setup such that a collimated light beam impinges on the shaded-ring filter and the transmitted light is focused into a (photosensitive) material by a focusing element, see also Ref. [89]. The shaded-ring filter is designed to reduce the elongation of the focus in axial direction, i.e., along the optical axis of the focusing element [18, 96, 97]. For appropriate parameters of the filter,  $\Theta_i$ ,  $\Theta_a$  and  $T$ , arising interference can considerably improve the axial resolution, while slightly worsening the lateral resolution at the same time, which will lead to a more spherical focus. However, one must also take into consideration that the arising interference also induces stronger side maxima in the intensity distribution. In the case of direct laser writing, such side maxima could expose the photoresist unintentionally well off the actual focus.

The shape of the focus, in particular, the distribution of the electromagnetic field in the focus region of the focusing element is calculated adopting the vectorial electromagnetic diffraction theory by Török *et al.* [87, 88], considering an interface with mismatched refractive indices while focusing into a homogeneous medium. The properties of the shaded-ring filter are implemented into the electromagnetic field calculations by modifying the amplitude of the incident field depending on the corresponding angular positions. For more detailed information about the applied electromagnetic diffraction theory, we refer to the publications of Richards and Wolf [98], Török *et al.* [87, 88] or M. Deubel [84], respectively.

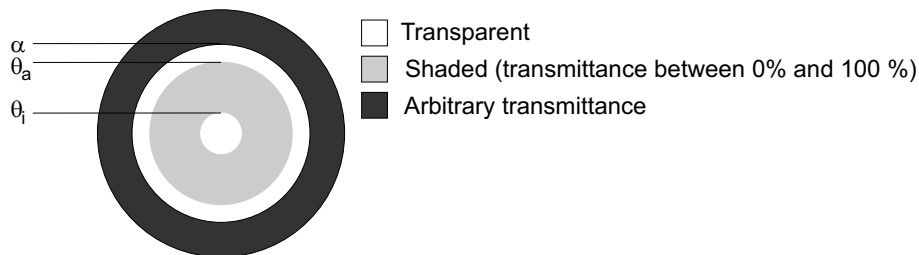


Figure A.1: Schematic sketch of the shaded-ring filter.  $\Theta_i$  and  $\Theta_a$  represent the angles referring to the inner and outer radius of the ring with respect to the opening angle  $\alpha$  of the focusing lens and its respective pupil diameter.

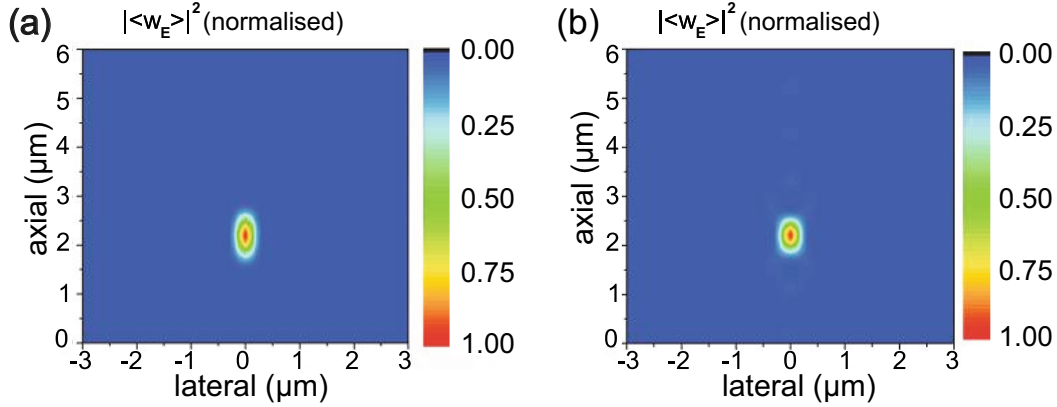


Figure A.2: Focusing via a microscope objective of NA=1.4 into SU-8 ( $n \approx 1.58$ ), the normalised square of the time-averaged electric energy density  $|\langle w_E \rangle|^2$  without the shaded-ring filter (a) and with the shaded-ring filter (b) is illustrated in colour code. The incident laser pulse is focused 2.2  $\mu\text{m}$  deep into SU-8 (in axial direction). A clear improvement of the elliptical shape of the focus and thus the voxel, i.e., a reduction of the ratio  $\chi$ , is visible.

The calculated electromagnetic field distribution indicates the elliptical shape of the focus, defined by the ratio  $\chi$  of axial and lateral extension of the focus. Focusing without the shaded-ring filter into a photosensitive material (here, SU-8,  $n \approx 1.58$ ) with the particular microscope objective (NA=1.4) used in the direct laser writing setup (described in section 4.1), the expected ratio  $\chi$  is 2.7, according to Ref. [84]. A suitable design of the shaded-ring filter with transmittance  $T = 10.21\%$  and an inner and outer radius corresponding to  $\Theta_i = 12^\circ$  and  $\Theta_a = 65.9^\circ$ , can reduce the ratio  $\chi$  theoretically by a factor of 1.5. This is illustrated in Fig. A.2 (a) without shaded-ring filter and Fig. A.2 (b) with such a shaded-ring filter, for the case of a microscope objective (NA=1.4) focusing into SU-8 ( $n \approx 1.58$ ). In this graph, the time-averaged electric energy density squared  $|\langle w_E \rangle|^2$  normalised to the maximum value in the focus is plotted colour-coded in the plane containing the optical axis. The square of the time-averaged electric energy density is assumed to reflect the exposed volume in the photoresist via two-photon absorption and thus the shape of the corresponding focus.

Please note that the actual voxel size obtained by direct laser writing depends on the adjusted intensity of the exposing laser pulse and the pulse width, since the relative position of the exposing threshold value shifts accordingly [84].

The shaded-ring filter itself is experimentally realised by manufacturing a ring of gold (of several nm thickness) on a glass substrate (BK7 glass, 20 mm diameter, 2 mm thickness).

More information can be found in Ref. [89].

# Bibliography

- [1] E. Yablonovitch, *Inhibited Spontaneous Emission in Solid-State Physics and Electronics*, Phys. Rev. Lett. **58** (20), p. 2059 (1987)
- [2] S. John, *Strong Localization of Photons in Certain Disordered Dielectric Superlattices*, Phys. Rev. Lett. **58** (23), p. 2486 (1987)
- [3] P. W. Anderson, *Absence of Diffusion in Certain Random Lattices*, Phys. Rev. **109** (5), p. 1492 (1958)
- [4] A. A. Asatryan, P. A. Robinson, R. C. McPhedran, L. C. Botten, C. Martijn de Sterke, T. L. Langtry, and N. A. Nicorovici, *Diffusion and anomalous diffusion of light in two-dimensional photonic crystals*, Phys. Rev. E **67** (3), p. 036 605 (2003)
- [5] D. Shechtman, I. Blech, D. Gratias, and J. W. Cahn, *Metallic Phase with Long-Range Orientational Order and No Translational Symmetry*, Phys. Rev. Lett. **53** (20), p. 1951 (1984)
- [6] K. Sakoda, *Optical Properties of Photonic Crystals*, Springer Series in Optical Sciences, vol. 80 (Springer-Verlag, Berlin, 2005)
- [7] J. D. Joannopoulos, R. D. Meade, and J. N. Winn, *Photonic Crystals: Molding the Flow of Light* (Princeton University Press, Princeton, NJ, 1995)
- [8] D. S. Wiersma, P. Bartolini, A. Lagendijk, and R. Righini, *Localization of light in a disordered medium*, Nature (London) **390** (6661), p. 671 (1997)
- [9] A. Taflove and M. E. Brodwin, *Numerical Solution of Steady-State Electromagnetic Scattering Problems Using the Time-Dependent Maxwell's Equations*, IEEE Trans. Microwave Theory and Techniques **23** (8), p. 623 (1975)
- [10] A. Taflove and S. C. Hagness, *Computational electrodynamics: the finite-difference time-domain method*, second edition (Boston, MA, London: Artech House, 2000)
- [11] N. W. Ashcroft and N. D. Mermin, *Solid State Physics*, Int. ed. (Harcourt Brace College Publishers, Fort Worth, 1976)
- [12] S. G. Johnson and J. D. Joannopoulos, *Block-iterative frequency-domain methods for Maxwell's equations in a planewave basis*, Opt. Express **8** (3), p. 173 (2001)
- [13] K. Busch and S. John, *Photonic band gap formation in certain self-organizing systems*, Phys. Rev. E **58** (3), p. 3896 (1998)

- [14] D.M. Whittaker and I.S. Culshaw, *Scattering-matrix treatment of patterned multilayer photonic structures*, Phys. Rev. B **60** (4), p. 2610 (1999)
- [15] S.G. Tikhodeev, A.L. Yablonskii, E.A. Muljarov, N.A. Gippius, and T. Ishihara, *Quasiguidded modes and optical properties of photonic crystal slabs*, Phys. Rev. B **66** (4), p. 045 102 (2002)
- [16] K.M. Ho, C.T. Chan, and C.M. Soukoulis, *Existence of a photonic gap in periodic dielectric structures*, Phys. Rev. Lett. **65** (25), p. 3152 (1990)
- [17] S. Noda, K. Tomoda, N. Yamamoto, and A. Chutinan, *Full three-dimensional photonic bandgap crystals at near-infrared wavelengths*, Science **289** (5479), p. 604 (2000)
- [18] M. Hermatschweiler, A. Ledermann, G.A. Ozin, M. Wegener, and G. von Freymann, *Fabrication of silicon inverse woodpile photonic crystals*, Adv. Funct. Mater. **17** (14), p. 2273 (2007)
- [19] K. Busch, S. Lölkes, R. B. Wehrspohn, and H. Föll (eds.), *Photonic Crystals: Advances in Design, Fabrication, and Characterization* (Wiley-VCH, Weinheim, 2004)
- [20] K. Inoue und K. O. (eds.), *Photonic Crystals: Physics, Fabrication and Applications*, Springer Series in Optical Sciences, vol. 94 (Springer-Verlag, Berlin, 2004)
- [21] K. Busch, G. von Freymann, S. Linden, S.F. Mingaleev, L. Tkeshelashvili, and M. Wegener, *Periodic nanostructures for photonics*, Phys. Rep. **444** (3-6), p. 101 (2007)
- [22] C. Janot, *Quasicrystals: A Primer* (Clarendon Press, Oxford, 1992)
- [23] S.H. Tseng, Y.L. Kim, A. Taflove, D. Maitland, V. Backman, and J.T. Walsh, Jr., *Simulation of enhanced backscattering of light by numerically solving Maxwell's equations without heuristic approximations*, Opt. Express **13** (10), p. 3666 (2005)
- [24] M.I. Mishchenko, L. Liu, D.W. Mackowski, B. Cairns, and G. Videen, *Multiple scattering by random particulate media: exact 3D results*, Opt. Express **15** (6), p. 2822 (2007)
- [25] S. Zhang, B. Hu, P. Sebbah, and A.Z. Genack, *Speckle Evolution of Diffusive and Localized Waves*, Phys. Rev. Lett. **99** (6), p. 063 902 (2007)
- [26] P.E. Wolf and G. Maret, *Weak localization and coherent backscattering of photons in disordered media*, Phys. Rev. Lett. **55** (24), p. 2696 (1985)
- [27] D.S. Wiersma, M.P. van Albada, B.A. van Tiggelen, and A. Lagendijk, *Experimental Evidence for Recurrent Multiple Scattering Events of Light in Disordered Media*, Phys. Rev. Lett. **74** (21), p. 4193 (1995)
- [28] A.Z. Genack, *Optical Transmission in Disordered Media*, Phys. Rev. Lett. **58** (20), p. 2043 (1987)
- [29] P.M. Johnson, S. Faez, and A. Lagendijk, *Full characterization of anisotropic diffuse light*, Opt. Express **16** (10), p. 7435 (2008)

- [30] T. Schwartz, G. Bartal, S. Fishman, and M. Segev, *Transport and Anderson localization in disordered two-dimensional photonic lattices*, Nature (London) **446** (7131), p. 52 (2007)
- [31] N. Garcia, A. Z. Genack, and A. A. Lisyansky, *Measurement of the transport mean free path of diffusing photons*, Phys. Rev. B **46** (22), p. 14 475 (1992)
- [32] M. Reufer, L. F. Rojas-Ochoa, S. Eiden, J. J. Sáenz, and F. Scheffold, *Transport of light in amorphous photonic materials*, Appl. Phys. Lett. **91** (17), p. 171 904 (2007)
- [33] N. Garcia and A. Z. Genack, *Anomalous Photon Diffusion at the Treshold of the Anderson Localization Transition*, Phys. Rev. Lett. **66** (14), p. 1850 (1991)
- [34] A. F. Ioffe and A. R. Regel, *Non-crystalline, amorphous, and liquid electronic semiconductors*, Prog. Semicond. **4**, p. 237 (1960)
- [35] G. Mie, *Beiträge zur Optik trüber Medien, speziell kolloidaler Metallösungen*, Ann. Phys. Lpz. **330** (3), p. 377 (1908)
- [36] D. S. Wiersma, *The physics and applications of random lasers*, Nature Phys. **4** (5), p. 359 (2008)
- [37] J. Fallert, R. J. B. Dietz, J. Sartor, D. Schneider, C. Klingshirn, and H. Kalt, *Co-existence of strongly and weakly localized random laser modes*, Nature Photon. **3** (5), p. 279 (2009)
- [38] P. Kramer and Z. Papadopoulos (Eds.), *Coverings of Discrete Quasiperiodic Sets: Theory and Applications to Quasicrystals*, Springer Tracts in Modern Physics, vol. 180 (Springer-Verlag, Berlin, 2002)
- [39] D. Levine and P. J. Steinhardt, *Quasicrystals. I. Definition and structure*, Phys. Rev. B **34** (2), p. 596 (1986)
- [40] U. Grimm and M. Schreiber, *Aperiodic Tilings on the Computer*, arXiv:cond-mat p. 9903010v1 (1999)
- [41] M. Baake, *A Guide to Mathematical Quasicrystals*, arXiv:math-ph p. 9901014 v1 (1999)
- [42] M. Baake, U. Grimm, and R. V. Moody, *What is Aperiodic Order?*, arXiv:math.HO p. 0203252v1 (2002)
- [43] L. Fibonacci, *Liber abaci* (1202)
- [44] A. Ledermann, G. von Freymann, and M. Wegener, *Laue-Beugung auf dem Schreibtisch. Photonische Quasikristalle*, Physik in unserer Zeit **38** (6), p. 300 (2007)
- [45] L. Bindi, P. J. Steinhardt, N. Yao, and P. J. Lu, *Natural Quasicrystals*, Science **324** (5932), p. 1306 (2009)
- [46] W. Steurer and D. Sutter-Widmer, *Photonic and phononic quasicrystals*, J. Phys. D: Appl. Phys. **40** (13), p. R229 (2007)
- [47] D. Levine and P. J. Steinhardt, *Quasicrystals: a new class of ordered structures*, Phys. Rev. Lett. **53** (26), p. 2477 (1984)

- [48] A. Ledermann, Three-Dimensional Icosahedral Photonic Quasicrystals: Fabrication via Direct Laser Writing and Optical Characterization, Diplomarbeit, Universität Karlsruhe (TH) (August 2006)
- [49] A. Ledermann, L. Cademartiri, M. Hermatschweiler, C. Toninelli, G. A. Ozin, D. S. Wiersma, M. Wegener, and G. von Freymann, *Three-dimensional silicon inverse photonic quasicrystals for infrared wavelengths*, *Nature Mater.* **5** (12), p. 942 (2006)
- [50] A. W. Rodriguez, A. P. McCauley, Y. Avniel, and S. G. Johnson, *Computation and visualization of photonic quasicrystal spectra via Bloch's theorem*, *Phys. Rev. B* **77** (10), p. 104 201 (2008)
- [51] M. Kohmoto, B. Sutherland, and K. Iguchi, *Localization of optics: Quasiperiodic media*, *Phys. Rev. Lett.* **58** (23), p. 2436 (1987)
- [52] K. Wang, *Light wave states in two-dimensional quasiperiodic media*, *Phys. Rev. B* **73** (23), p. 235 122 (2006)
- [53] K. Mnaymneh and R. C. Gauthier, *Mode localization and band-gap formation in defect-free photonic quasicrystals*, *Opt. Express* **15** (8), p. 5089 (2007)
- [54] W. Gellermann, M. Kohmoto, B. Sutherland, and P. C. Taylor, *Localization of Light Waves in Fibonacci Dielectric Multilayers*, *Phys. Rev. Lett.* **72** (5), p. 633 (1994)
- [55] T. Hattori, N. Tsurumachi, S. Kawato, and H. Nakatsuka, *Photonic dispersion relation in a one-dimensional quasicrystal*, *Phys. Rev. B* **50** (6), p. 4220 (1994)
- [56] J. Hendrickson, B. C. Richards, J. Sweet, G. Khitrova, A. N. Poddubny, E. L. Ivchenko, M. Wegener, and H. M. Gibbs, *Excitonic polaritons in Fibonacci quasicrystals*, *Opt. Express* **16** (20), p. 15 382 (2008)
- [57] L. Dal Negro, M. Stolfi, Y. Yi, J. Michel, X. Duan, L. C. Kimerling, J. LeBlanc, and J. Haavisto, *Photon band gap properties and omnidirectional reflectance in Si/SiO<sub>2</sub> Thue-Morse quasicrystals*, *Appl. Phys. Lett.* **84** (25), p. 5186 (2004)
- [58] S. S. M. Cheng, L.-M. Li, C. T. Chan, and Z. Q. Zhang, *Defect and transmission properties of two-dimensional quasiperiodic photonic band-gap systems*, *Phys. Rev. B* **59** (6), p. 4091 (1999)
- [59] C. Jin, B. Cheng, B. Man, Z. Li, D. Zhang, S. Ban, and B. Sun, *Band gap and wave guiding effect in a quasiperiodic photonic crystal*, *Appl. Phys. Lett.* **75** (13), p. 1848 (1999)
- [60] M. E. Zoorob, M. D. B. Charlton, G. J. Parker, J. J. Baumberg, and M. C. Netti, *Complete photonic bandgaps in 12-fold symmetric quasicrystals*, *Nature (London)* **404** (6779), p. 740 (2000)
- [61] G. Zito, B. Piccirillo, E. Santamato, A. Marino, V. Tkachenko, and G. Abbate, *Two-dimensional photonic quasicrystals by single beam computer-generated holography*, *Opt. Express* **16** (8), p. 5164 (2008)

- [62] Y. Roichman and D. G. Grier, *Holographic assembly of quasicrystalline photonic heterostructures*, Opt. Express **13** (14), p. 5434 (2005)
- [63] W. Man, M. Megens, P. J. Steinhardt, and P. M. Chaikin, *Experimental measurement of the photonic properties of icosahedral quasicrystals*, Nature (London) **436** (7053), p. 993 (2005)
- [64] J. Xu, R. Ma, X. Wang, and W. Y. Tam, *Icosahedral quasicrystals for visible wavelengths by optical interference holography*, Opt. Express **15** (7), p. 4287 (2007)
- [65] I. Bitá, T. Choi, M. E. Walsh, H. I. Smith, and E. L. Thomas, *Large-Area 3D Nanostructures with Octagonal Quasicrystalline Symmetry via Phase-Mask Lithography*, Adv. Mater. **19** (10), p. 1403 (2007)
- [66] D. Shir, H. Liao, S. Jeon, D. Xiao, H. T. Johnson, G. R. Bogart, K. H. A. Bogart, and J. A. Rogers, *Three-Dimensional Nanostructures Formed by Single Step, Two-Photon Exposures through Elastomeric Penrose Quasicrystal Phase Masks*, Nano Lett. **8** (8), p. 2236 (2008)
- [67] M. C. Rechtsman, H.-C. Jeong, P. M. Chaikin, S. Torquato, and P. J. Steinhardt, *Optimized Structures for Photonic Quasicrystals*, Phys. Rev. Lett. **101** (7), p. 73 902 (2008)
- [68] X. Zhang, Z.-Q. Zhang, and C. T. Chan, *Absolute photonic band gaps in 12-fold symmetric photonic quasicrystals*, Phys. Rev. B **63** (8), p. 081 105 (2001)
- [69] M. Hase, H. Miyazaki, M. Egashira, N. Shinya, K. M. Kojima, and S. Uchida, *Isotropic photonic band gap and anisotropic structures in transmission spectra of two-dimensional fivefold and eightfold symmetric quasiperiodic photonic crystals*, Phys. Rev. B **66** (21), p. 214 205 (2002)
- [70] J. Yin, X. Huang, S. Liu, and S. Hu, *Photonic bandgap properties of 8-fold symmetric photonic quasicrystals*, Opt. Commun. **269** (2), p. 385 (2007)
- [71] M. Notomi, H. Suzuki, T. Tamamura, and K. Edagawa, *Lasing Action due to the Two-Dimensional Quasiperiodicity of Photonic Quasicrystals with a Penrose Lattice*, Phys. Rev. Lett. **92** (12), p. 123 906 (2004)
- [72] M. H. Kok, W. Lu, W. Y. Tam, and G. K. L. Wong, *Lasing from dye-doped icosahedral quasicrystals in dichromate gelatin emulsions*, Opt. Express **17** (9), p. 7275 (2009)
- [73] B. Freedman, G. Bartal, M. Segev, R. Lifshitz, D. N. Christodoulides, and J. W. Fleischer, *Wave and defect dynamics in nonlinear photonic quasicrystals*, Nature (London) **440** (7088), p. 1166 (2006)
- [74] S.-N. Zhu, Y.-Y. Zhu, and N.-B. Ming, *Quasi-Phase-Matched Third-Harmonic Generation in a Quasi-Periodic Optical Superlattice*, Science **278** (5339), p. 843 (1997)
- [75] S.-N. Zhu, Y.-Y. Zhu, Y.-Q. Qin, H.-F. Wang, C.-Z. Ge, and N.-B. Ming, *Experimental Realization of Second Harmonic Generation in a Fibonacci Optical Superlattice of LiTaO<sub>3</sub>*, Phys. Rev. Lett. **78** (14), p. 2752 (1997)

- [76] F. Xu, J.-L. He, J. Liao, Q. Wang, Q. Xu, N.-H. Shen, H.-T. Wang, and N. B. Ming, *Simultaneous high-efficiency and equal-level second- and third-harmonic generation achieved by controllable linear gratings in a quasiperiodic optical superlattice*, Phys. Rev. A **68** (5), p. 053 803 (2003)
- [77] R. T. Bratfalean, A. C. Peacock, N. G. R. Broderick, K. Gallo, and R. Lewen, *Harmonic generation in a two-dimensional nonlinear quasi-crystal*, Opt. Lett. **30** (4), p. 424 (2005)
- [78] A. Bahabad, A. Ganany-Padowicz, and A. Arie, *Engineering two-dimensional nonlinear photonic quasi-crystals*, Opt. Lett. **33** (12), p. 1386 (2008)
- [79] Z. S. Zhang, B. Zhang, J. Xu, K. Xu, Z. J. Yang, Z. X. Qin, T. J. Yu, and D. P. Yu, *Effects of symmetry of GaN-based two-dimensional photonic crystal with quasicrystal lattices on enhancement of surface light extraction*, Appl. Phys. Lett. **88** (17), p. 171 103 (2006)
- [80] M. Zoorob and G. Flinn, *Photonic quasicrystals boost LED emission characteristics*, LEDs Magazine **08**, p. 21 (2006)
- [81] F. H. Li and L. C. Wang, *Analytical formulation of icosahedral quasi-crystal structures*, J. Phys. C **21** (3), p. 495 (1988)
- [82] A. Ledermann, M. Wegener, and G. von Freymann, *Rhombicuboctahedral three-dimensional photonic quasicrystals*, Adv. Mater., accepted (2009)  
[DOI: 10.1002/adma.200903885]
- [83] K. M. Ho, C. T. Chan, C. M. Soukoulis, R. Biswas, and M. Sigalas, *Photonic band gaps in three dimensions: New layer-by-layer periodic structures*, Solid State Commun. **89** (5), p. 413 (1994)
- [84] M. Deubel, *Three-Dimensional Photonic Crystals via Direct Laser Writing: Fabrication and Characterization*, Dissertation, Universität Karlsruhe (TH) (February 2006)
- [85] G. von Freymann, A. Ledermann, M. Thiel, I. Staude, S. Essig, K. Busch, and M. Wegener, *Three-Dimensional Nanostructures for Photonics*, Adv. Funct. Mater., accepted (2009) [DOI: 10.1002/adfm.200901838]
- [86] M. Deubel, G. von Freymann, M. Wegener, S. Pereira, K. Busch, and C. M. Soukoulis, *Direct laser writing of three-dimensional photonic-crystal templates for telecommunications*, Nature Mater. **3** (7), p. 444 (2004)
- [87] P. Török, P. Varga, and G. R. Booker, *Electromagnetic diffraction of light focused through a planar interface between materials of mismatched refractive indices: structure of the electromagnetic field. I*, J. Opt. Soc. Am. A **12** (10), p. 102 136 (1995)
- [88] P. Török and P. Varga, *Electromagnetic diffraction of light focused through a stratified medium*, Appl. Opt. **36** (11), p. 112 305 (1997)
- [89] *European Patent No. DE 102007032181A1 / WO 002009006976A1: Optical arrangement and its use* (2009)

- [90] U. S. Patent No. 4882245 (1989)
- [91] A. Ledermann, D. S. Wiersma, M. Wegener, and G. von Freymann, *Multiple scattering of light in three-dimensional photonic quasicrystals*, Opt. Express **17** (3), p. 1844 (2009)
- [92] J. T. Roesener, Nahfeldmikroskopie an 3D Photonischen Kristallen, Diplomarbeit, Universität Karlsruhe (TH) (September 2007)
- [93] D. C. Meisel, M. Diem, M. Deubel, F. Pérez-Willard, S. Linden, D. Gerthsen, K. Busch, and M. Wegener, *Shrinkage Pre-Compensation of Holographic Three-Dimensional Photonic Crystal Templates*, Adv. Mat. **18** (22), p. 2964 (2006)
- [94] A. F. Koenderink, A. Lagendijk, and W. L. Vos, *Optical extinction due to intrinsic structural variations of photonic crystals*, Phys. Rev. B **72** (15), p. 153 102 (2005)
- [95] M. Kallenberg, Zeitaufgelöste Spektroskopie an Drei-Dimensionalen Photonischen Quasikristallen, Diplomarbeit, Universität Karlsruhe (TH) (July 2009)
- [96] M. Martínez-Corral, C. Ibáñez-López, G. Saavedra, and M. T. Caballero, *Axial gain resolution in optical sectioning fluorescence microscopy by shaded-ring filters*, Opt. Express **11** (15), p. 1740 (2003)
- [97] C. Ibáñez-López, G. Saavedra, G. Boyer, and M. Martínez-Corral, *Quasi-isotropic 3-D resolution in two-photon scanning microscopy*, Opt. Express **13** (16), p. 6168 (2005)
- [98] B. Richards and E. Wolf, *Electromagnetic diffraction in optical systems. II. Structure of the image field in an aplanatic system*, Proc. R. Soc. London, Ser. A **253** (1274), p. 358 (1959)



# Acknowledgements

At this place, it is a great pleasure for me to thank all the people who have supported me and contributed to the success of this thesis in various manners.

First of all, I would like to express my gratitude to Prof. Dr. Martin Wegener for giving me the opportunity to work in his group on this new and exciting field of photonic quasicrystals. I am very thankful for the excellent working conditions concerning not only the experimental facilities and laboratory equipment, but also his unique ability to guide the activities of the group and to promote the research projects by his precious advice and his profound knowledge in the field of optics and photonics. I am also very grateful for having received the opportunity to present my results on several international conferences.

I thank Prof. Dr. Kurt Busch for kindly agreeing to co-referee this thesis. I like to thank Dr. Georg von Freymann for supervising and supporting my research project within his DFG Emmy-Noether group. He has granted me autonomy during my work and simultaneously supported my progress by giving helpful advice and assistance, whenever necessary. I appreciate the pleasant and productive collaboration. Additionally, my thanks go to my colleague Isabelle Staude for her substantial contribution in rebuilding the sophisticated direct laser writing setup after the laboratory relocation.

I thank all the members of the Wegener group for their team spirit and their helpful discussions, which adds to the welcome and pleasant working atmosphere. It has also been a great pleasure to work with the diploma student Michael Renner, who will carry on with my studies on the field of aperiodic photonic structures and who has operated the time-resolved transmittance spectroscopy setup for the measurements on rhombicuboctahedral quasicrystals.

Furthermore, I want to thank Dr. Costanza Toninelli and Prof. Dr. Diederik S. Wiersma for the fruitful cooperation in performing time-resolved transport measurements in Florence and for discussing the obtained results.

My thanks also go to several facilities of the Karlsruhe Institute of Technology. I thank the secretariats of the two institutes I have worked with during my thesis, in particular, I thank Renate Helfen, Christa Weisenburger (retd.), Gisela Habitzreither and Monika Brenkmann of the Institute for Applied Physics and Erika Schütze of the Institute of Nanotechnology for their friendly and permanent support. Likewise, I give thanks to the electronics and the mechanics workshop of the Institute for Applied Physics as well as to the technicians Thorsten Kuhn (†) and Johann Westhauser for their reliable support. Furthermore, I want to thank Patrice Brenner, Erich Müller and Jacques Hawecker for operating the focused ion-beam cutting and the scanning electron microscope, and Daniel Weissenberger and Jacques Hawecker for running the two-dimensional laserlithography system required in the fabrication process of the shaded-

ring filter. I also thank the Karlsruhe School of Optics & Photonics (KSOP) and the DFG-Center for Functional Nanostructures (CFN) for the support during my thesis.

My thanks go to all critical readers of this thesis who have helped to improve its readability and comprehensibility.

Last, but definitely not least, I want to thank my parents, as well as my brothers, my sister and my friends, for their permanent support during my work and for their continuous interest in my progress. A special thank goes to Andreas Walter for his enduring support and encouragement, especially in the final year of my thesis.